UILU-ENG 89-3605

Report No. 151

A VARIABLE AMPLITUDE MULTIAXIAL FATIGUE LIFE PREDICTION METHOD

by

Julie Ann Bannantine
Department of Materials Science and Engineering

A Report of the

MATERIALS ENGINEERING—MECHANICAL BEHAVIOR

College of Engineering, University of Illinois at Urbana-Champaign

October 1989

A VARIABLE AMPLITUDE MULTIAXIAL FATIGUE LIFE PREDICTION METHOD

Julie Ann Bannantine, Ph.D.
Department of Mechanical and Industrial Engineering
University of Illinois at Urbana-Champaign, 1989

ABSTRACT

A method to estimate the fatigue life of a component subjected to variable amplitude multiaxial loading has been developed. It is based upon an extension of the strain-life approach which achieved success in correlating the fatigue lives of components subjected to uniaxial variable amplitude loading. In addition, it incorporates multiaxial damage models that relate fatigue damage to remote loading parameters. A computer model was developed to implement the proposed method.

Measured or estimated strain histories are used as input in the method. Corresponding stress histories are calculated using a nonproportional cyclic plasticity model. Damage is calculated using the stress and strain histories and the multiaxial damage models. The plane experiencing the maximum damage is identified as the critical plane and the fatigue life of the component is estimated from the damage calculations on this plane.

Experimental test results were used to verify and evaluate the proposed method. The measured stress-strain response of thin wall tubes loaded in combined tension and torsion was used to verify the nonproportional cyclic plasticity model. Good correlation between predicted and measured responses was observed. Results from tests conducted on SAE 1045 steel components, loaded in bending, proportional bending and torsion, and nonproportional bending and torsion, were used to evaluate the overall method. Again, good correlation between predicted and actual fatigue lives was achieved.

The computer model was also used to gain a better understanding of the local stress and strain states developed under nonproportional cyclic multiaxial

loading and the effects of this loading on fatigue life. Observations and examples leading to this increased understanding are presented.

ACKNOWLEDGMENTS

This research was supported by the Fracture Control Program at the University of Illinois at Urbana-Champaign. Additional funding and support were provided by Deere and Company.

Darrell Socie, thesis advisor, is acknowledged for the initial idea to begin this work and for his thought-provoking discussions during the course of it. He is thanked for providing opportunities and support for technical development during the course of my graduate career. Tom Cordes, of Deere and Company, is thanked for his constant care and attention to the data collection. His interest and support of this work were very much appreciated. Phil Dindinger, of Radian Corporation, is acknowledged for conducting the nonproportional variable amplitude tests. His thoroughness and attention to detail were also appreciated. Additionally, Swami Subramanian and Peter Kurath are acknowledged for the use of the SAE 1045 steel thin-wall tube data.

My fellow graduate students are thanked for their friendship and encouragement. Shiing Hwa Doong and Dave Jones are thanked for their friendship and helpful discussions related to this work. Jim Handrock and Jess Comer are especially thanked for their support and perspective on this research and for their sense of humor during the long hours of working on the book.

My parents are sincerely thanked for their constant support and love. It has been through their example that I have learned the most, including the will to persevere. Finally and most importantly, an immeasurable debt of gratitude is due my husband, Sandy Parlier. His unselfish sacrifice and unfaltering love have allowed this work to be completed.

TABLE OF CONTENTS

LIST OF TABLES

LIST OF FIGURES

1. INTRODUCTION AND OBJECTIVE

Engineering components are often subjected to complicated states of stress and strain. Complex stress states--stress states in which the three principal stresses are nonproportional or whose directions change during a loading cycle--very often occur at geometric discontinuities such as notches or joint connections. Fatigue under these conditions, termed multiaxial fatigue, is important both from the viewpoint of the original design and from the need to evaluate or assess the fatigue life of a component once in service. It is an important consideration for the reliable operation and optimization of engineering components and structures.

The objective of this research has been to develop and implement a method for estimating the fatigue life of a component subjected to variable amplitude multiaxial loading. Specifically, the aim has been to assess the variable amplitude multiaxial fatigue life using strain information, obtained either experimentally or analytically, as input.

A proposed methodology has been developed to meet this objective. It is based upon an extension of the uniaxial variable amplitude fatigue life prediction method which is reviewed in Chapter 2. Incorporated in the proposed method are damage models which have been developed as a result of recent multiaxial fatigue research. These damage models, which relate the fatigue damage to bulk loading parameters, are also discussed in Chapter 2.

Chapter 3 provides the details of the proposed methodology, as well as a description of the computer code written to implement the procedure. From the measured or estimated strain histories, corresponding stress histories must be predicted for use in the damage models. This requires a cyclic nonproportional plasticity model. Details of the plasticity model are given in this chapter. From the stress and strain histories, the damage on each plane is calculated using

the multiaxial damage models. The plane experiencing the maximum damage is identified as the critical plane for the nucleation and early growth of fatigue cracks. The fatigue life of the component is then predicted using the damage calculations on this plane. Details of the method and the manner of implementation are provided.

Experimental tests results have been used to verify the computer program and evaluate the proposed method. Results obtained from tests of thin wall tubes subjected to tension and torsion are used to verify the plasticity model. SAE 1045 steel components, tested in bending, proportional bending and torsion, and nonproportional bending and torsion, have been used to evaluate the method. Details of the experimental procedures, materials, and test results are given in Chapter 4. Strain histories obtained in these tests have been used as input into the computer code. The estimated fatigue lives obtained from the computer code have then been compared to the experimental values. Results of the analyses are presented in Chapter 5. An evaluation of the methodology, as well as general comments and observations, are discussed.

In addition to allowing an evaluation of the proposed method to be made, the computer code allowed example loading cases to be studied in order to better understand the local stress and strain states developed under nonproportional cyclic multiaxial loading and the effects on fatigue life predictions. Observations and examples leading to this increased understanding are provided in Chapter 6.

Finally, the major conclusions and observations made in this work are summarized in Chapter 7.

2. BACKGROUND

Current research has led to an increased understanding of the behavior of materials subjected to multiaxial loading. Along with the knowledge gained in the study of uniaxial variable amplitude fatigue, this understanding provides a basis from which to attempt to develop a variable amplitude multiaxial fatigue life prediction method. This chapter presents a review of the background pertinent to the development of such a method.

First, a very brief review of the strain-life approach is presented. This approach was successfully used to estimate the fatigue lives of components subjected to uniaxial variable amplitude loading. A summary of observations made of material behavior developed under multiaxial loading is then given. Multiaxial damage models are subsequently discussed and compared in light of this understanding. Finally, a brief discussion is presented on suggested variable amplitude multiaxial fatigue life prediction approaches.

2.1 Uniaxial Variable Amplitude Fatigue Life Estimations

In the mid 1970's, techniques were developed and relative success was achieved in estimating the fatigue lives of components subjected to uniaxial variable amplitude loading using the strain-life approach. Ref [2.1] is a compendium of ten papers that compares the results of life predictions to experimental uniaxial variable amplitude fatigue data.

A schematic outline of the information needed in a strain-life approach is presented in Fig. 2.1. Basically, the following items are needed:

1. Material properties
2. Loading information
3. Component geometry
4. Analysis techniques

The strain-life approach has gained acceptance as a useful fatigue life estimation method, and information and discussion concerning each of these four items may be found in the literature. Both the American Society for Testing and Materials (ASTM) and the Society of Automotive Engineers (SAE) have recommended procedures and practices for conducting strain-controlled tests and using this data to predict fatigue life [2.2-2.4].

Because the strain-life method has achieved relatively good success in predicting the fatigue lives of components subjected to uniaxial variable amplitude loading, it provides a reasonable basis from which to attempt to develop a multiaxial variable amplitude fatigue life estimation procedure. An understanding of multiaxial material response, as well as methods to relate the multiaxial damage to the applied loading, are also required in the attempt to extend this theory. These topics are discussed in the following section.

2.2 Multiaxial Fatigue

2.2.1 Introduction

A primary consideration in the development of multiaxial fatigue damage models is the need to reconcile the analytical approaches with observed material behavior. The following section first presents observations of material behavior under multiaxial loading, including the stress-strain response of materials loaded nonproportionally as well as the observed fatigue damage in materials subjected to tension, torsion, and combined loading. Proposed

multiaxial damage models and theories are then discussed and compared in light of these observations.

2.2.2 Observed Material Behavior

2.2.2.1 Stress-Strain Response

Researchers and engineers initially thought that components subjected to proportional loading would exhibit shorter fatigue lives than components loaded nonproportionally. In other words, it was thought that proportional loading was more damaging than nonproportional loading. Neglecting a phase difference between normal and shear stresses or strains was therefore thought to be a conservative approach. Results of more recent tests show that this is usually only true for components tested in load control [2.5,2.6]. Results of combined tension-torsion strain-controlled tests have shown that out-of-phase loading (the peak shear strain lags or leads the peak tensile strain by some phase angle), especially at high load levels, is more damaging than in-phase loading. Kanazawa [2.7] was one of the first to report that a phase angle of 90 degrees gave the shortest fatigue lives, while in-phase cyclic straining resulted in the longest fatigue lives when tested at the same maximum shear strain range.

The reason for this difference between strain controlled and load controlled tests can be explained by the nonproportional hardening exhibited by many materials as described below.

The stress-strain response of a material subjected to multiaxial loading may differ dramatically from the uniaxial stress-strain response. A significant increase in hardening is observed for some materials when loaded nonproportionally. This phenomenon, termed nonproportional hardening, is an increase in the cyclically stable stress response for a material loaded

nonproportionally compared to the uniaxial cyclically stable stress response when loaded to the same effective strain level.

Initially, Kanazawa et al., [2.7] attributed this increase in hardening to an increase in dislocation interactions. However, they made no mention that the amount of hardening was material dependent. Recent work has been done that shows that the stress response of a material tested under nonproportional loading depends upon the dislocation substructure formed [2.8-2.10]. The type of dislocation substructure formed is, in turn, material dependent. Materials such as stainless steels and copper show a 30-50% increase in the stable stress response compared to the uniaxial or torsional stress response, while materials such as pure aluminum and 7075 aluminum exhibit little nonproportional hardening.

The reason for this material dependency can be traced to the ease of cross slip [2.8]. In materials such as stainless steel and copper, where cross slip is difficult (wavy or wavy/planar slip materials), single slip structures form under uniaxial loading. When the loading remains proportional, and the major slip plane remains fixed, the amount of secondary slip depends upon the applied strain range. As the strain range increases, the amount of secondary slip increases and the dislocation substructure changes to a multi-slip structure (such as dislocation cells and labrynths). In addition, if the loading is non-proportional, the maximum shear planes are no longer fixed, but rotate. This activates more slip systems and a multi-slip response is observed at a strain level where only single slip was observed for uniaxial loading. This brings about an increased hardening or an increase in the stress response for nonproportional loading. Alternatively, materials such as pure aluminum and aluminum alloys do not show much nonproportional hardening. These materials form multi-slip structures under both proportional and nonproportional

loading since cross slip is easy. Thus these materials form similar dislocation substructures (dipoles and cells) under both types of loading and no major difference in the stress response is observed between the loading cases.

In summary, materials which can cross slip easily (materials with a high stacking fault energy--planar slip materials), form multi-slip structures under both proportional and nonproportional loading. Thus no nonproportional hardening is observed. Materials where cross slip is difficult (low stacking fault energy materials--wavy and wavy/planar slip materials) form single slip structures under proportional loading and multi-slip structures under nonproportional loading. These materials exhibit a significant increase in the stable stress response when loaded nonproportionally and exhibit a stress response that is more sensitive to the loading path.

This increase in stable stress response can significantly affect the fatigue life of a component subjected to nonproportional strain controlled loading. A successful multiaxial damage model must be able to incorporate this effect. The capabilities of various damage models, including the ability to incorporate this response are discussed in Section 2.2.3.

2.2.2.2 Fatigue Damage Development

Fatigue is a complicated metallurgical process. It is very difficult to accurately describe and model this process in detail as evidenced by the wealth of literature on this subject. Even a widely accepted definition of fatigue damage is not available. Despite these complexities, fatigue damage assessment for the design and analysis of structures and components must be made. The following section presents a brief discussion of fatigue damage and reviews one aspect of this damage by presenting observations of cracking in different materials. These observations can then be used to evaluate the ability

of the multiaxial fatigue damage models, presented in the following section, to reconcile life prediction methods with physically observed damage.

2.2.2.2.1 Fatigue Damage

The question "What is fatigue damage?" was recently asked to researchers and engineers attending a conference on fatigue mechanisms [2.11]. A wide variety of definitions and responses were expressed. Some of the definitions of fatigue damage given were related to metallurgical processes such as irreversible slip that nucleates a crack, the formation of persistent slip bands (PSB's), the development of intrusions and extrusions and surface roughness, and the development of damage at grain boundaries (such as cavity formation). Other definitions were related to the load carrying capability of the component or structure. Among these were a reduction in the service life (or fraction of life expended), the lack of ability to carry design loads, and finally the change in a material resulting from cyclic loads which reduces its ability to perform its intended function.

The definitions in either of these categories may be more applicable under different situations and applications. Relating the fatigue life or fatigue damage to microstructural changes requires a method to measure these changes. This often requires sophisticated equipment and/or a laboratory environment. Consequently, for the engineer or designer interested in damage assessment or fatigue life prediction for the design or reliability of structures and components, the definitions in the second category may be more useful. However, an understanding of the initiation and growth of microcracks is important in the development of multiaxial damage models. Continuum approaches, such as the strain-life approach, which relate fatigue damage to the stresses and strains in the critical location, must reflect the physical damage

process on the metallurgical level. Therefore, fatigue damage may be related to the load carrying capability of the component or structure and fatigue life estimates may be made without attempting to explicitly model or measure the mechanics of the fatigue process. The employed models, however, must be representative of the observed damage and incorporate the dominant or controlling parameters consistent with the damage.

Historically, initiation approaches, such as the strain-life method, have considered fatigue damage as the "life used up." Fatigue life is then defined by separation of the specimen, some specified reduction in load carrying capability, or the development of a crack to some specified length. This type of approach, which uses laboratory data to predict the fatigue life of a component, requires similitude between the damaged process in the laboratory specimen and the actual component. In other words, cracks are assumed to nucleate and grow in the structure in the same manner as they nucleate and grow in the laboratory specimen. Consequently, for the application of the strain-life approach to a multiaxial fatigue situation, an understanding of the initiation and development of microcracks under various types of loading is required.

2.2.2.2.2 Crack Observations

Detailed crack observations have been made on a variety of materials tested in tension, torsion, and combined loading [2.12-2.15]. Generally, cracking behavior has been shown to depend upon material type, strain amplitude, and loading mode. Cracking observations on several materials under different loading conditions and strain amplitudes clearly support this. These observations are summarized below. Results, as well as experimental testing procedures and material information, have been reported in detail in Refs. [2.13-2.15].

Detailed crack observations were made on the three materials. These materials exhibit different types of cracking behavior and represent extremes in the behavior observed in isotropic materials during tensile and torsional fatigue testing.

The behavior of the three materials in tension and torsion is summarized in Figs. 2.2-2.4. In these figures, the vertical axis is in terms of life fraction, N/N_f, and the horizontal scale is presented in terms of fatigue life, N_f, in cycles. The solid line represents the first observation of a surface crack of 100 μm and serves as a demarcation between crack nucleation and growth. It could be argued that nucleation occurs much earlier, say, for example, 10 μm. This would simply shift the line down without changing the qualitative phenomena represented by the plots. The dashed line represents the demarcation between crack growth on planes of maximum shear strain amplitude and crack growth on planes of maximum principal strain amplitude. Cracking behavior is categorized into three general regions, Regions A, B, and C. Region A denotes a failure mode that is dominated by shear crack growth. In Region B, shear crack nucleation is followed by crack growth on planes of maximum principal strain (Stage II planes). Crack nucleation dominates the fatigue life in Region C. Materials may exhibit cracking behavior that is representative of one, two, or all three of these regions. The cracking behavior of each of the three materials is discussed in detail below.

Stainless steel 304 tested in torsion exhibited cracking behavior which could be categorized into two regions, Region A and B, as shown in Fig. 2a. The stainless steel tested at high torsional strain levels exhibited behavior characteristic of Region A. Microcracks initiated on shear planes. Once initiated, the cracks become more distinct but showed no significant increase in length. A small amount of branching onto tensile planes (Stage II planes) was

observed. Failure cracks grew on shear planes (Stage I) or tensile planes (Stage II) by a slow linking of previously initiated shear cracks. At lower values of strain, the stainless steel tested in torsion exhibited Region B behavior with large amounts of crack growth on tensile planes. A small number of cracks initiated on shear planes but quickly branched to tensile planes. Growth on these planes occurred by the propagation of the main crack rather than by a linking process.

In tension, the stainless steel exhibited no perceptible evidence of Stage I growth. As a result, no region A behavior is shown in Fig. 2b. Scanning electron examination showed that the fracture surfaces appeared to be almost entirely dominated by Stage II growth.

The behavior of Inconel 718 is presented in Fig. 3. Unlike the stainless steel, which displayed mixed behavior, results of the Inconel 718 torsion tests showed that cracks initiated and remained on maximum shear planes. As shown in Fig. 3a, Region A behavior was observed in torsion for all values of shear strain investigated. Even at the lowest strain amplitude, in which the normal stress-strain response was essentially elastic, cracks initiated and remained on shear planes throughout the life. Crack density decreased in specimens tested at longer fatigue lives as it did in stainless steel, but no branching onto tensile planes was observed.

In Inconel 718 tested in tension, cracks remained on shear planes for the majority of fatigue life and a large zone of Region A behavior was observed as shown in Fig. 3b. Final failure in all tension tests was in a macroscopic tensile direction comprised of large portions of microscopic shear growth. Large amounts of shear growth were observed at failure for short and intermediate fatigue lives. Growth on Stage II planes occurred only late in life.

Damage accumulation in Inconel is shear dominated. This is attributed to localized shear deformation bands developed during cyclic loading. Reversed movement of dislocations progressively shears precipitates in these bands. Crack propagation then occurs along the bands with extensive shear crack growth throughout the fatigue life.

Two types of cracking systems have been observed in SAE 1045 steel. One type, termed the R system by Marco and Starkey [2.16], exhibits a large density of microcracks with the final failure occurring by a very rapid linking of these cracks. This type of damage occurred at high strain amplitudes. Alternatively, the S system, which exhibits one dominant crack that grows to failure, was observed at low strain amplitudes.

In torsion, at high amplitudes, the R system crack behavior was characteristics of Region A shown in Fig. 4a. In this region, the number of microcracks increased with the number of loading cycles. In addition, the surface length of microcracks, which appeared in the early stages of life, remained almost unchanged during the fatigue life. Darkness and clarity of the microcracks substantially increased with the increasing cycles. Cracks developed equally on both planes of maximum shear and were uniformly distributed over the entire gauge length. The failure was similar to that observed in the stainless steels at high amplitudes except that the linking of microcracks and final failure in 1045 occurred over a very few cycles, while the growth of the Region A failure crack in stainless steels occurred progressively throughout the life.

Region B behavior was observed in 1045 only at long lives. At the lowest strain amplitude, 0.26 percent, the crack branched and growth occurred on the tensile plane by a linking of previously initiated shear cracks. After a period of tensile growth, the crack linked with a large shear crack which had

simultaneously developed. Final failure occurred by a mixture of Regions A and B behavior.

SAE 1045 tested in tension exhibited cracking behavior characteristics of both the R and S systems which developed on Stage II planes. As shown in Fig. 4b, microcracks initiated on shear planes at high amplitudes, in a manner representative of the R crack system. A very rapid linking of these microcracks occurred immediately prior to failure such that the failure crack was on tensile (Stage II) planes. At low amplitudes, cracks initiated on shear planes but progressive growth occurred on Stage II planes.

In Region C, crack nucleation plays the dominant role. This region has been extensively studied by others. Nisitani [2.17] and Nisitani and Kawano [2.18] made observations of long life fatigue failures in low carbon steels. They concluded that at the fatigue limit, cracks formed within single grains but were unable to propagate into neighboring grains because of the differences in crystallographic orientation.

Robillard and Cailletaud [2.19] also made detailed crack observations in a ferritic stainless steel (Z12CNDV12-2). Like the observations reported in Ref. [2.13], they found that under torsional loading the crack behavior is dependent upon the loading level. At high shear strain amplitudes they observed shear cracking, while at low strain amplitudes they observed tensile cracking.

They also conducted two level tests under constant amplitude torsion and tension using equivalent strain ranges. They found that torsional loading followed by tensile loading was more damaging (resulted in a shorter fatigue life) than tensile loading followed by torsional loading. The difference in the damage developed under these two types of loading cases was explained by an understanding of the damage developed on different planes. In the first case, where torsion was followed by tension, the torsional loading initiated shear

cracks parallel and perpendicular to the axis of the specimen. The tensile loading then propagated the cracks oriented perpendicular to the axis by Mode I growth. In the tensile loading followed by torsion, the initial tensile loading developed shear damage on planes oriented 45 degrees to the axis of the specimen. These planes did not correspond to the propagating planes for the torsional loading at this high load level. Instead, the cracks propagated on planes aligned with, and perpendicular to, the axis of the specimen.

Cracking observations have also clearly shown the importance of mean stresses in the damage development in a material subjected to multiaxial loading [2.19-2.21]. The mean stress is observed to affect both the orientation and distribution of the cracks.

Socie and Shield [2.20] reported that a mean stress had a significant effect on cracking behavior. In proportional loading tests, with a tensile mean stress, cracking occurred on the shear plane with the maximum tensile stress. These cracks formed and grew to failure on this plane. In tests with compressive mean stresses, a higher crack density was observed. In this case, multiple cracking was observed to occur on both shear planes. However, the failure crack always occurred on the plane with the maximum (least compressive) mean stress. In addition, they concluded that mean normal strain in itself is not detrimental to the fatigue life unless it produces a mean stress.

Robillard and Cailletaud [2.19] also observed an effect of the mean stress on cracking behavior. They observed that fully reversed torsional loading with a compressive mean stress caused cracks to grow on the planes parallel to the axis of the specimen as shown in Fig. 2.5. The cracks perpendicular to the axis of the specimen were closed by the compressive stress. For completely reversed tension tests with a mean torque, cracks developed on only one set of shear planes (oriented 45 degrees to the axis of the specimen) due to the

applied mean torque. Cracks grew on the 45 degree planes that experienced the tensile mean stress due to the mean torque as shown in Fig. 2.6.

From these observations, it has been shown that cracks initiate and form on certain planes, the orientation of which is determined by both the stresses and strains in the critical location. These observations are the physical basis of the multiaxial fatigue critical plane approaches. Critical plane approaches, as well as other multiaxial fatigue models, are discussed and compared in the following section.

2.2.3 Multiaxial Fatigue Theories

Using the strain life approach to predict the fatigue life of a component, a damage model is required. Following is a brief review of multiaxial fatigue approaches followed by a critical review and comparison between the theories.

Multiaxial fatigue review articles are published in the literature and are given in Refs. [2.22-2.26]. The article by Ellyin is of particular note as it presents a very thorough, up-to-date review. In general, multiaxial fatigue failure theories can be classified into three categories. In the first are theories which are based upon extensions of static yield theories to fatigue under combined stresses. In the second category, the energy-based approaches relate the fatigue life to work or strain energy. Finally, the critical plane approaches make up the third category. These theories in the last category are founded upon the premise that failure occurs due to damage developed on a critical plane and are usually based upon cracking observations.

2.2.3.1 Equivalent Stress/Strain Approaches

Early attempts to deal with combined loading resulted in multiaxial fatigue theories based upon von Mises or Tresca yield criteria. Further extensions and modifications were made in this area by researchers such as Sines [2.27,2.28] and Fuchs [2.29]. This type of theory has been adopted by the American Society of Mechanical Engineers (ASME) for their Boiler and Pressure Vessel Code [2.30].

In the ASME code, an equivalent strain range is calculated

$$\Delta\varepsilon_{eq} = \text{the value of } \left[\frac{\sqrt{2}}{3}\left[(\Delta\varepsilon_{11} - \Delta\varepsilon_{22})^2 + (\Delta\varepsilon_{22} - \Delta\varepsilon_{33})^2 + (\Delta\varepsilon_{33}-\Delta\varepsilon_{11})^2 + 6(\Delta\varepsilon_{12}^2+\Delta\varepsilon_{23}^2+\Delta\varepsilon_{31}^2)\right]^{1/2}\right] \begin{matrix}\text{maximized with} \\ \text{respect to time}\end{matrix} \qquad (2.5)$$

where

$\Delta\varepsilon_{ij} = \varepsilon_{ij}(t_1) - \varepsilon_{ij}(t_2)$ are the strain differences between time t_1 and t_2

$\varepsilon_{ij}(t_1)$ = components of strain tensor at time t_1

$\varepsilon_{ij}(t_2)$ = components of strain tensor at time t_2

For proportional loading this term is proportional to the octahedral shear strain. It is not in general, though, equal to the octahedral shear strain (von Mises) theory.

This theory predicts no path dependence of the fatigue life. In other words, it predicts that it doesn't matter how the strain states at time t_1 and t_2 were reached. Instead the fatigue life is only dependent on the strains at two instances in time, t_1 and t_2.

This predicted lack of path dependency has been experimentally shown to be incorrect. (See Section 2.2.3.4.) The fatigue life is dependent upon the loading path, not just the extreme strain points obtained during the loading cycle or loading block. In addition, for a variable amplitude loading situation with a large number of cycles in the loading block, the implementation of this method quickly becomes infeasible. A very large number of calculations would have to be done simply in order to determine the maximum equivalent strain range (Eq. (2.5)) for the loading history.

Equivalent stress or strain theories have also met with two other main objections. First, these theories do not predict any mean stress effect. It was shown in early uniaxial fatigue research that mean stresses affect fatigue life. In subsequent multiaxial research, as discussed in the previous section, it has been shown that mean stresses affect both fatigue life and cracking direction. (As a side note, these theories have sometimes been criticized because they do not predict a sensitivity to hydrostatic stresses as discussed in Ref. [2.24]. However, in the experimental tests used for the basis of this argument, unequal mean stresses were developed in the different directions. Consequently it may be a mean stress acting in a particular direction rather than the hydrostatic stress, that affects the fatigue life.) Another main criticism of these approaches is that they predict that a component subjected to out-of-phase loading will exhibit a longer fatigue life than one in which the applied loads are in-phase. This prediction has been experimentally shown to be incorrect. Strain-controlled out-of-phase loading has been shown to be more damaging than in-phase loading. As discussed in Section 2.2.2.1, the increased damage in out-of-phase loading is believed to be due to the large increase in strain hardening (nonproportional hardening) observed in some materials.

2.2.3.2 Energy Approaches

Energy approaches relate the fatigue life to work or strain energy. These types of methods have been developed and are presented in Refs. [2.31-2.33]. Garud's method [2.31], which is the most well-known, relates the plastic work per cycle to the fatigue life. This is

$$W_c = \int_{cycle} \sigma_x \, d\varepsilon_x^p + \sigma_y \, d\varepsilon_y^p + \sigma_z \, d\varepsilon_z^p + \tau_{xy} \, \gamma_{xy}^p + \tau_{xz} \, \gamma_{xz}^p + \tau_{yz} \, \gamma_{yz}^p \qquad (2.6)$$

Garud's method is more physically well-founded than the equivalent stress or strain theories. However, as pointed out by Jordan [2.34], this approach suffers from several shortcomings. First, this theory is based upon the plastic work per cycle and is independent of damage developed on observed critical planes. Second, this general theory, Eq (2.6), reduces to

$$W_c = \int_{cycle} \sigma \, d\varepsilon^p + \tau d\gamma^p \qquad (2.7)$$

for the case of tension-torsion. However, for better correlation with tension-torsion data, Garud included a weighting factor or constant that is empirically determined so that Eq (2.7) becomes

$$W_c = \int_{cycle} \sigma \, d\varepsilon^p + 0.5 \, \tau d\gamma^p \qquad (2.8)$$

Since Garud used tension-torsion data, it is unknown how his theory would correlate fatigue lives of components subjected to a more general stress state. Specifically, the value of, or need of, a weighting factor is unknown or even if the theory would work at all. Several researchers [2.5,2.35] have found that

different values of this weighting factor were more successful in correlating multiaxial data, depending upon the material and conditions. In addition, for lives greater than 2000 cycles, where the plastic strain energies become small, Jordan [2.34] reported that the results obtained using this model seem to diverge. Also at longer lives, the fatigue life is significantly affected by a mean stress, while this method predicts no effect.

Finally, energy based methods have not met with wide-spread acceptance. Unfortunately, the development of cyclic nonproportional constitutive relations is such that they limit the ability of this method to be used in a predictive capability since the success of the method is very sensitive to any inaccuracies in the stress-strain predictions.

2.2.3.3 Critical Plane Approaches

Findley [2.36] first proposed a model which was based upon the idea that the primary cause of fatigue is the alternating shear stress, with the normal stress on the critical shear plane having an influencing factor. McDiarmid [2.37] subsequently proposed a theory which was based upon the critical range of shear modified for the effects of the normal stress acting on the plane of maximum shear stress. In the critical plane approaches, mean stress effects are accounted for with the inclusion of the normal stress term. The ability of these models to account for mean stress effects is consistent with experimental results and consequently overcomes a weakness in the equivalent stress or strain theories.

In work related to McDiarmid's, Brown and Miller [2.22] developed an approach based upon a physical interpretation of the mechanisms of fatigue crack growth. Brown and Miller believed that fatigue lives could be correlated by considering both the maximum shear strain and the tensile strain acting

across the maximum shear strain plane as primary controlling parameters. Based upon this idea, they developed gamma planes, which were contours of constant life plotted with the normal strain on the horizontal axis and the shear strain on the vertical axis as shown in Fig. 2.7. Although these contours are relatively successful in correlating multiaxial fatigue data, they are not good for predictive capabilities. They require a significant amount of data to develop these plots and additionally, predict that fatigue life is not a unique function of γ and ε_n. Rather, two fatigue lives are predicted for one set of γ and ε_n as shown in Fig. 2.7. (The difference between these fatigue lives is the type of crack developed. Brown and Miller defined two type of cracks, Type A cracks and Type B cracks. Type A cracks were defined as long, shallow cracks that grow along the surface of the specimen. Shear cracks formed in torsion are a good example of Type A cracks. Alternatively, Type B cracks grow into the depth of the specimen.)

In a later paper [2.38], Kandil, Brown and Miller extended this theory and expressed it in equational form as

$$\Delta\gamma + S\Delta\varepsilon_n = \text{constant} \tag{2.9}$$

where $\Delta\gamma$ is shear the range on the plane experiencing the maximum range of shear, $\Delta\varepsilon_n$ is the normal strain on this plane, and S is a material constant.

In 1980, Lohr and Ellison [2.39] reasoned that it is more correct to consider only shear planes that assist in propagating the crack into the thickness of the specimen, Type B cracks. They expressed this idea as

$$\Delta\gamma^* + S\Delta\varepsilon_n^* = \text{constant} \tag{2.10}$$

where $\Delta\gamma^*$ and $\Delta\varepsilon_n^*$ are the strain values on planes growing into the thickness of the specimen. Using only Type B cracks, the fatigue life was now a unique function of γ and ε_n. A better correlation of test results was obtained using their theory compared to that obtained by using Eq. (2.9). However, they violated a major point that made critical plane approaches so appealing. Physical observations did not support their predictions. They predicted that for torsional loading the cracks would grow at a angle of 45 degrees into the surface of the specimen even at short fatigue lives. However, low cycle fatigue cracking observations showed that cracks developed under torsional loading grew on planes parallel to the surface of the specimen.

In 1984, based upon the observations that mean stresses affect the development, density, and orientation of microcracks, Socie et. al [2.14] modified Brown and Miller's parameter by including a mean stress term. This then took the form

$$\hat{\gamma} + \hat{\varepsilon}_n + \frac{\sigma_n}{E} = \frac{\tau_f'}{G}(2N_f)^b + \gamma_f'(2N_f)^c \qquad (2.11)$$

where $\hat{\gamma}$ is the maximum shear strain amplitude, $\hat{\varepsilon}_n$ is the tensile strain perpendicular to the plane of maximum shear strain amplitude, σ_n is the mean stress perpendicular to this plane, τ_f' is the torsional fatigue strength coefficient, γ_f' is the torsional fatigue ductility coefficient, and G is the shear modulus. Equation (2.11) was successful in correlating the fatigue lives of Inconel 718 specimens loaded in a variety of multiaxial loading paths. In subsequent work, Fatemi and Socie [2.40] and Fatemi and Kurath [2.41] developed this shear based parameter to

$$\hat{\gamma}\ (1 + K\frac{\sigma_n}{\sigma_y}) = \frac{\tau_f'}{G}(2N_f)^b + \gamma_f'(2N_f)^c \qquad (2.12)$$

where $\hat{\gamma}$, σ_n, τ_f', γ_f' are defined as in Eq. (2.11), and K is a material constant. In Ref. [2.41], Fatemi and Kurath stated that the value of K varies with fatigue life. For long fatigue lives (high cycle fatigue) they reported the value of K approached 1, while at short lives it was reduced in their tests. At a life between 10^3 and 10^4 cycles, it was approximately 0.4. They used a representative value of 0.6 for 1045 steel for their low cycle fatigue calculations. This equation, Eq. (2.12), was shown to be successful in correlating a material whose damage development was shear dominated.

Since the basic concept behind the critical plane models is that the bulk parameters must be consistent with damage, it is not surprising that a shear based model was not particularly successful in correlating a material that developed tensile cracks. Instead, it was shown in Ref [2.13] and discussed further in Refs. [2.21] and [2.42] that the Smith Watson Topper [2.43] model applied to multiaxial loading resulted in a better fatigue life correlation of components which developed tensile cracks. This model is

$$\frac{\Delta\varepsilon_1}{2}\sigma_1 = \frac{\sigma_f'^2}{E}(2N_f)^{2b} + \varepsilon_f'\sigma_f'(2N_f)^{b+c} \qquad (2.13)$$

where $\frac{\Delta\varepsilon_1}{2}$ is the maximum principal strain amplitude and σ_1 is the maximum stress on the plane of maximum principal strain amplitude.

From these results it was concluded that multiaxial damage models must be consistent with observed damage for successful multiaxial fatigue life predictions.

2.2.3.4 Discussion and Comparison of Multiaxial Theories

The effectiveness of different multiaxial fatigue theories in correlating test results has been evaluated and compared by different researchers [2.5,2.34,2.35,2.44]. The following briefly presents their results and conclusions and provides some general discussion on the theories.

Jordan [2.34] ran nonproportional tests on thin walled tubes made from 1Cr-Mo-V steel at room temperature. He conducted tests using four types of loading conditions. In all four types of loading, the same constant amplitude torsional shear strain was applied. The differences between the loading types was in the manner in which the tension was applied. In one case, the tensile strain was simply out of phase with the torsional strain. In the other three cases, very sharp spikes of tensile loading were applied in various points in the torsional cycle. From this work, he concluded that fatigue is not only a function of the strain amplitude but also of straining path. Using the ASME Boiler and Pressure Vessel Code Case N47, the life predictions between the four test cases were the same. However, experimentally obtained fatigue lives differed significantly (over a factor of 7) between the test cases. He concluded that life estimates based on amplitudes of strain alone, such as the equivalent strain approaches, are unsatisfactory for nonproportional straining.

Jordan evaluated Garud's approach by measuring the area within the experimentally determined hysteresis loops. He also used Kandil's form of the Brown and Miller critical plane theory to correlate the test results. He concluded that these two methods are equally successful in predicting the fatigue life in the low cycle fatigue regime. Finally, as a side note, he found that the phase of the applied maximum shear strain relative to the normal strain across the plane of maximum shear did not affect the fatigue life in any tests.

Tipton [2.5,2.44] also correlated the fatigue lives of SAE 1045 steel notched shafts, obtained in the SAE notched shaft program [2.45], with various multiaxial fatigue theories. He found that both the Tresca and von Mises based equivalent strain correlations were non-conservative for out-of-phase loading. Alternatively, he found that the Brown and Miller critical plane approach, as well as Garud's energy based method, was successful in correlating the in-phase and out-of-phase tests. In Garud's approach he found that using a weighting factor of 0.5 made the predictions non-conservative. Instead a factor of 0.9 would have improved these particular life predictions.

Andrews [2.35] conducted strain controlled tension-torsion tests on 316 stainless steel at 550 degrees Celsius. He ran tests at different biaxiality ratios under both proportional and nonproportional straining. He correlated tests results with the equivalent strain ASME Boiler and Pressure Vessel Design Code Case N47, Garud's plastic work method, and a critical plane approach.

Like Jordan and Tipton, he found that the ASME equivalent strain approach yielded predictions that were non-conservative (up to an order of magnitude) for the out-of-phase tests. He also employed Garud's method by measuring the area of the experimentally obtained hysteresis loops. He used Garud's empirical scaling factor of 0.5 and obtained good results. Like Tipton, he found that better results might have been obtained if this scaling factor had been changed. Although Tipton found that an increase in the factor to 0.9 resulted in better correlations, Andrews found a decrease in the factor to 0.3 would have yielded better results. Like Jordan he also found the correlations began to diverge at longer lives.

For the critical plane approach, he attempted to correlate both the in-phase and out-of-phase results with Brown and Miller's critical plane model taken in the form of Eq. (2.9). He obtained a good correlation for the in-phase results, but

found the predictions to be quite conservative for the out-of-phase results. Consequently, he made a modification to this equation to account for the biaxiality and nonproportionality of the loading path. He obtained relatively good results using this approach.

From these three studies on the ability of various multiaxial theories to correlate nonproportional multiaxial fatigue data, the following conclusions are derived.

The initial attempts to use only the strain amplitudes or strain ranges to predict multiaxial fatigue lives is due to the historical development of multiaxial fatigue theories from uniaxial fatigue. It was desired to somehow relate multiaxial damage to that developed in the uniaxial situation since there was an abundance of uniaxial fatigue data. Unfortunately, this approach has not been found to be very successful. In fact, Leis [2.46] stated that "octahedral equivalence quantities do not provide a tenable basis to extend uniaxial data to serve as a reference damage state" for a damage analysis for nonproportional loading. Rather he concluded that the damage rate is three-dimensional and path dependent.

Jordan also observed in his study that fatigue damage is a function of strain amplitude and straining path. He concluded that life estimates based on amplitude of strain are unsatisfactory for nonproportional straining. It is not surprising since the peak stresses obtained in a multiaxial loading case are highly dependent upon the strain path. If attempts to use multiaxial theories in a predictive capability, where stresses are generally unknown, are to be successful some method to account for this path dependency of the stress response must be incorporated into the model.

Garud's method provides a means to account for the path dependency of the stress-strain response. As stated earlier, however, this type of approach

suffers from the weakness that the development of cyclic nonproportional constitutive relations is such that they limit the ability of this method to be used in a predictive capability. The success of the method is very sensitive to any inaccuracies in the stress-strain predictions. In addition, even though both Andrews and Jordan's used the experimentally obtained hysteresis loops (instead of predicted hysteresis loops), correlations at longer lives, where there was little plastic strain, began to diverge.

The critical plane approaches are based upon physical observations of cracking behavior. As discussed, experimental cracking observations, and resulting fatigue lives, have shown that multiaxial damage development is affected by mean stresses. The original strain-based critical plane models proposed by Kandil, Brown and Miller, and Lohr and Ellison did not include a stress term. However, Leis [2.46] stated that an "approach based strictly on maximum shear or shear strain range on the plane of maximum shear, therefore, cannot alone be expected to be correct at lower damage rates (longer lives) where there is insufficient inelastic action to relax mean stress."

Critical plane models such as those given in Eqs. (2.12) and (2.13) can account for the path dependency of the stress response, as well as observed mean stress effects, through the incorporation of the stress term. In addition, these models can account for such effects as out-of-phase hardening and hydrostatic pressure. Finally, unlike both the equivalent strain and energy approaches, these models may be applied to the variable amplitude loading situation relatively easily. Thus, although the exact form of the damage models may undoubtedly change as more multiaxial fatigue data becomes available, these models will be used in their current form to develop the variable amplitude multiaxial fatigue life prediction methodology.

2.2.4 Variable Amplitude Multiaxial Fatigue

Much of the multiaxial fatigue research to date has dealt with proportional and nonproportional loading where the maximum shear strain and the maximum tensile strain in the loading cycle, although not the same, were constant amplitude. In other words, the maximum strains attained in the loading cycle did not vary between cycles. Little, if any, actual multiaxial variable amplitude experimental test data has been published. This lack of data has been due in part to our lack of understanding of the more basic multiaxial loading conditions, as well as the difficulty in obtaining this type of data. It has been understood, however, that the actual service loads of many components were multiaxial and of varying amplitude. Consequently, some initial ideas and methods have been proposed to estimate the fatigue life of a component subjected to variable amplitude multiaxial loading. These are briefly discussed below.

McDiarmid [2.47] proposed a method to design for high-cycle biaxial fatigue resistance of components using variable amplitude strain information. He suggested that a conservative approach was obtained by assuming that the principal strains always occur in the same direction. However, as discussed previously, strain-controlled out-of-phase loading is more damaging than in-phase loading. In addition, he suggested that a conservative approach was to idealize the out-of-phase variable amplitude strains to in-phase constant amplitude strains with the amplitude corresponding to the outer envelope or maximum strains in the actual history. This approach would yield very conservative results for long histories where there are many small subcycles. Since no nonproportional data was available to evaluate the model, no attempt was made to quantify the error for loading nonproportional variable amplitude paths.

Macha also suggested a fatigue criterion for components subjected to random multiaxial loading and is presented in Ref. [2.48]. This approach is based upon a critical plane concept where the quantities of shear and normal strains determine the fracture plane. The strain values on this plane can then be related to fatigue life. Again, no attempt was made to evaluate the model using experimental data.

A shortcoming of both McDiarmid's and Macha's approaches is that they do not incorporate any stress terms. Consequently, they suffer from the weaknesses described in Section 2.2.3. Namely, they cannot account for mean stress effects and they predict no strain path dependency of the fatigue life.

In the study of variable amplitude torsional loading presented in Ref. [2.49], the strain-life approach was used to estimate the fatigue lives of large turbine-generator shafts loaded in torsion. The method was evaluated by comparing predicted results with experimental variable amplitude tests results obtained from small notched specimens and large fillet specimens. Very good agreement was observed.

As stated, the strain-life approach has achieved success in correlating fatigue lives of components subjected to both uniaxial variable amplitude loading and torsional variable amplitude loading. Consequently, the idea of attempting to extend the local strain-life approach to variable amplitude multiaxial fatigue has been suggested and discussed by several researchers. In a published discussion of the information or techniques needed for a variable amplitude loading situation, Leis [2.46] stated that "the framework must inherently define the necessary cycle counting rules to resolve complex deformation histories into events directly comparable to those of the reference state." Hoffman and Seeger [2.50] also discussed this and other tools needed, as well as current limitations that exist, in extending the strain-life approach to multiaxial

variable amplitude fatigue. In Ref [2.51] a strain-life method, similar to the idea on which the current work is based, was outlined which suggested that this method may be appropriate to use in predicting the fatigue life of a component subjected to variable amplitude multiaxial loading. The details of the methodology to extend the strain-life approach to multiaxial variable amplitude fatigue which is being proposed in the current work, as well as the implementation of this method, are given in the following chapter.

2.3 Summary

As stated in the preceding chapter, a primary objective in the choice of a multiaxial damage model is the need to reconcile the analytical approaches with observed material behavior. Critical plane models are based upon observations of the damage developed in a material subjected to combined loading. By the incorporation of a stress term, these models can account for mean stress effects, the effect of nonproportional hardening, and the strain path dependency of the fatigue life. Critical plane models are also relatively easy to apply in a variable amplitude loading situation. Consequently these approaches provide a basis from which to develop a variable amplitude multiaxial life estimation method. In addition, the strain-life approach has achieved success in correlating the fatigue lives of components subjected to uniaxial variable amplitude loading, as well as components subjected to torsional variable amplitude loading. The use of these models in the proposed method is described in the following chapter.

3. PROPOSED MODEL

3.1 Introduction and Overview

A method to predict the fatigue life of a component subjected to variable amplitude multiaxial fatigue has been developed and implemented in a computer code. An overview of the proposed method is given below with the technical details then presented in the remainder of the chapter. Pertinent information concerning the implementation of this method in the computer code is also provided. Results of the analysis are presented and discussed in the next chapter.

The proposed variable amplitude multiaxial fatigue life prediction procedure is based upon an extension of the strain-life approach which, as discussed in Chapter 2, achieved relatively good success in predicting the fatigue life of components subjected to uniaxial variable amplitude fatigue. In addition, this proposed method employs critical plane concepts, also discussed in Chapter 2, that have been developed from recent multiaxial fatigue research.

A general outline of the procedure is presented in Fig. 3.1. Strain data, obtained either from a strain gauge rosette or from a known or approximated history, is used as input. After the data has been inspected and edited for peaks and valleys, the stress histories are determined. Since problems occur in critical locations where the stresses often exceed the yield stress, a plasticity model must be used in predicting the stresses. Fortunately, however, fatigue cracks generally occur on the surface of the component where a plane stress state exists. This plane stress state simplifies the stress history calculations.

Details of the plasticity model are given later in this chapter. In general, the two surface nonproportional cyclic plasticity model incorporates the von Mises yield criteria, the normality flow rule, and Mroz kinematic hardening. A stable

material response is assumed such that no transient hardening effects of nonproportional hardening are included.

Once the strain and stress histories are known, the critical plane damage models are used to estimate fatigue life. The critical plane is defined as the plane experiencing the maximum damage and the fatigue life of the component is estimated using the stress-strain response on this plane. In general, the critical plane is not known before the analysis. This requires that damage on all candidate planes be computed in order to identify the critical plane. Fatigue damage associated with each plane is calculated as follows.

The effect of the applied loading on a plane is determined by a tensor rotation of the stresses and strains to this plane. Damaging events--the appropriate cycles of strain--are identified by rainflow counting the strain history acting on this plane. The amplitude of the strain cycle is then used in the damage model that is consistent with observed material behavior. For example, for a tensile crack dominated material, the tensile strain on the plane is rainflow counted. Alternatively, for a shear crack dominated material, cycles of shear strain are rainflow counted. Once the strain range for a cycle is determined, the damage parameter can then be calculated using the tensile or shear damage parameters given in equations of Chapter 2. For the tensile model, the damage parameter is the product

$$\frac{\Delta\varepsilon}{2}\sigma$$

where σ is the peak tensile stress during the current cycle of strain on this plane. Fatigue life corresponding to the magnitude of this damage parameter can then be determined through use of Eq. (2.13). This is done for all cycles in the history on this plane. The damage is summed using Miner's rule, a linear damage summation technique, such that

$$D = \sum_{i=1}^{n} \frac{1}{N_{fi}}$$

where n is the number of cycles, N_{fi} is the fatigue life for the i-th cycle, and D is the damage value for this plane.

(If the shear model was used instead of the tensile model, the same procedure would be used except that cycles of shear strain would be rainflow counted and the damage parameter and corresponding fatigue life calculated from Eq. (2.12).)

This process continues until damage corresponding to all possible planes is evaluated. (The number of planes that must actually be analyzed is reduced by exploiting the plane stress state situation.) The fatigue life of the component subjected to multiaxial variable amplitude loading, in terms of blocks to failure, is then determined from the plane experiencing the maximum damage.

A general outline of the computer code which implements this method is presented in Fig. 3.2. The remainder of this chapter presents and discusses the background and technical details used in the code in the order presented in Fig. 3.2.

3.2 Peaks Procedure

During component testing under service-like loading, a large amount of data is collected and stored. A need to reduce this large amount of data to a manageable size brings about the need for editing or condensing the load history while maintaining the essential features that contribute to fatigue damage.

To edit multiaxial histories a method is needed that is capable of identifying peaks on all channels, of individually editing out the smaller cycles on the different channels, and of storing identified peaks in sequence with respect to time. A method that is able to meet these objectives has been developed and is presented here. In general, the concepts used for uniaxial loading are simply extended to multiaxial loading. However, a few important modifications must be made and certain restrictions met when editing a multiaxial history.

For multiaxial loading, when the combined stresses exceed the yield stress (using the von Mises or Tresca yield criteria), the stress-strain response is path dependent. For example, in Fig. 3.3 both histories start at point O and end at point P. However, the stress levels obtained from the two histories at point P are different due to the different strain paths that were followed when going from point O to point P. The dependency of the stress-strain response on the combined strains and the loading path affects the editing procedure. First, it imposes the restriction or requirement that the relationship between the strains for a point in time must be maintained. Any time one channel reaches a valid peak, the values of strain on all channels for that point in time must be stored. Second, since the material response is path dependent, the sequence of events also affects the stress-strain response. The edited file therefore must maintain the essential features of the original data–including the sequence. This requires some modification of the editing procedure developed for uniaxial loading. If the uniaxial editing method was used on each individual channel of a multiaxial history, the data points stores in the edited peaks file would be out of sequence according to time. This sequence problem is easily seen in the following example.

An example of a multiaxial strain gauge rosette history is given in Fig. 3.4. Shown are the strain histories corresponding to the three legs of the rosette. The corresponding predicted stress-strain response for the unedited Channel 1 strain, termed axial strain, is presented in Fig. 3.5. The success of different editing schemes must be compared to the stress-strain response. A successful editing scheme would edit out the small subcycles while maintaining the essence of the stress-strain response.

For this example, assume that the editing level - sometimes termed 'hysteresis level' - is 0.0006 such that any cycles with ranges below this level are ignored or edited out. A successful editing scheme would edit out the small sub-cycles on Channel 1 while maintaining both the time sequence of the strains and the relationships between the strains.

Using the uniaxial method described in Appendix A and storing the strain values on all channels whenever one channel reaches a valid peak results in the stress-strain response in Fig. 3.6b. Comparing this to the unedited stress-strain response for the original history, given in Fig. 3.6a, shows that the stress-strain response was incorrectly altered. Sub-cycles are predicted in the edited history that do not appear in the original history. This procedure results in erroneous results. The reason for this is shown in Fig. 3.7. Although the relationships between the strains is maintained, the time sequence is lost. This loss of time sequence is due to the fact that a valid peak, F, was identified on Channel 1 and all strain values corresponding to time F stored before peak E, on Channel 3, was identified and all values of strain corresponding to point E stored. The edited file is then chronologically out of sequence and results in the incorrect stress-strain response shown in Fig. 3.5. For the edited stress-strain to be close to the actual response, the strains must be stored in sequence. Using this procedure, the peaks file would have to be sorted according to time after the

histories were edited. Instead of resorting the file, however, a modification to the uniaxial editing procedure is made to store the data as discussed in Appendix A.

This modified method which is described in Appendix A was used to edit the original history given in Fig. 3.4. As can be seen in Fig. 3.8, this method is successful in that the stress-strain response for the edited history is very similar to the original one yet without the subcycles. The reason for this can be seen in Fig. 3.9. Both the time sequence and the relationship between the three strains are maintained.

To overcome the sequence problem, in the multiaxial editing procedure anytime a valid peak is identified on one channel the current "possible peaks", if there are any, on the other channels are stored, if they occur at an earlier time than the present "valid peak". This requirement causes additional data to be stored in that some "possible peaks" which are stored may never have been identified as a valid peak in the uniaxial procedure. However, storing possible peaks allows the essential features of the original data to be maintained without sorting the file after the original strain history is edited.

Although the general concepts used in this editing method are similar to the uniaxial editing procedure, significant modifications are made to ensure the time sequence and relationships are between the strains is maintained. This method is made clear through the discussion of an example given in Appendix A.

3.3 Stress History Predictions

3.3.1 Introduction and Requirements

To predict the stress-strain response of a material subjected to nonproportional loading, an incremental cyclic plasticity model is required.

Incremental plasticity models have been developed [3.1-3.7] and have been reviewed and compared. Researchers dealing with nonproportional multiaxial plasticity models have continued to develop sophisticated models that attempt to reproduce the detailed material response including transient hardening effects due to nonproportional loading. However, for the application in this procedure, these more sophisticated models are not appropriate. Attaining increased accuracy in this portion of the variable amplitude multiaxial fatigue life prediction method does not significantly increase the accuracy of the total approach due to errors or unknowns that exist in the remainder of the procedure. Instead, the application of an incremental plasticity model to the problem of estimating the fatigue life of a component subjected to variable amplitude loading places certain restrictions and requirements on these models as discussed below.

First, the stress-strain response must remain numerically stable under the application of repeated loads. Because the strain histories are often made up of hundreds of cycles, a small instability or numerical error for one cycle could accumulate so that a significant error in the stress response might be predicted at the end of a long loading history if the routine was not stable.

Second, since the stress-strain response is path dependent, the stress-strain predictions depend on the correct "starting location" of the stresses. This need to predict the correct initial stress state is explained and made clear by first referring to the understanding gained in uniaxial variable amplitude loading.

In the uniaxial method, it was assumed that the actual loading history could be modeled by a repeating block of strain cycles. The stress-strain response of the current block was therefore affected by the previous loading block. The previous loading block "set up" the stress state which was then used as the starting location for the prediction of the stress response for the actual history.

For example, Fig. 3.10a presents a uniaxial strain history made up of repeating loading blocks. The stress-strain response for the first block is shown in Fig. 3.10b. The stress-strain response for the second block and all repeating blocks is shown in Fig. 3.10c. In uniaxial methods the history was usually rearranged to start at the largest excursion to account for this difference. In doing this, the predicted stress-strain response for the first block is the same as that shown in Fig. 3.10c.

In a multiaxial situation, the need to predict the correct stress state at the beginning of the loading block becomes even more important. In addition, the location of the yield surface center in stress space must also be predicted. The prediction of these quantities is critical as these terms appear directly in the equations used to calculate the stress history for the actual loading block.

To predict the correct "starting location" of both the stress and yield surface center, the stress response for a set-up block is first predicted. This initial prediction is made by assuming the stresses and strains initially start at zero. The location of the stress and yield surface center at the end of the set-up block is then used as the "starting location" for the actual loading block. The stress history used in the damage model calculations is then predicted using these initial values.

Although, one would ideally like to apply several large set-up cycles that would allow the "starting location" to be determined. This method would not insure that the correct "location" was determined due to the path dependency of the multiaxial stress response. For example, in Fig. 3.3 the final strain state in both loading cases is point P. However, the stress response is different for these two cases. An incorrect stress state would be predicted for the "starting location" of the next block if the path OP, whose end points represent the

extreme endpoints for the actual loading path, was used as the set-up cycle, instead of the actual history was O-A-P.

A third restriction or requirement of the plasticity procedure is that to insure applicability for a wide variety of materials, only readily available material constants must be used as input. For the average engineer these are values obtained from a cyclically stable stress-strain response such as the cyclic strength coefficient, K', and the cyclic strain hardening exponent, n', as well as the yield stress, σ_y, limit stress, σ_L, and modulus of elasticity, E.

As a final simplification, the material response is assumed stable. In other words, no nonproportional transient hardening effects are modeled. Not enough information or knowledge is available to date to attempt to implement a transient plasticity model for a wide variety of materials using only readily available material constants. In addition, since the assumption is made that the total loading history may be modeled by a repeating loading block, neglecting the transient material behavior is justified. Most of the transient response will occur in the first several loading blocks.

A cyclically stable, incremental plasticity model which requires only readily available material constants has been developed. The technical details and the method of implementation in the computer program are presented and discussed in the following sections.

3.3.2 Theoretical Development and Background

A yield criteria, a flow rule and a hardening rule are needed in the development of an incremental plasticity theory. The following describes and develops the equations used in the incremental plasticity theory implemented in this model.

Yield Criteria

The yield criteria is used to determine if plastic strains (plastic flow) will occur during an increment of loading. Due to Drucker's postulate [3.8], the yield surface may be pictured as a convex surface in stress space. The stress response is considered elastic if the stress state lies within this surface. The von Mises [3.9] and Tresca [3.10] criteria, the two most common yield criteria, are pictured in Fig. 3.11a in a biaxial stress space and in Fig. 3.11b in deviatoric stress space. The Tresca yield criterion predicts yielding to occur when any of the following six conditions is reached.

$$\text{Tresca:} \begin{cases} \sigma_1 - \sigma_2 = \pm \sigma_y \\ \sigma_2 - \sigma_3 = \pm \sigma_y \\ \sigma_1 - \sigma_3 = \pm \sigma_y \end{cases} \tag{3.1}$$

The von Mises criterion is related to the second invariant of the stress tensor and predicts yielding to occur when the following relation is satisfied.

$$\text{von Mises: } 3/2\,(S_{ij})\,(S_{ij}) = \sigma_y^2$$

$$\text{or} \qquad \frac{1}{2}\left[(\sigma_1 - \sigma_2)^2 + (\sigma_2 - \sigma_3)^2 + (\sigma_1 - \sigma_3)^2\right] = \sigma_y^2 \tag{3.2}$$

where σ_y is the yield stress. Alternatively, the equations of these yield surfaces may be written as

$$\text{Tresca:} \quad f = \sigma_1 - \sigma_3 - \sigma_y = 0$$

$$\text{von Mises:} \quad f = S_{ij}S_{ij} - 2/3\,\sigma_y^2 = 0 \tag{3.3}$$

where σ_1 and σ_3 are the maximum and minimum principal stresses.

Hardening Rules

Since most metals exhibit work hardening or strain hardening after yielding, hardening rules were developed. Two general types of models have been first developed to attempt to mathematically model this behavior. These are kinematic or isotropic hardening models. Isotropic hardening models, with models developed by Hill and Hodge [3.11, 3.12], assume that the center of the yield surface remains fixed but the size of the surface increases. A disadvantage of the isotropic hardening model is that it doesn't account for a decrease in the yield stress during reversed loading. Consequently, kinematic models were developed. Kinematic hardening models first developed by Prager [3.13] assume that the size and shape of the yield surface remains constant while the center of the surface translates in stress space. Combinations of these rules have also been developed [3.4-3.6,3.14] which attempt to more accurately model the material response. Increased complexity and difficulty of implementation accompany these combined rules. Using the von Mises yield criteria, the equations of the loading surface or yield surface in these models may be written as

$$\begin{aligned} &\text{Isotropic: } f = (S_{ij})(S_{ij}) - 2/3\,\bar{\sigma}^2 = 0 \\ &\text{Kinematic: } f = (S_{ij} - S^c_{ij})\,(S_{ij} - S^c_{ij}) - 2/3\,\sigma_y^2 = 0 \\ &\text{Combined: } f = (S_{ij} - S^c_{ij})\,(S_{ij} - S^c_{ij}) - 2/3\,\bar{\sigma}^2 = 0 \end{aligned} \qquad (3.4)$$

where $\bar{\sigma}$ is the largest value of combined stress attained in the loading path, and S^c_{ij} is the location of the center of the yield surface in deviatoric stress space and

also depends upon the loading path. References [3.11-3.18] present and discuss different hardening rules.

Studies have been done that compare the effectiveness of different hardening rules in modeling observed material response [3.16-3.18]. The Mroz [3.16] hardening model was observed to best model the stress-strain response of components subjected to nonproportional loading, and is therefore implemented in this procedure.

Mroz proposed a model that introduced a "field of workhardening moduli". These are surfaces of constant workhardening (conceptually similar to concentric "yield surfaces" in stress space as shown in Fig. 3.12). The stress-strain curve is then approximated by the piecewise linear series of line segments whose endpoints correspond to these surfaces of constant workhardening. The movement of the centers of these surfaces is in the direction of the vector connecting the outward normal of the current surface (the surface on which the current stress state lies) and the same outward normal on the next surface. (See Fig. 3.13.)

A simplification of the Mroz model has been subsequently proposed and used by a series of researchers [3.5-3.7,3.16]. In this simplification, only two surfaces, a yield surface and a limit surface or bounding surface, are used as shown in Fig. 3.14. In both the models developed by Dafalias [3.5] and Krieg [3.6], the outer (limit) surface is allowed to translate. However, Lamba [3.16] used a fixed surface to get good results compared to experimental data. In these models, the stress-strain response after yielding is modeled by an analytical function that asymptotically approaches the stress-strain response at very large strains. In other words, the strain hardening depends upon a distance (length of the vector) from the current stress state to the limit surface, as shown in Fig. 3.15.

The plasticity model to be used is a two surface model with a fixed limit surface, similar to that proposed by Lamba [3.16]. This model uses a von Mises yield criteria with Mroz kinematic hardening. These calculations will result in the stress histories for σ_x, σ_y, and σ_{xy} and the strain history for ε_z. The Mroz hardening model is discussed further and the needed equations presented in Section 3.3.3.

Flow Rule

The flow rule relates the plastic strain increment to the existing state of stress and to the stress increment. The generally accepted normality flow rule, sometimes called the Prandtl-Reuss [3.19, 3.20] equation, can be stated

$$d\varepsilon_{ij}^{p} = d\lambda \frac{\partial f}{\partial \sigma_{ij}} \tag{3.5}$$

This equation states that the plastic strain increment is in the direction of the normal to the yield surface at the current stress state, σ_{ij}. (The term $\partial f/\partial \sigma_{ij}$ is the gradient of the yield surface which by definition is perpendicular or normal to the tangent of the yield surface at σ_{ij}). Drucker, in Ref. [3.21], also developed and proved this relation based upon a thermodynamic definition of work hardening. Using this equation

$$d\varepsilon_{ij}^{p} = d\lambda \frac{\partial f}{\partial \sigma_{ij}} \tag{3.5}$$

he then further derived

$$d\varepsilon_{ij}^{p} = G \frac{\partial f}{\partial \sigma_{ij}} \frac{\partial f}{\partial \sigma_{kl}} d\sigma_{kl} \tag{3.6}$$

or

$$d\lambda = G \frac{\partial f}{\partial \sigma_{kl}} d\sigma_{kl} \tag{3.7}$$

The expression for $d\lambda$ may then be obtained as follows. Let $Cd\varepsilon_{ij}^{p}$ be the projection of $d\sigma_{ij}$ on the exterior normal to the yield surface as shown in Fig. 3.16. Since the dot product of the exterior normal and a vector tangent to the yield surface is zero

$$(d\sigma_{ij} - Cd\varepsilon_{ij}^{p}) \frac{\partial f}{\partial \sigma_{ij}} = 0 \tag{3.8}$$

Substituting in the normality relation, Eq. (3.5),

$$(d\sigma_{ij} - Cd\lambda \frac{\partial f}{\partial \sigma_{ij}}) \frac{\partial f}{\partial \sigma_{ij}} = 0$$

$$d\lambda = \frac{1}{C} \frac{d\sigma_{ij} \dfrac{\partial f}{\partial \sigma_{ij}}}{\dfrac{\partial f}{\partial \sigma_{mn}} \dfrac{\partial f}{\partial \sigma_{mn}}}$$

$$d\varepsilon_{ij}^{p} = \frac{1}{C} \frac{d\sigma_{kl} \dfrac{\partial f}{\partial \sigma_{kl}}}{\dfrac{\partial f}{\partial \sigma_{mn}} \dfrac{\partial f}{\partial \sigma_{mn}}} \frac{\partial f}{\partial \sigma_{ij}} \tag{3.9}$$

where C is the generalized plastic modulus.

Equation (3.9) may also be expressed in terms of deviatoric stresses (using the identities presented in Appendix B) as

$$d\varepsilon_{ij}^{p} = \frac{1}{C} \frac{\dfrac{\partial f}{\partial S_{kl}} dS_{kl} \dfrac{\partial f}{\partial S_{ij}}}{\dfrac{\partial f}{\partial S_{mn}} \dfrac{\partial f}{\partial S_{mn}}} \tag{3.10}$$

The deviatoric stress is

$$S_{ij} = \sigma_{ij} - 1/3\delta_{ij}\sigma_{kk}$$

where repetition of the subscript "k" implies summation and δ_{ij} is the Kronecker delta. Using the von Mises yield criteria with kinematic hardening

$$f = 3/2\ (S_{ij} - S^c_{ij})\ (S_{ij} - S^c_{ij}) \tag{3.11}$$

this becomes

$$d\varepsilon^p_{ij} = \frac{1}{C}\ \frac{(S_{kl} - S^c_{kl})\ dS_{kl}\ (S_{ij} - S^c_{ij})}{(S_{mn} - S^c_{mn})\ (S_{mn} - S^c_{mn})} \tag{3.12}$$

The generalized plastic modulus, C, can then be related to the uniaxial plastic modulus, Ep, where

$$Ep = \frac{d\sigma_{11}}{d\varepsilon^p_{11}} \tag{3.13}$$

by evaluating Eq. (3.12) for uniaxial loading. By substituting

$$S_{11} = 2/3\ \sigma_{11}$$
$$S_{22} = S_{33} = -1/3\ \sigma_{11} \tag{3.14}$$

into Eq. (3.12), it is shown that

$$\frac{d\sigma_{11}}{d\varepsilon^{p}_{11}} = \frac{3}{2} C$$

Therefore, since E_p is the slope of the uniaxial stress-plastic strain curve, which can be measured, the general plastic modulus, C, can be related to this measurable quantity. This is

$$C = \frac{2}{3} Ep \tag{3.15}$$

From these equations, convenient expressions for the deviatoric stress increment may be obtained for implementation in the computer procedure. For an elastic stress increment or change this is simply

$$\Delta S_{ij} = 2G\ \Delta e_{ij} \tag{3.16}$$

where Δe_{ij} is the deviatoric strain change

$$\Delta e_{ij} = \Delta \varepsilon_{ij} - 1/3\ \delta_{ij}\ \Delta \varepsilon_{kk} \tag{3.17}$$

and repetition of subscript "k" implies summation and δ_{ij} is the Kronecker delta. For an elastic-plastic strain change the deviatoric stress increment can be determined as follows.

The total strain is the sum of the elastic and plastic strains

$$d\varepsilon^{T}_{ij} = d\varepsilon^{E}_{ij} + d\varepsilon^{P}_{ij} \tag{3.18}$$

In terms of deviatoric strains, since $de_{ij}^P = d\varepsilon_{ij}^P$

$$de_{ij}^T = de_{ij}^E + d\varepsilon_{ij}^P$$

$$(d\varepsilon_{ij}^T - \frac{1}{3}\delta_{ij}\, d\varepsilon_{kk}^T) = \frac{dS_{ij}}{2G} + d\varepsilon_{ij}^P \qquad (3.19)$$

Restating Eqs. (3.9) and (3.10) for the plastic strain increment

$$d\varepsilon_{ij}^P = \frac{1}{C}\frac{\frac{\partial f}{\partial \sigma_{kl}}\, d\sigma_{kl}\, \frac{\partial f}{\partial \sigma_{ij}}}{\frac{\partial f}{\partial \sigma_{mn}}\, \frac{\partial f}{\partial \sigma_{mn}}} \qquad (3.20)$$

or

$$d\varepsilon_{ij}^P = \frac{1}{C}\frac{\frac{\partial f}{\partial S_{kl}}\, dS_{kl}\, \frac{\partial f}{\partial S_{ij}}}{\frac{\partial f}{\partial S_{mn}}\, \frac{\partial f}{\partial S_{mn}}}$$

and dotting both sides of this equation with $\underset{\sim}{n}$, where $\underset{\sim}{n} = \dfrac{\frac{\partial f}{\partial \sigma_{ij}}}{\sqrt{(\frac{\partial f}{\partial \sigma_{mn}}\, \frac{\partial f}{\partial \sigma_{mn}})}}$

gives

$$(d\varepsilon_{ij}^T - 1/3\, \delta_{ij}\, d\varepsilon_{kk}^T)\, \frac{\frac{\partial f}{\partial \sigma_{ij}}}{\sqrt{(\frac{\partial f}{\partial \sigma_{mn}}\, \frac{\partial f}{\partial \sigma_{mn}})}} =$$

$$\frac{dS_{ij}}{2G}\, \frac{\frac{\partial f}{\partial \sigma_{ij}}}{\sqrt{(\frac{\partial f}{\partial \sigma_{mn}}\, \frac{\partial f}{\partial \sigma_{mn}})}} + \frac{1}{C}\, \frac{\frac{\partial f}{\partial \sigma_{kl}}\, d\sigma_{kl}\, \frac{\partial f}{\partial \sigma_{ij}}\, \frac{\partial f}{\partial \sigma_{ij}}}{\sqrt{\frac{\partial f}{\partial \sigma_{mn}}\, \frac{\partial f}{\partial \sigma_{mn}}\, (\frac{\partial f}{\partial \sigma_{rs}}\, \frac{\partial f}{\partial \sigma_{rs}})}} \qquad (3.21)$$

Using the von Mises criteria

$$\frac{\partial f}{\partial \sigma_{ij}} \delta_{ij} = 0$$

since

$$\frac{\partial f}{\partial \sigma_{ij}} \delta_{ij} = 3 \, (S_{ij} - S_{ij}^{c}) \, \delta_{ij}$$

$$= 3 \, (S_{ij} \, \delta_{ij} - S_{ij}^{c} \, \delta_{ij})$$

$$= 0$$

Equation (3.21) is now

$$d\varepsilon_{ij}^{T} \frac{\partial f}{\partial \sigma_{ij}} = \frac{\partial f}{\partial \sigma_{ij}} \frac{dS_{ij}}{2G} + \frac{1}{C} \frac{\partial f}{\partial \sigma_{kl}} d\sigma_{kl} \qquad (3.22)$$

As shown in Appendix B

$$\frac{\partial f}{\partial \sigma_{ij}} = \frac{\partial f}{\partial S_{ij}}$$

and

$$\frac{\partial f}{\partial \sigma_{ij}} d\sigma_{ij} = \frac{\partial f}{\partial S_{ij}} dS_{ij}$$

Therefore

$$d\varepsilon_{ij}^{T} \frac{\partial f}{\partial S_{ij}} = \frac{\partial f}{\partial S_{ij}} dS_{ij} \left[\frac{1}{2G} + \frac{1}{C} \right]$$

$$\frac{\partial f}{\partial S_{ij}} dS_{ij} = d\varepsilon_{ij}^{T} \frac{\partial f}{\partial S_{ij}} \left[\frac{2GC}{2G+C}\right] \tag{3.23}$$

Using (3.19), (3.20) and (3.23) this gives

$$(d\varepsilon_{ij}^{T} - \frac{1}{3}\delta_{ij}\, d\varepsilon_{kk}^{T}) = \frac{dS_{ij}}{2G} + \frac{2G}{2G+C} \left[\frac{\frac{\partial f}{\partial S_{ij}} \frac{\partial f}{\partial S_{mn}} d\varepsilon_{mn}^{T}}{\frac{\partial f}{\partial S_{kl}} \frac{\partial f}{\partial S_{kl}}}\right]$$

and rearranging gives an expression for the deviatoric stress increment

$$dS_{ij} = 2G \left\{ d\varepsilon_{ij}^{T} - 1/3\ \delta_{ij}\ d\varepsilon_{kk}^{T} - \frac{2G}{2G+C} \frac{d\varepsilon_{mn}^{T} (S_{mn} - S_{mn}^{c}) (S_{ij} - S_{ij}^{c})}{(2/3\ \sigma_y^2)} \right\} \tag{3.24}$$

To determine the stress increment, dS_{ij}, using strain gauge rosette data and Eq. (3.24), an expression for $d\varepsilon_z^T$ in terms of $d\varepsilon_x^T$, $d\varepsilon_y^T$, $d\gamma_{xy}^T$, and C is needed. This can be developed as follows.

If the strains are all elastic ($d\varepsilon_{ij}^{T} = d\varepsilon_{ij}^{E}$) the expression for $d\varepsilon_z^T$ can be determined for a plane stress situation ($\sigma_z = 0$) from Hooke's law. This is

$$d\varepsilon_z^E = \frac{-\nu}{(1-\nu)} (d\varepsilon_x^E + d\varepsilon_y^E) \tag{3.25}$$

where ν is Poisson's ratio.

For an elastic-plastic situation Eq. (3.25) can be rewritten in terms of total strains, plastic strains as

$$(d\varepsilon_z^T - d\varepsilon_z^P) = \frac{-\nu}{(1-\nu)} (d\varepsilon_x^T - d\varepsilon_x^P + d\varepsilon_y^T - d\varepsilon_y^P) \tag{3.26}$$

Using the expression derived in Eq. (3.24) for the plastic strains, this can be rewritten

$$\left(d\varepsilon_z^T - \left(\frac{2G}{2G + C}\right) \frac{d\varepsilon_{mn}^T \frac{\partial f}{\partial S_{mn}} \frac{\partial f}{\partial S_z}}{(2/3\ \sigma_y^2)} \right)$$

$$= \frac{-\nu}{(1-\nu)} \left[d\varepsilon_x^T + d\varepsilon_y^T - \left(\frac{2G}{2G + C}\right) \frac{d\varepsilon_{mn}^T \frac{\partial f}{\partial S_{mn}} \left(\frac{\partial f}{\partial S_x} + \frac{\partial f}{\partial S_y}\right)}{(2/3\ \sigma_y^2)} \right] \tag{3.27}$$

Expanding this equation gives

$$d\varepsilon_z^T - K\,(S_{zz} - S_{zz}^c) \left[d\varepsilon_x^T\,(S_{xx} - S_{xx}^c) + d\varepsilon_y^T\,(S_{yy} - S_{yy}^c) + d\gamma_{xy}^T\,(S_{xy} - S_{xy}^c) + d\varepsilon_z^T\,(S_{zz} - S_{zz}^c) \right]$$

$$= \frac{-\nu}{(1-\nu)} \left\{ d\varepsilon_x^T + d\varepsilon_y^T - K \left[(S_{xx} - S_{xx}^c) + (S_{yy} - S_{yy}^c) \right] * \right.$$

$$\left. \left[d\varepsilon_x^T\,(S_{xx} - S_{xx}^c) + d\varepsilon_y^T\,(S_{yy} - S_{yy}^c) + d\varepsilon_z^T\,(S_{zz} - S_{zz}^c) + d\gamma_{xy}^T\,(S_{xy} - S_{xy}^c) \right] \right\} \tag{3.28}$$

where $K = \dfrac{2G}{(2G+C)(2/3\ \sigma_y^2)}$

Rearranging and combining terms gives the following expression for $d\varepsilon_z^T$ for a plane stress case.

$$d\varepsilon_z^T = \left\{ K \left[d\varepsilon_x^T (S_{xx} - S_{xx}^c) + d\varepsilon_y^T (S_{yy} - S_{yy}^c) + d\gamma_{xy}^T (S_{xy} - S_{xy}^c) \right] * \right.$$

$$\left[(S_{zz} - S_{zz}^c) + \frac{\nu}{(1-\nu)} \left\{ (S_{xx} - S_{xx}^c) + (S_{yy} - S_{yy}^c) \right\} \right] -$$

$$\left. \left[\frac{\nu}{(1-\nu)} (d\varepsilon_x^T + d\varepsilon_y^T) \right] \right\} \Big/ \left\{ 1 - K(S_{zz} - S_{zz}^c) \left[(S_{zz} - S_{zz}^c) \right. \right.$$

$$\left. \left. + \frac{\nu}{(1-\nu)} \left\{ (S_{xx} - S_{xx}^c) + (S_{yy} - S_{yy}^c) \right\} \right] \right\} \qquad (3.29)$$

These equations have been included in an incremental plasticity computer procedure to predict the stress response of a component using strain gauge rosette data as input. The flow chart of the computer procedure is given in Fig. 3.17. Additional technical details used in the model are discussed in the following sections.

3.3.3 Mroz Hardening

The Mroz kinematic hardening model states that the movement of the of the yield surface, f_L, center, will be in the direction of the vector connecting the current stress point and the point on the next surface, f_{L+1}, with the same

outward normal. This is illustrated in Fig. 3.13. The change in the location of the yield surface center can be described in stress space as

$$d\alpha_{ij} = d\mu\ (\sigma_{ij}^{L+1} - \sigma_{ij}^{L}) \tag{3.30}$$

where α_{ij} is the center of the yield surface in stress space , σ_{ij}^{L} is current stress point and σ_{ij}^{L+1} is the point on next surface that has the same outward normal as the normal to the yield surface at σ_{ij}^{L}.

In terms of deviatoric stresses, this is

$$dS_{ij}^{c} = d\mu\ (S_{ij}^{L+1} - S_{ij}^{L}) \tag{3.31}$$

The point on the next surface that has the same outward normal is

$$S_{ij}^{L+1} - S_{ij}^{cL+1} = \frac{S_o^{L+1}}{S_o^{L}}\ (S_{ij}^{L} - S_{ij}^{cL}) \tag{3.32}$$

where S_o^{L+1} and S_o^{L} are constants. Using the von Mises yield criteria, these are the radii of the surfaces in deviatoric stress space.

Substituting (3.32) into (3.31) gives

$$dS_{ij}^{c} = \frac{d\mu}{S_o^{L}}\left[(S_o^{L+1} - S_o^{L})\ S_{ij}^{L} - (S_{ij}^{c\,L}\ S_o^{L+1} - S_{ij}^{c\,L+1}\ S_o^{L})\right] \tag{3.33}$$

Using the consistency equation (the requirement that the stress point must stay on the yield surface during loading) which is

$$df = 0$$

the following expression is developed.

$$\frac{\partial f_L}{\partial S_{ij}} dS_{ij} + \frac{\partial f_L}{\partial S^c_{ij}} dS^c_{ij} = 0$$

Using the von Mises yield criteria, this is

$$\frac{\partial f_L}{\partial S_{ij}} = 3(S_{ij} - S^c_{ij}) \qquad \frac{\partial f_L}{\partial S^c_{ij}} = -3(S_{ij} - S^c_{ij})$$

$$\frac{\partial f_L}{\partial S_{ij}} = \frac{-\partial f}{\partial S^c_{ij}}$$

$$\frac{\partial f_L}{\partial S_{ij}} (dS_{ij} - dS^c_{ij}) = 0 \qquad (3.34)$$

Using (3.31) and (3.34)

$$\frac{\partial f_L}{\partial S_{ij}} (dS^L_{ij} - d\mu (S^{L+1}_{ij} - S^L_{ij})) = 0$$

$$d\mu = \frac{\frac{\partial f_L}{\partial S_{ij}} dS^L_{ij}}{\frac{\partial f_L}{\partial S_{mn}} (S^{L+1}_{mn} - S^L_{mn})}$$

Substituting this back into Eq. (3.33) yields

$$dS_{ij}^{c} = \frac{\frac{\partial f_L}{\partial S_{mn}} dS_{mn}^{L}}{\frac{\partial f_L}{\partial S_{kl}} (S_{kl}^{L+1} - S_{kl}^{L})} \left[(S_o^{L+1} - S_o^{L}) S_{ij}^{L} - (S_{ij}^{cL} S_o^{L+1} - S_{ij}^{cL+1} S_o^{L}) \right] \frac{1}{S_o^{L}}$$

(3.35)

Using the von Mises yield criteria

$$dS_{ij}^{c} = \frac{(S_{mn}^{L} - S_{mn}^{cL})\, dS_{mn}^{L}}{(S_{kl}^{L} - S_{kl}^{cL})(S_{kl}^{L+1} - S_{kl}^{cL})} \left[\frac{(S_o^{L+1} - S_o^{L}) S_{ij}^{L} - \left[S_{ij}^{cL} S_o^{L+1} - S_{ij}^{cL+1} S_o^{L} \right]}{S_o^{L}} \right]$$

From Eq. (3.32)

$$S_{ij}^{L+1} = \frac{S_o^{L+1}}{S_o^{L}} (S_{ij}^{L} - S_{ij}^{cL}) + S_{ij}^{cL+1}$$

$$dS_{ij}^{c} = \left\{ \frac{(S_{mn}^{L} - S_{mn}^{cL})\, dS_{mn}^{L}}{(S_{kl}^{L} - S_{kl}^{cL}) \left[\frac{S_o^{L+1}}{S_o^{L}} (S_{kl}^{L} - (S_{kl}^{c})^{L}) + (S_{kl}^{c})^{L+1} - S_{kl}^{cL} \right]} \right\} *$$

$$\left[\frac{(S_o^{L+1} - S_o^{L}) S_{ij}^{L} - \left[(S_{ij}^{c})^{L} S_o^{L+1} - (S_{ij}^{c})^{L+1} S_o^{L} \right]}{S_o^{L}} \right]$$

For a two surface model with fixed limit surface ($(S^c_{ij})^{L+1} = 0$), this reduces to

$$dS^c_{ij} = \frac{(S_{mn} - S^c_{mn})\, dS_{mn}}{(S_{kl} - S^c_{lk}) \left[\frac{S^{L+1}_o}{S^L_o} (S_{kl} - S^c_{kl}) - S_{kl} \right]} * \left\{ \frac{(S^{L+1}_o - S^L_o)\, S_{ij} - S^c_{ij}\, S^{L+1}_o}{S^L_o} \right\}$$

Therefore, the movement of the center of the yield surface using the Mroz hardening rule is

$$dS^c_{ij} = \frac{(S_{mn} - S^c_{mn})\, dS_{mn} \left\{ S_{ij} (S^{L+1}_o - S^L_o) - S^c_{ij}\, S^{L+1}_o \right\}}{(S_{kl} - S^c_{kl}) \left[S_{kl} (S^{L+1}_o - S^L_o) - S^{L+1}_o\, S^c_{kL} \right]} \qquad (3.36)$$

3.3.4 Plastic Modulus

In a two surface model, it is assumed that the generalized plastic modulus, C, is a function of the distance from the current stress point of the yield surface, S_{ij}, to the point on the limit surface with the same outward normal, S^L_{ij}, so that

$$C = f(S^L_{ij} - S_{ij})$$

It is desired to relate this modulus to common material properties, specifically K' and n'.

Since the uniaxial plastic modulus, E_p, is defined as

$$E_p = \frac{d\sigma}{d\varepsilon^p} \qquad (3.37)$$

where σ and ε^p are the uniaxial stress and uniaxial plastic strain, respectively, the Ramberg-Osgood equation

$$\sigma = K' (\varepsilon^p)^{n'} \tag{3.38}$$

may be used to get an expression for E_p in terms of K' and n'. This results in

$$Ep = \frac{d\sigma}{d\varepsilon^p} = K'(n') \left(\frac{\sigma}{K'}\right)^{\frac{n'-1}{n'}} \tag{3.39}$$

To relate these to the general plastic modulus, C, used in Eq. (3.9) or Eq. (3.10) in terms of deviatoric stress

$$d\varepsilon_{ij}^p = \frac{\frac{\partial f}{\partial S_{mn}} dS_{mn} \frac{\partial f}{\partial S_{ij}}}{C\left(\frac{\partial f}{\partial S_{kl}} \frac{\partial f}{\partial S_{kl}}\right)} \tag{3.40}$$

a factor of 2/3 must be multiplied to the uniaxial modulus as described in Section 3.3.3

$$C = 2/3\, E_p^{uniaxial} = 2/3 \frac{d\sigma}{d\varepsilon^p} = \frac{2}{3} K'(n') \left(\frac{\sigma}{K'}\right)^{\frac{n'-1}{n'}} \tag{3.41}$$

To develop an expression for the modulus as a function of S_{ij} and S_{ij}^L, it is helpful to look at a uniaxial hysteresis loop as in Fig. 3.18. In this figure, the tips of the loop are at $+\sigma_L$ and $-\sigma_L$, the limit stress in tension and compression, respectively. Also shown is the elastic unloading range, $2\sigma_y$, which is based upon Massings hypothesis that the hysteresis curve is twice the monotonic curve. These observations can be used to determine a functional dependence of the plastic modulus on S_{ij} and S_{ij}^L.

The plastic modulus, E_p, is a function of the distance possible between the current stress and the limit stress, point B. As the current stress approaches the limit stress, E_p goes to zero. Representing this distance as η, it is graphically shown in Fig. 3.18 for a uniaxial situation. The maximum distance, as shown, is the distance between point A, where reversed yielding first begins, and point B, the limit stress. As shown in both Figs. 3.18 and 3.19, this maximum distance is

$$\eta_{max} = 2(\sigma_L - \sigma_y)$$

In a multiaxial situation, η represents the distance from the current stress point to a point on the limit surface having the same outward normal as shown in Fig. 3.20. An expression for this distance may be determined in the same manner as the expression for the movement of the center of the yield surface using the Mroz hardening rule. The point on the limit surface with the same outward normal is

$$\sigma_{ij}^{L} = \frac{\sigma_L}{\sigma_y}(\sigma_{ij} - \alpha_{ij})$$

where α_{ij} is the center of the yield surface in stress space, σ_{ij}^{L} is the point on the limit surface, σ_L is the limit stress, and σ_y is the yield stress. The distance η can be expressed as

$$\eta = \sqrt{\left[\frac{\sigma_L}{\sigma_y}(\sigma_{ij} - \alpha_{ij}) - \sigma_{ij}\right]\left[\frac{\sigma_L}{\sigma_y}(\sigma_{ij} - \alpha_{ij}) - \sigma_{ij}\right]} \qquad (3.42)$$

Now letting D be the normalized difference between η and η_{max}

$$D = \frac{\eta_{max} - \eta}{\eta_{max}} \tag{3.43}$$

$$D = \frac{2(\sigma_L - \sigma_y) - \sqrt{\left[\frac{\sigma_L}{\sigma_y}(\sigma_{ij} - \alpha_{ij}) - \sigma_{ij}\right]\left[\frac{\sigma_L}{\sigma_y}(\sigma_{ij} - \alpha_{ij}) - \sigma_{ij}\right]}}{2(\sigma_L - \sigma_y)} \tag{3.44}$$

In the terms of deviatoric stresses this is

$$D = \frac{2(\sigma_L - \sigma_y) - \sqrt{3/2\left[\frac{\sigma_L}{\sigma_y}(S_{ij} - S^c_{ij}) - S_{ij}\right]\left[\frac{\sigma_L}{\sigma_y}(S_{ij} - S^c_{ij}) - S_{ij}\right]}}{2(\sigma_L - \sigma_y)} \tag{3.45}$$

(The $\sqrt{3/2}$ factor is needed for deviatoric stresses since the projection of σ_y into the π plane is $\sqrt{2/3}\,\sigma_y$.)

The value of D varies between zero and one. As shown in Fig. 3.21, it is zero when yielding first starts after elastic unloading, point A in Fig. 3.17. This value of D corresponds to a uniaxial stress of

$$\sigma = (\sigma_L - 2\sigma_y)$$

or

$$\sigma = 2\sigma_y - \sigma_L$$

D is equal to one when the stress touches the limit surface. The uniaxial stress in this case is

$$\sigma = \pm \sigma_L$$

An expression for the plastic modulus can now be developed using this term D, and relating it to the uniaxial stress strain response. It is assumed that the plastic modulus of a multiaxial stress-strain response will be the same as the uniaxial response for identical values of D. In other words, in a multiaxial situation, when the point on the yield surface is some specified distance from the limit surface, the plastic modulus will have the same value as if a uniaxial stress was this same distance from the uniaxial limit stress. Using Eq. (3.45) this results in the following expression for the plastic modulus

$$C = \frac{2}{3} K' n' \left[\frac{(2(\sigma_L - \sigma_y)(D - 1) + \sigma_L)}{K'} \right]^{1 - \frac{1}{n'}} \qquad (3.46)$$

if the term in brackets is positive. Physically the term in brackets must be positive. When this term is numerically negative, the plastic modulus is set to a large value (~100,000 ksi). This condition only occurs immediately after yielding and results in a small number of strain increments having a very small plastic strain component. This small plastic strain is consistent with observed material behavior in that the plastic strain component is small compared to the elastic strain component immediately after yielding. After several nearly elastic strain increments, the value of D quickly increases to a value that causes the term inside brackets to be positive. This increase in D means that the yield surface is getting closer to the limit surface. Consequently the plastic modulus, C, which is calculated from Eq. (3.46), becomes smaller and the plastic strain term makes up a greater portion of the total strain increment.

The results presented in Chapter 5 show that good agreement is obtained between experimental and predicted stress-strain response using this method of calculating C.

3.3.5 Number of Increments

In an incremental plasticity model, the predicted stress-strain response is dependent upon the number of increments used in calculating the change in stress for some finite change in strain. The solution algorithm can become unstable if too few increments are used. This instability is due to the fact that the stresses are determined after the plastic strain increment is first calculated such that

$$de_{ij}^{T} = de_{ij}^{P} + de_{ij}^{E}$$

$$de_{ij}^{E} = de_{ij}^{T} - de_{ij}^{P}$$

$$dS_{ij} = 2G\, de_{ij}^{E}$$

If the number of increments is too small, a plastic strain increment may be calculated that is larger than the total strain increment. In this case, a negative elastic strain increment for a positive total strain increment is predicted, thereby resulting in a negative increment in stress. As expected, the solution quickly diverges and becomes unstable.

It is desired to have enough increments that the solution converges to a stable stress response. However, it is conversely desired to minimize the number of additional increments so that extraneous computer time and storage is not needlessly used. This desire brings about the need for an efficient scheme to determine the number of increments needed for a finite strain change that insures accuracy and stability yet avoids excess calculations. The following is such a scheme.

Shown in Fig. 3.22 is some current stress state A which is within the yield surface (elastic response). If a strain change occurs such that the stress response is no longer elastic, some combination of elastic and plastic response occurs during the change. Since the elastic response is not dependent upon the number of increments, the change in stress corresponding to the change in strain occurring when going from stress point A to the yield surface is determined directly in one step. After the stresses reach the yield surface, plastic strains are developed. The solution now becomes dependent upon the number of increments. The number of increments needed depends both on the size of the strain increment, $\Delta\varepsilon_{ij}$, and the degree of nonproportionality in the strain change. The more nonproportional, the greater the number of increments needed.

To determine the number of increments required, first suppose that point B in Fig. 3.22 corresponds to the stress state that would be predicted if the change in strains was totally elastic. The algorithm to determine the number of increments must be a function of the size of the effective strain change and the degree of nonproportionality, which is defined by the angle, θ, between $\overrightarrow{AB}$ and the normal to the yield surface at the point of intersection with $\overrightarrow{AB}$, as shown in Fig. 3.22.

To develop this algorithm, the stress state corresponding to point B must be determined. This is

$$\varepsilon_{ij}^{B} = \varepsilon_{ij}^{A} + \Delta\varepsilon_{ij}$$

$$e_{ij}^{B} = \varepsilon_{ij}^{B} - 1/3\ \delta_{ij}\ \varepsilon_{kk}^{B}$$

$$S_{ij}^{B} = 2G\ e_{ij}^{B}$$

In addition, the stress state where the vector $\overrightarrow{AB}$ intersects the yield surface must be calculated. This is

$$\frac{3}{2}\left[S_{ij}^{A} + a(S_{ij}^{B} - S_{ij}^{A}) - S_{ij}^{C}\right]\left[S_{ij}^{A} + a(S_{ij}^{B} - S_{ij}^{A}) - S_{ij}^{C}\right] = \sigma_y^2$$

$$\frac{3}{2}\left[(S_{ij}^{A} - S_{ij}^{C}) + a(2G\Delta\, e_{ij}^{T})\right]\left[(S_{ij}^{A} - S_{ij}^{C}) + a(2G\Delta\, e_{ij}^{T})\right] = \sigma_y^2 \qquad (3.47)$$

Solving the quadratic for the positive root gives the scaling factor "a" and the stress point, S_{ij}^{*}, on the yield surface can now be determined.

$$S_{ij}^{*} = S_{ij}^{A} + a(S_{ij}^{B} - S_{ij}^{A}) \qquad (3.48)$$

The stress charge from S_{ij}^{A} to S_{ij}^{*} is all elastic. The corresponding strain tensor for this point is

$$\varepsilon_{ij}^{*} = a\Delta\varepsilon_{ij} + \varepsilon_{ij}^{A} \qquad (3.49)$$

The remainder of the strain change

$$(1 - a)\,\Delta\varepsilon_{ij}$$

is elastic-plastic and must be broken into increments to calculate the corresponding stress increments. To determine the number of increments needed, the following information is needed.

The radius of the surface that goes through the stress point B is

$$R_B = \sqrt{3/2\ (S_{ij}^B - S_{ij}^C)\ (S_{ij}^B - S_{ij}^C)} \tag{3.50}$$

The size of the combined strain change can now be related to the ratio of R_B to R_y. The term R_y is the radius of the yield surface, σ_y. Therefore,

$$R = \frac{R_B}{R_y} = \frac{R_B}{\sigma_y}$$

gives some measure of the size of the effective strain change.

The angle θ, can be determined as follows

$$\cos\theta = \frac{S_{ij}^{*}(S_{ij}^B - S_{ij}^{*})}{\sqrt{(S_{mn}^{*}\ S_{mn}^{*})(S_{kl}^B - S_{kl}^{*})(S_{kl}^B - S_{kl}^{*})}} \tag{3.51}$$

A relationship that relates the number of increments needed to these values is

$$nn = 2^{(\frac{R}{4} + 1)}\ [(1 - \cos\theta)\ X + Y] \tag{3.52}$$

where X and Y are constants and nn is the number of increments. The value of X insures that a larger number of increments is used as the strain change is more nonproportional. The value of Y insures that at least some minimum number of increments is used when the loading is totally proportional.

The values X and Y were determined by evaluating the stress-strain response for a number of paths including uniaxial, 90° out-of-phase and other combined nonproportional paths. These values were empirically determined to be X =20, Y = 2.

Using Eq. (3.52) for the determination of the number of increments avoids use of an excess number of increments for small, proportional strain changes yet provides a larger number of increments for nonproportional or large strain changes. This method avoids a waste in computer time and space yet insures that enough increments are used for a stable stress response.

3.3.6 Neutral Loading

For neutral or nearly neutral loading the stresses remain on the yield surface but the center of the yield surface does not move. In other words, the stress increment is along the tangent to the yield surface. Neutral loading is described mathematically

$$\frac{\partial f}{\partial S_{ij}} dS_{ij} - 0$$

An algorithm is needed to insure that the stresses remain on the yield surface. This algorithm is generally needed only for neutral loading or nearly neutral loading such as 90° out-of-phase loading.

The need for this algorithm is made clear through the study of 90° out-of-phase loading. In this case, the stress increment is nearly tangent to the yield surface as shown in Fig. 3.23. However, the plastic strain is proportional to the normal to the yield surface through the constant, $d\lambda$, where

$$d\lambda = \frac{1}{C} \frac{\frac{\partial f}{\partial \sigma_{ij}} d\sigma_{ij}}{\frac{\partial f}{\partial \sigma_{mn}} \frac{\partial f}{\partial \sigma_{mn}}}$$

Since the stress increment is parallel to the yield surface and is perpendicular to the yield surface normal, the dot product

$$\frac{\partial f}{\partial \sigma_{ij}} \, d\sigma_{ij}$$

is zero. This causes $d\lambda$ to be zero and consequently predicts the plastic strain to be zero. Therefore, in this case, the elastic strain is equal to the total strain and the stress increment is related to the total strain.

Since the movement of the center of the yield surface is related to the amount of plastic strain, no movement is predicted. Therefore, an elastic stress increment is added to the current stresses while no movement in the yield surface occurs. The addition of this elastic increment would then result in stresses that are not on the yield surface (S'_{ij} in Fig. 3.23). To correct this situation the stresses are radially returned to the yield surface, S^*_{ij}, while leaving the yield surface center stationary.

To ensure that the stresses remain on the yield stress the value of the current yield function is calculated after the stress increments, dS_{ij}, have been added to obtain the current stress state, S_{ij}.

$$\text{yieldfunction} = 3/2 \, (S_{ij} - S^c_{ij}) \, (S_{ij} - S^c_{ij})$$

The ratio of this value to the yield stress is then determined which is

$$K = \sqrt{\frac{(\text{yieldstress})^2}{\text{yieldfunction}}} \qquad (3.53)$$

This value is then used to radially return the stresses back to the yield surface.

3.3.7 Limit Plasticity

In a two surface model, a yield surface and a limit or bounding surface are used. When the effective stress reaches the limit stress, flow takes place. The limit stress represents a limiting value of tensile stress that can be applied to a material in uniaxial loading. Perfectly plastic behavior or limit behavior occurs when the stress reaches the limit stress. The von Mises equation for the limit surface is

$$f = 3/2\ S_{ij}\ S_{ij} - \sigma_L^2 = 0 \tag{3.54}$$

which, like the yield surface, is also a circle in deviatoric stress space. Flow, or plastic strain change at constant stress, occurs when the stress point, S_{ij}, lies on the limit surface and Eq. (3.54) is satisfied.

The following equations are used in the computer code to model limit behavior.

$$de_{ij}^{T} = de_{ij}^{E} + de_{ij}^{P}$$

$$de_{ij}^{T} = \frac{dS_{ij}}{2G} + d\lambda \frac{\partial f}{\partial \sigma_{ij}}$$

Multiplying both sides of the equation by S_{ij} gives

$$S_{ij}\ de_{ij}^{T} = \frac{S_{ij}\ dS_{ij}}{2G} + d\lambda \frac{\partial f}{\partial \sigma_{ij}} S_{ij}$$

Since

$$\frac{\partial f}{\partial \sigma_{ij}} = \frac{\partial f}{\partial S_{ij}} = 3S_{ij}$$

$$S_{ij}\, de^{T}_{ij} = \frac{S_{ij}\, dS_{ij}}{2G} + d\lambda 3 S_{ij}\, S_{ij} \qquad (3.55)$$

Since the stresses may not exceed the limit surface, only neutral loading is allowed or

$$S_{ij}\, dS_{ij} = 0$$

which can be physically interpreted as shown in Figure 3.23. The gradient $\frac{\partial f}{\partial \sigma_{ij}}$ is perpendicular to the limit surface and dS_{ij} must be tangent since the dot product of these two is equal to zero. Therefore, in the above equation

$$S_{ij} de^{T}_{ij} = d\lambda 3\, (2/3\, \sigma_L^2) \qquad (3.56)$$

and

$$d\lambda = \frac{S_{ij} de^{T}_{ij}}{2\, \sigma_L^2} \qquad (3.57)$$

where

$$de^{T}_{ij} = d\varepsilon^{T}_{ij} - 1/3\, d_{ij}\, d\varepsilon^{T}_{kk}$$

$$d\varepsilon^{p}_{ij} = d\lambda \frac{\partial f}{\partial \sigma_{ij}}$$

$$d\varepsilon^{p}_{ij} = d\lambda\, 3 S_{ij}$$

results in

$$d\varepsilon_{ij}^{p} = \frac{3}{2}\frac{S_{lk}\, de_{lk}^{T}}{\sigma_L^2} S_{ij} \tag{3.58}$$

An expression for the deviatoric stress increment analogous to Eq. (3.24) of is now developed.

$$dS_{ij} = 2G\left\{ d\varepsilon_{ij}^{T} - 1/3\; d\varepsilon_{kk}^{T}\, \delta_{ij} - \frac{S_{mn}\, de_{mn}^{T}}{2/3\; \sigma_L^2} S_{ij} \right\} \tag{3.59}$$

since

$$S_{mn}\, de_{mn}^{T} = S_{mn}\,(d\varepsilon_{mn}^{T} - \frac{\delta_{mn}}{3} d\varepsilon_{kk})$$

and

$$S_{mn}\, \delta_{mn} = 0$$

$$dS_{ij} = 2G\left\{ d\varepsilon_{ij}^{T} - 1/3\; d\varepsilon_{kk}^{T}\, \delta_{ij} - \frac{S_{mn}\, d\varepsilon_{mn}^{T} S_{ij}}{2/3\; \sigma_L^2} \right\} \tag{3.60}$$

Similar to the discussion presented in Section 3.3.6 for neutral loading, the stresses must remain on the limit surface. Therefore, after the stress increment, dS_{ij}, is added to determine the new stress state, the stresses are projected back onto the limit surface. This procedure is done using the following equations.

Using dS_{ij} calculated from Eq. (3.60) above, the new equivalent stress, F_S, is calculated which is

$$Fs = \left[3/2 \left\{ (S_{ij} + dS_{ij})(S_{ij} + dS_{ij}) \right\} \right]^{1/2}$$

The stresses are then projected back to the yield surface by the following

$$S_{ij}^{b} = 0.99 \frac{S_L}{Fs} (S_{ij} + dS_{ij}) \tag{3.61}$$

where $S_L = \sqrt{2/3}\, \sigma_L$.

(The factor of 0.99 is used for numerical reasons. This factor causes the stresses to be almost on the limit surface.) Finally, the new stress increments which cause stresses to remain on or just below limit surface are calculated. These are

$$dS_{ij}^{*} = S_{ij}^{b} - S_{ij} \tag{3.62}$$

The corresponding change in the center of the yield surface is

$$S_{ij}^{c^*} = (1 - \frac{\sigma_y}{\sigma_L}) (S_{ij} + dS_{ij}^{*}) \tag{3.63}$$

$$dS_{ij}^{c} = S_{ij}^{c^*} - S_{ij}^{c} \tag{3.64}$$

From the equations presented in this section, the stress histories may be calculated. Figure 3.17 shows the flow chart of the computer procedure to do this.

3.4 Planes

To evaluate the damage caused by the applied loading on an arbitrary plane, the stresses and strains acting on the plane must be determined. The following section describes the procedure used to determine these. In addition, the applied loads develop a plane stress state on the surface of the component. This plane stress state allows a reduction in the number of planes that must actually be evaluated. This is also discussed in the following section.

3.4.1 Local Stresses and Strains

The orientation of a plane is defined by the vector normal to the plane. The normal vector, $\underset{\sim}{n}$, is referenced to the x-y-z coordinate system using the angles ϕ and θ as shown in Fig. 3.24. The right-handed x-y-z coordinate system is defined by the position of the strain gauge as shown in Fig. 3.25. If strain gauge data is not used, the x-y-z coordinate system is defined by the user where the z direction is always normal to the free surface. The θ is the angle from the z axis, while the angle ϕ is the angle from the x axis in the x-y plane. The positive value of ϕ is from the positive x-axis to the positive y-axis.

To obtain the normal and shearing strains acting on an arbitrary plane, a tensor rotation is performed. The strains and stresses are rotated from the x-y-z coordinate system defined by the stain gauges or the user to the x'-y'-z' coordinate system, which is the local coordinate system with respect to the plane. In the local coordinate system, the z' direction is the same direction as the normal vector, $\underset{\sim}{n}$, and the x'-y' axes lie in the plane. The x'-y'-z' coordinate system is right-handed and is oriented such that when θ and ϕ are equal to zero, the x' direction is in the direction of the y axis and the y' direction is in the direction of the negative x axis. (See Fig. 3.24.)

As stated, a tensor rotation is performed such that

$$\varepsilon_{ij} = a_{ip}\varepsilon_{pq}a_{qj}$$

where a_{ip} and a_{qj} are transformation matrices made up of direction cosines. For example, the transformation matrix a_{ip} is

$$a_{ip} = \begin{bmatrix} \cos(x'x) & \cos(y'x) & \cos(z'x) \\ \cos(y'x) & \cos(y'y) & \cos(z'y) \\ \cos(z'x) & \cos(z'y) & \cos(z'z) \end{bmatrix}$$

Using the angles ϕ and θ defined above, these matrices are

$$a_{ip} = \begin{bmatrix} -\sin\phi & \cos\phi & 0 \\ -\cos\phi\cos\theta & -\cos\theta\sin\phi & \sin\theta \\ \sin\theta\cos\phi & \sin\theta\sin\phi & \cos\theta \end{bmatrix}$$

$$a_{qj} = \begin{bmatrix} -\sin\phi & -\cos\phi\cos\theta & \sin\theta\cos\phi \\ \cos\phi & -\cos\theta\sin\phi & \sin\theta\sin\phi \\ 0 & \sin\theta & \cos\theta \end{bmatrix}$$

For the shear and tensile models used in this code, the normal stress and strain, as well as the shearing strains, acting on the plane are needed. In terms of the local coordinate system, these are $\varepsilon_{3'3'}$, (the normal strain), $\sigma_{3'3'}$ (the normal stress), and $\varepsilon_{2'3'}$ and $\varepsilon_{1'3'}$ (the shearing strains, $\gamma_{1'3'}/2 = \varepsilon_{1'3'}$, $\gamma_{2'3'}/2 = \varepsilon_{2'3'}$). Performing the tensor rotation and using the fact that $\gamma_{xz} = \gamma_{yz} = \tau_{xz} = \tau_{xz} = \sigma_z = 0$, since it is a plane stress situation, these components become

$$\varepsilon_{2'3'} = -\varepsilon_{xx}(\cos^2\phi\cos\theta\sin\theta) - \varepsilon_{yy}(\sin^2\phi\cos\theta\sin\theta) + \varepsilon_{zz}(\sin\theta\cos\theta) - \gamma_{xy}(\cos\theta\sin\theta\cos\phi\sin\phi)$$

$$\varepsilon_{1'3'} = -\varepsilon_{xx}(\sin\phi\cos\phi\sin\theta) + \varepsilon_{yy}(\sin\phi\cos\phi\sin\theta) + \frac{\gamma_{xy}}{2}(-\sin^2\phi\sin\theta + \cos^2\phi\sin\theta)$$

$$\varepsilon_{3'3'} = l^2\varepsilon_{xx} + m^2\varepsilon_{yy} + n^2\varepsilon_{zz} + \gamma_{xy}lm \qquad (3.65)$$

$$\sigma_{3'3'} = l^2\sigma_{xx} + m^2\sigma_{yy} + 2\tau_{xy}lm$$

where l, m, n are the direction cosines and are

$l = \cos\phi\sin\theta$

$m = \sin\phi\sin\theta$

$n = \cos\theta$

Figure 3.26 shows the orientation of the local coordinate system and the shearing strains, $\varepsilon_{1'3'}$ and $\varepsilon_{2'3'}$, for $\theta = 45°$ and $\phi = 0°$. Appendix C presents additional examples of different plane orientations for several values of θ and ϕ.

3.4.2 Possible Planes

The number of planes on which the damage must be calculated is reduced by taking advantage of the plane stress state. The representation of the strain state for the two possible loading cases is shown in Fig. 3.27 using Mohr's circle. In case A, both the applied strains ε_x and ε_y are positive. This induces a contraction in the z direction. In other words, ε_z is negative. In case B, one applied strain is positive and the other is negative. Consequently, ε_z, which may be positive or negative, is located some place between ε_x and ε_y.

Using this information allows a reduction in the number of planes that must be analyzed. For the tensile model, the plane experiencing the maximum damage must be located in the x-y plane ($\theta = 90$) as shown in Fig. 3.28. For the shear model, the plane experiencing the maximum shear damage can lie either in a plane oriented 45° from the z axis ($\theta = 45$), Case B, or in the x-y plane ($\theta = 90$), case A. In addition, the shearing strain has a direction

associated with it. Therefore, the damage associated with both $\varepsilon_{1'3'}$ and $\varepsilon_{2'3'}$ must be calculated and summed individually.

(A third case, other than case A and case B could exist where ε_z could be larger than both ε_x and ε_y. However in the tensile model, no damage is predicted. Since no shearing strain occurs on the free surface ($\gamma_{xz} = \gamma_{yz} = 0$), ε_z is the principal strain, ε_1, and σ_z is the principal stress, σ_1, and $\frac{\Delta\varepsilon_z}{2}\sigma_z = \frac{\Delta\varepsilon_1}{2}\sigma_1$. Consequently, the tensile model is such that $(\Delta\varepsilon_{zz}/2)\sigma_z = 0$ since σ_z is zero due to the plane stress state. In the shear model, although damage is predicted, the maximum shear occurs 45 degrees from ε_z ($\theta = 45$) which is already taken into consideration in case A. Therefore, this case need not be analyzed using either the tensile or shear model.)

Using the shear damage model, the code first calculates the damage on a plane for the shearing strain $\varepsilon_{2'3'}$ with $\theta = 45$ and ϕ varying from 0 to 180 degrees, in increments of 10 degrees. The value of 10° was chosen as the increment size due to the fact that the damage calculated on the planes within 5 degrees on either side of the critical plane is very similar to the damage calculated on this plane. This similarity is evident from the damage or fatigue life plots presented in Chapter 5. The code then calculates damage for $\varepsilon_{1'3'}$ with $\theta = 45$ and ϕ varying from 0 to 180 degrees in 10 degree increments. Finally, since no shearing strain exists on the free surface, there is only one possible shearing strain direction for $\theta = 90$. The damage calculations for $\theta = 90$ are done last with ϕ varying between 0 and 180 degrees. Using the tensile model the program only calculates damage on planes corresponding to $\theta = 90°$, $\phi = 0$ to 180° in 10° increments. The flow chart for the computer program used to implement this procedure is shown in Fig. 3.29.

3.5 Rainflow Counting with Tensile and Shear Models

Once the loading history has been edited or condensed and the stresses and strains have been rotated to a plane, damaging events must be identified on this plane. Damaging events--the appropriate cycles of strain--are identified using a rainflow counting procedure.

Rainflow counting is a method of cycle counting first developed by Matsuishi and Endo [3.22]. It has since become a generic term for any cycle counting method which attempts to identify closed hysteresis loops in the stress-strain response of another loaded component cycled in tension of compression. ASTM Standards E1049 [3.23] gives several rainflow counting algorithm easily adapted into computer codes. An efficient "one-pass" algorithm developed by Downing and Socie [3.24] is used in the code. The results obtained using this method are identical to the results obtained using a method which starts at the largest peak or valley.

Using this rainflow counting method, cycles of the normal or tensile strain, $\varepsilon_{3'3'}$, are identified for use in the tensile model, while the shearing strains, $\gamma_{1'3'}$ or $\gamma_{2'3'}$, are identified for use in the shear model. The strain amplitudes corresponding to these cycles of strain are then used to calculate the damage parameter. This parameter, in turn, can be related to fatigue damage or fatigue life for this cycle. For example, using the tensile damage model given in Eq. (2.13), the damage parameter is the product

$$\frac{\Delta\varepsilon}{2}\sigma$$

where σ is the peak tensile stress occurring during the current cycle of strain on this plane.

This interpretation of the damage parameter is slightly different than the interpretation used in the analysis of very short multiaxial loading histories made up of repeating cycles. For example, in that application, as discussed in Chapter 2 for the Smith Watson Topper parameter, the term $\Delta\varepsilon/2$ has been defined as normal strain amplitude on the plane experiencing the maximum amplitude of tensile strain and σ as the normal stress on this plane. Therefore, the critical plane was defined as the plane experiencing the maximum range of tensile strain. However, in the multiaxial variable amplitude life prediction methodology, this interpretation is slightly modified. In this approach, $\Delta\varepsilon/2$ is the normal strain amplitude and σ is the normal stress for the current cycle on the plane being analyzed. The critical plane is then defined as the plane experiencing the maximum damage.

A simple example to point out the need for this modification is the loading case made up of one cycle of tension followed by many smaller cycles of torsion. It is intuitively obvious that the plane experiencing the largest alternation of tensile strain will not be the failure plane. Rather, the many thousands of torsion cycles will cause the majority of the damage, and the critical plane will be the plane most damaged by the torsion cycles.

This same interpretation is used with the shear parameter given in Eq. (2.12). Instead of the critical plane being defined as the plane experiencing the maximum alternation of shear strain, $\hat{\gamma}$, the critical plane is again defined as the plane experiencing the maximum damage. Using this parameter, damage is calculated by the product of $\hat{\gamma}$ and $(1 + \frac{\sigma_n}{\sigma_y})$ where $\hat{\gamma}$ is the shear strain amplitude and σ_n is the normal stress for the current cycle of strain acting on the plane being analyzed.

It should be noted that this interpretation causes a slight irregularity to occur for pure torsion. In this case, the critical plane is predicted to be planes ±10° from the planes experiencing the maximum shear strain, as shown in Fig. 3.30. This 10° deviation from the maximum shear strain plane is due to the normal stress term. The Mohr's circles for the stress and strain states in torsion are shown in Fig. 3.31. As seen, for planes very close to the maximum shear planes, the shear strain amplitude is very close to the maximum shear strain. However, on these planes a normal stress term is included as shown. (On the maximum shear planes the normal stress is zero.) Consequently, the predicted planes are slightly different than the maximum shear planes. However, this problem is not felt to be significant since the predicted failure plane is very close to the maximum shear plane or the actual failure plane.

Using these damage parameters, the fatigue life, N_f, or fatigue damage, $1/N_f$, associated with each cycle of strain can be determined using Eq. (2.12) or Eq. (2.13) and uniaxial or torsional material properties, respectively.

The shear or torsional material properties needed in Eq. (2.12), $\gamma_{f'}$, $\tau_{f'}$ are obtained from torsional strain life fatigue data. If these properties are not available, they may be derived from the uniaxial material properties $\sigma_{f'}$, $\varepsilon_{f'}$, using a von Mises equivalency such that

$$\gamma_{f'} = \varepsilon_{f'}\sqrt{3}$$

$$\tau_{f'} = \frac{\sigma_{f'}}{\sqrt{3}}$$

However, it is better to use measured values, if possible. The derived values usually differ from the measured values. For example, Table 3.1 shows the derived and measured shear values for stainless steel 304 and SAE 1045 steel.

The damage associated with each cycle is summed using Miner's rule [3.25], a linear damage summation technique, such that

$$D = \sum_{i=1}^{n} N_{fi}$$

where n is the number of cycles and N_{fi} is the fatigue life for the i-th cycle. A damage value, D, is then determined for each plane. The critical plane is identified as the plane with the maximum damage, D, and the fatigue life of the component, in blocks to failure, is determined using the damage associated with this plane.

3.6 Summary

A method to estimate the fatigue life of a component subjected to multiaxial loading and the details of a computer code developed to implement the method have been presented. Technical details and objectives have also been discussed. Using the code and experimental data, an evaluation of the proposed method has been made. Results of the evaluation are presented in Chapter 5.

4. EXPERIMENTAL PROCEDURE AND TEST RESULTS

4.1 Introduction

Data from two types of experimental tests were used to evaluate and verify the variable amplitude multiaxial fatigue life estimation procedure presented in Chapter 3. Tension-torsion tests, conducted on thin-wall tubes, were used to verify and evaluate the constitutive modelling. Predicted stresses determined using the constitutive model were compared to measured stresses obtained experimentally for the same strain history. Variable amplitude tests conducted on strain-gauged components were used to evaluate the complete variable amplitude life prediction method, of which the constitutive modelling is just a part. The following section describes the experimental procedures, materials, and specimen geometries used for both types of tests.

4.2 Thin-Wall Tubes

Thin-wall tubes were tested using a MTS model 809 tension-torsion servo-hydraulic load frame with an MTS model 463 processor/interface. A PDP 11/23 computer was used to run the tests in strain control while an internal extensometer described in Ref. [4.1] was used to measure strains. Tension and torsion loads and deflections were digitally stored using the computer, allowing both stress and strain data to be determined and recorded. The shear strains were controlled to mid-surface values.

Thin wall tubes of AISI 304 stainless steel and normalized SAE 1045 steel were machined from hot rolled bar stock both containing manganese sulfide stringers. The 1045 steel tubes had a wall thickness of 0.1 inch while the 304 tubes had a wall thickness of 0.15 inch. Both had a 1.0 inch internal diameter. The specimens were polished to 0.5 micron surface finish. Refs [4.2-4.4]

provide additional details on the testing procedures, materials, and geometries of the test specimens.

In general, the out-of-phase tension-torsion tests were run at equivalent von Mises strain amplitudes. In other words, the maximum shear strain, γ, was a factor of $\sqrt{3}$ times the maximum axial strain, ε. The stress-strain response for these tests was assumed to be stable at half the fatigue life and it is this response that is reported here. Failure or fatigue life was defined as a 10% drop in the stabilized load.

4.3 Variable Amplitude Loading of Notched Components

Variable amplitude tests loaded in bending, proportional bending and torsion, and nonproportional bending and torsion were conducted on strain gauge components. The test procedures and specimen geometry for the bending and proportional loading are presented in the following section. The corresponding information for the nonproportional loading is in Section 4.3.2

4.3.1 Proportional Loading Tests

Proportional loading variable amplitude tests were conducted on the notched component shown in Fig. 4.1. The component was machined out of normalized SAE 1045 steel furnished as 63.5 mm diameter hot-rolled bar stock. The component had holes drilled in the flat end so that the loading could be applied to achieve either pure bending or combined bending and torsion. The combined loading was obtained by applying the load through a 6 inch lever arm secured using these holes, as shown in Fig. 4.2.

The SAE transmission loading history presented in Fig. 4.3, which was developed and used in the uniaxial variable amplitude test program described in Ref. [4.5], was applied to the component. The load history was scaled so that

the maximum peak in the history corresponded to the maximum desired load level. The components were run in load control using the fixture shown in Fig. 4.4.

White paint was applied to the component in the notch area allowing easy detection of cracks during periodic visual inspections throughout the fatigue life of the component. The fatigue life to crack initiation was reported when any unquestionable crack or cracks were visible. These were on the order of 0.2 to 0.5 mm. Life to failure corresponded to separation of the component for the pure bending tests and the development of a long crack (>1") for the combined loading tests.

Variable amplitude tests were initially run on an unstrain-gauged component until failure for a desired load level. The crack location was identified from this test. Another component, with a strain gauge rosette applied at this location, was then loaded with the same history at the same load level. After repeated loading blocks were applied to allow the strain response to stabilize, the strains were recorded using a SOMAT 2000. This strain gauge rosette information was then used as input for the variable amplitude multiaxial fatigue life prediction computer program. Figure 4.5 shows a component with the strain gauges applied.

4.3.2 Nonproportional Loading Tests

Nonproportional variable amplitude tests were conducted on the notched component shown in Fig. 4.6. This is basically the same geometry as that of the shaft used in the SAE notched shaft round robin program discussed in Ref. [4.6]. The only modification made to the SAE geometry was that the notch root radius was enlarged to reduce the stress concentration and allow

easy placement of a strain gauge. The shaft was also made out of SAE 1045 normalized steel in a hot-rolled condition with an as-machined surface finish.

A test frame, very similar to that described in Ref. [4.7], was used to apply the bending and torsional loads to the notched component. The system, shown in Fig. 4.7, consisted of two 5000 pound actuators and load cells with MTS 406 controllers. In addition, an MTS 871 programmable test site controller was used to control the variable amplitude load signals. The 871 controller was set up with two independent output channels, each feeding into a 406 controller. The two channels were linked together for starting, holding, and stopping at the same time. The history fed into the 406 controllers consisted of 200 discreet points that were taken from the SAE transmission history. These were approximately the 200 largest excursions in the transmission history and were manually input into the 871 system. Appendix D lists the values used in the history with the largest value given as 100%. Identical histories were fed into each controller, with an offset in time between the two signals corresponding to 111 excursions in the history as shown in Appendix D. This resulted in truly nonproportional loading as shown in Fig. 4.8 , which is a strip chart recording of the two load signals. The loading rate between peaks was held approximately constant as shown.

Like the proportional tests, a SOMAT 2000 was used to obtain the strain histories and white paint was applied to the specimen surface to allow easy detection of cracks. In both proportional loading and nonproportional loading tests, stacked strain gauge rosettes, Micromeasurements WK-06-060WR350 gauges, were used.

Nonproportional variable amplitude loading tests were conducted at three load levels. The smallest load level had a maximum peak in the history that was 46% of full scale, where full scale was approximately 5000 pounds. The

middle load level had a maximum peak of 51% of full scale, while the maximum load level tested had a maximum peak of 55%.

Again tests were run on components to failure. The cracking location was observed and one strain gauged component was then run to obtain the three strain histories. The strain-gauged shaft was first loaded with a variable amplitude loading history whose maximum peak was 46% of full scale, hereafter termed the 46% load level. Blocks 1-7 were recorded at this load level. The test was continued and blocks 19 through 25 were again recorded with the strain gauges rezeroed before the initial recording (before block 19). The strain gauges were rezeroed to remove any drift in the gauges. Subsequently, the test was again continued and blocks 33-34 recorded at the 46% load level. The load level was then increased to 51% and strain histories were taken at blocks 35-44 and 45-46. The block count continued from the 46% test such that block 35 represented the first block after the loading was increased. Finally, the load level was increased to 55% and blocks 46-51 and 52-53 were recorded.

The strain histories recorded varied between blocks. In other words, the strain history for block 19 did not have the same appearance as block 20 and block 20 did not have the same appearance as block 34, as shown in Fig. 4.9. Output from the strip chart recorder, Fig. 4.8, insured that there was no difference in the timing of the load signals. Instead, it was believed that this behavior was due to transient material response. Normalized SAE 1045 steel cyclically softens and it is reasoned that the boundary between the plastic zone on the outside of the shaft and the elastic core continued to change (the size of the plastic zone became larger) throughout the life of the shaft. This theory was supported by the fact that a bend or permanent set occurred in the shafts tested at the 51% and 55% load levels. Instead of occurring at the beginning of the

life of the shaft, however, the bend or set progressively developed throughout the fatigue life. In other words, the elastic load carrying capacity of the shaft continued to decrease with fatigue life.

In addition to the strain histories obtained as described above, a shaft tested at a 55% load level to failure (Specimen NP5) was strain gauged at a midpoint in life. Strain histories at blocks 542 and 674 were then obtained for comparison to the strain history obtained at block 52 at the 55% load level in the incremental test described above. The actual test specimen tested at 51% (NP6) was also strain gauged. Block numbers 2, 5, and 665 were recorded for comparison to the incremental test histories. Again, the strain gauges were re-zeroed before each reading.

4.4 Test Results

Table 4.1 presents the results of tests conducted on the two types of SAE 1045 notched components. Three types of tests were conducted: bending, in-phase bending and torsion, and out-of-phase bending and torsion. Two tests were run in bending with a maximum load of approximately 5500 N for the peak load in the variable amplitude SAE transmission history. Two tests were also conducted in proportional loading with a maximum load of approximately 4500 N, as well as two nonproportional tests at the 55% load level. One non-proportional test was run at each of the two load levels, 46% and 51%. Good repeatability was observed for the duplicated tests as reported in Table 1.

In all the tests, the cracks initiated at or very near the tangency point of the notch. The fracture surface of specimen PB4, tested in pure bending, is shown in Fig. 4.10. Multiple crack initiation sites occurred on a plane located approximately 3.1 inches from the flat end of the component, the tangency point of the notch root radius. Although a macroscopic tensile failure was observed

for the pure bending tests, the cracks initiated in a shear mode as evidenced by the "factory roof top" fracture surface. Also, the side view of the fracture surface, presented in Fig. 4.10b, shows significant 45 degree cracking, indicative of shear crack initiation. The final failure plane was oriented perpendicular (90 degrees) from the direction of maximum principal stress. Clearly defined regions of crack growth can be seen on the fracture surface.

The plane on which cracking occurred in the pure bending tests was identified from test specimens PB2 and PB4. Due to the symmetry of the loading and the component geometry, the maximum load occurred along the center line of the component, 3.1 inches from the flat end of the component. Therefore, two strain gauge rosettes were placed on either side of the center line at this location. One gauge was oriented such that the legs of the rosette made angles of 0, 45, and 90 degrees with a line perpendicular to the center line of the component as shown in Fig. 4.5. The second gauge made angles of -45, 0, and 45 degrees from this same line. The second gauge allowed verification of the first strain gauge data. In addition, it allowed two different sets of strain gauge readings (with different values due to the different orientations) to be used as input to the computer program. The fatigue life predictions should be independent of gauge orientation. This information allowed verification that the program did, in fact, produce similar fatigue life predictions regardless of gauge orientation.

In the proportional loading tests, the cracks first initiated at the tangency point of the notch root radius, approximately 1/4 inch from the specimen edge. Thus the strain gauge was placed at this location on the specimen used to obtain the strain history, as shown in Fig. 4.11. In the proportionally loaded specimens run to failure, PL2 and PL3, many small cracks were observed in this general vicinity before a major crack developed. This is predictable since the

stress distribution is relatively constant in the area 3/16 inch and 1/2 inch from the specimen edge.

The fracture surface of the proportionally loaded specimen PL3 is shown in Fig. 4.12. As seen, it had a "factory roof top" appearance, although much less pronounced than that observed in the pure bending. Multiple crack initiation sites were observed, which is typical of a fatigue failure at this high load level. These cracks linked to form a macroscopic failure crack on a plane that was oriented generally perpendicular to the center line of the specimen.

In the nonproportionally loaded tests, cracks initiated from machining marks in all except one test. (See Fig. 4.13.) Fash [4.8] reported the same surface finish sensitivity of the SAE notched shafts when tested under constant amplitude loading. In only one test, NP6 (51% load level), was the surface painted to allow easier detection of the cracks. In this case, the crack initiated and grew on a plane oriented about 70-80 degrees clockwise from the center line of the specimen as shown in Fig. 4.14.

Cracks initiated on the top surface of the specimen, at the tangency point of the notch root radius. Consequently, a strain gauge was placed at this location on the specimen used to obtain the strain histories and on NP6 and NP5. In all cases, the middle leg of the rosette, labeled "Channel 2" was placed parallel to the axis of the shaft. The leg of the rosette labeled "Channel 1" was oriented 45 degrees clockwise to the middle leg and "Channel 3" was oriented 45 degrees counter-clockwise, as shown in Fig. 4.15.

The strain histories obtained in the three types of tests were used as input to the multiaxial variable amplitude life prediction procedure. The results of these analyses and the comparison of the predicted fatigue lives to the experimentally determined lives is presented in the following chapter.

5. MODEL EVALUATION

5.1 Introduction

The model presented in Chapter 3 was evaluated and verified in several methods. First, the constitutive model was verified by comparing the predicted stress-strain responses to experimentally determined results from thin wall tubes. The variable amplitude multiaxial fatigue life prediction model was then evaluated using simple nonproportional variable amplitude loading test results obtained experimentally on a thin wall tube. Finally, results from analyses, which used experimentally obtained strain histories as input, were compared to the corresponding fatigue lives of components determined experimentally. The results of these comparisons are presented and discussed below.

5.2 Constitutive Model Verification

The constitutive model, described in detail in Chapter 3, was evaluated by comparing predicted stress-strain responses with the responses determined experimentally from tests conducted on thin wall tubes. The tensile and torsional loads and deflections were measured in these tests. Although the actual stress response varied with the wall thickness, it was assumed that this variation was negligible and that the axial and shear stress was constant over the wall thickness. This assumption is consistent with the assumptions made by other researchers [5.1-5.3].

The constitutive model was modified from a general plane stress version (where three strains are used as input) to a version for predicting the stress-strain response of thin wall tubes. This modification was done by setting the circumferential and radial strains equal and relating them to the axial strain through the following equation

$$d\varepsilon_z^T = \left\{K\left[d\varepsilon_x^T(S_{xx} - S_{xx}^c) + d\gamma_{xy}^T(S_{xy} - S_{xy}^c)\right]\left[(S_{zz} - S_{zz}^c) + \nu(S_{xx} - S_{xx}^c)\right]\right.$$

$$\left.-\nu d\varepsilon_x^T\right\} \Big/ \left\{1 - 2K(S_{zz} - S_{zz}^c)\left[(S_{zz} - S_{zz}^c) + \nu(S_{xx} - S_{xx}^c)\right]\right\} \quad (5.1)$$

where $K = \dfrac{2G}{(2G + C)(2/3\sigma_y^2)}$ and ε_x and γ_{xy} are the axial strain and torsional strain, respectively.

The predicted and measured stress-strain responses are presented in Figs. 5.1 - 5.4 for the stainless steel 304 and Figs. 5.5 - 5.9 for the SAE 1045 steel. Tables 5.1 and 5.2 present the material properties used as input for the constitutive code. It should be noted that the 1045 steel does not exhibit much nonproportional hardening. Therefore, the information needed for input to the model was easily obtainable from the cyclically stable uniaxial stress-strain response, shown in Fig. 5.10. Alternatively, the stainless steel exhibits a significant amount of nonproportional hardening. The stress-strain curve for a general nonproportional test for this material lies someplace between the cyclically stable uniaxial stress-strain curve and the stable stress-strain curve obtained for 90 degrees out-of-phase loading, both of which are shown in Fig. 5.11. The values listed in Table 5.2 represent those taken from a stress-strain curve between these two extremes.

As can be seen from the measured and predicted responses for the stainless steel 304, the model was successful in predicting the general shape of the curves. In addition, the maximum stress values predicted are close to the measured values for all tests except the 90 degrees out-of-phase test. In this test, the increased nonproportional hardening obtained experimentally causes the maximum stress values to be larger than the predicted stress response.

This represents an upper bound, however, in the difference between a predicted and measured response for relatively simple loading paths such as these. (In Fig. 5.3, the input strain history was the experimentally obtained strain history which had been subsequently edited for peaks. The editing caused the unusual little jump in the axial strain vs. shear strain plot and the axial stress vs. shear stress plot.) From these results, it is felt that predictions from the constitutive model and the experimental results are in good agreement.

To verify that the model worked well for more than one material, a series of nonproportional strain histories were evaluated using the 1045 steel. Again, the predictions were quite successful in predicting the general shape and trends observed in the measured stress-strain response. In addition, the maximum stresses predicted were very close to the measured values for the lower strain ranges. Only for the histories with the large strain ranges, shown in Figs. 5.8 and 5.9, did the predicted values differ appreciably from the measured values. As seen in these figures, at high strain values for the SAE 1045 steel, the predicted absolute maximum stress values were below the actual values. The predicted stress-strain response was "too rounded" at high values. This predicted response was very possibly due to the material parameters chosen to be used as input. However, no attempt was made to "tinker" with the parameters since most engineers would not have the luxury of this "tinkering". Instead, it was felt it was more important to leave these predictions as they were an attempt to understand the limitations of the model.

In general, it was concluded that the two-surface model employing Mroz kinematic hardening was successful in predicting the stress-strain response of a thin wall tube loaded in combined nonproportional tension and torsion. From the data presented, the methods used to represent the plastic modulus from readily available material constants seemed to be successful.

Like many two surface models with fixed limit surfaces, the model does not predict "material memory" behavior well. Instead a stress response like that shown in Fig. 5.12 is predicted using this type of model. This predicted behavior is due to the method of modeling the plastic modulus. In these two surface models, the plastic modulus is taken to be a function of the distance from the current stress point to the limit surface. Fixing the limit surface results in an absolute value of the predicted peak stress response slightly smaller than that for the actual stress response for the sub-cycles. The advantages of this type of two surface model, however, are such that this known error is accepted. It is not felt to significantly affect the life prediction results.

Tests were performed to insure repeatability and stability of the stress-strain response. Stability of the model is especially critical in predicting the stress-strain response of long variable amplitude loading histories. The stress-strain response for a number of identical cycles applied consecutively was predicted. It was verified that the model was stable and repeatable for repeated loading.

Based upon the evaluations and comparisons made between the model predictions and experimental results, it was felt that significant accuracy in the stress predictions was obtainable to incorporate it into the variable amplitude life prediction model. Evaluation of the total method could then be made. The results of the evaluation are discussed in the following section.

5.3 Evaluation of the Variable Amplitude Multiaxial Fatigue Life Prediction Method

5.3.1 Comparison with Test Results of Thin Wall Tubes

The variable amplitude multiaxial fatigue life prediction method was initially evaluated by comparing experimental results from a test conducted on a

stainless steel 304 thin wall tube to results predicted using the proposed method. The details and conclusions from this comparison are discussed below.

As discussed in the methodology presented in Chapter 3, the critical plane is defined as the plane experiencing the maximum damage. The fatigue life calculations are then made using the stress-strain response on this plane. To determine the critical plane, the damage on all planes must be evaluated. This evaluation is done, as described in Chapter 3, by rotating the stresses and strains to a plane, rainflow counting the appropriate cycles of strain for the chosen damage model, determining damage for all cycles, and summing damage. Using the measured stresses and strains from a test on the thin wall tube, this procedure was analyzed and verified in detail.

A stainless steel 304 thin wall tube was subjected to the tension-torsion strain controlled history shown in Fig. 5.13. Also shown in Fig. 5.13 are the axial strain history and the shear strain history for this nonproportional loading history. The axial and shear stress responses, as well as the stress-strain responses, are shown in Fig. 5.14.

Since stainless steel 304 was observed to form tensile cracks for a wide variety of loading modes and strain ranges as discussed in Chapter 2, the Smith Watson Topper tensile model, given in Eq. (2.13), was used. In this model, the normal strain and the normal stress must be determined on the different planes. Figs. 5.15a - 5.15c shows the normal stress-strain response for the planes oriented at -70, +70, -50, +50, - 40, +40, -30, +30, -20, +20, -10, +10 degrees from the horizontal. (If the loading was completely uniaxial, the maximum tensile stress or strain would be the 0 degree plane while in a completely reversed torsion test, the +45 and -45 degree planes experience the maximum tensile stress or strain.)

As discussed in Chapter 3, in the variable amplitude multiaxial life prediction methodology the damage associated with a cycle of strain is determined by the product of the normal strain amplitude, $\frac{\Delta\varepsilon}{2}$, and the normal stress, σ, acting on the plane being analyzed. Therefore, although both the -30 degree plane and the +30 plane experience the same range (or amplitude) of normal strain, the -30 plane is predicted to experience more damage because the maximum normal or peak stress is 10 percent larger than the normal stress on the +30 plane. This prediction is experimentally supported by observations of cracking behavior developed under this loading. Fig. 5.16 shows that the cracking occurred on a plane oriented between -30 and -40 degrees from the horizontal. The peak stress caused the critical plane to be oriented on this plane rather than one oriented at + 30 degrees.

The computer model used the measured strains as input. Fig. 5.3a and 5.3b show the predicted and measured stress-strain responses, respectively. The results of the complete analysis are shown in Fig. 5.17. As can be seen, the plane predicted to experience the maximum damage (minimum fatigue life) is oriented at -20 degrees from the horizontal. A fatigue life of 188,000 cycles was predicted from the damage analysis on this plane, with the damage on the -20 and -30 degree planes almost equal. These results are in good agreement with the actual fatigue life of approximately 90,000 cycles with the failure crack oriented at an angle between -30 and -40 degrees.

This method seems to work well from the variable amplitude, low-cycle fatigue test conducted on thin wall tubes in the laboratory. A more critical test of this method is the ability of the model to predict fatigue lives of actual components. This is discussed in detail in the following section.

5.3.2 Variable Amplitude Loading Analyses of Strain-Gauged Components

The strain histories obtained in the SAE 1045 steel component tests were used as input into the variable amplitude multiaxial fatigue life prediction computer program to evaluate the proposed method. The following section describes the results of these analyses and discusses some of the technical details and conclusions.

5.3.2.1 Bending

Two tests were loaded in pure bending as described in Chapter 4. These test specimens, PB2 and PB4, were subjected to the SAE transmission history with the maximum load equal to approximately 5500 N. Strain histories were obtained for two gauge orientations as described. These strain histories were used as input into the computer code. The original strain histories from each leg of the strain gauge rosette are shown in Fig 5.18a for the 0, 45, 90 degree gauge orientation. Also shown in Figs. 5.18b and 5.18c are the edited ε_x, ε_y, and γ_{xy} strain histories and the σ_x, σ_y, and τ_{xy} stress histories. The corresponding strain and stress histories for the -45, 0, 45 gauge orientation are shown in Figs. 5.19a - 5.19c. Note that although a significant number of data points were removed from the original histories to obtain the edited histories, in these figures the same horizontal ("time") scale was used to plot both the original and edited histories for ease of comparison and verification. (The editing level was set at 0.0002 in/in so that small sub-cycles, with strain ranges below this value, were edited out.)

Both shear and tensile analyses, using Eqs. (2.12) and (2.13) respectively, were performed. The predicted fatigue life using the shear model was 773 blocks and the predicted fatigue life obtained using the tensile model was 2714

blocks. The experimentally determined initiation fatigue lives obtained were 544 blocks for PB2 and 678 blocks for PB4.

It is not surprising that the results obtained with the shear analysis were closer to the actual lives since the damage development was shear dominated as was reported in Chapter 4. The observation that damage development in SAE 1045 steel is shear dominated has been made by other researchers. As discussed in Chapter 3, Hua et. al. [5.4] found that even in pure tensile loading of thin wall tubes, shear damage dominated at low fatigue lives or high strains. Fatemi and Socie [5.5] also found that damage in nonproportionally loaded 1045 steel tubes was shear dominated. Consequently, it is expected that the shear damage model would better correlate the fatigue lives of the other 1045 steel variable amplitude tests since damage development is shear dominated.

As stated previously, two strain gauge rosette histories were obtained for the bending test using different gauge orientations. The analyses made using data from the two gauges insured that the life prediction scheme was independent of gauge orientation. For the gauge with the legs of the rosette oriented at 0, 45, and 90 degrees from a line parallel to the flat end of the specimen (termed the 0, 45, 90 gauge), a shear fatigue life of 773 blocks was predicted. The normal to the predicted failure plane was oriented at $\theta = 45$ and $\phi = 90$ as shown in Fig. 5.20. Recall from Chapter 3, the orientation of the gauge defines the x-y-z coordinate system from which theta and phi are referenced. In this case, the x direction was defined by the 0 degree leg. Therefore, the failure plane intersected the surface of the specimen at a line perpendicular to the loading direction and was oriented at a 45 angle into the surface of the specimen.

Using the strain history from the strain gauge rosette with the legs oriented at -45, 0, and +45 to a line parallel to the flat end of the specimen (the -45, 0, 45

gauge), the shear analysis results predicted a fatigue life of 769 blocks. This result is virtually identical to the life predicted by the 0, 45, 90 gauge. The normal to the failure plane predicted using the -45, 0, 45 histories had an orientation of θ =45 and ϕ =140 degrees. Since the 45° leg defines the x-direction, the ϕ = 140° plane is almost perpendicular to the axis of the shaft. Again, this predicted plane is virtually identical to the failure plane predicted in the first analysis. The exact plane would have had an orientation of θ =45 and ϕ =135 degrees. However, the increment size for phi in the damage analysis was 10 degrees and therefore, the program only analyzes the damage on planes corresponding to ϕ = 130 and ϕ = 140 degrees. Consequently, ϕ = 140 degrees is chosen as the failure plane. The difference in the predicted fatigue lives resulting from the difference between ϕ = 135 and ϕ = 140 degrees is negligible.

The difference in the predictions from the tensile analyses is again less than 1 percent. The fatigue life predicted from the 0, 45, 90 gauge was 2714 blocks while 2735 blocks were predicted for the -45, 0, 45 gauge. The predicted failure planes were θ = 90 and ϕ = 90 degrees and θ = 90 and ϕ = 140 degrees, respectively. These represent virtually the same plane. It is the plane perpendicular to the bending direction. (Again, the 5 degree difference in phi is due to the 10 degree increment size used in the analyses. This difference causes the very small difference in the fatigue lives.)

The damage plots for the shear and tensile analyses, for both the 0,45,90 degree and the -45,0,45 degree gauge orientations are shown in Fig. 5.21a and 5.21b, and 5.22a and 5.22b, respectively. As shown in Fig. 5.21a, the plane predicted to experience the maximum shear damage for the 0-45-90 gauge orientation is θ = 45 and ϕ = 90. The θ = 90, ϕ = 45 degree and θ = 90, ϕ = 135 degree planes are predicted to experience approximately half that damage. The reason for this difference is explained as follows.

In a cyclic tensile test of a small round bar, the maximum shear planes are oriented at 45 degrees to the tensile axis. Thus, all planes oriented 45 degrees to the axis, as shown in Fig. 5.23, experience equal values of shear strain amplitude. This fact can also be seen from the Mohr's circle diagram for uniaxial strain, also shown in Fig. 5.23. Since in a small round bar the ε_x and ε_z strains are equal, the maximum shear strain is defined as any plane oriented 45 from the tensile direction, ε_y, as shown. Therefore, using the orientation defined by the 0, 45, 90 gauge, if this test specimen was a small round bar the damage on the plane with normal at $\theta = 45$, $\phi = 90$ degrees (the plane oriented 45° into the thickness of the specimen) would be equal to the damage on the $\theta = 90$, $\phi =$ 45 degree plane (the plane oriented 45° to the axis of the specimen which intersects the surface at 90°).

As discussed, however, in the analyses of the actual test specimens, the damage on the $\theta = 45$, $\phi = 90$ degree plane is larger than the damage on the $\theta = 90$, $\phi = 45$ plane. Although in a small round bar the ε_x and ε_y strains are equal, in the actual test specimen the ε_x strains were smaller than the ε_y strains. The width of the test specimen constrains the contraction in the width or x direction. Consequently, ε_x is much smaller than $-\nu\varepsilon_y$ which can be easily seen in Fig. 5.18b. The maximum value of ε_y is approximately 0.0038 in/in while the corresponding value of ε_x is approximately -0.00018, or nearly zero instead of -0.00114. (This value, -0.00114, would approximately be the contraction in the small bar, $-\nu\varepsilon_y$, using a Poisson's ratio of 0.3.) However, since the z direction is the through-thickness direction, or the direction normal to the free surface, a contraction occurs in this direction. Using the usual engineering assumptions, it is assumed that this is equal to $-\nu\varepsilon_y$. Therefore, the strain state can be represented by the Mohr's circle shown in Fig. 5.24, with the absolute value of ε_z larger than ε_x. The larger value of ε_z causes the maximum shear strain to

occur on the plane that makes a 45 degree angle into the surface. This is the plane whose normal vector makes the angles of $\theta = 45$ and $\phi = 90$ degrees to the x-y-z coordinate system, as was predicted in the analysis.

The lateral constraint, or the constraint in the x direction, also induces a tensile stress in the lateral direction as shown in Fig. 5.18c. This strain state is a plane strain condition and causes the value of the y stress to be greater than if the material was allowed to contract in the x direction. The increased stress, in turn, affects the fatigue life prediction since both the tensile model and shear model incorporate a stress term. This prediction was shown to be true from results of a uniaxial analysis that was performed using only the ε_y strain history. Using a traditional uniaxial Smith-Watson-Topper analysis, the predicted fatigue life was 4912 blocks to failure. This fatigue life is almost twice the value predicted using the multiaxial tensile analysis and over six times the value predicted by the shear analysis. Therefore, the effect of incorporating the constraint is a reduction in the predicted fatigue life, resulting in a life prediction much closer to the actual fatigue life.

This constraint also explains why the cracks were observed to initiate in the center (in the x direction) of the specimen. The constraint is greatest along the center line. As the distance to the edge of the specimen decreases, the constraint in the x direction decreases. Consequently, the cracks initiate where the lateral tensile stress, σ_x, induced by the constraint is largest. This is at the center of the specimen.

These points emphasize the importance of understanding the multiaxial stress state, even in a situation (pure bending) where a uniaxial analysis would typically be performed.

5.3.2.2 Proportional Loading

Proportional loading variable amplitude tests were performed using the SAE transmission history. The results of these tests, PL2 and PL3, were compared to the predicted results which used the experimentally obtained strain histories as input. The strain gauge rosette histories are shown in Fig. 5.25a. In the gauge orientation, shown in Fig. 4.11, the rosette legs made angles of 0, 45, and 90 degrees from a line parallel to the flat end of the specimen. The gauge orientation is such that using a right-hand coordinate system, the positive direction of the shearing stresses and strains is as shown in Fig. 5.26.

Using the shear model, the predicted fatigue life was 109 blocks to failure while the actual initiation life was 221 blocks for PL2 and 185 blocks for PL3. The normal to the predicted failure plane was oriented at $\theta = 45$ and $\phi = 100$ degrees. The predicted fatigue life using the tensile model was 392 blocks with the normal to the failure plane oriented at $\theta = 90$ and $\phi = 100$ degrees. Like the pure bending test, shear damage was observed from inspection of the fracture surface in the proportional loading tests. Consequently, use of the shear model for fatigue life prediction is more appropriate. Comparisons between actual and predicted fatigue lives using this model were approximately within a factor of two.

The damage plots for the shear and tensile models are given in Figs. 5.27a and 5.27b, respectively. It is not surprising that the failure planes were predicted at $\phi = 100$ degrees since the bending stresses and strains were much larger than the shear stresses and strains. (The value of ϕ for the pure bending was 90 degrees.) In other words, the applied bending moment had a much greater effect than the applied torque. The greater bending strains caused the maximum damage to occur on a plane oriented only 10 degrees away from the

plane normal to the bending load. Again, as in the pure bending situation, the lateral constraint caused the predicted failure plane to be oriented 45 degrees from the normal to the free surface or 45° into the specimen thickness. However, as shown in Fig. 5.27a, the damage on the $\theta = 90$ and $\phi = 50$ and $\phi = 140$ degrees planes was almost as large as the damage on the predicted failure plane. These planes represent the planes experiencing the maximum shear damage in the x-y plane. (Remember, when $\theta = 90$ degrees, the normal to the plane lies in the x-y plane, or parallel to the surface of the specimen. Consequently, these planes intersect the surface at right angles.)

The fracture surfaces of the failed specimens, PL2 and PL3, exhibited a "factory roof top" appearance, indicative of shear damage. This shear damage is on planes whose normals lie in the x-y plane. Alternatively, the predicted failure plane was oriented 45 degrees into the surface of the specimen. As stated above, however, the damage predicted on the planes producing the "factory roof top" fracture surface was very similar to that on the planes oriented 45 degrees into the surface of the specimen. Consequently, the observed shear growth into the specimen on the x-y planes is not inconsistent with the predicted results.

5.3.2.3 Nonproportional Loading

Nonproportional loading tests were conducted at three load levels as described in Chapter 4. As was discussed, in these tests the specimens were subjected to a loading history made up of approximately the 200 largest excursions in the SAE transmission history. The input load history was scaled to three different loading values -- termed the 46%, 51%, and 55% load levels. The strain histories from these load levels were then used as input

to the variable amplitude multiaxial fatigue life prediction program. The results of these analyses are presented below.

46% Load Level

The strain gauge orientation is shown in Fig. 4.15. The legs of the rosette made angles of -45,0,+45 to the axis of the shaft. The x direction is defined by the gauge labeled "Channel 1". It is 45 degrees clockwise from the axis of the shaft. This is the gauge orientation used for all the nonproportional tests.

The strain gauge rosette histories, the ε_x, ε_y, and γ_{xy} histories, and the σ_x, σ_y, and τ_{xy} histories are shown in Figs. 5.28a-28c. These are the histories obtained from the strains measured during the 33rd loading block on the strain survey shaft. Using the shear model, the predicted fatigue life was 13,453 blocks to failure. The actual initiation life was approximately 3715 blocks. The predicted failure plane was $\theta = 45$ and $\phi = 50$ degrees which is the plane shown in Fig. 5.29. The predicted life using the tensile model was 33,354 blocks on the plane whose normal was oriented at $\theta = 90$ and $\phi = 50$ degrees. Like the proportional loading situation, the bending load had the greatest influence on the fatigue failure.

As discussed in Chapter 4, the fatigue crack initiated from the machining marks. These happen to be aligned with the plane normal to the bending load ($\phi = 45$ degrees). The influence of these machining marks served as a microscopic stress concentration or crack initiation site. A reason that the life prediction differs from the experimental life and is non-conservative may be due to this influence. Another reason for the non-conservative predictions is due to the stress predictions from the constitutive model. As shown in Fig. 5.8 and 5.9, the constitutive model under-predicts the stresses for histories with large nonproportional strains. These factors both cause the predicted fatigue life to

be greater than the actual life. However, the life prediction is still within a factor of four of the experimental value.

51% Load Level

The strain and stress histories for the 51% load level are presented in Fig. 5.30. These histories were obtained from block 45 of the strain survey shaft. The predicted fatigue life was 7048 blocks using the shear model, on a plane whose normal is oriented at $\theta = 45$, $\phi = 50$ degrees. The actual fatigue life was 1675 blocks. The tensile model predicted a fatigue life of 22161 blocks with failure on the $\theta = 90$ and $\phi = 50$ degrees plane. The difference between the predicted life (using the shear model) and the actual life was again only slightly larger than a factor of four. Again, it is felt that the stress predictions were probably lower than the actual values, resulting in the non-conservative life prediction.

A second analysis was performed with the strain history taken from the actual shaft, NP6. In this case, this corresponded to loading block number 665. The life predictions yielded similar results. The shear life prediction was 7386 blocks compared to 7048 blocks from the previous analysis. The tensile analysis yielded a fatigue life of 27802 blocks compared to 22161 blocks from the first analysis.

In the actual shaft, from which the history for the second analysis was obtained, the shaft was painted. The gauge was therefore placed on a painted surface at the same location on the shaft as the gauge on the as-machined surface. The failure plane predicted in this analysis was in the x-y plane ($\theta = 90°$) whose normal was oriented at $\theta = 90$, and $\phi = 120$ degrees, with very similar damage predicted on $\phi = 30$, 50, and 120 degree planes. The crack in the

specimen actually grew on a plane 10-20 degrees counterclockwise from the horizontal as shown in Fig. 4.14. This corresponds to $\theta = 90°$, $\phi = 55°$-$65°$.

55% Load Level

The strain and stress histories for the 55% load level are presented in Fig. 5.31. These histories were obtained from loading block number 52 on the strain survey shaft. The shear analysis results yielded a life prediction of 3309 blocks on a plane whose normal was $\theta = 90$ and $\phi = 50$ degrees. The actual life was 1003 for NP3 and 983 for NP5. Again, both shafts had machined surfaces (were not painted) and fatigue cracks initiated from machining marks. This corresponded to planes whose normal was oriented at $\theta = 90$ and $\phi = 45$ degrees. However, it may not be appropriate to try to correlate the predicted planes with the actual planes due to the influence of the machining marks. The fatigue life correlation, using the shear model, though, was again within a factor of 3.5.

The strain gauge histories taken from the actual shaft, NP5, at block number 542 and 674 were also used as input for an analysis. The shear analysis for block 542 resulted in a fatigue life prediction of 4726 on a plane with a normal oriented at $\theta = 45$, $\phi = 50$ degrees, while that for block 674 was predicted to be 2825 on a plane with $\theta = 90°$, $\phi = 40°$. As described in Chapter 4, progressive bending of the shaft occurred throughout the life for the shafts tested at this load level. The difference between the analyses conducted on the strain survey shaft and the actual shaft may have been due to this bending. In addition, it is understandable that a longer life was predicted using the input from block 672 compared to that predicted from block 542. For load control tests, as microcracks and damage are developed in the critical locations, the

strains become larger. The increase in strains results in a shorter life prediction, in this case one that turns out to be closer to the actual fatigue life.

5.3.2.4 Summary

Figure 5.32 presents a summary of the results of the comparisons between the experimental and predicted fatigue lives for the three types of tests. These values are tabulated in Table 5.1. As can be seen, the overall correlation is good. The results of the bending and proportional tests fall within a factor of two, while the nonproportional tests results generally fall within a factor of four. As discussed, the reason for the non-conservative error in the nonproportional tests is believed to be due in part to the stress predictions. As shown in comparisons to thin wall tube test results, the predicted stresses are below the actual values for nonproportional loading with large strains.

In general, it is felt that the results of the correlations provide strong support for the proposed methodology.

6. MULTIAXIAL STRESS AND STRAIN EFFECTS

6.1 Introduction

The development and verification of the variable amplitude multiaxial fatigue life estimation computer code allowed example loading cases, as well as the variable amplitude histories, to be studied in order to better understand the effects of nonproportional cyclic multiaxial loading. Specifically, two main areas were addressed. First, the effect of the local multiaxial stress state on fatigue life predictions was studied. Second, the effect of the local cyclic multiaxial strain state on the damage developed per plane and the eventual identification of the critical plane was analyzed.

The results of these studies are discussed in the following chapter. Several example loading cases are presented that emphasize the importance of these effects.

6.2 Local Multiaxial Stress State Effects

The local stress state obviously affects fatigue life since a normal stress term is incorporated in both the shear and tensile damage models, Eqs. (2.12) and (2.13), respectively. What can often be misleading, though, is the fact that the local stress state may vary appreciably from that associated with the remotely applied loads. This is especially true in situations involving engineering components with complex geometries.

A good example of this was presented in Section 5.3.2.1 in connection with the component loaded in pure bending. Although the remotely applied loading was uniaxial, the local stress state developed at the notch was multiaxial, even in this relatively simple geometry. A stress was developed in the lateral direction (x direction) due to the constraint caused by the width of the

specimen. This lateral stress caused an increase of approximately 12-13% in the bending stress compared to a true uniaxial situation. This increase in stress caused an increase in fatigue damage, especially for the cycles with small strain ranges.

The difference in the fatigue life predicted using a multiaxial analysis and a uniaxial analysis, both using a Smith Watson Topper parameter, was approximately a factor of two, with the uniaxial being more non-conservative. Using the multiaxial shear damage parameter, the difference was over a factor of six. The effect of considering the multiaxial stress state resulted in a life prediction much closer to the experimentally determined value, even in a situation where the applied loading was uniaxial.

Another example of the importance of considering the multiaxial stress state is provided by comparing the estimated fatigue lives obtained from a uniaxial analysis and a multiaxial analysis. For instance, using the shear damage model to analyze the 46% load level, nonproportional test (NP4) resulted in a life prediction of 13,453 blocks to failure on a plane oriented 45 degrees into the specimen and intersecting the specimen surface at 90 degrees to the bending direction. The predicted life using the multiaxial tensile damage analysis was 33,354 blocks on a plane oriented perpendicular to the bending direction. For comparison, uniaxial analyses were performed using the strain histories obtained from each of the three legs of the strain gauge rosette. These resulted in life predictions of 365,330 blocks, 52,650 blocks, and 230,889 blocks to failure for the three legs oriented at -45 degrees, 0 degrees, and +45 degrees from the axis of the shaft, respectively. The actual life value, as reported in Chapters 4 and 5, was 3715 blocks to crack initiation. Consequently, the uniaxial life predictions were very non-conservative. The best uniaxial prediction, from the 0 degree gauge, differed from the actual life by

a factor of 14, while the multiaxial analysis was within a factor of 4. These results support the need to understand and account for the local multiaxial stress state, as well as the need to use the appropriate multiaxial damage model.

The need to understand the local multiaxial stress state is further substantiated from the results presented in Table 6.1. In this table, the uniaxial estimations, the multiaxial estimations and the actual fatigue lives are listed. (The uniaxial life listed for each test represents the most non-conservative fatigue life estimated from the three strain histories of the rosette. This is the value closest to the actual fatigue life.) Again, these results clearly support the need to account for the local multiaxial stress response in the damage analysis.

A third example of the need to understand or predict the multiaxial stress response is shown graphically in Fig. 6.1. This figure presents the actual stress and strain data obtained in the four box loading path of the stainless steel tube rotated to the -20 degree plane ($\theta = 90$, $\phi = 70$ from the horizontal). If a single strain gauge had been oriented to allow the strain history on this plane to be measured, the measured history would have been that shown in Fig. 6.1a. Using this strain history as input, the predicted uniaxial stress strain response would be that shown in Fig. 6.1c which is very different from the measured response shown in Fig. 6.1b. Using uniaxial stress prediction techniques, the unusual subcycles "hung on the outside" of the major hysteresis loop are not predicted. This error in the prediction of the stress history affects the fatigue life estimate. As discussed in the examples above, the differences between the stresses predicted using uniaxial techniques and those predicted using multiaxial techniques significantly affect fatigue life estimations, especially for long histories with many cycles.

Finally, as discussed in Chapter 2, mean stresses may significantly affect the fatigue life of a component subjected to multiaxial loading. Local multiaxial mean stresses may be developed due to the path dependency of the stress response as shown in Fig. 5.9a. As shown in this figure, both an axial mean stress and a shear mean stress are developed due to the applied strain path, even though the strains are completely reversed. In addition, the effect, or even presence, of mean stresses is dependent upon the applied strain range. For example, like the uniaxial situation, the multiaxial mean stresses relax out at high strain amplitudes. Additionally, mean stresses may not be developed at all in the multiaxial situation if the strain amplitude is too large. This strain amplitude dependency is shown in the following example.

Shown in Fig. 6.2 is an example loading path made up of reversed uniaxial straining with a mean torsional strain. It is assumed that this loading is applied to a component such as a thin wall tube. In this example, the torsional and axial strains are first applied proportionally to point "0". Subsequently, the torsional strain is held constant while the uniaxial strain is cycled.

Fig. 6.3 shows the predicted axial and shear stress-strain response for loading case one. In this case, the axial strain amplitude is 0.0025 and the torsional mean strain is 0.0025. Notice that the mean shear stress decreases as the axial strain is cycled. However, a small mean shear stress exists during the axial cycling. This biases failure to the plane rotated 45 counterclockwise from the axial axis (the plane whose normal is oriented at $\theta = 90$ and $\phi = 45$ degrees from the horizontal) as shown in Fig. 6.4. This prediction is consistent with the experimental observations made by Robillard and Cailletaud and shown in Fig. 2.6.

The predicted axial and shear stress-strain responses for loading case two are shown in Fig. 6.5. The axial strain amplitude is 0.005 and the torsional

mean strain is 0.003 in this loading case. In this case, the torsional mean stress is decreased almost to zero. This decrease is due to the material's inability to carry both the large torsional load and the large axial load. Therefore, the material begins to shed the torsional load, resulting in a very small mean torsional stress. This lack of torsional mean stress causes the predicted damage to be very similar on both the planes rotated 45 clockwise and 45 counterclockwise from the axial direction. Consequently, mean stresses are not developed and do not affect the predicted fatigue life at this high strain level.

This example shows that the existence of multiaxial mean stresses, as in uniaxial loading, is dependent upon the applied strain range. Consequently, a understanding of the resulting stress state is needed in both evaluating the effect of mean strains and in evaluating damage on the correct failure plane. The affect of the cyclic strain state on different planes is discussed in more detail in the following section.

6.3 Local Cyclic Multiaxial Strain State Effects

Several example cases were developed and analyzed to study the effect of the applied loading on various planes in the material. The following examples emphasize the need to understand how the loading combines on different planes in order to identify the correct critical plane and to then predict the corresponding fatigue life from the damage on this plane.

In the first example, the two loading paths in Fig. 6.6 were analyzed. In both loading paths, the strain ranges were the same, $\Delta\varepsilon_x = \varepsilon$ and $\Delta\varepsilon_y = \varepsilon$. In the first loading path, however, there was a compressive mean strain in the y-direction, while in the second loading path there was a tensile mean strain in the y-direction. Using the shear damage model, the fatigue lives and failure planes predicted in the analyses were very different. In fact, the loading path

with the mean tensile strain resulted in a longer predicted life than that predicted for the loading path with the compressive mean strain. Only after analyzing the effect of the applied loading on different planes can this be understood and explained.

Figs. 6.7 and 6.8 show the applied loading on an incremental cube of material, the Mohr's circle representation of the strain state, and the value of the shearing strain acting on three planes at three points in the loading path for both of the loading cases. The damage per plane plots for both loading cases are shown in Figs. 6.9 and 6.10.

As can be seen from Fig. 6.9, all planes with the normal vector lying in the x-y plane ($\theta = 90$) experience no damage. The shearing strain on all $\theta = 90°$ planes is equal and constant. This can be seen easily from Fig. 6.6 for the γ_{xy} shearing strain. Thus, although a shearing strain exists, it does not vary. Consequently, no strain reversals occur on this plane. (A basic assumption in the development of fatigue damage is that the damage occurs by to and fro slip. When the strain on a plane remains constant, it is therefore predicted that no fatigue damage occurs.) Alternatively, as shown in Fig. 6.6, both the γ_{xy} and γ_{yz} experience a variation in shearing strain, with the strain amplitude equal to $\frac{(1+\nu)}{(1-\nu)}\varepsilon$. Since the normal stress, σ_n, acting on the γ_{xy} plane ($\theta = 45$, $\phi = 0$ or $\phi = 180$) is slightly larger than that acting on the γ_{yz} plane ($\theta = 45$, $\phi = 90$), using Eq. (2.12), the damage predicted on the γ_{xz} plane is slightly larger. These results are shown in Fig. 6.9.

The strain occurring on the three planes is shown in Fig. 6.8 for the second loading path. In this case, the largest alternation of shear occurs on the γ_{xy} plane ($\theta = 90$, $\phi = 45$ and $\theta = 90$, $\phi = 135$). This is consistent with the damage predictions shown in Fig. 6.10.

Comparing the first and second loading paths, it is now understandable why path one is predicted to have the shorter fatigue life. The maximum alternation of shear strain for this case is $\frac{(1+\nu)\varepsilon}{(1-\nu)}$. Assuming Poisson's ratio to be approximately 0.4 for this elastic-plastic situation, this results in 2.3ε for path one compared to the maximum alternation of shear strain of 2ε for loading path two. Therefore, only by understanding or evaluating the effect of the combined loading on the different planes can the critical plane be identified and an appropriate multiaxial life prediction made.

A second example that emphasizes the need to understand the effect of the combined loading on different planes was also developed. The loading paths used in this example are shown in Fig. 6.11. In this example, all end points in the loading paths have the same von Mises equivalent strain.

The strain histories associated with these loading paths are shown in Figs. 6.12 and 6.13. The strain in the x direction was input as $-\nu\varepsilon_y$, where ν was assumed to be approximately 0.3. Figs. 6.14 and 6.15 present the shear damage plots and Figs. 6.16 and 6.17 show the predicted normal stress-strain and the shear stress-strain responses on the plane perpendicular to the axial loading direction ($\theta = 90°$, $\phi = 90°$).

For loading path three, the failure plane was predicted to occur on a plane whose normal was oriented at $\theta = 90$ and $\phi = 120$ or 130 degrees from the horizontal (x-directon). This represents a plane rotated approximately 45 degrees clockwise from the axial loading axis. The failure plane predicted for loading path four was on the plane perpendicular to the axial loading direction ($\theta = 90°$, $\phi = 90°$). In addition to different failure planes, loading path three was predicted to have approximately twice the fatigue life of loading path four.

Again, to understand this, one must look at the effect of the combined loading on different planes.

The predicted shear stress-strain response for the first loading path, path three, on the failure plane $\phi = 130$, is shown in Fig. 6.18. As can be seen, there is a major cycle with a shear strain amplitude of 0.0032 and a subcycle with a shear strain amplitude of 0.00075. Thus, although the amplitude of the shear strain cycle on the $\phi = 90$ plane is larger than the major cycle on the $\phi = 130$ plane, the presence of the subcycle on the $\phi = 130$ plane causes a greater fatigue damage on this plane.

The failure plane predicted for the second loading path, path four, was the plane whose normal vector was oriented at $\theta = 90$ and $\phi = 90$ from the horizontal. This is the plane normal to the axial loading. Therefore, the applied shear stress-strain response shown in Fig. 6.17 is also the shear stress-strain response on the failure plane. Two cycles of shear strain occur on this plane, each with an amplitude of 0.00306. (They are superimposed in Fig. 6.17. The presence of two cycles is more clearly seen from the strain history shown in Fig. 6.13.)

From the shear stress-strain predictions on the failure planes for each loading path, it is clearly seen why loading path four is predicted to have the shorter fatigue life. It experiences two large cycles of shear strain while loading path three experiences only one major cycle of strain. Consequently, the fatigue life predicted for loading path three is almost twice that predicted for loading path four.

Again, this example emphasizes the need to understand the effect the combined loading has on various planes. This understanding is required for the correct identification of the critical plane and for the corresponding multiaxial fatigue life prediction.

6.4 Summary

The need to understand both the local multiaxial stress and strain states and the effects of these on various planes has been shown in the above examples. This understanding is essential for the correct identification of the critical plane and for the corresponding fatigue life predictions using critical plane models. Although the exact form of these models will surely change as more multiaxial fatigue data becomes available, the need to understand the effect of the combined loading on the different planes is fundamental for the use of these methods.

7. CONCLUSIONS

1. A variable amplitude multiaxial fatigue life estimation methodology has been developed which is based upon an extension of the uniaxial variable amplitude fatigue strain-life approach. It incorporates critical plane damage models that are representative of the physically observed damage. A computer code that implements the proposed methodology has been developed and verified.

2. A relatively simple two-surface plasticity model, needed in the proposed method, has been developed. It has been shown to be successful in predicting the stress-strain response observed in tests conducted on thin wall tubes. The model, which needs only readily available material constants for input, remains numerically stable for long variable amplitude multiaxial strain histories.

3. Experimental strain gauge rosette data and corresponding fatigue lives have been obtained from components subjected to proportional and nonproportional variable amplitude loading. Good correlations between predicted and actual fatigue lives have been achieved.

4. Understanding and incorporating the local multiaxial stress and strain response in the damage models is important in successfully estimating the fatigue life of a component subjected to variable amplitude multiaxial loading.

Table 3.1 Measured and Derived Shear Constants

	Measured		Derived	
Material	γ_f'	τ_f' (ksi)	$\gamma_f' = \sqrt{3}\varepsilon_f'$	$\tau_f' = \sigma_f'/\sqrt{3}$ (ksi)
SS 304	0.413	102.8	0.296	83.7
SAE 1045	0.413	73.2	0.450	79.4

Table 4.1 Experimental Fatigue Lives of Components Subjected to Proportional and Nonproportional Loading

Loading Conditions	Life at First Detected Crack (Blocks)	Life at Final Failure (Blocks)
Pure Bending (SAE Transmission History) (Max Load = 5500N)		
Specimen No. 2 (PB2)	544	759
Specimen No. 4 (PB4)	678	1180
Proportional Loading (SAE Transmission History) (Max Load = 4500N)		
Specimen No. 2 (PL2)	221	411
Specimen No. 3 (PL3)	185	331
Non-Proportional Loading (Non-proportional History) (100% = 5000 lbs.)		
46% TEST (NP4)	3715	4176+
51% TEST (NP6)	1675	1937
55% TEST (NP5, NP3)	983, 1003	1110, 1003

Table 5.1 SS304 Material Properties

Modulus of Elasticity, E	27,000 ksi
Yield Stress, σ_y	35.0 ksi
Limit Stress, σ_L	100.0 ksi
Poisson's Ratio, ν	0.3
Fatigue Strength Coefficient, σ_f'	145.0 ksi
Torsional Fatigue Strength Coefficient, τ_f'	103.0
Fatigue Duictility Coefficient, ε_f'	0.171
Torsional Fatigue Strength Coefficient, γ_f'	0.413
Fatigue Strength Exponent, b	-0.114
Fatigue Ductility Exponent, c	-0.402
Cyclic Strength Coefficient, K'	240.0 ksi
Cyclic Strain Hardening Exponent, n'	0.287

Table 5.2 SAE 1045 Steel Material Properties

Modulus of Elasticity, E	30,000 ksi
Yield Stress, σ_y	40 ksi
Limit Stress, σ_L	80 ksi
Poisson's Ratio, ν	0.3
Fatigue Strength Coefficient, σ_f'	137.5 ksi
Torsional Fatigue Strength Coefficient, τ_f'	73.2
Fatigue Duictility Coefficient, ε_f'	0.26
Torsional Fatigue Strength Coefficient, γ_f'	0.413
Fatigue Strength Exponent, b	-0.092
Fatigue Ductility Exponent, c	-0.445
Cyclic Strength Coefficient, K'	182.0 ksi
Cyclic Strain Hardening Exponent, n'	0.208

Table 5.3 Predicted versus Experimental Fatigue Lives

	$N_{experimental}$ (Blocks)	$N_{predicted}$ (Blocks)	N_{pred}/N_{exp}
Pure Bending			
PB2	544	770	1.4
PB4	678	770	1.1
Proportional Loading			
PL2	221	109	0.5
PL3	185	109	0.6
Non-Proportional Loading			
NP4	3715	12,453	3.6
NP6	1675	7048	4.2
NP6	983	3309	3.4
NP3	1003	3309	3.3
SS 304 Thin Wall Tube			
SS37[1]	~90,000	188,000	2.1

[1] Prediction made using tensile model, all other predictions (pure bending, proportional and nonproportional loading) were made using shear model.

Table 6.1 Uniaxial and Multiaxial Estimates of Fatigue Lives

Loading Mode (Blocks)	Actual Life (Blocks)	Multiaxial Estimate (Blocks)	Uniaxial Estimate
Bending	544 678	770	4912
Proportional Loading	221 185	109	456
Nonproportional Loading 46% 51% 55%	 3715 1675 983 1,003	 12,453 7,048 3,309	 52,654 29,700 19,323

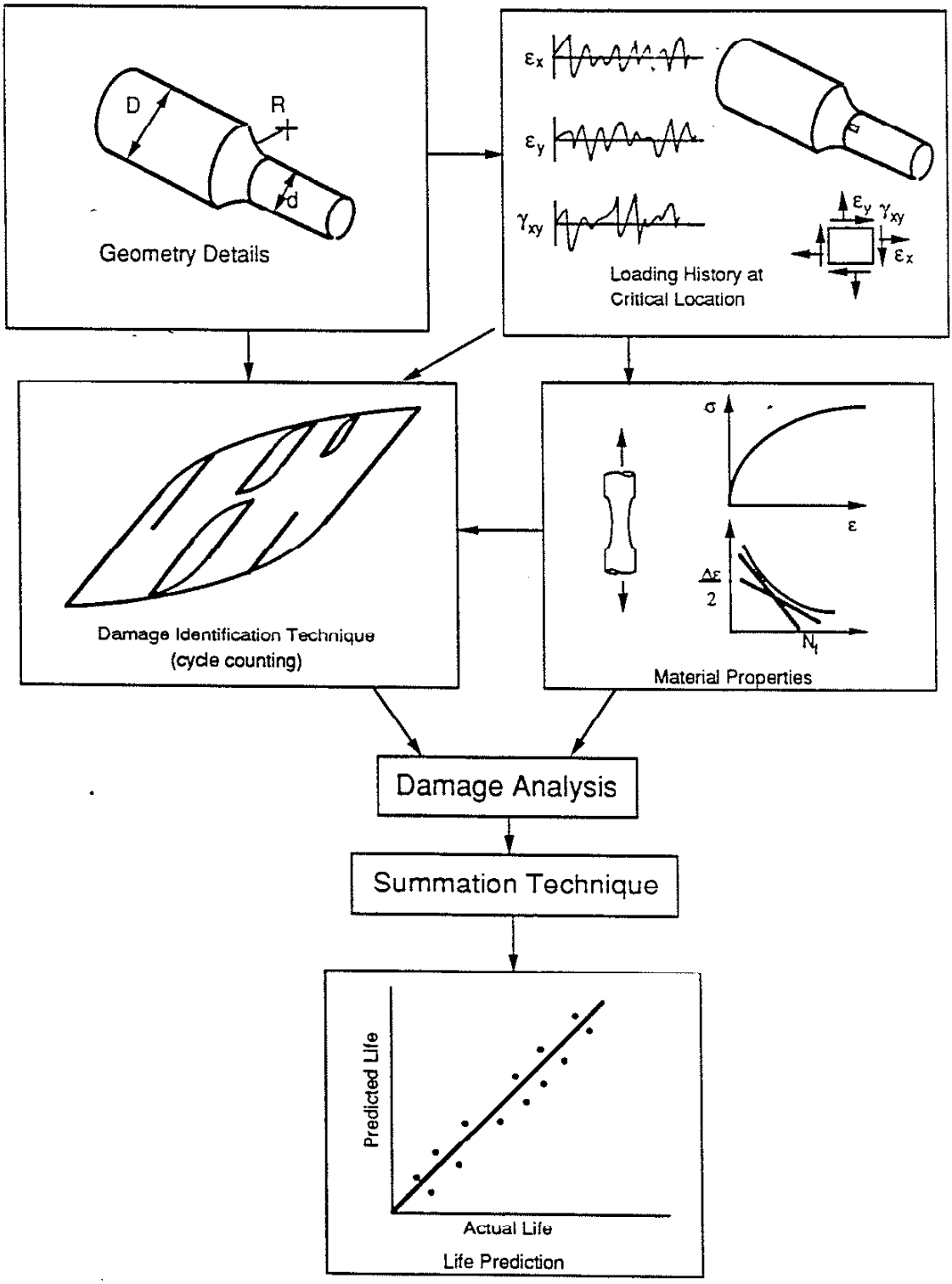

Figure 2.1 Outline of Strain-Life Approach

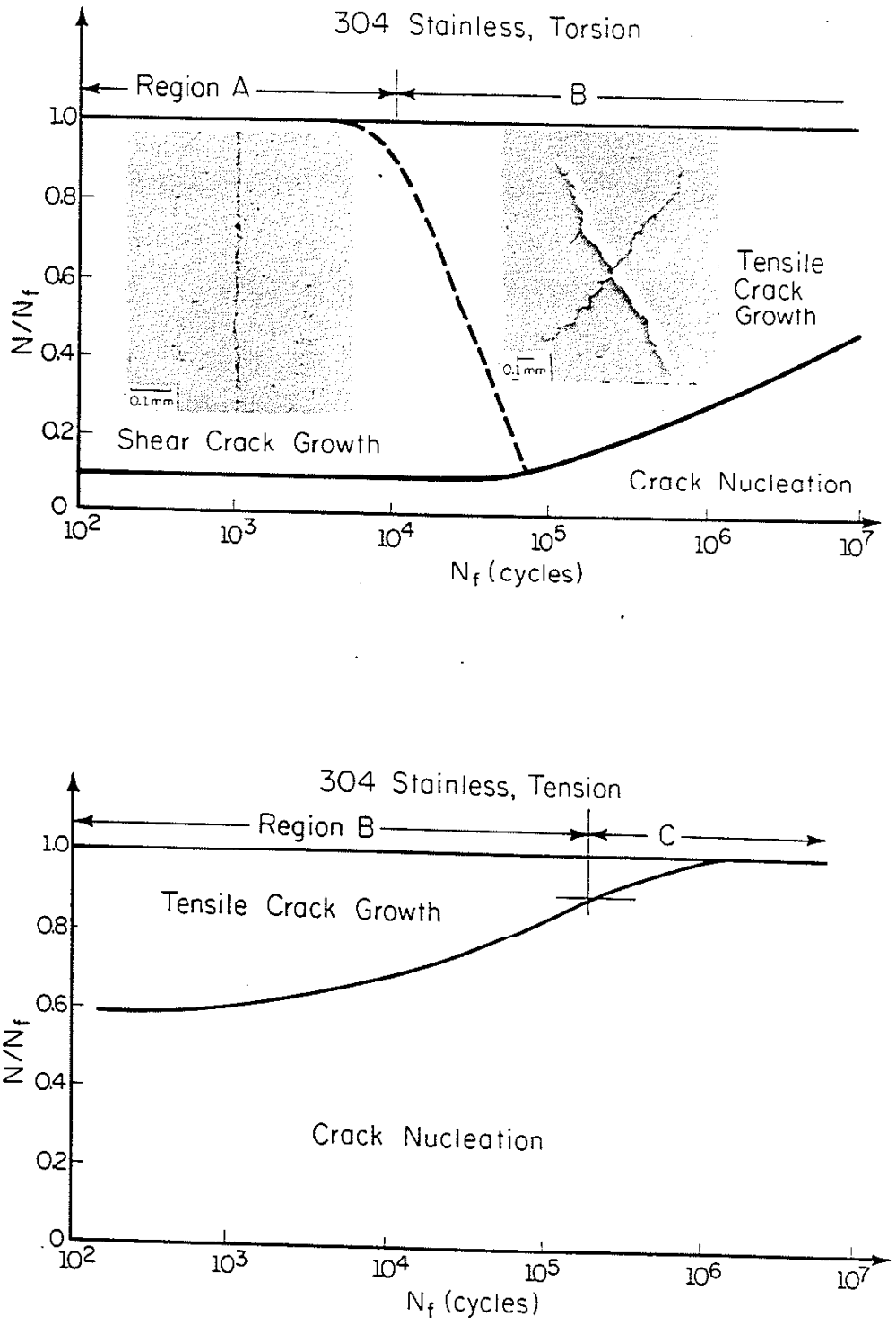

Figure 2.2 Damage Map for Stainless Steel 304 (a) Torsion (b) Tension

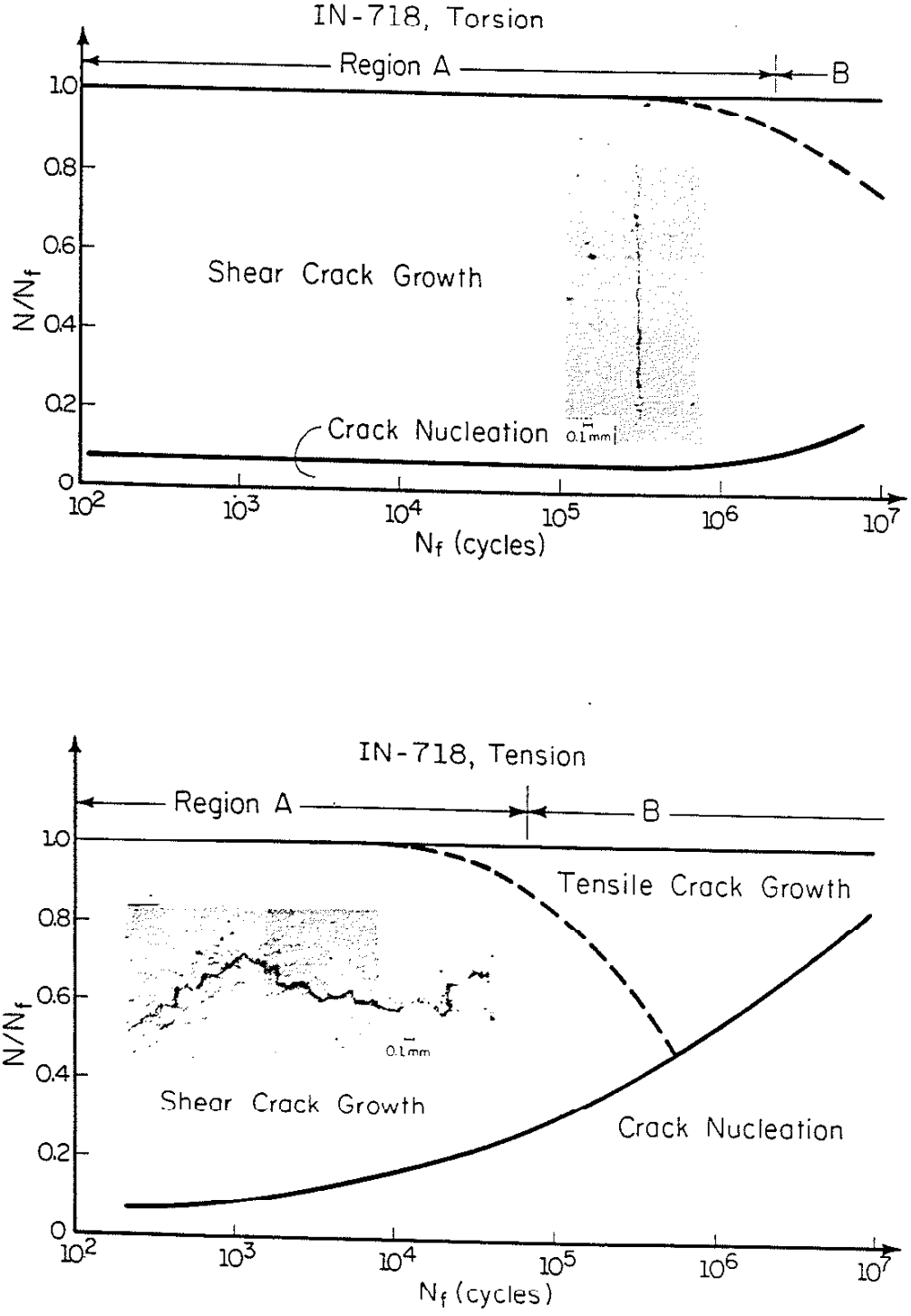

Figure 2.3 Damage Map for Inconel 718 (a) Torsion (b) Tension

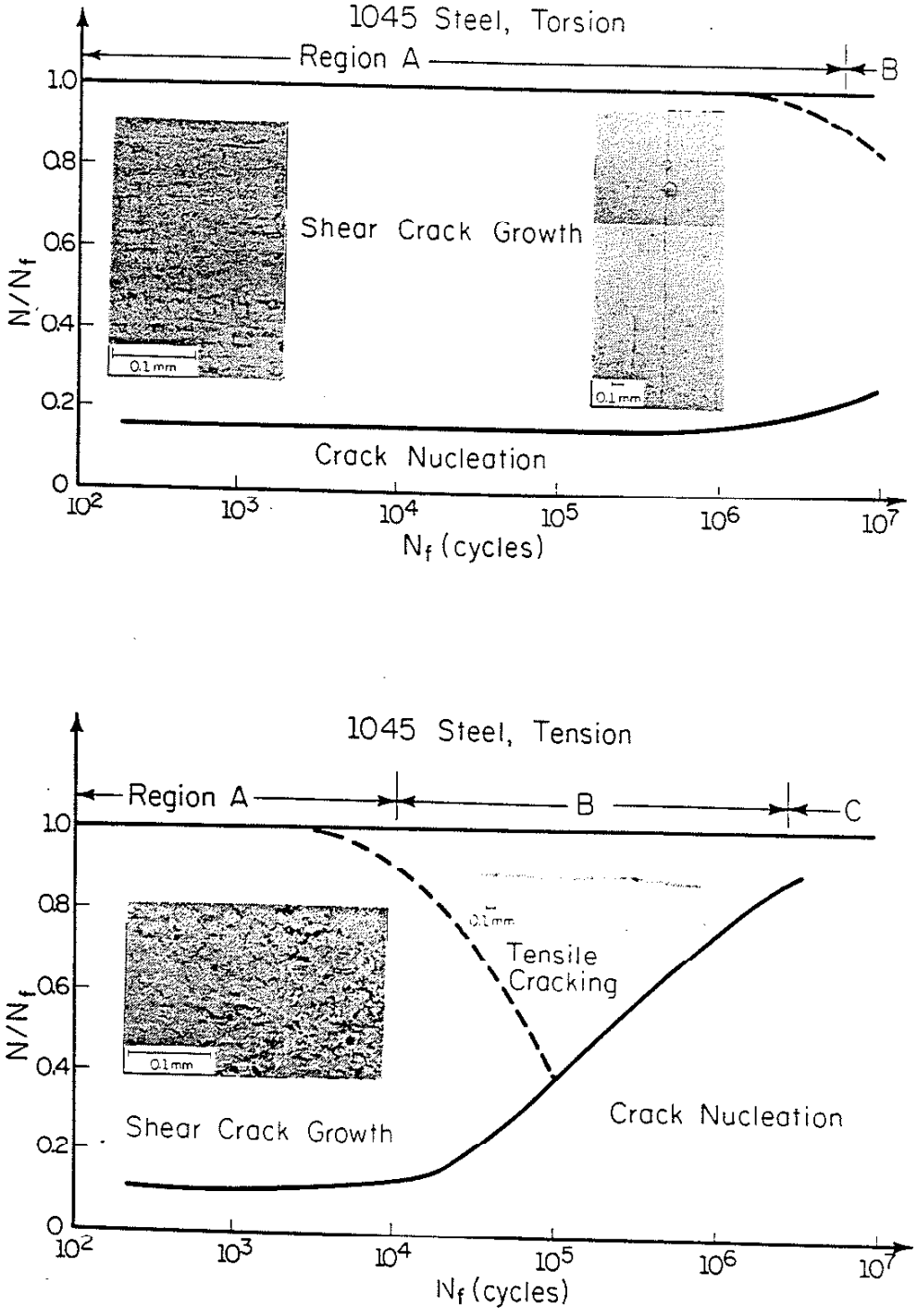

Figure 2.4 Damage Map for SAE 1045 Steel (a) Torsion (b) Tension

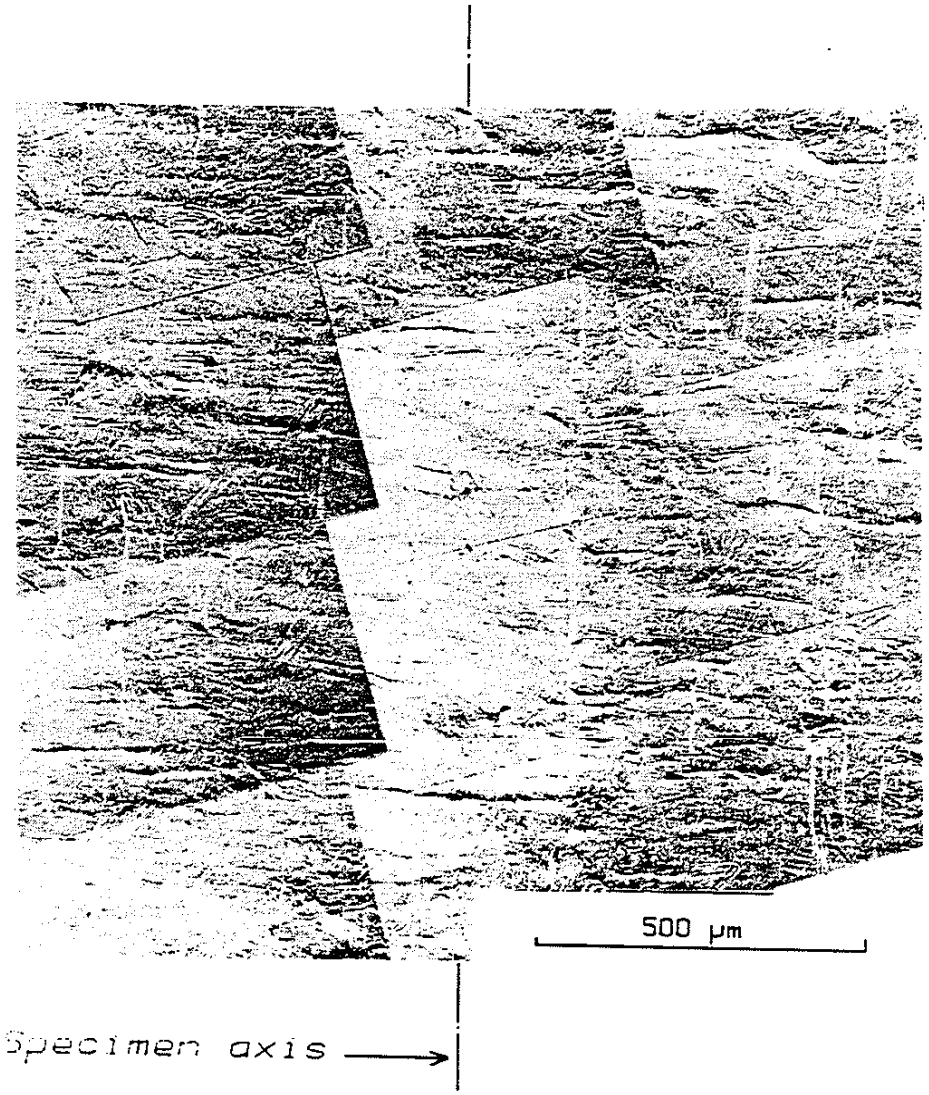

11H3-180 : $\frac{\Delta\tau}{2}$ = 417 MPa $\frac{\Delta\gamma}{2}$ = 0.83 %

σ_m = -200 MPa

N_F = 3792

Figure 2.5 Damage Observed in Test with a Fully Reversed Torsional Loading and a Compressive Mean Stress (from Ref. [2.19])

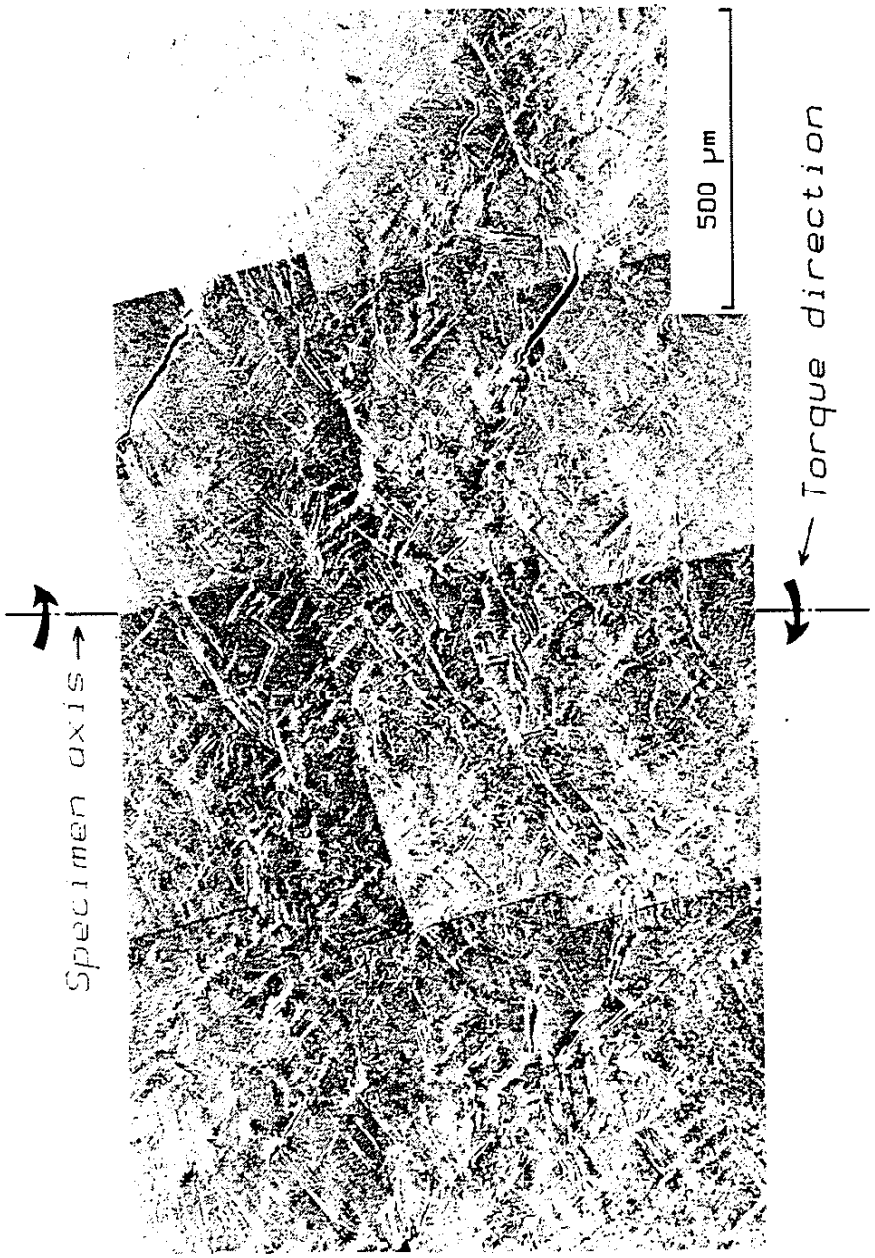

Figure 2.6 Damage Observed in Test with Completely Reversed Tensile Loading and Mean Torque (from Ref. [2.19])

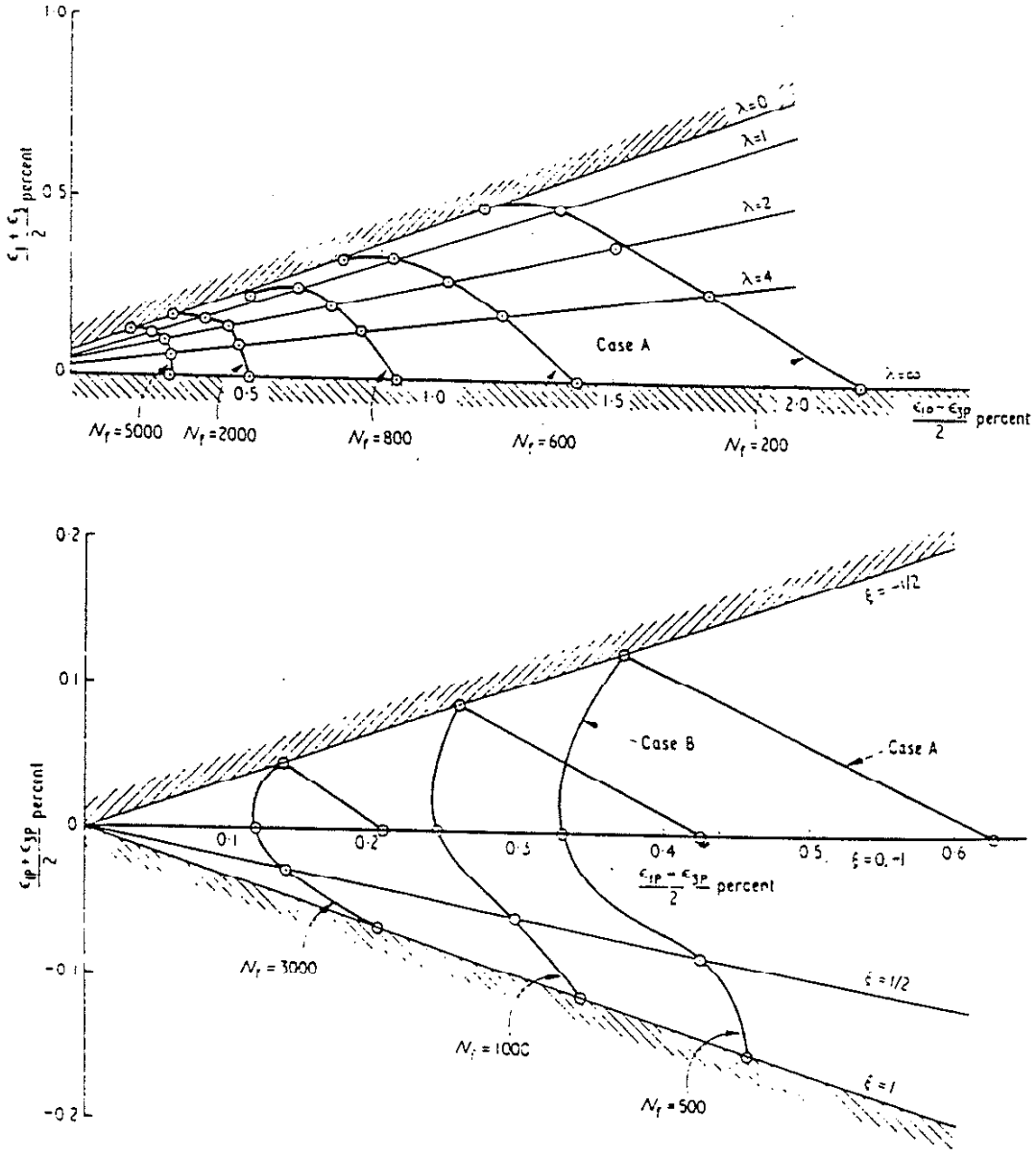

Figure 2.7 Gamma Plane (from Ref. [2.22])

Given Strains

$\varepsilon_x \quad \varepsilon_y \quad \gamma_{xy}$

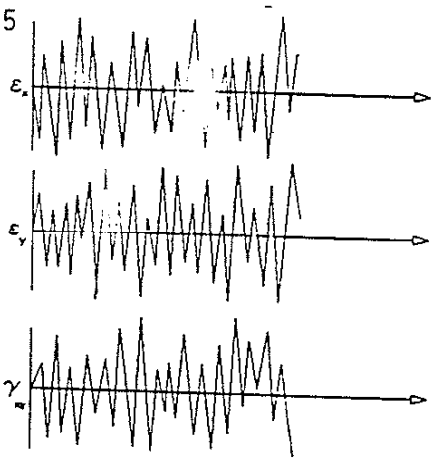

Determine Stresses

$\sigma_x \quad \sigma_y \quad \tau_{xy}$

Rotate Stresses and Strains to Critical Plane

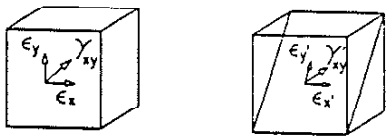

Rainflow Count Cycles

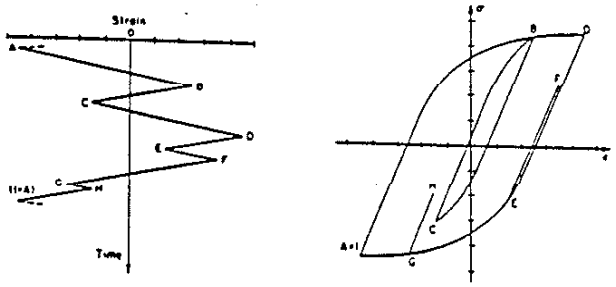

Sum Damage and Predict Fatigue Life

$$D = \sum_{i=1}^{n} \frac{1}{N_{fi}}$$

n = number of cycles

N_{fi} = cycles to failure for i strain range

D = damage per block

Figure 3.1 Outline of Variable Amplitude Multiaxial Fatigue Life Prediction Method

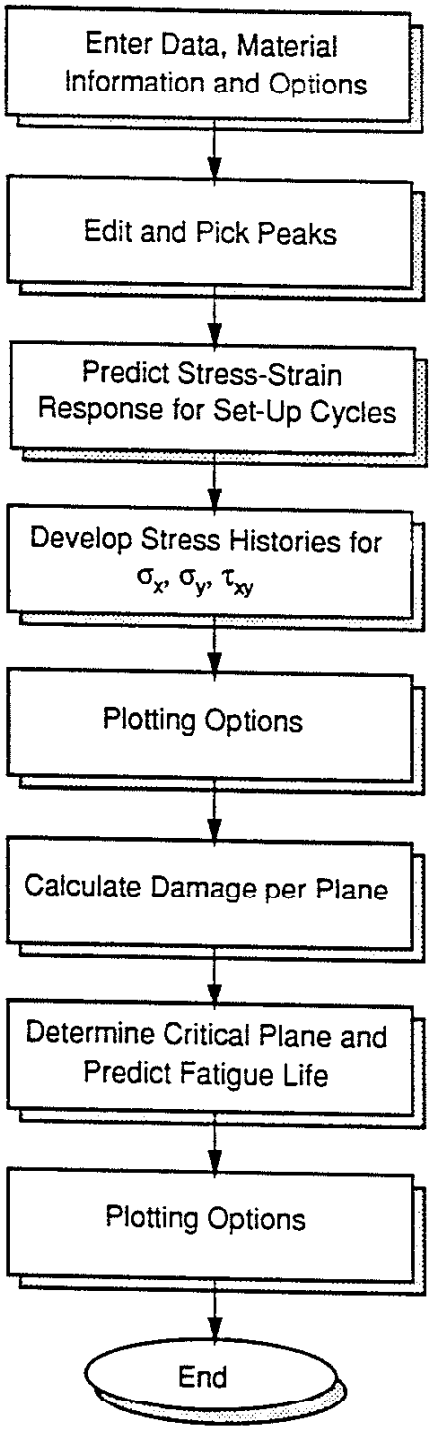

Figure 3.2 Outline of Variable Amplitude Multiaxial Fatigue Life Prediction Computer Code

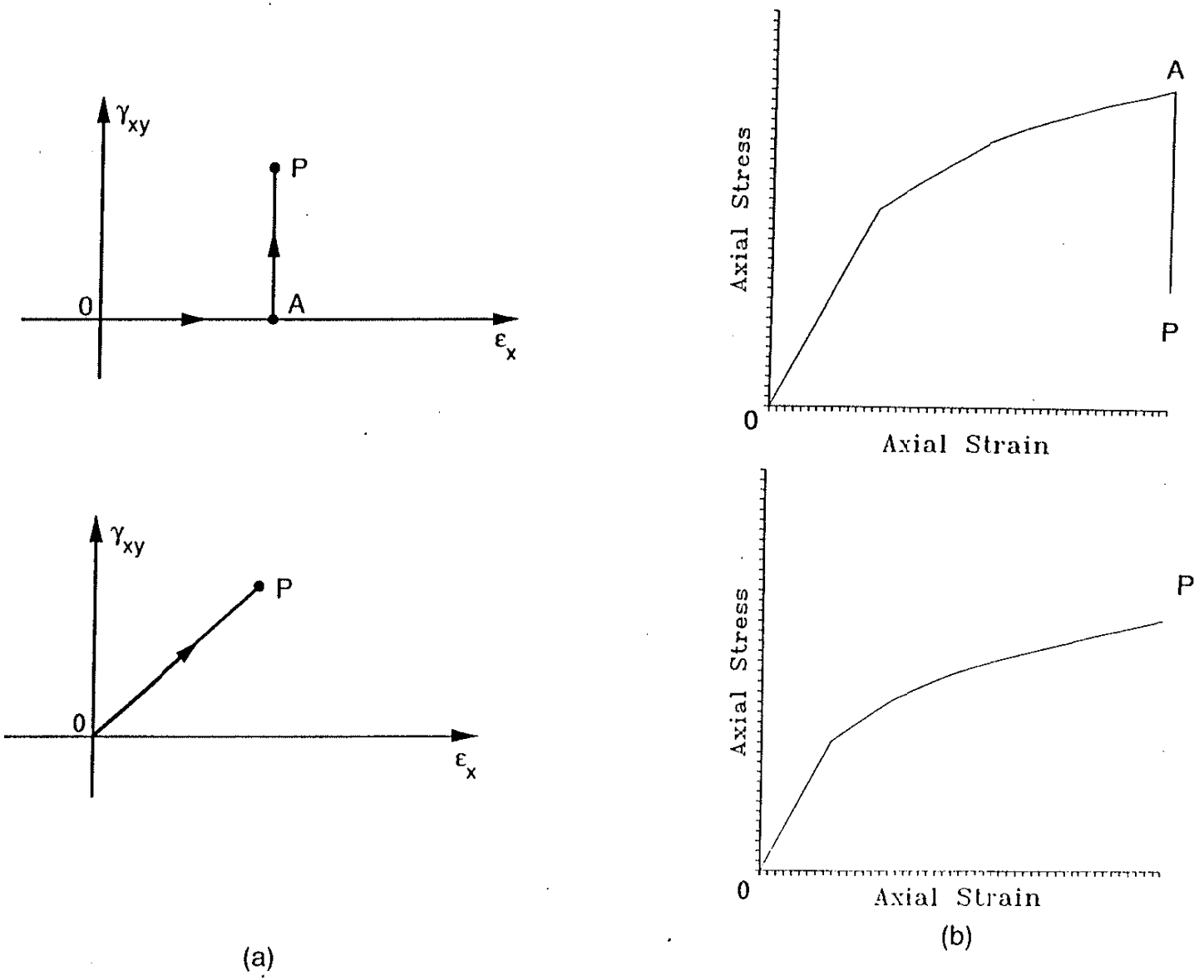

Figure 3.3 (a) Strain-Controlled Loading Paths
(b) Axial Stress-Strain Response for Each Loading Path Showing Path Dependency

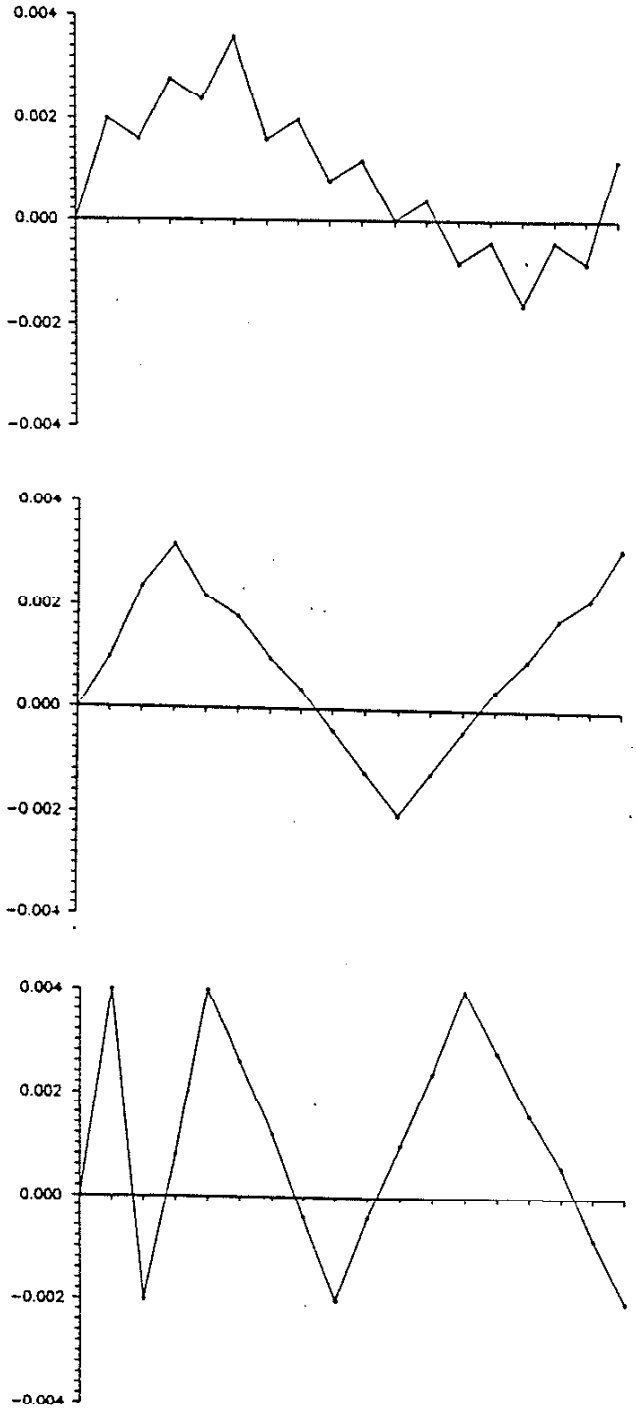

Figure 3.4 Multiaxial Strain Histories

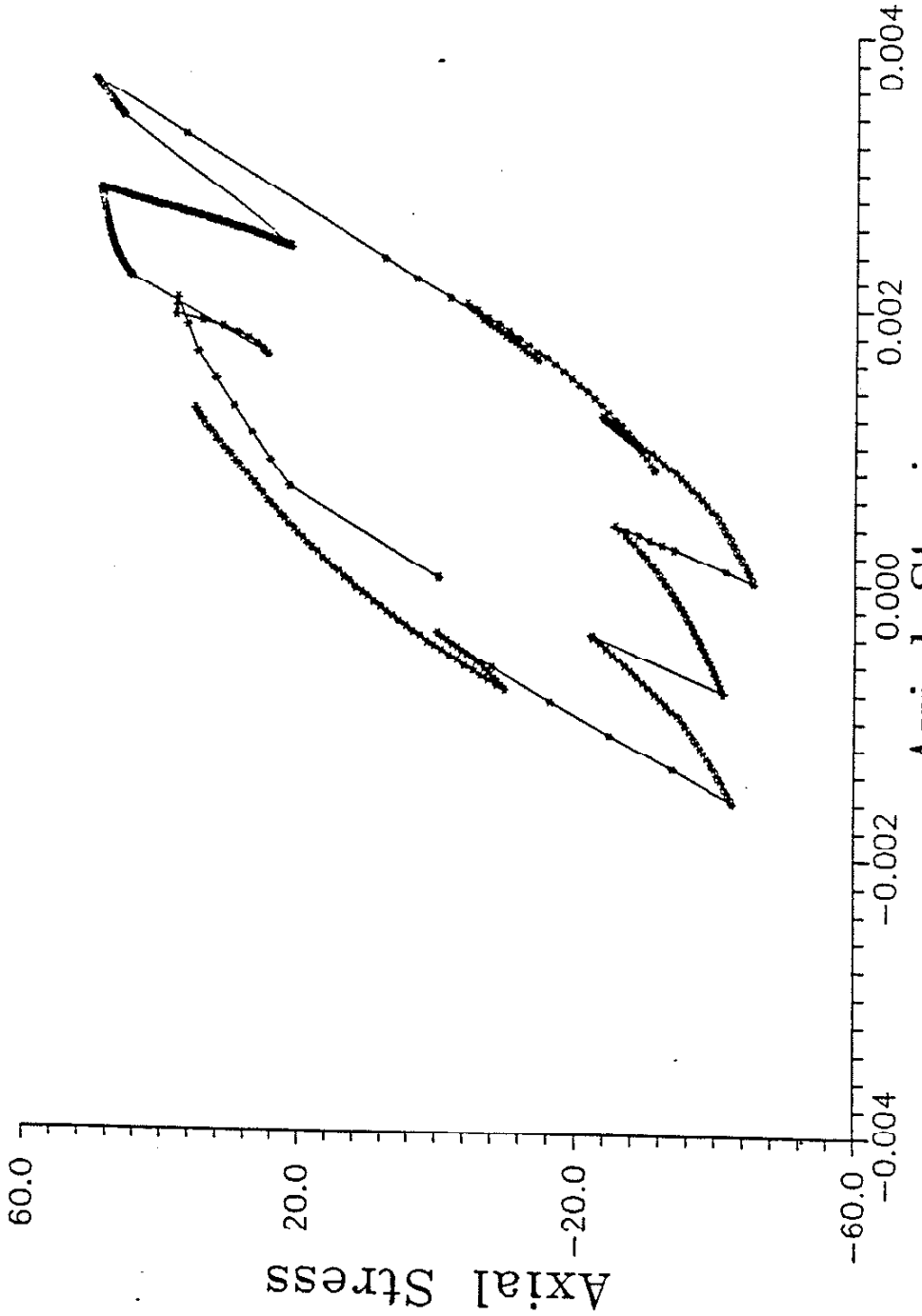

Figure 3.5 Stress-Strain Response for Channel 1 of Example History

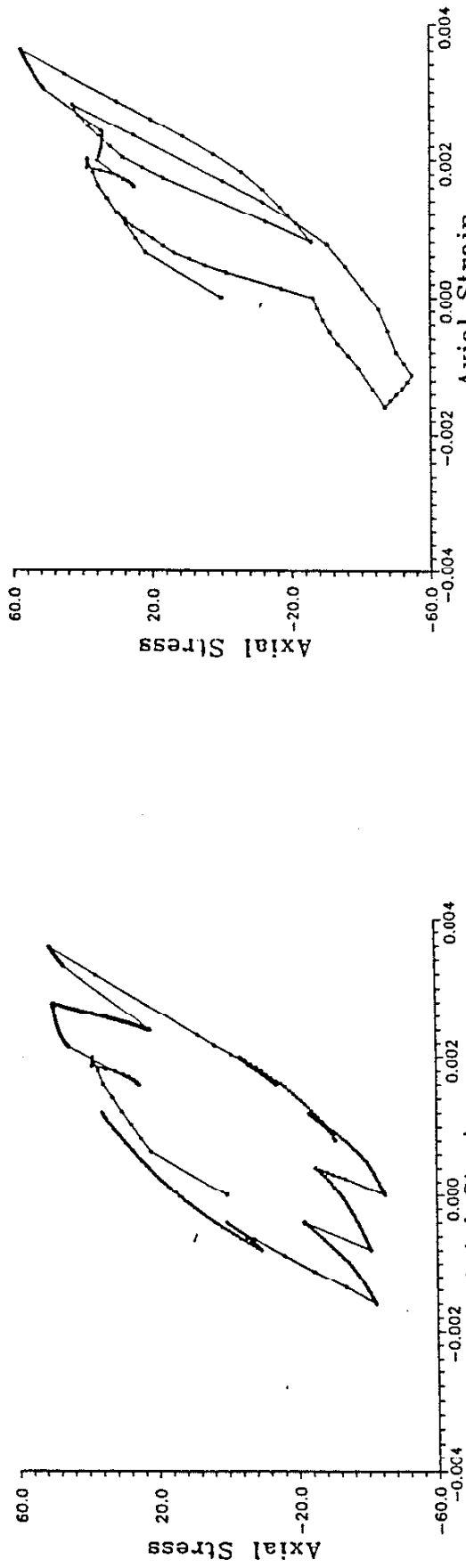

Figure 3.6 Stress-Strain Response for (a) Unedited History (b) Edited History using Uniaxial Editing Methods

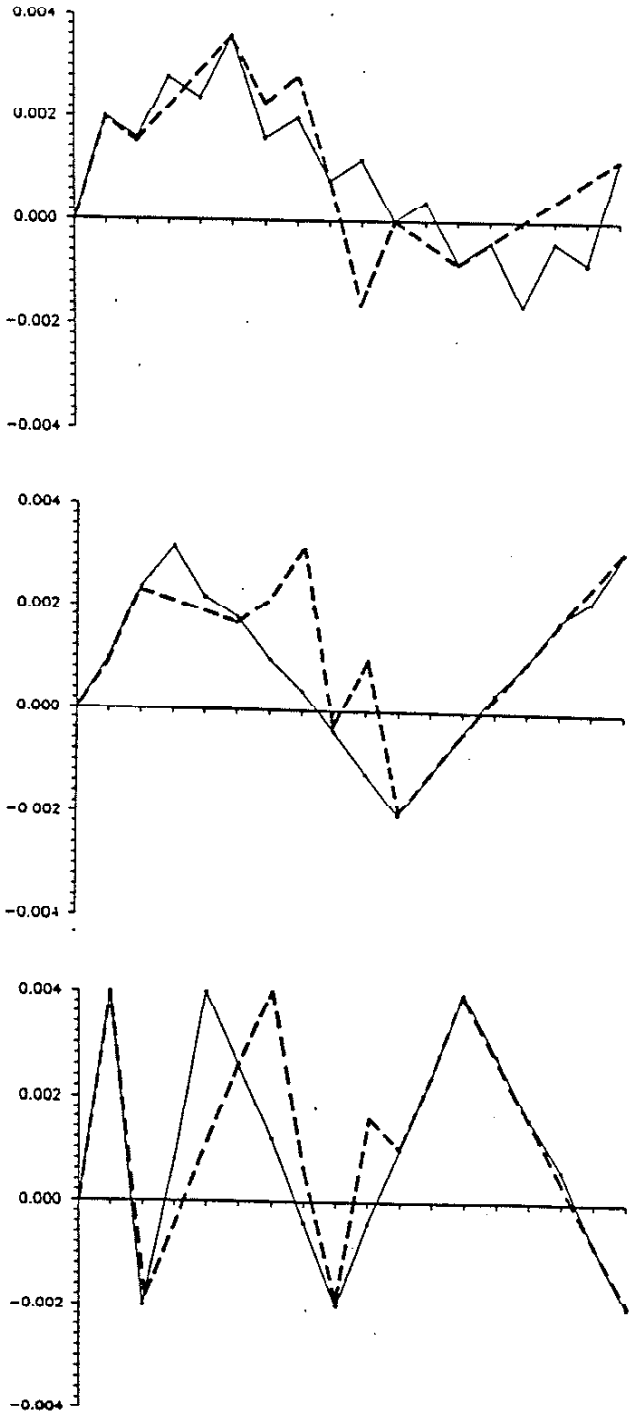

Figure 3.7 Edited Strain Histories Showing Loss of Time Sequence

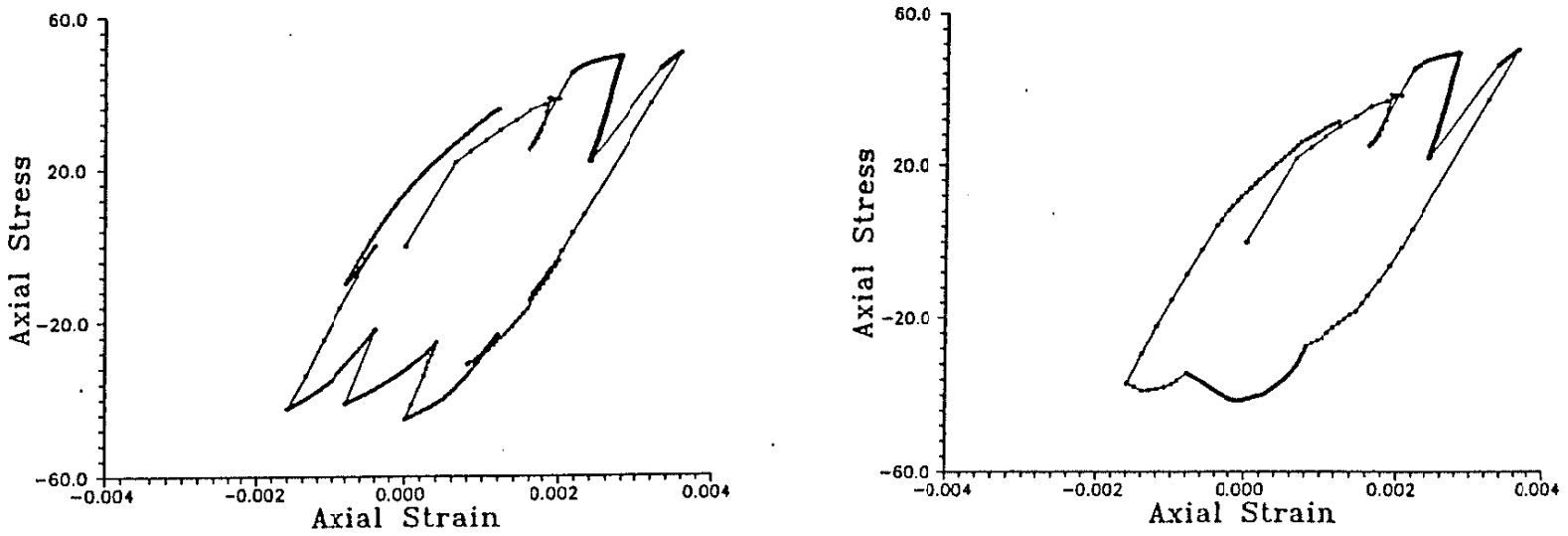

Figure 3.8 Stress-Strain Response for (a) Unedited History (b) Edited History using Multiaxial Editing Method

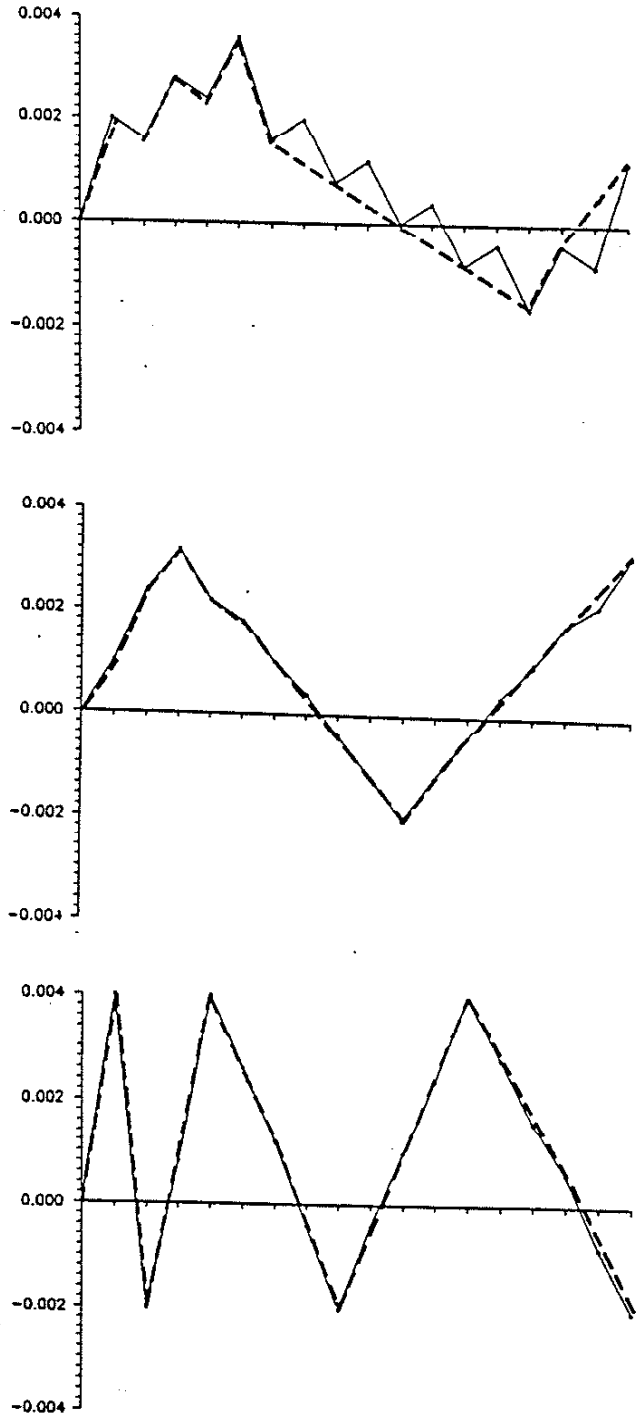

Figure 3.9 Edited Strain History with Time Sequence Maintained

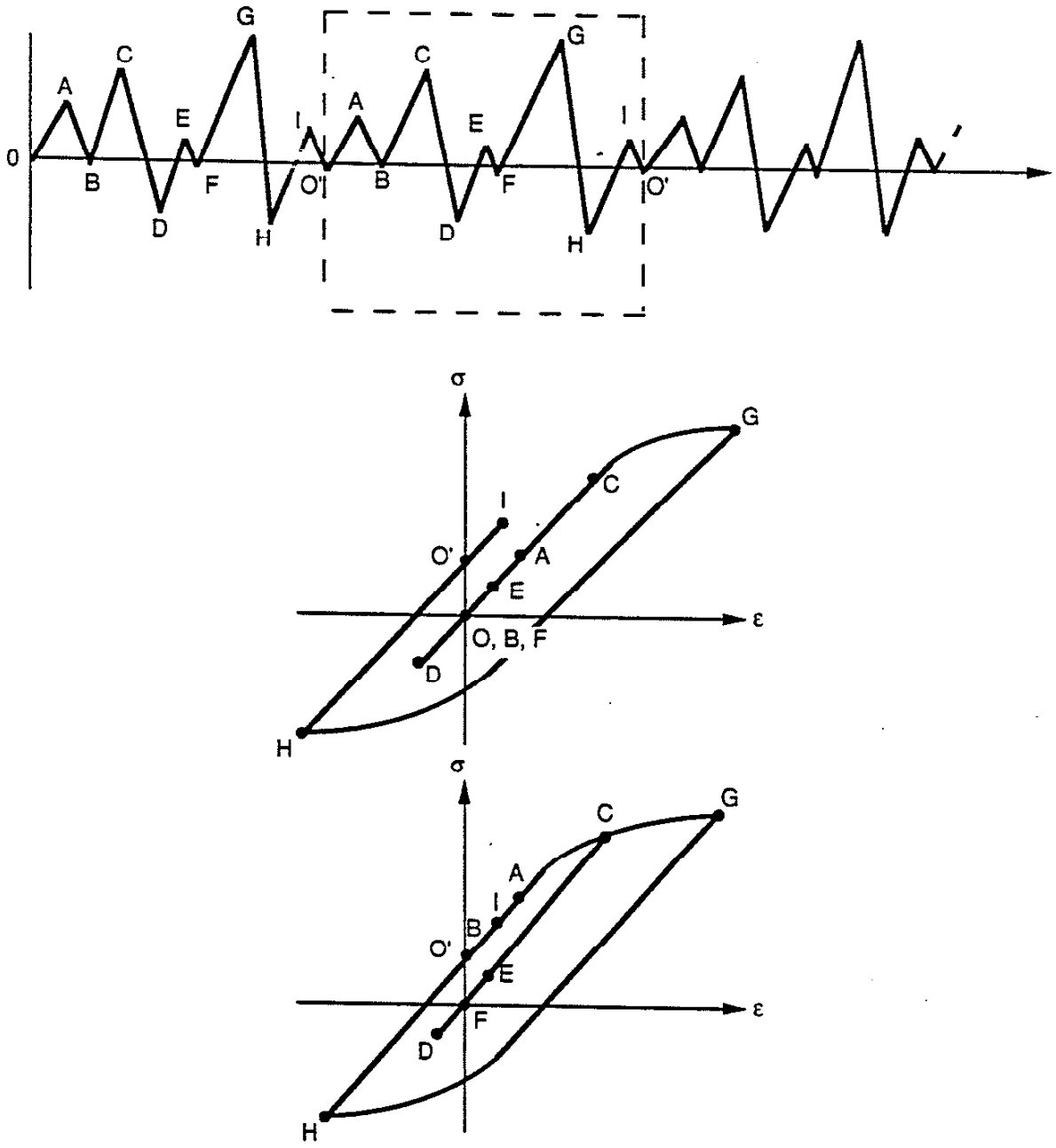

Figure 3.10 (a) Loading History Made up of Repeating Blocks
(b) Stress-Strain Response for First Block
(c) Stress-Strain Response for Second Block and All Other Blocks

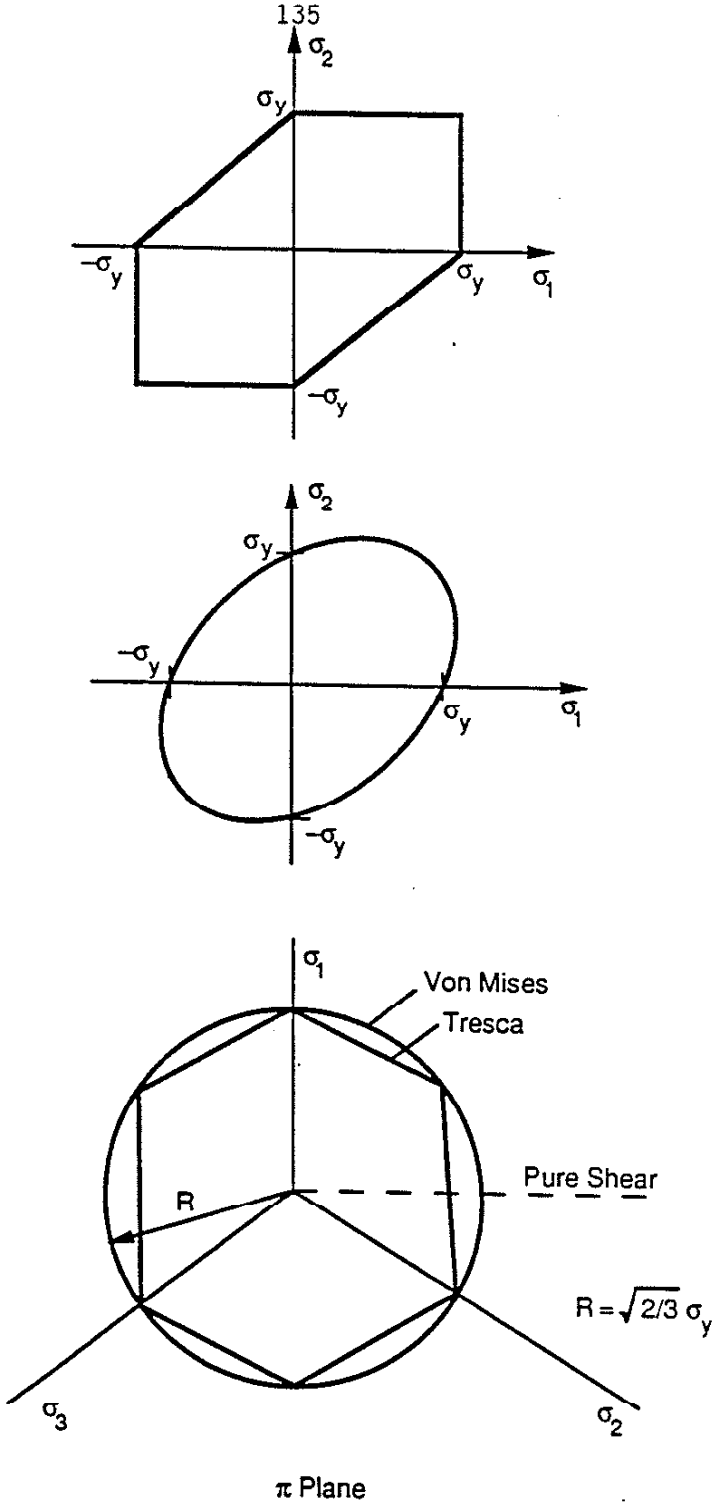

Figure 3.11 Tresca and von Mises Yield Criteria in (a) Biaxial Stress Space (b) Deviatoric Stress Space

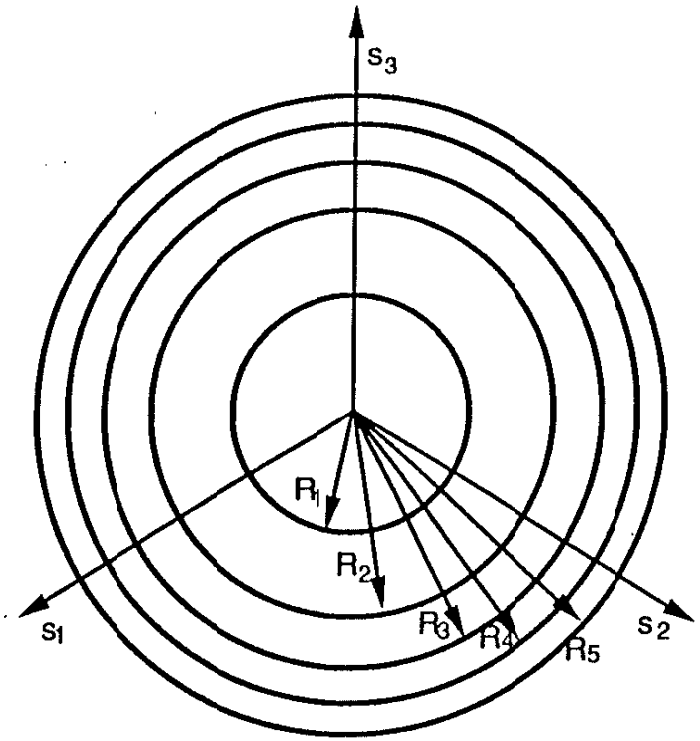

Von Mises Criteria in π Plane

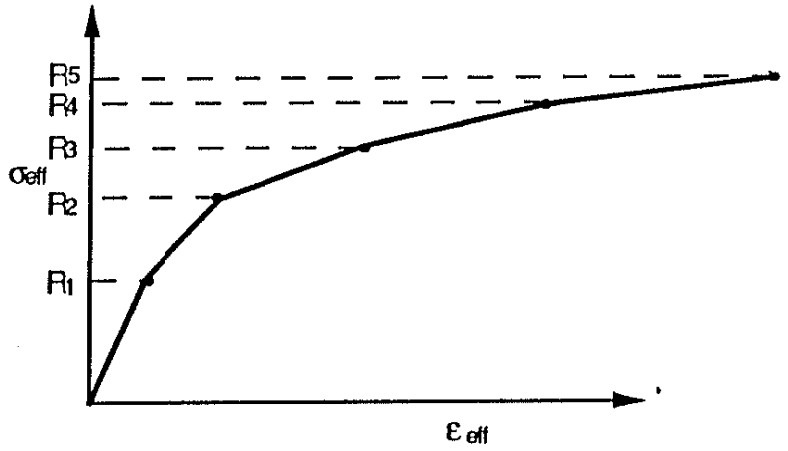

Piecewise Linearization of Cyclic Effective Stress - Strain Curve

Figure 3.12 (a) Field of Constant Work Hardening Moduli
(b) Piecewise Linearization of Stress-Strain Curve

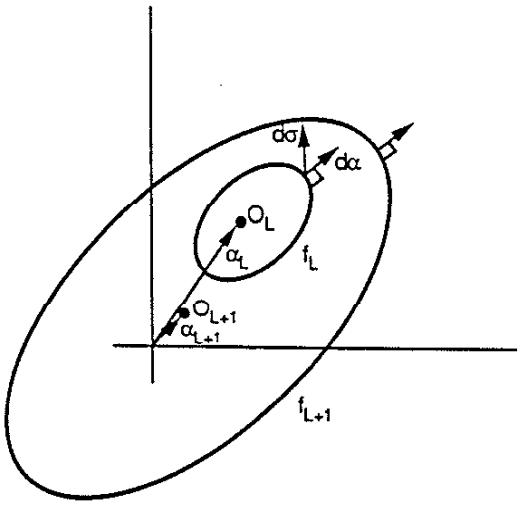

Figure 3.13 Representation of Mròz Hardening Model

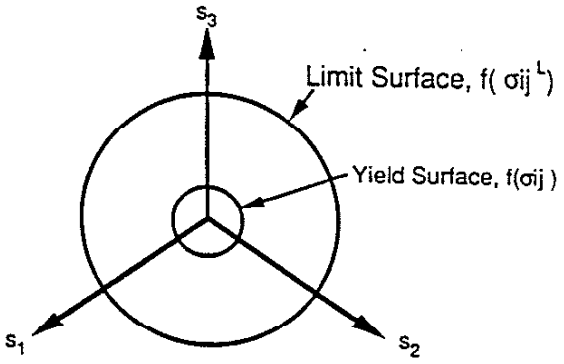

Two Surface (Von Mises) Model in π Plane

Figure 3.14 Two Surface Model in π Plane

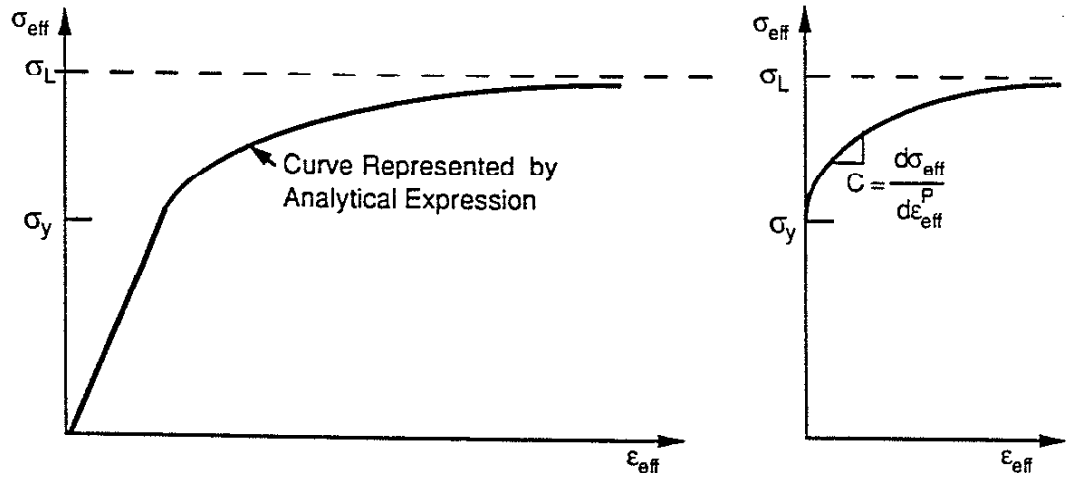

$$C = \frac{d\sigma_{eff}}{d\varepsilon^P_{eff}} = f(\sigma^L_{\bar{i}} - \sigma_{\bar{i}})$$

Strain hardening modulus, C, is a function of the distance between the stress point, $\sigma_{\bar{i}}$, and the point of the limit surface, $\sigma^L_{\bar{i}}$, having the same exterior normal. When $\sigma_{\bar{i}} = \sigma^L_{\bar{i}}$, C (slope of σ vs ε^P curve) goes to zero.

Figure 3.15 Plastic Modulus, C, is a Function off Distance Between Current Stress and the Limit Stress

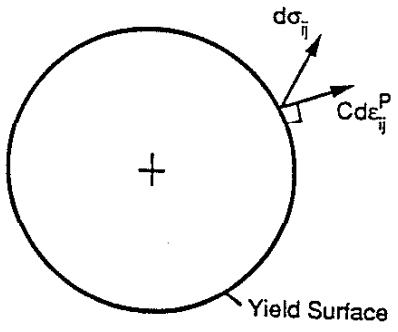

Figure 3.16 Projection of $d\sigma_{ij}$ on the Exterior Normal to the Yield Surface

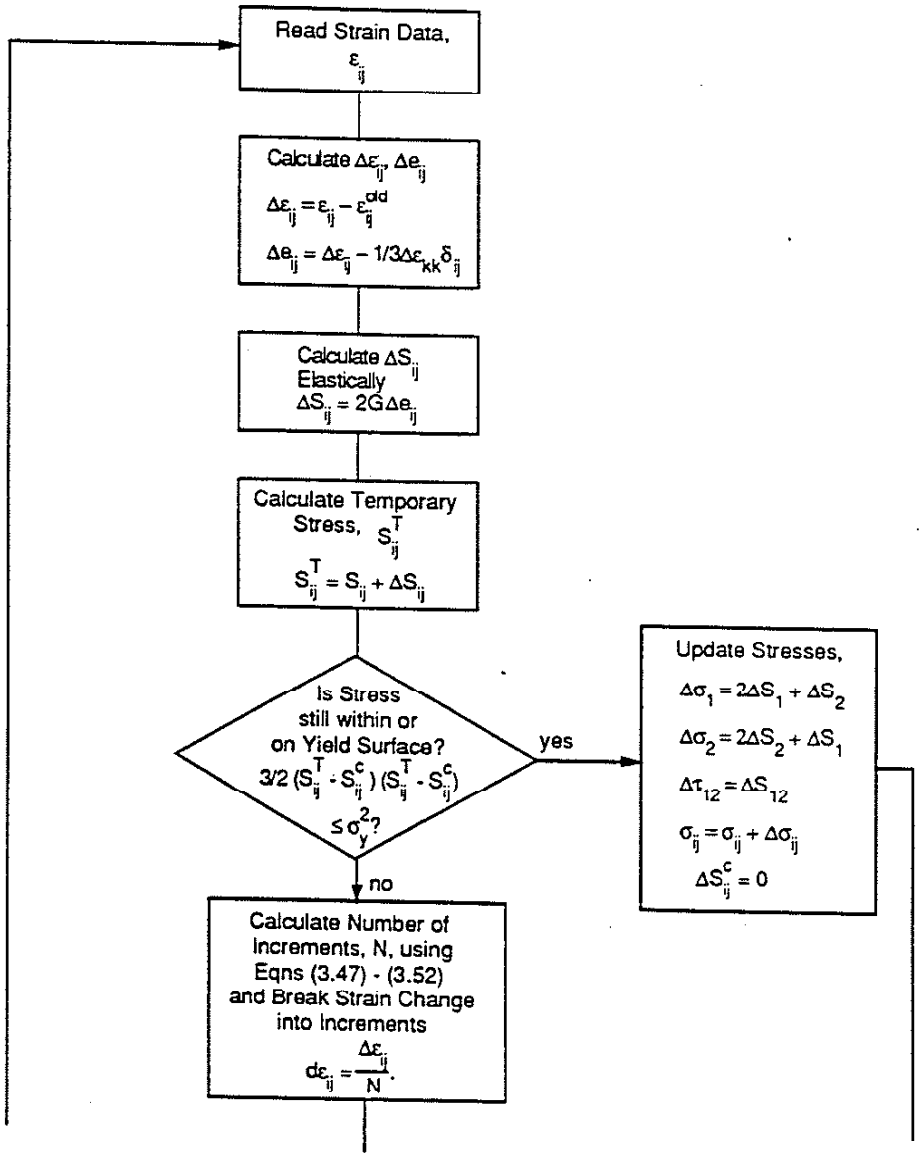

(Continued on Figure 3.17b)

Figure 3.17a Flow Chart of Incremental Plasticity Procedure

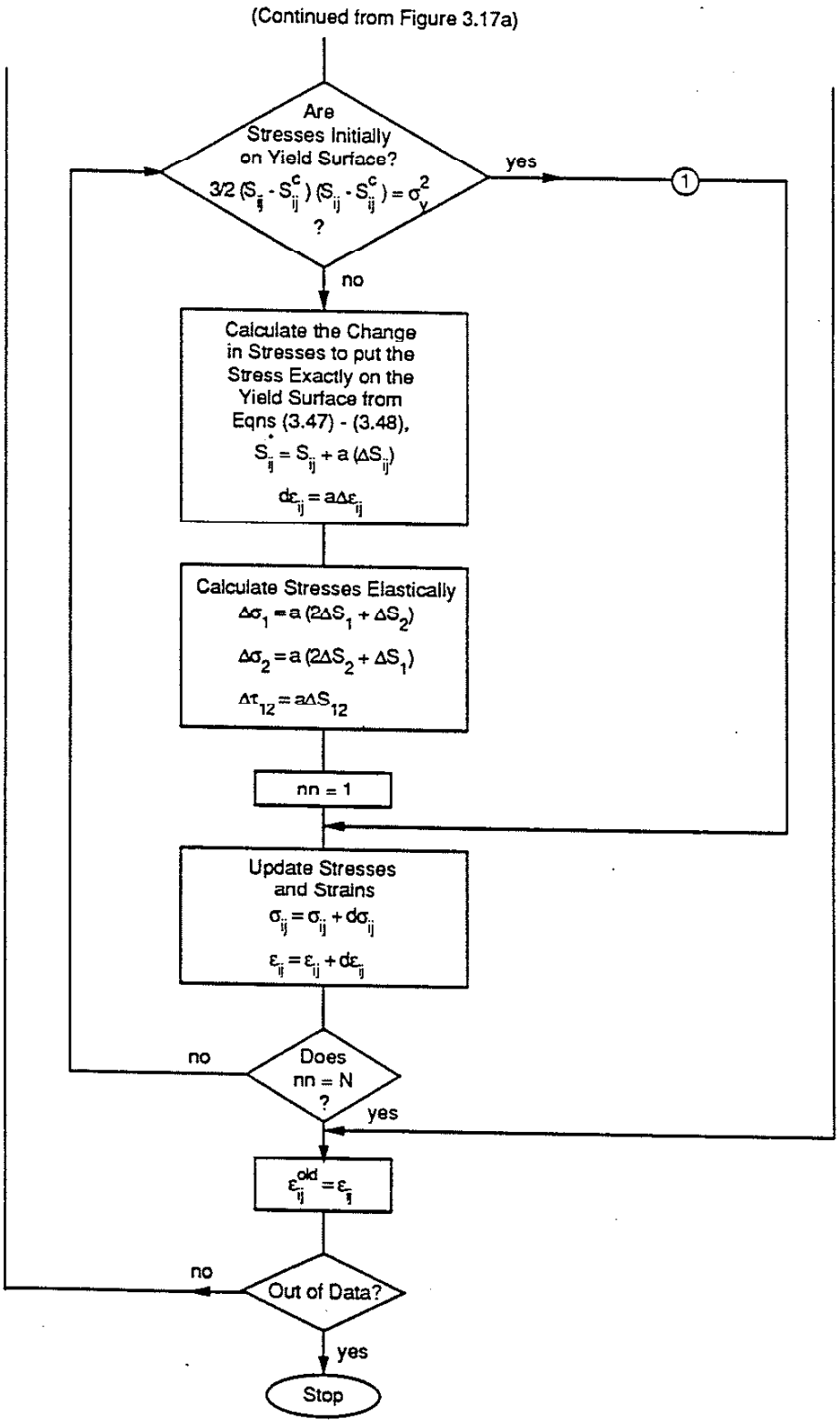

Figure 3.17b Flow Chart of Incremental Plasticity Procedure

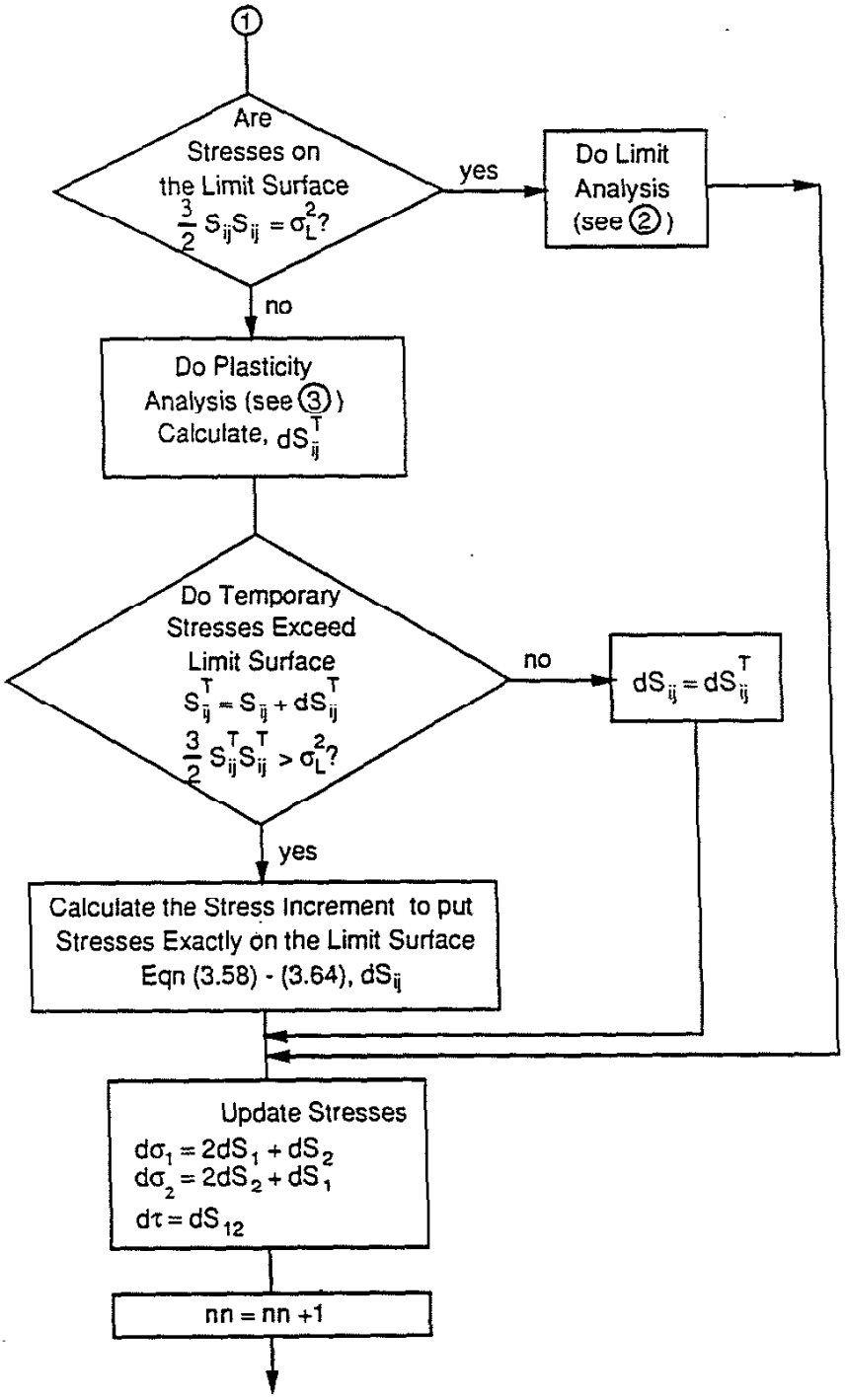

Figure 3.17c Flow Chart of Incremental Plasticity Procedure

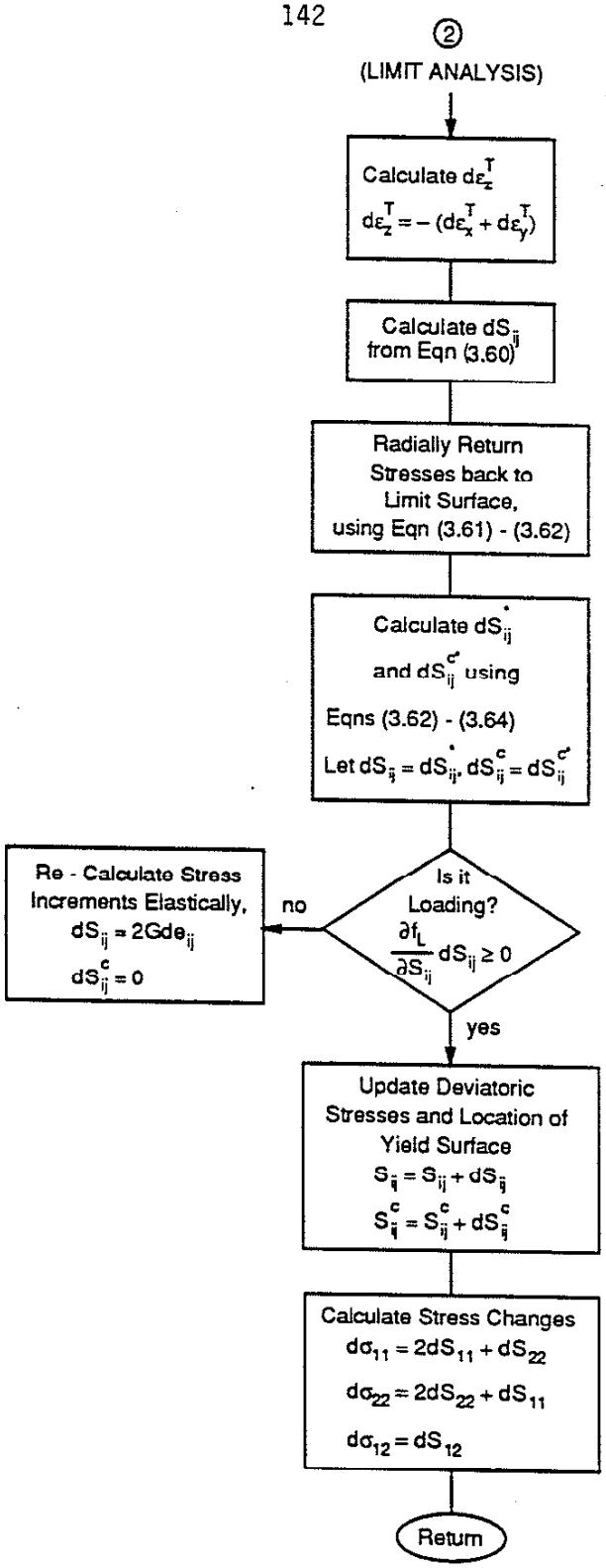

Figure 3.17d Flow Chart of Incremental Plasticity Procedure

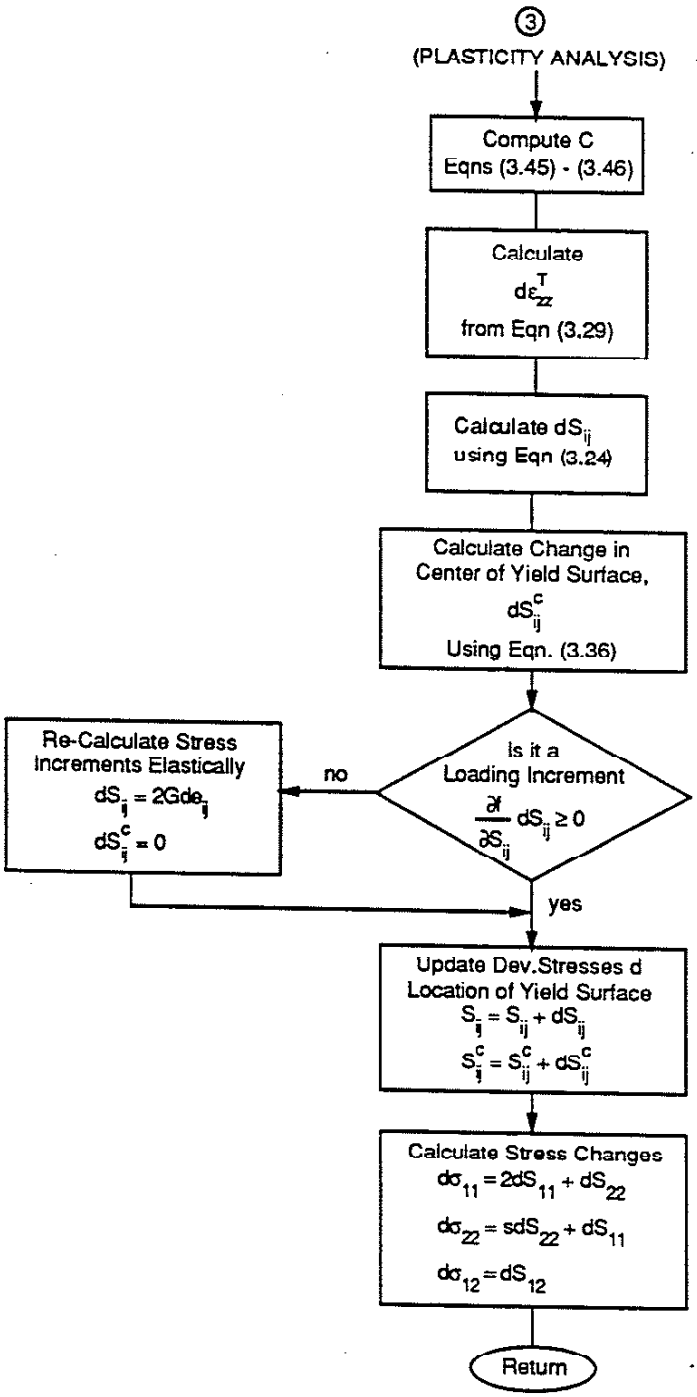

Figure 3.17e Flow Chart of Incremental Plasticity Procedure

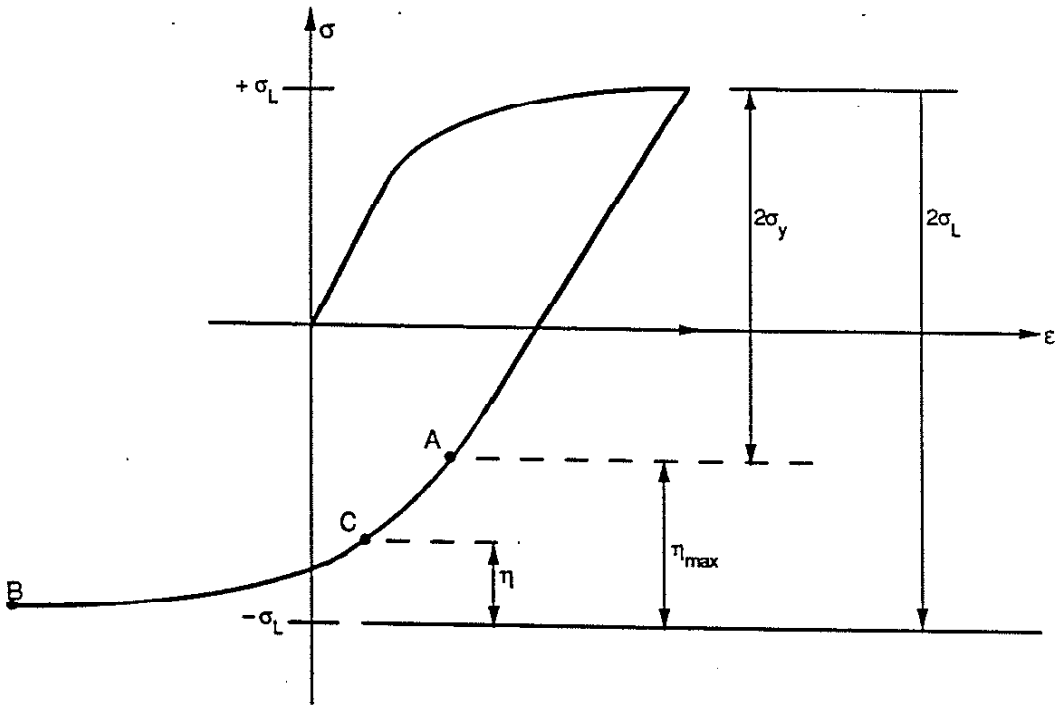

Figure 3.18 Uniaxial Stress-Strain Response

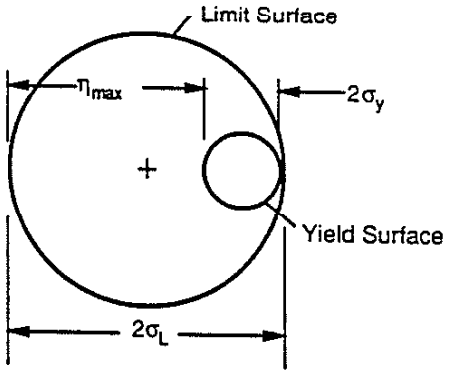

Representation of maximum distance, η_{max}, between yield surface and limit surface.

Figure 3.19 Maximum Distance, η_{max}, Between Yield Surface and Limit Surface

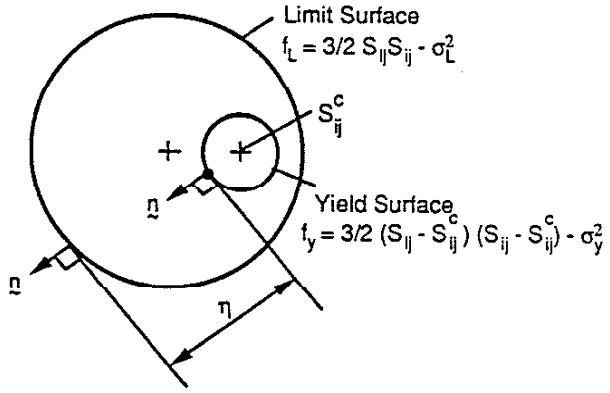

Figure 3.20 The Distance, η, Between Current Stress Point on Yield Surface and Point on the Limit Surface

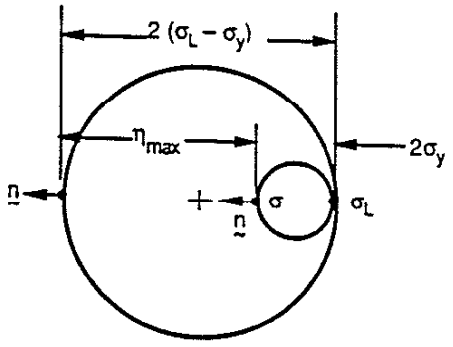

$$\sigma = \sigma_L - 2\sigma_y$$

$$D = \frac{2\ (\sigma_L - \sigma_y) - \sqrt{(-\sigma_L - (\sigma_L - 2\sigma_y))(-\sigma_L - (\sigma_L - 2\sigma_y))}}{2\ (\sigma_L - \sigma_y)} = 0$$

(σ_y and σ_L, shown here for clarity, are actually S_y and S_L)

Figure 3.21 D Equals Zero Immediately After Elastic Unloading

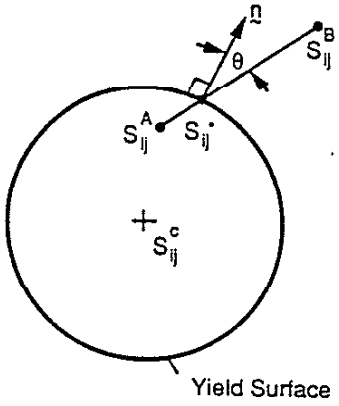

$$\Delta S_{ij} = S_{ij}^B - S_{ij}^A$$
$$a\Delta S_{ij} = S_{ij}^* - S_{ij}^A$$

Figure 3.22 Number of Increments Needed Depends Upon θ and the Distance from S_{ij}^B to the Yield Surface

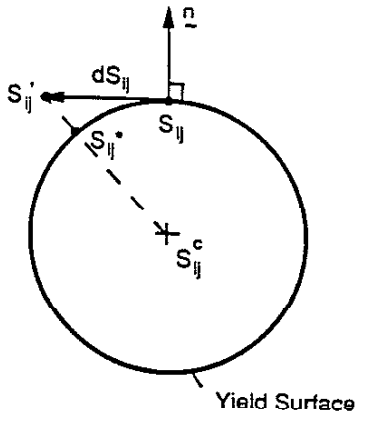

Figure 3.23 Neutral Loading

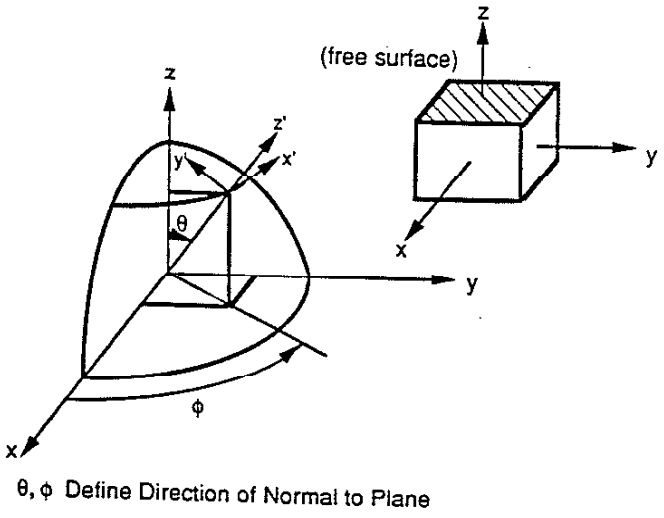

Figure 3.24 Orientation of a Plane Defined by Normal Vector with Angles θ and ϕ from X-Y-Z System

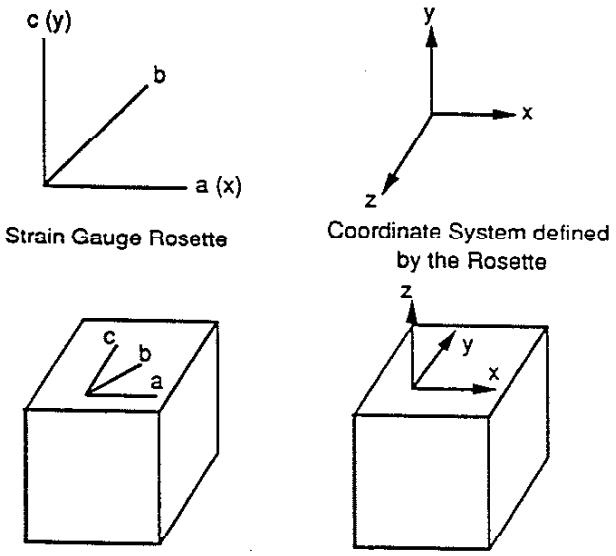

Figure 3.25 Strain Gauge Rosette Position Defines X-Y-Z Coordinate System

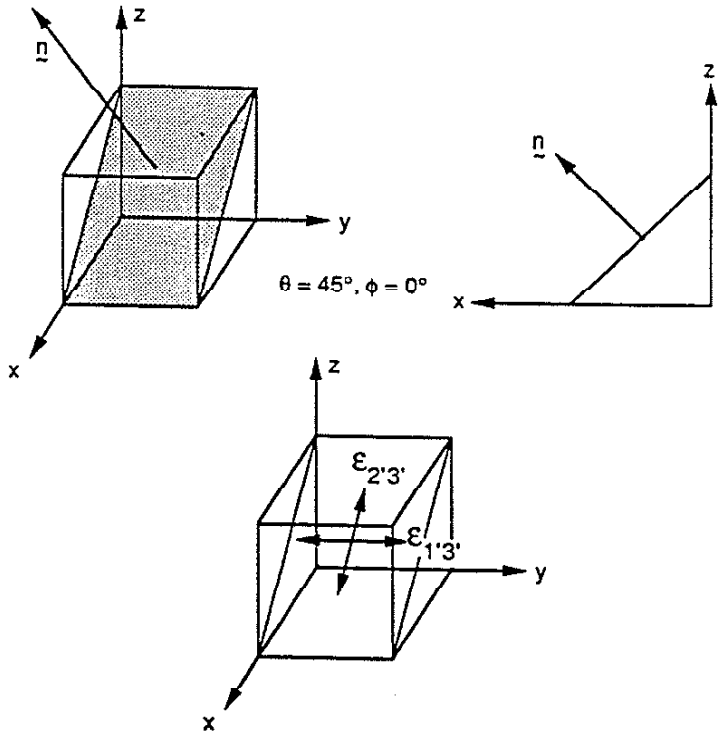

Figure 3.26 Orientation of Local Coordinate System for $\theta = 45°$, $\phi = 0°$

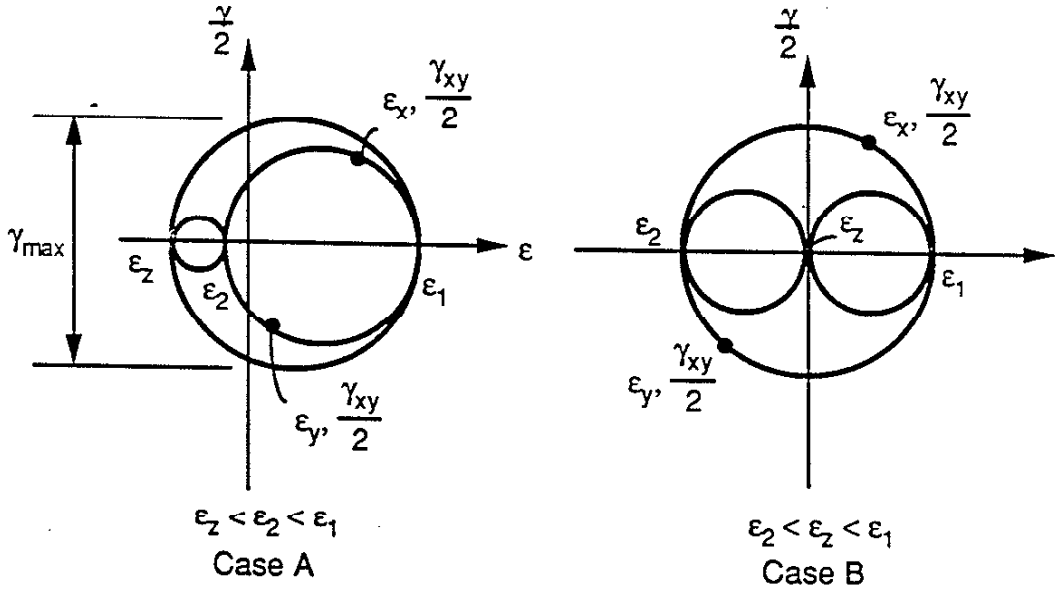

Tensile Model:

In both case A and case B, the maximum tensile strain, ε_1 , occurs in x-y plane.

($\theta = 90°, \phi = 0°$ to $180°$)

Shear Model:

In case A, the maximum shear strain is 45° from z axis.

($\theta = 45°, \phi = 0°$ to $180°$)

In case B, the maximum shear strain is in the x-y plane.

($\theta = 90°, \phi = 0°$ to $180°$)

Figure 3.27 Mohr's Circle for Two Possible Loading Cases

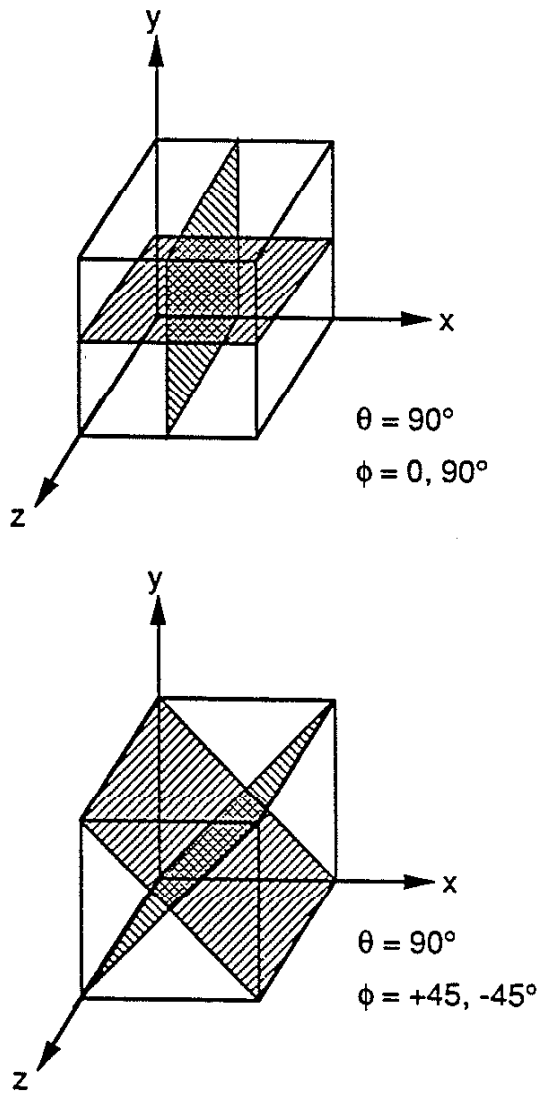

Figure 3.28 Several Possible Critical Plane Orientations using Tensile Model ($\theta = 90°$)

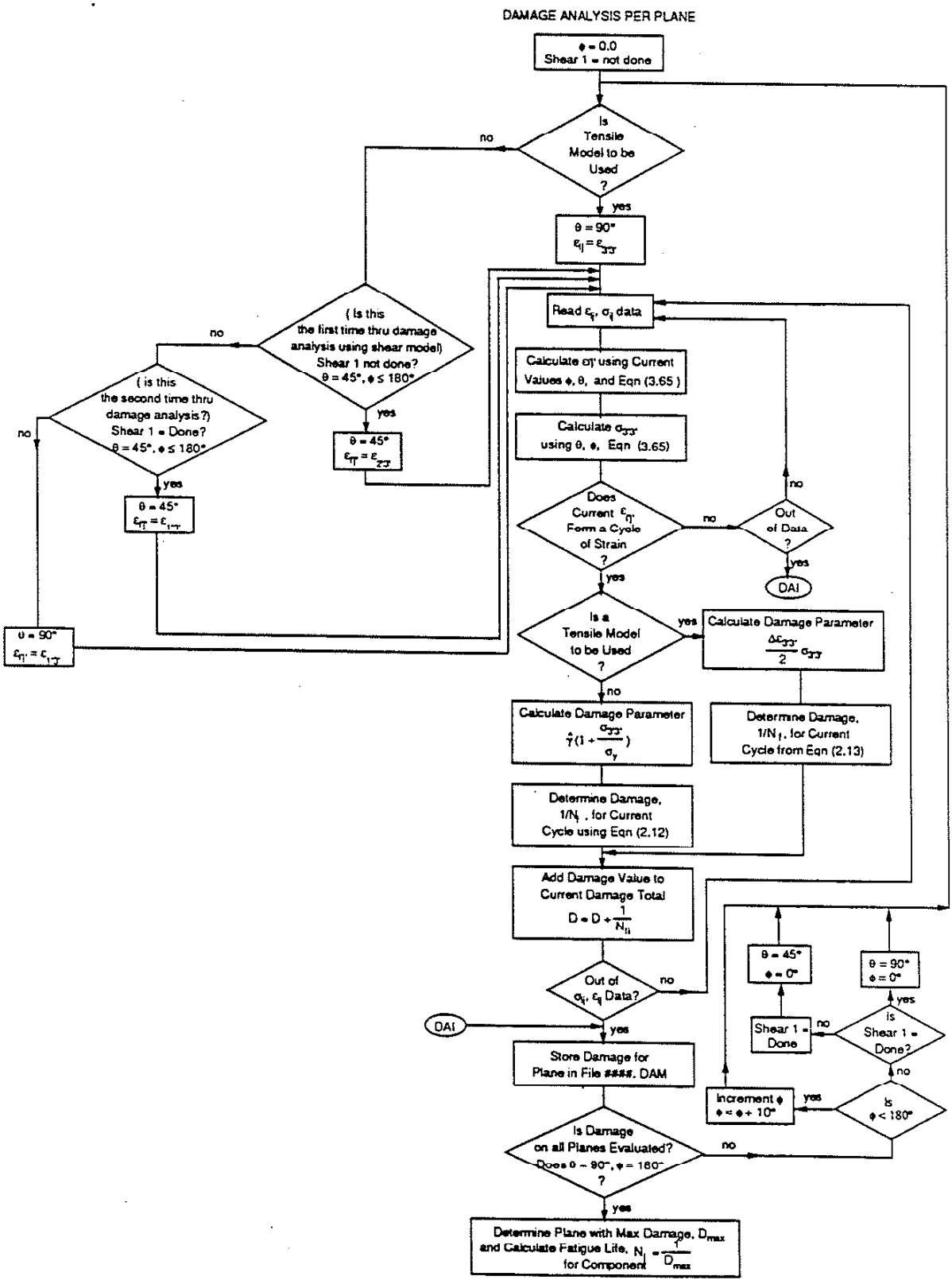

Figure 3.29 Flow Chart for Computer Procedure to Calculate Damage per Plane

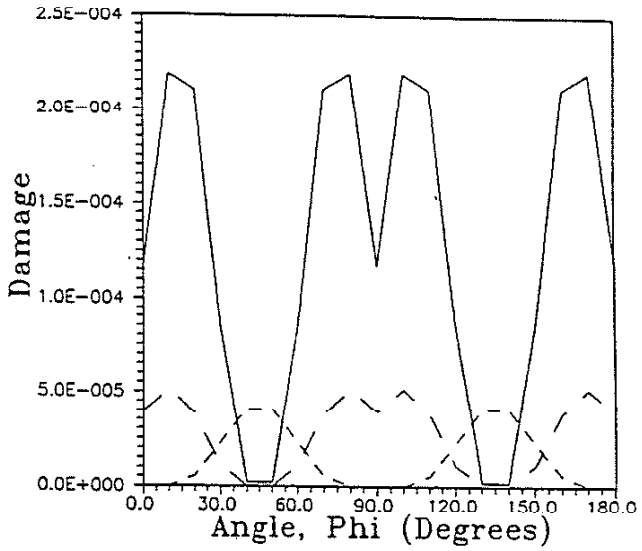

Figure 3.30 Shear Damage Plot for Pure Torsion Loading

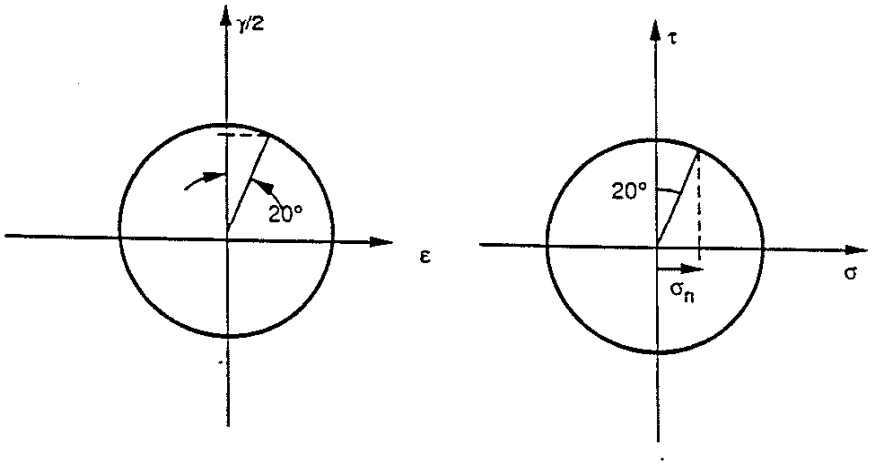

Figure 3.31 Mohr's Circle for Pure Torsion Stress and Strain States

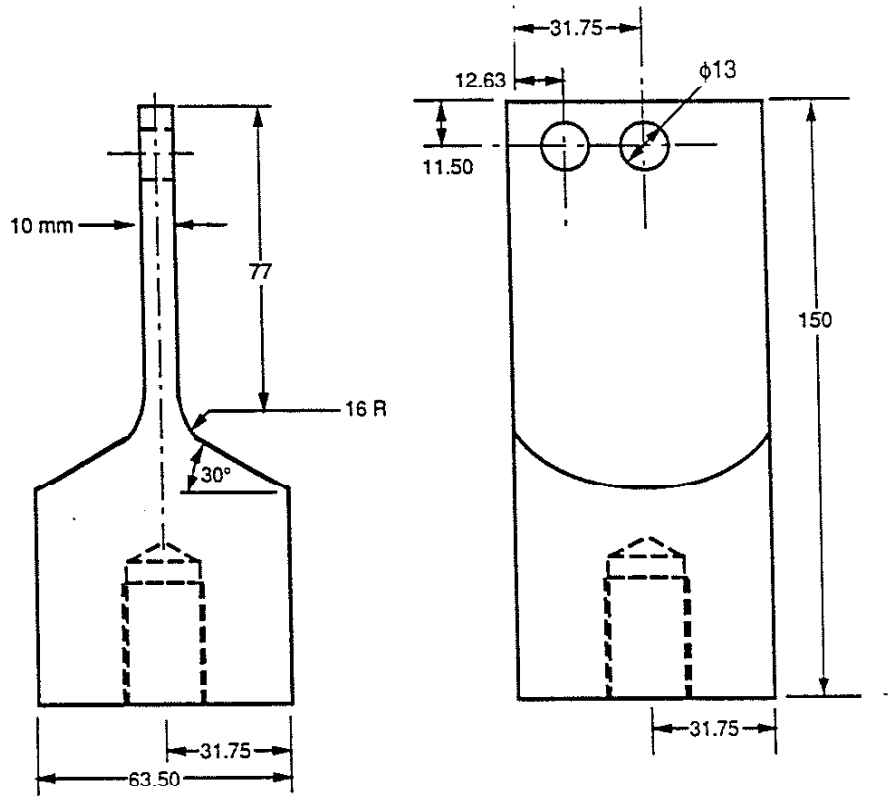

Figure 4.1 Notched Component used for Proportional Loading and Pure Bending Tests

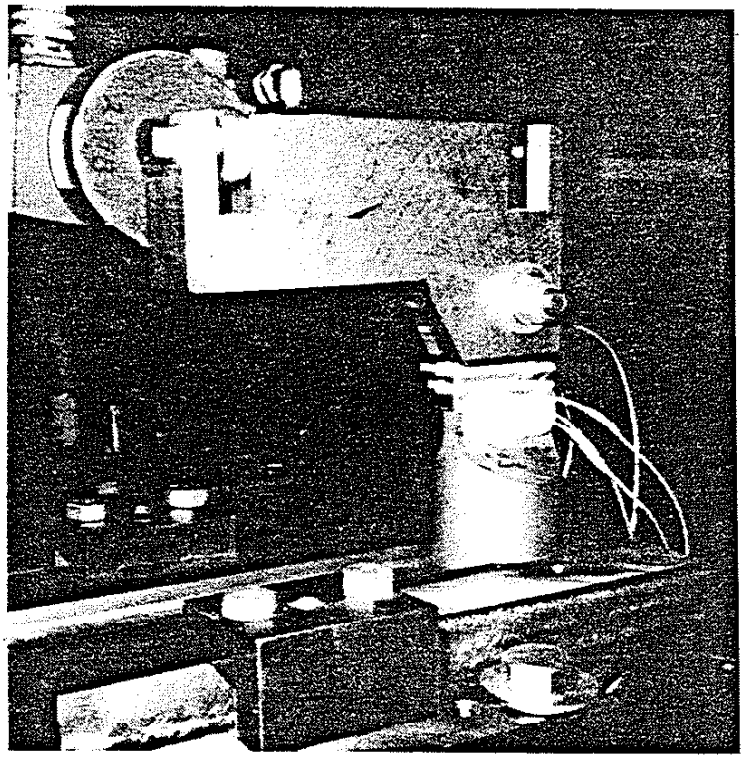

Figure 4.2 Component Subjected to Combined Loading

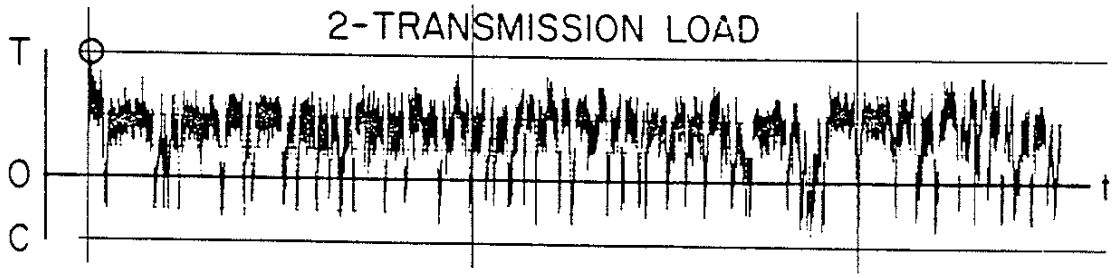

Figure 4.3 SAE Transmission History

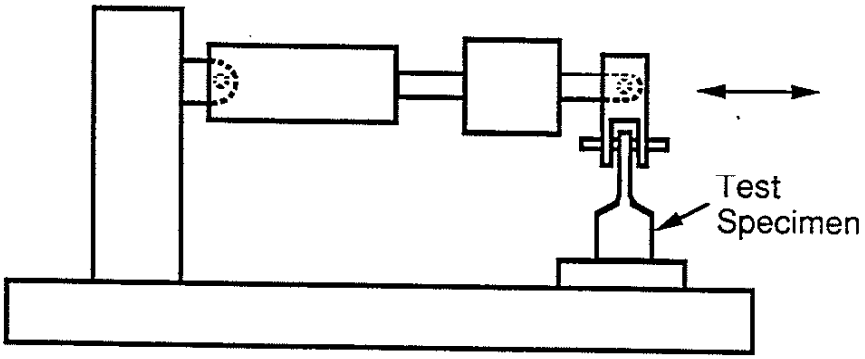

Figure 4.4 Test Fixture for Proportional and Pure Bending Tests

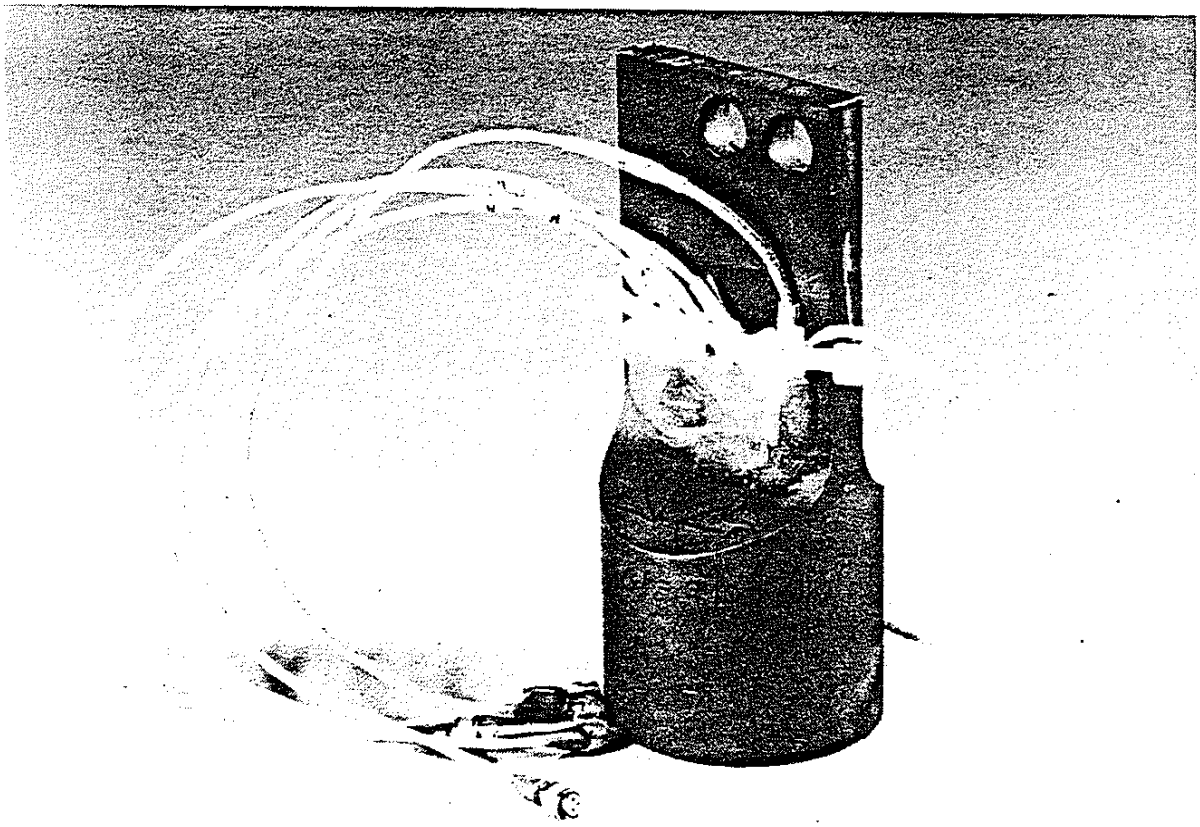

Figure 4.5 Strain-Gauged Specimen used for Proportional and Pure Bending Tests

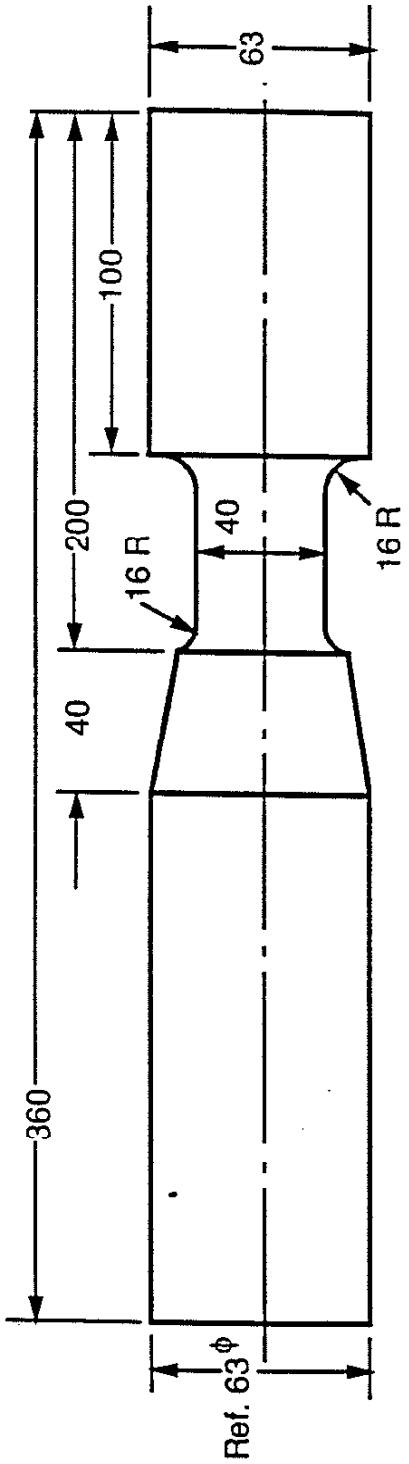

Figure 4.6 Modified SAE Notched Shaft Used for Nonproportional Loading Tests

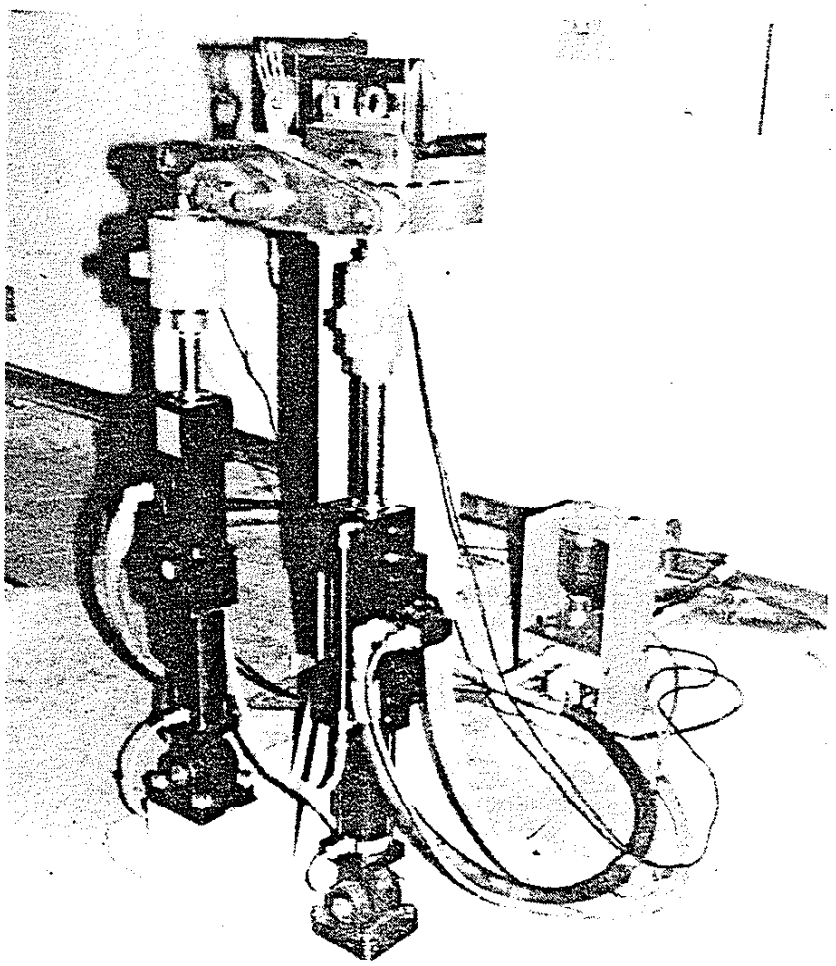

Figure 4.7 SAE Notched Shaft Test Fixture Used for Nonproportional Loading Tests

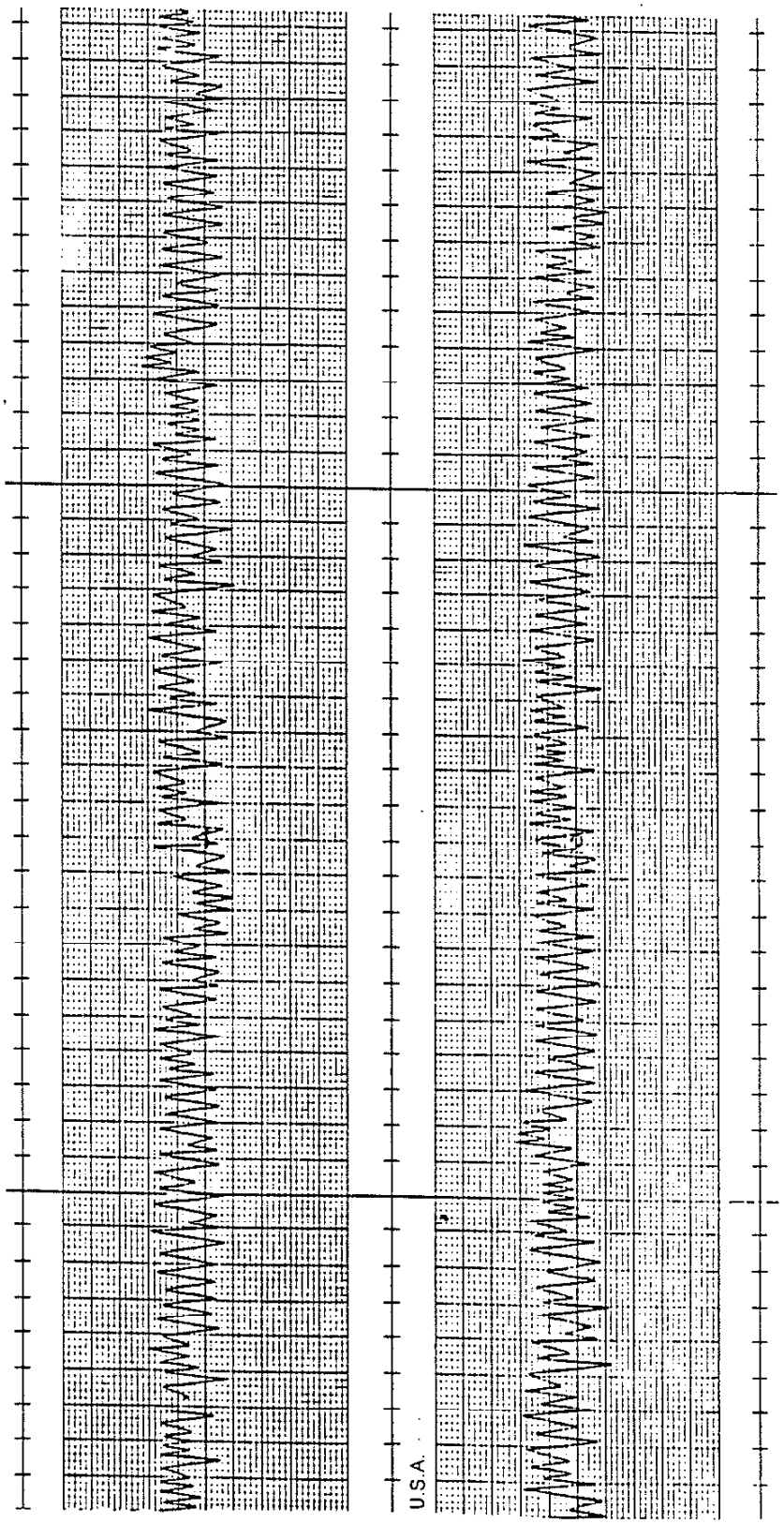

Figure 4.8 Strip-Chart Recording of Input Load Signals for Nonproportional Tests

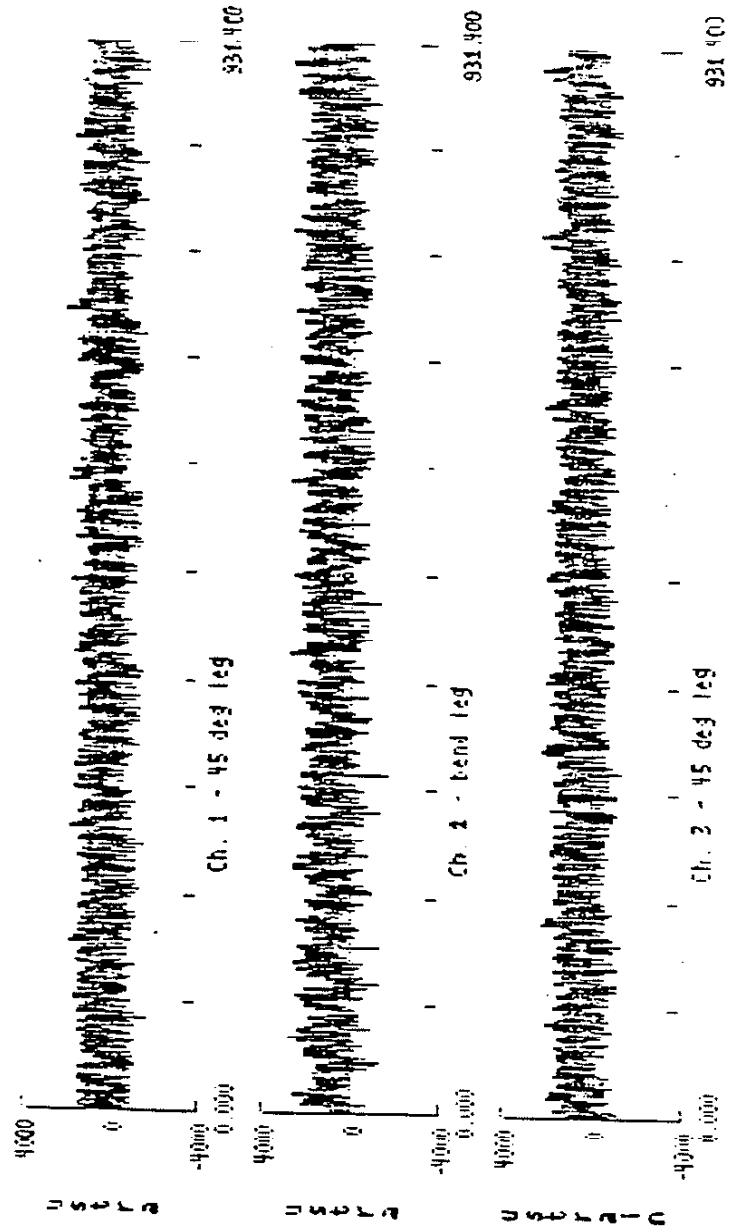

Figure 4.9a Strain Histories for Blocks 19-25

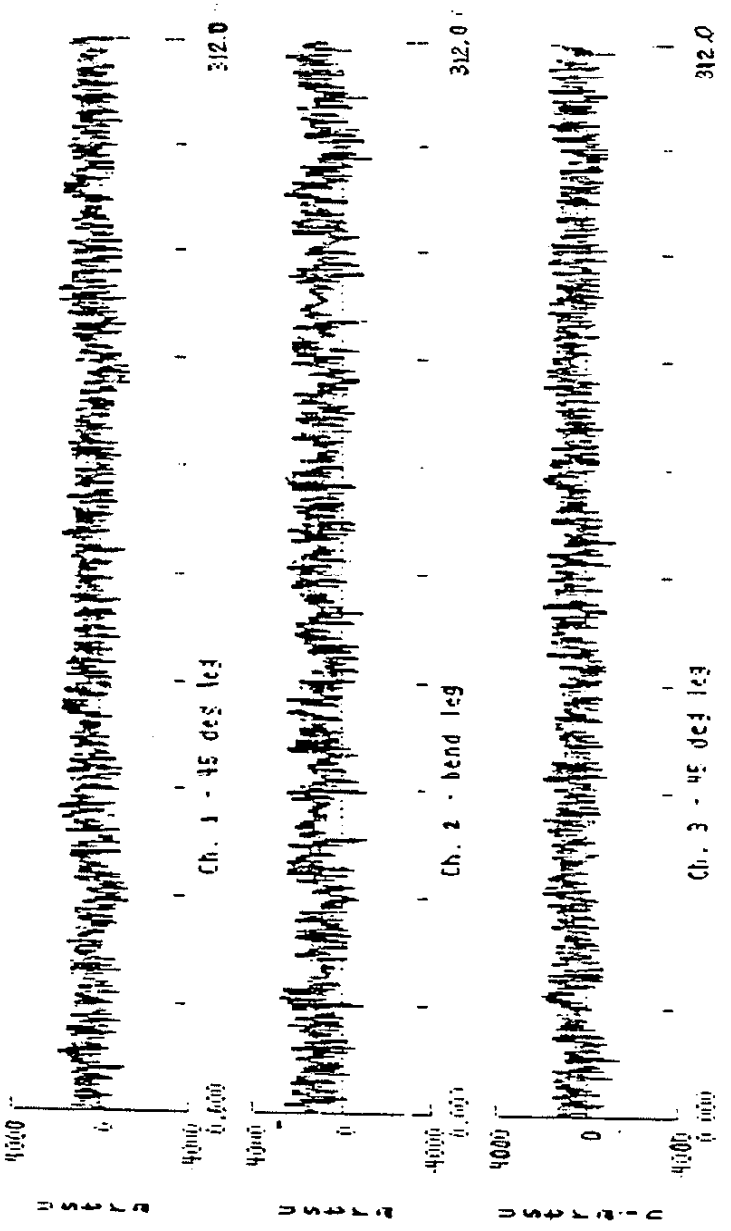

Figure 4.9b Strain Histories for Blocks 33-34

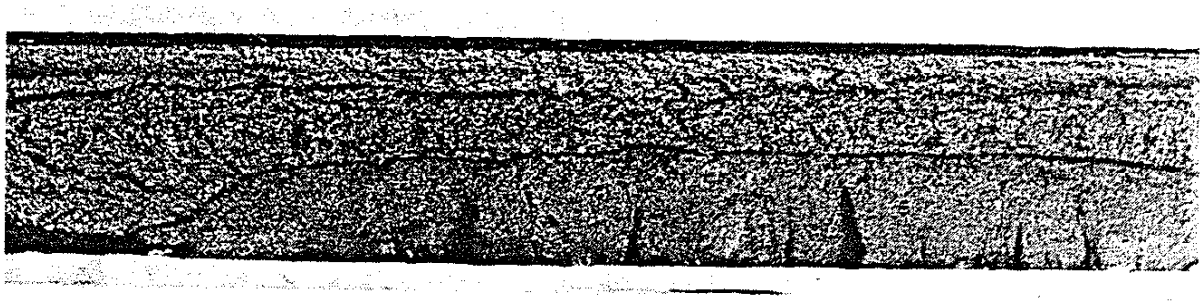

(a)

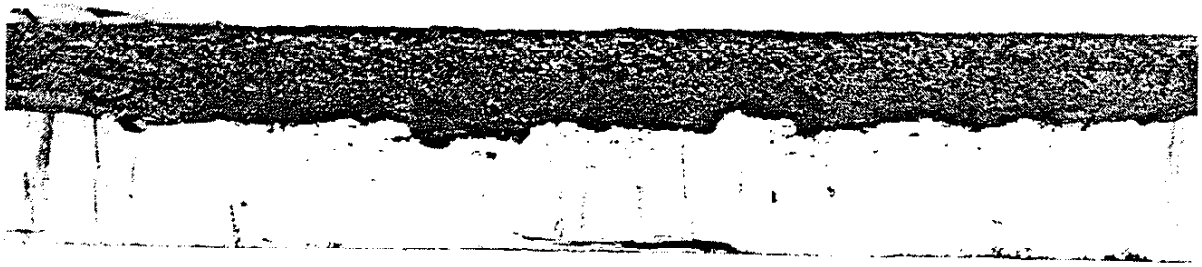

(b)

Figure 4.10 Fracture Surface of Component Tested under Pure Bending Variable Amplitude Loading (a) Top View (b) Side View

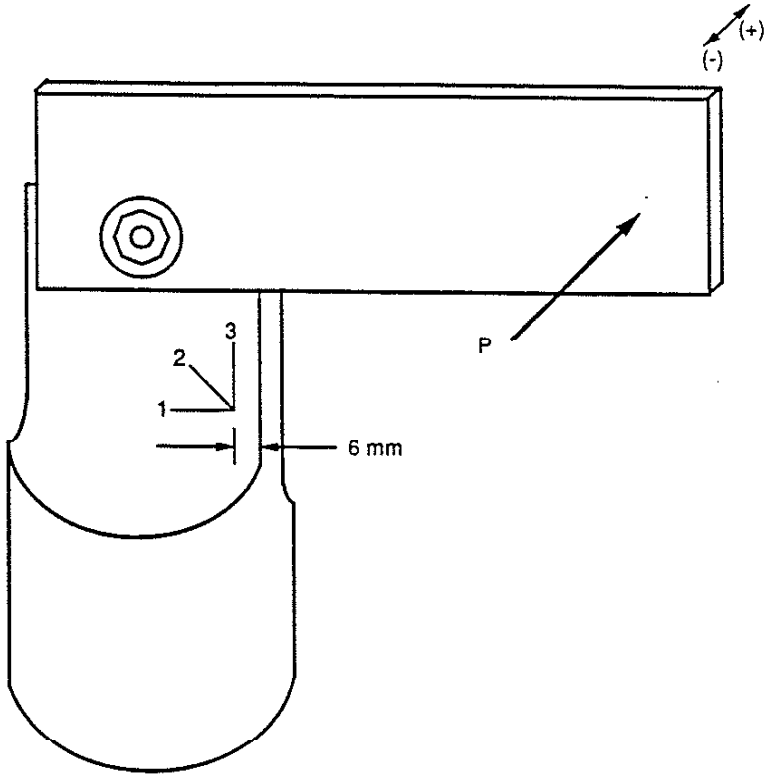

Figure 4.11 Strain Gauge Orientation on Proportionally Loaded Notched Shaft

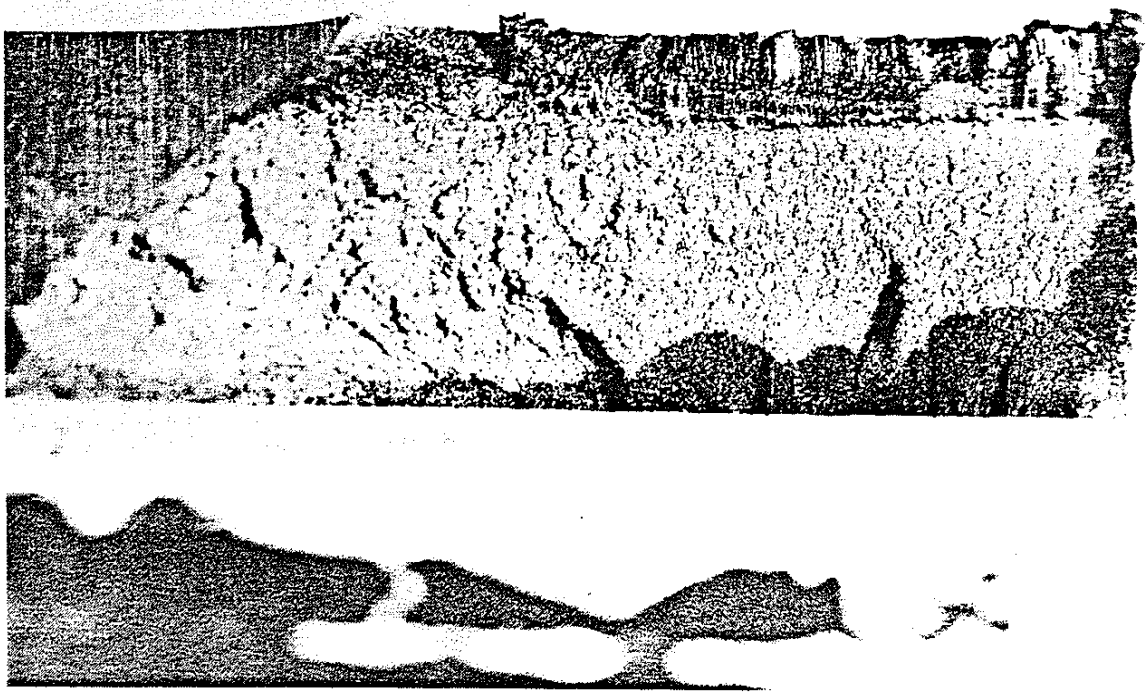

Figure 4.12 Fracture Surface of Proportionally Load Components, Specimen PL3

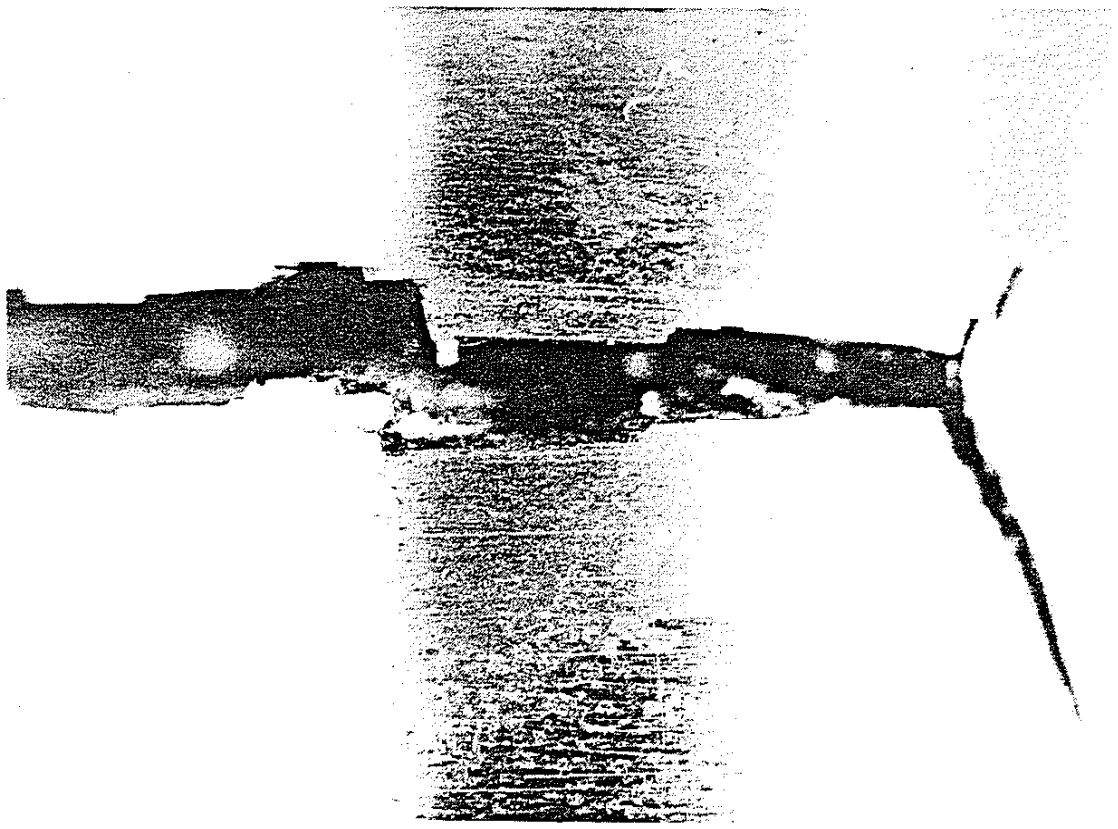

Figure 4.13 Cracking Observed in Nonproportionally Loaded Component, NP3. Cracking Initiated from Machining Marks

Figure 4.14 Cracking Observed in Nonproportionally Loaded Component, NP6

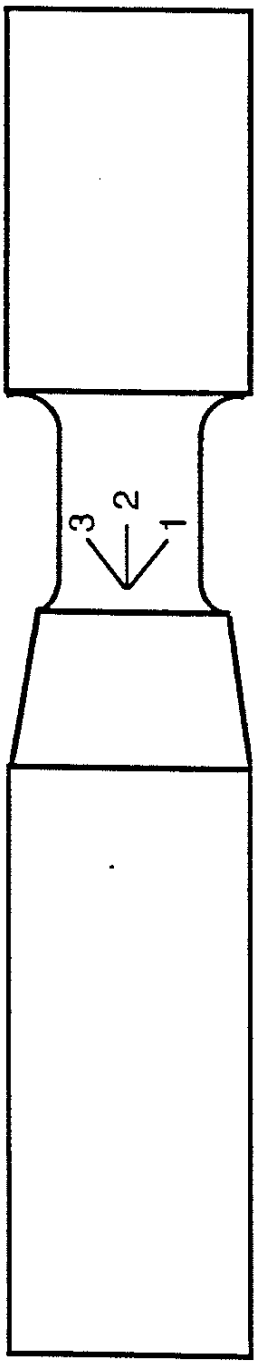

Figure 4.15 Strain-Gauge Orientation on Notched Component Used for Nonproportional Tests

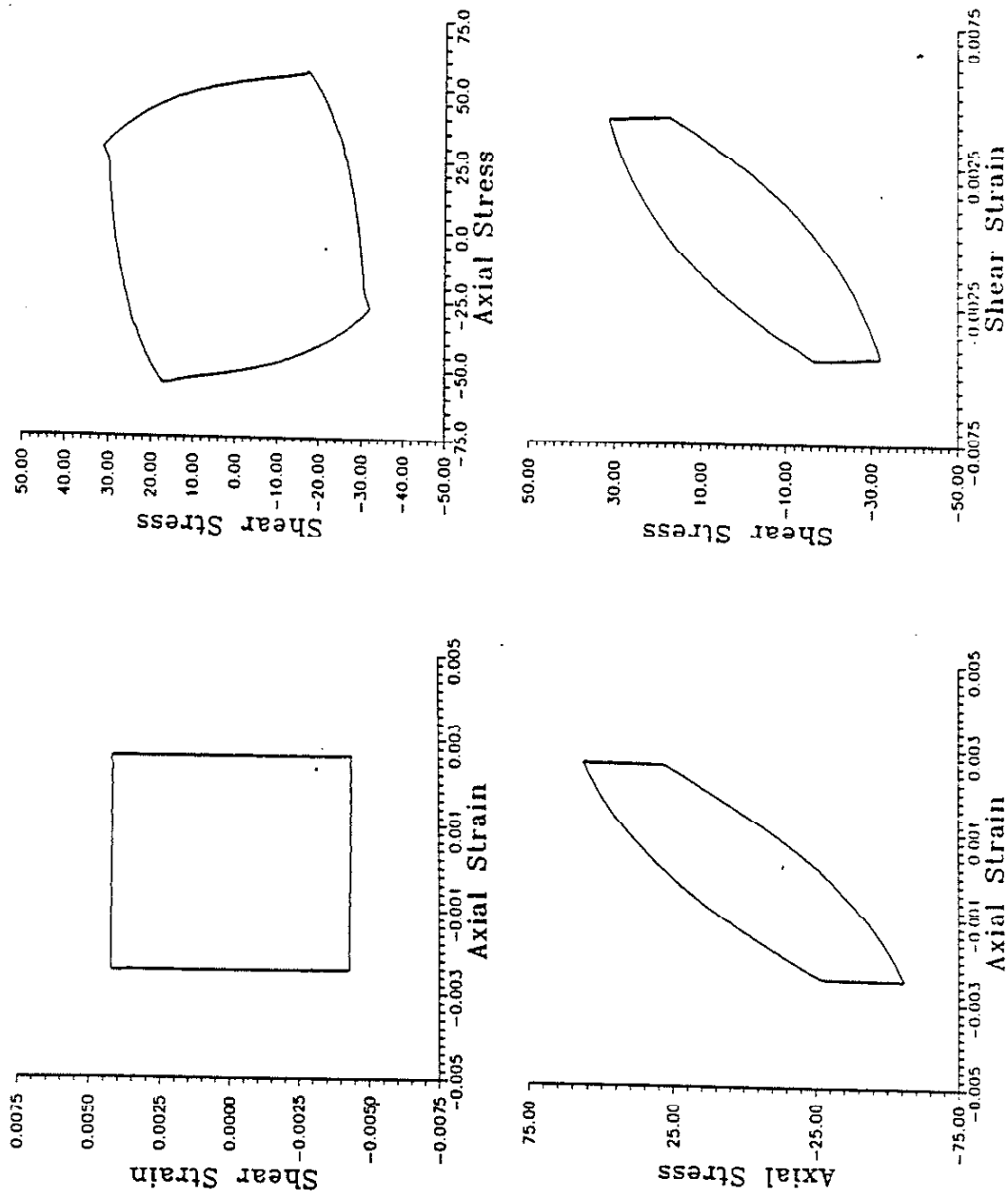

Figure 5.1a Measured Stress-Strain Response for SS304 Box Path

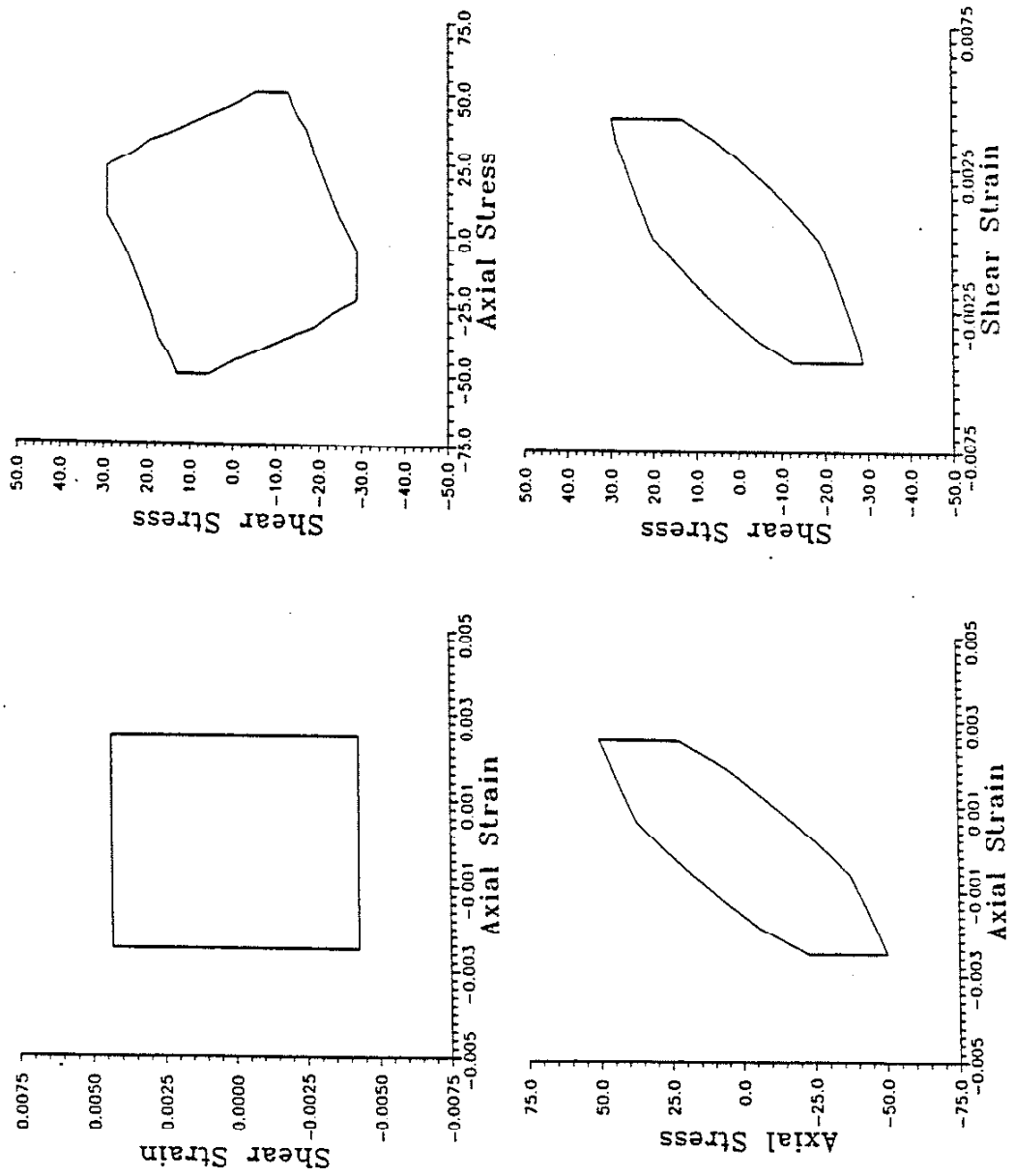

Figure 5.1b Predicted Stress-Strain Response for SS304 Box Path

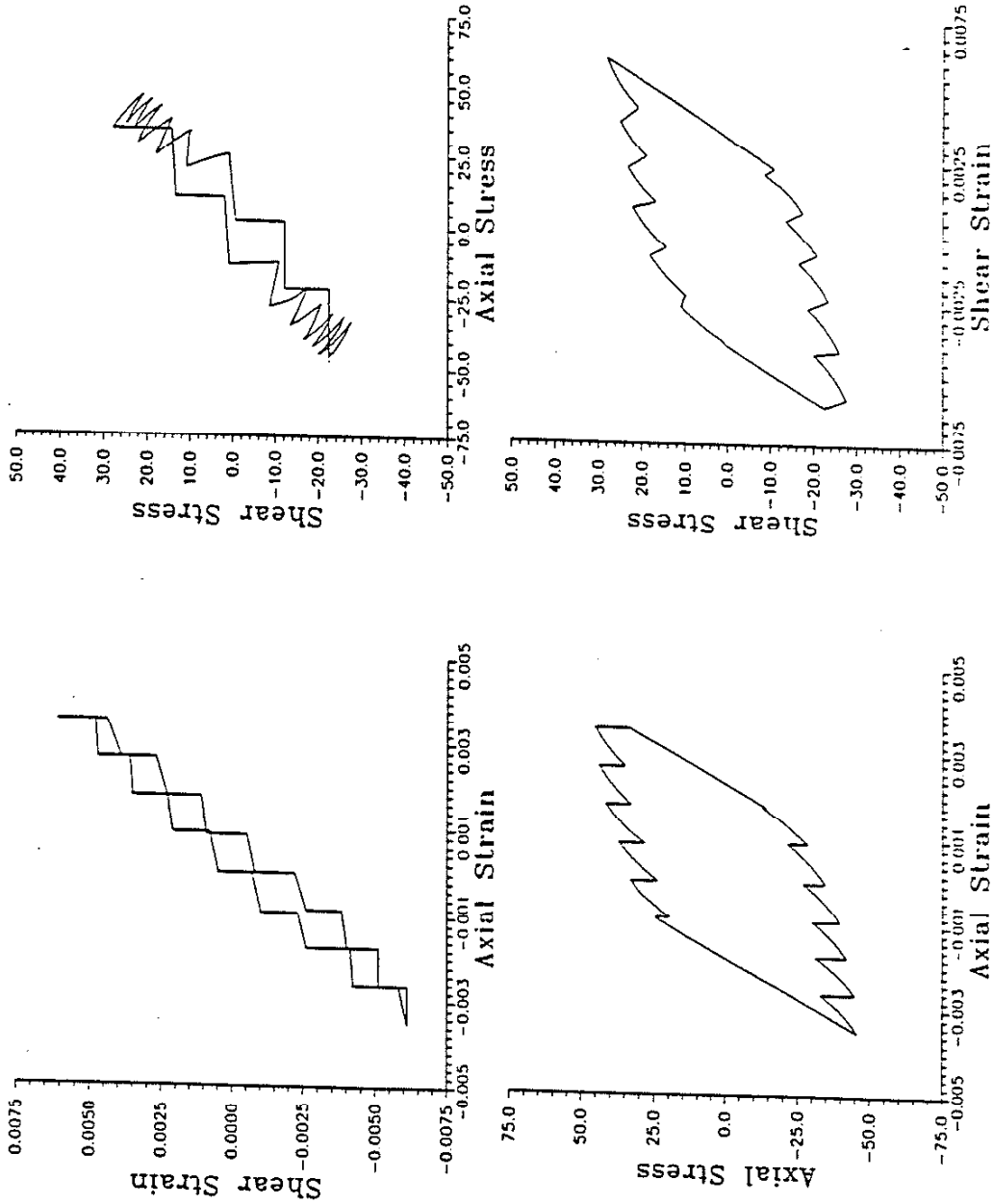

Figure 5.2a Measured Stress-Strain Response for SS304 8 Stair-Step Path

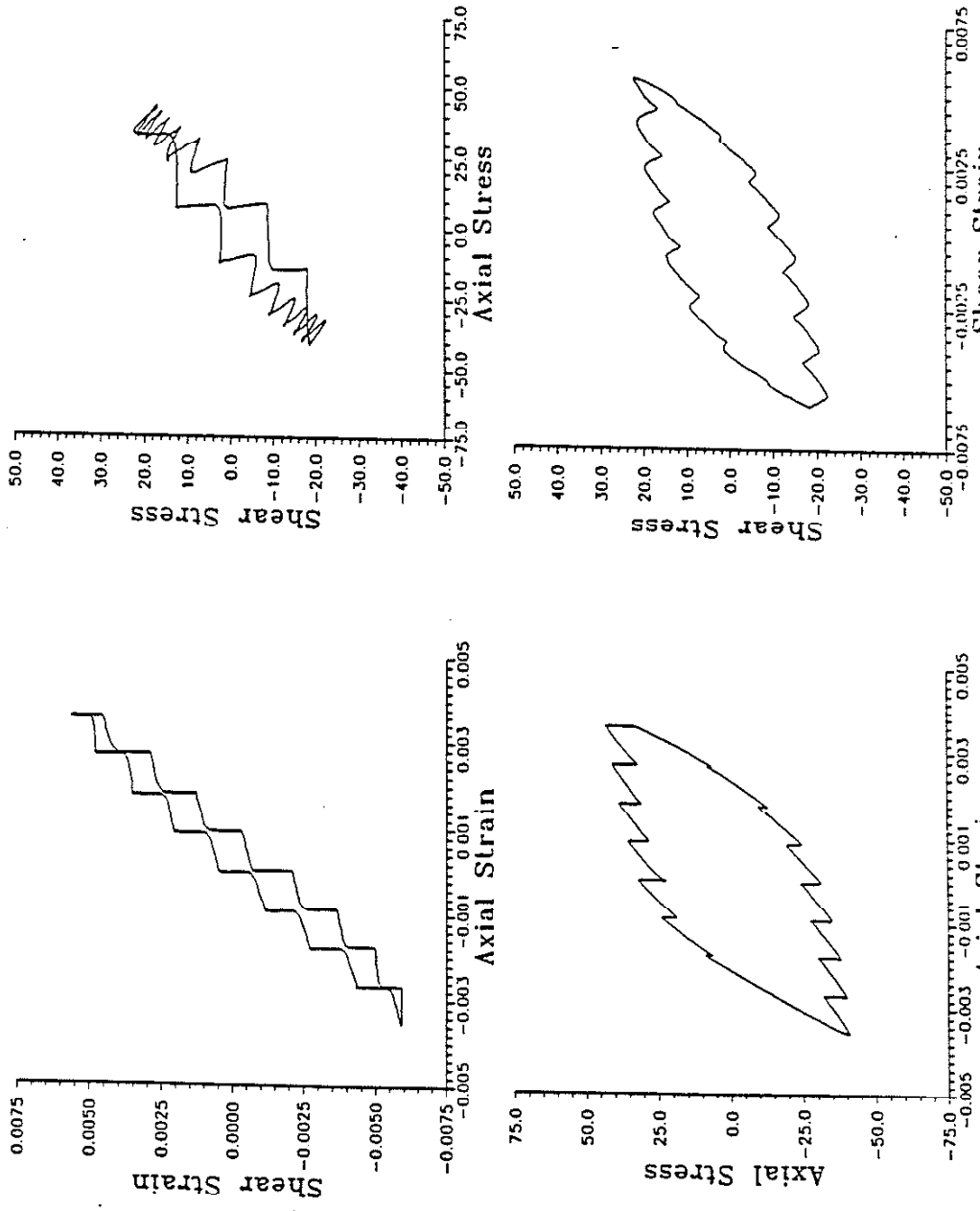

Figure 5.2b Predicted Stress-Strain Response for SS304 8 Stair-Step Path

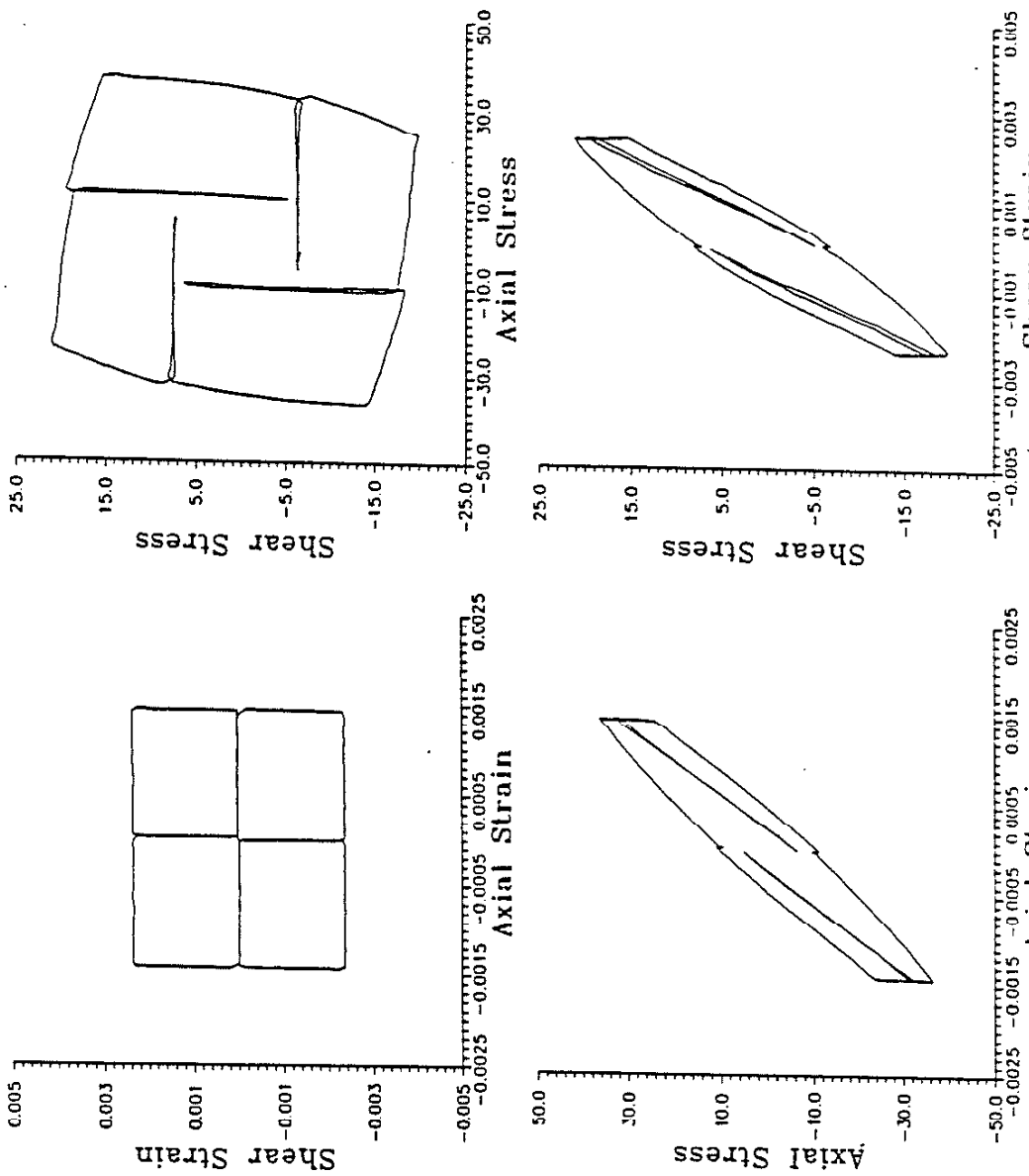

Figure 5.3a Measured Stress-Strain Response for SS304 4 Box Path

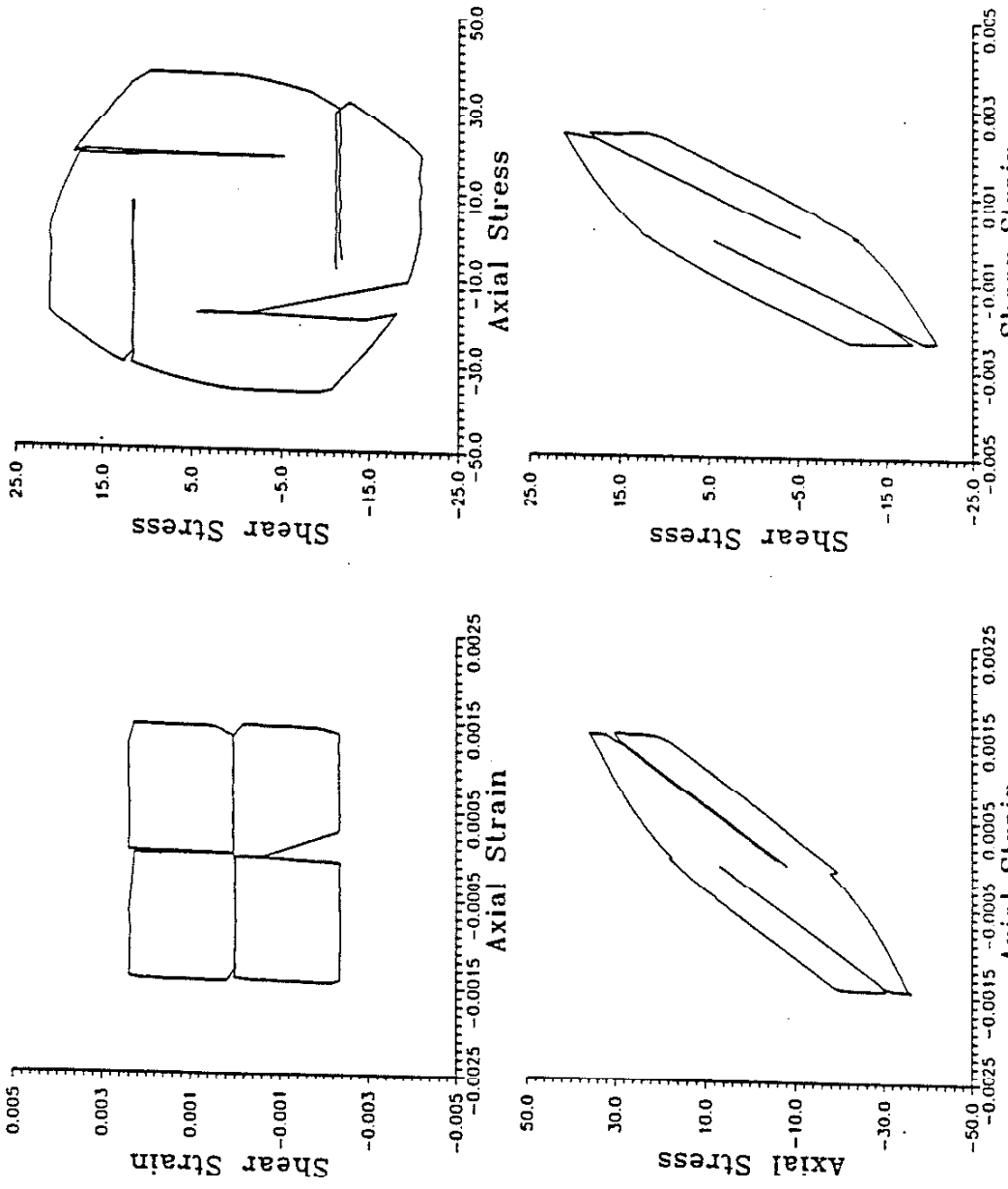

Figure 5.3b Predicted Stress-Strain Response for SS304 4 Box Path

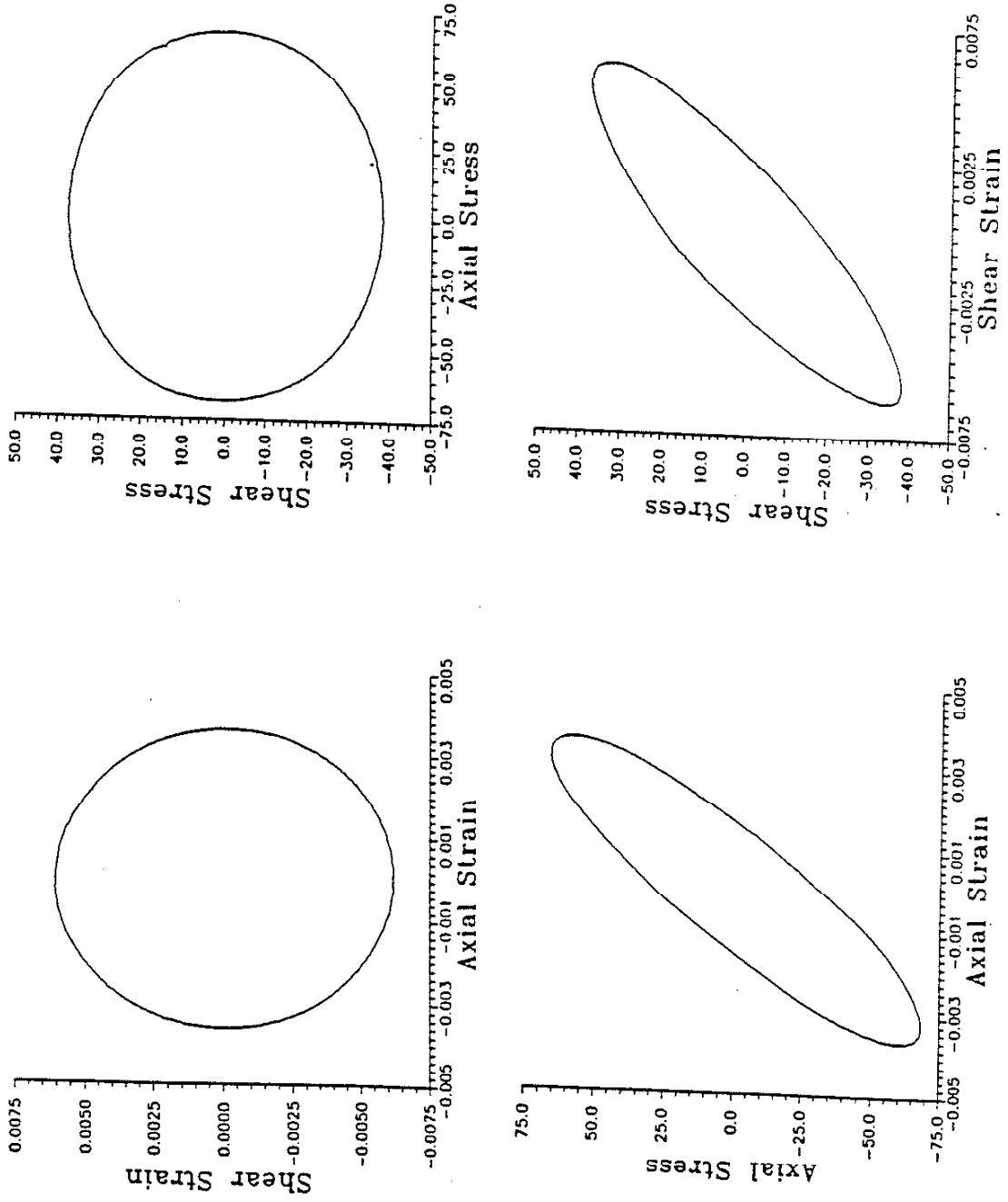

Figure 5.4a Measured Stress-Strain Response for SS304 90 Out-of Phase Path

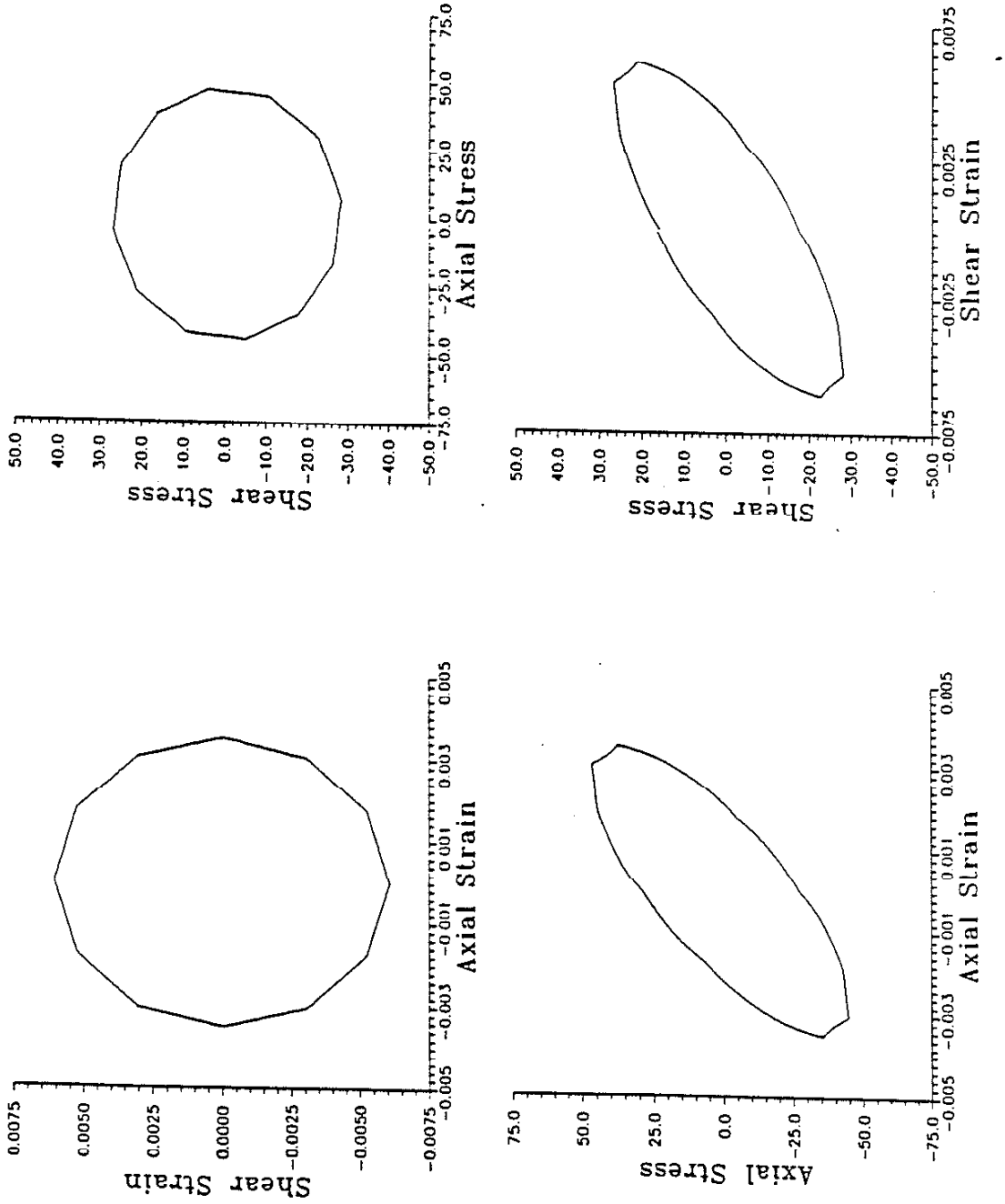

Figure 5.4b Predicted Stress-Strain Response for SS304 90 Out-of Phase Path

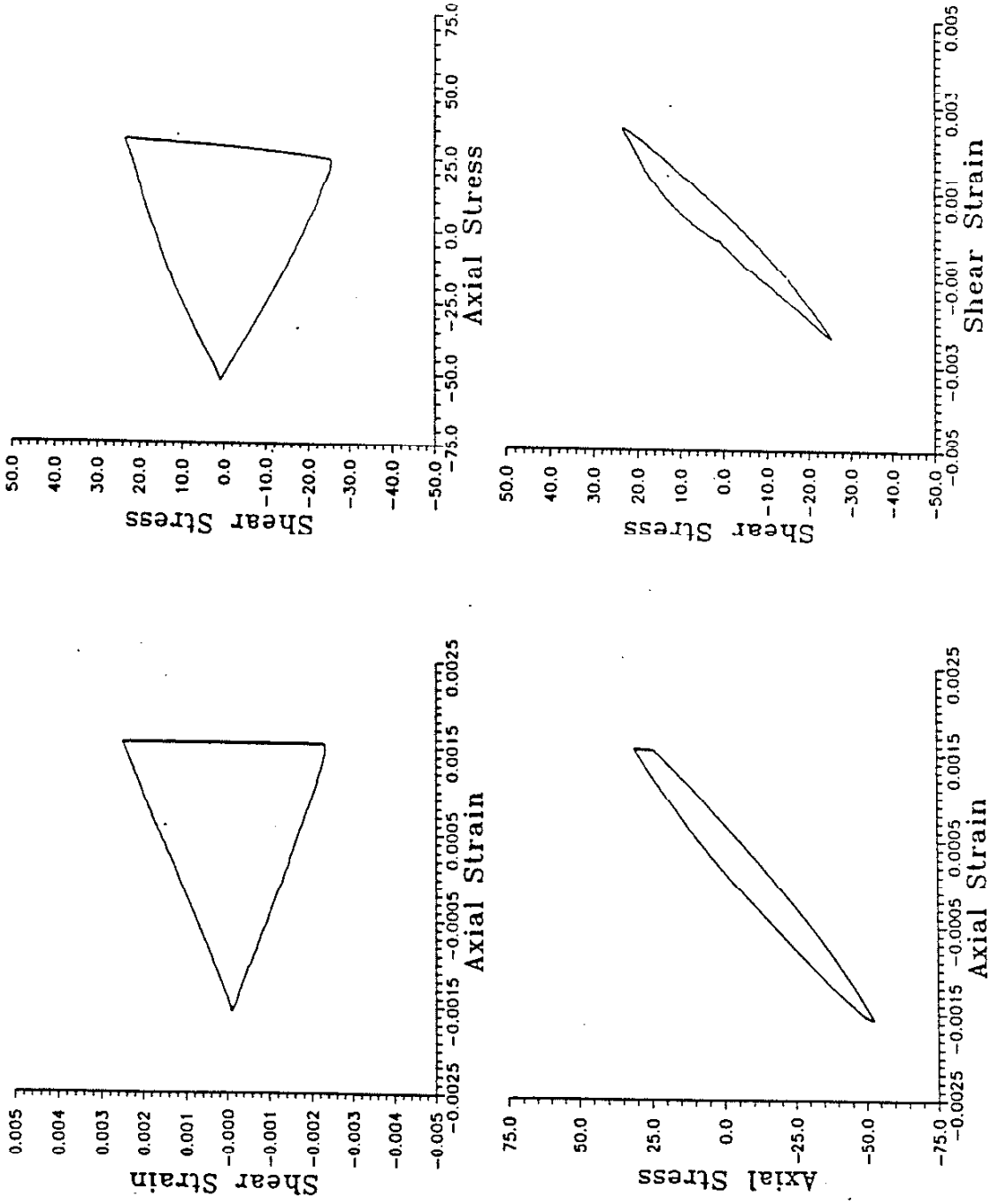

Figure 5.5a Measured (ε_{eff} = 0.0015 in/in) Stress-Strain Response for SAE 1045 Steel Triangle Path

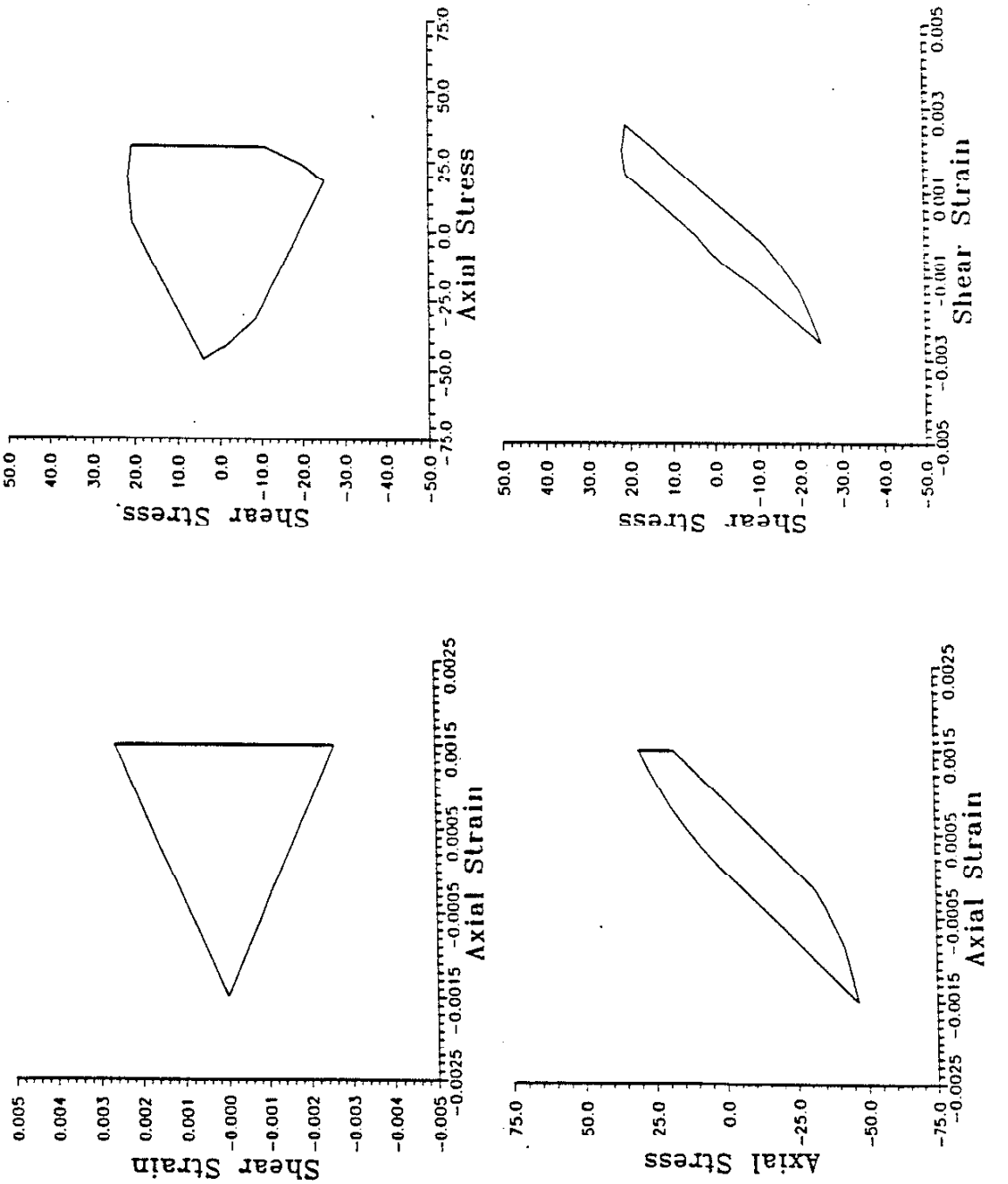

Figure 5.5b Predicted (ϵ_{eff} = 0.0015 in/in) Stress-Strain Response for SAE 1045 Steel Triangle Path

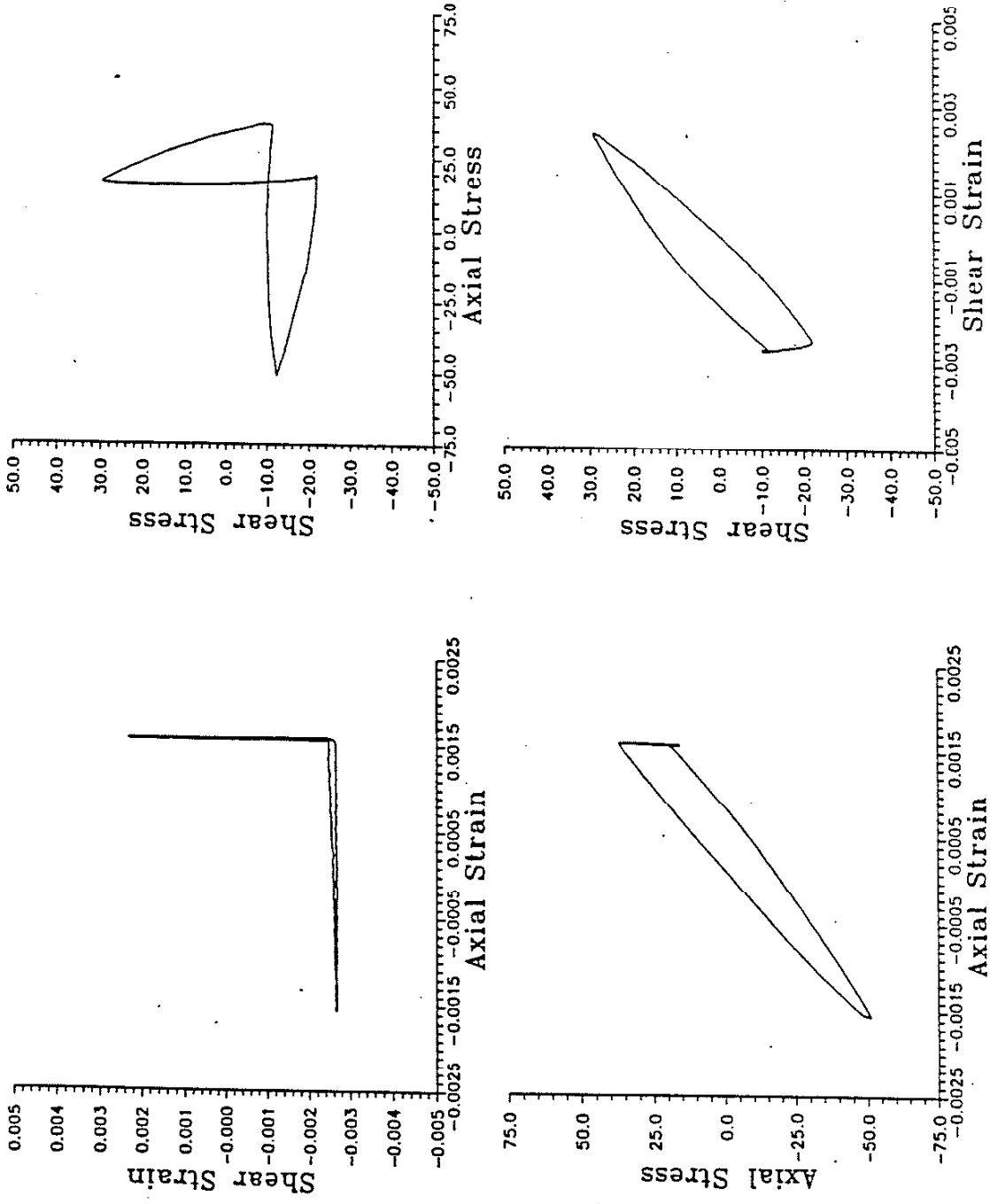

Figure 5.6a Measured (ε_{eff} = 0.0015 in/in) Stress-Strain Response for SAE 1045 Steel Right Angle Path

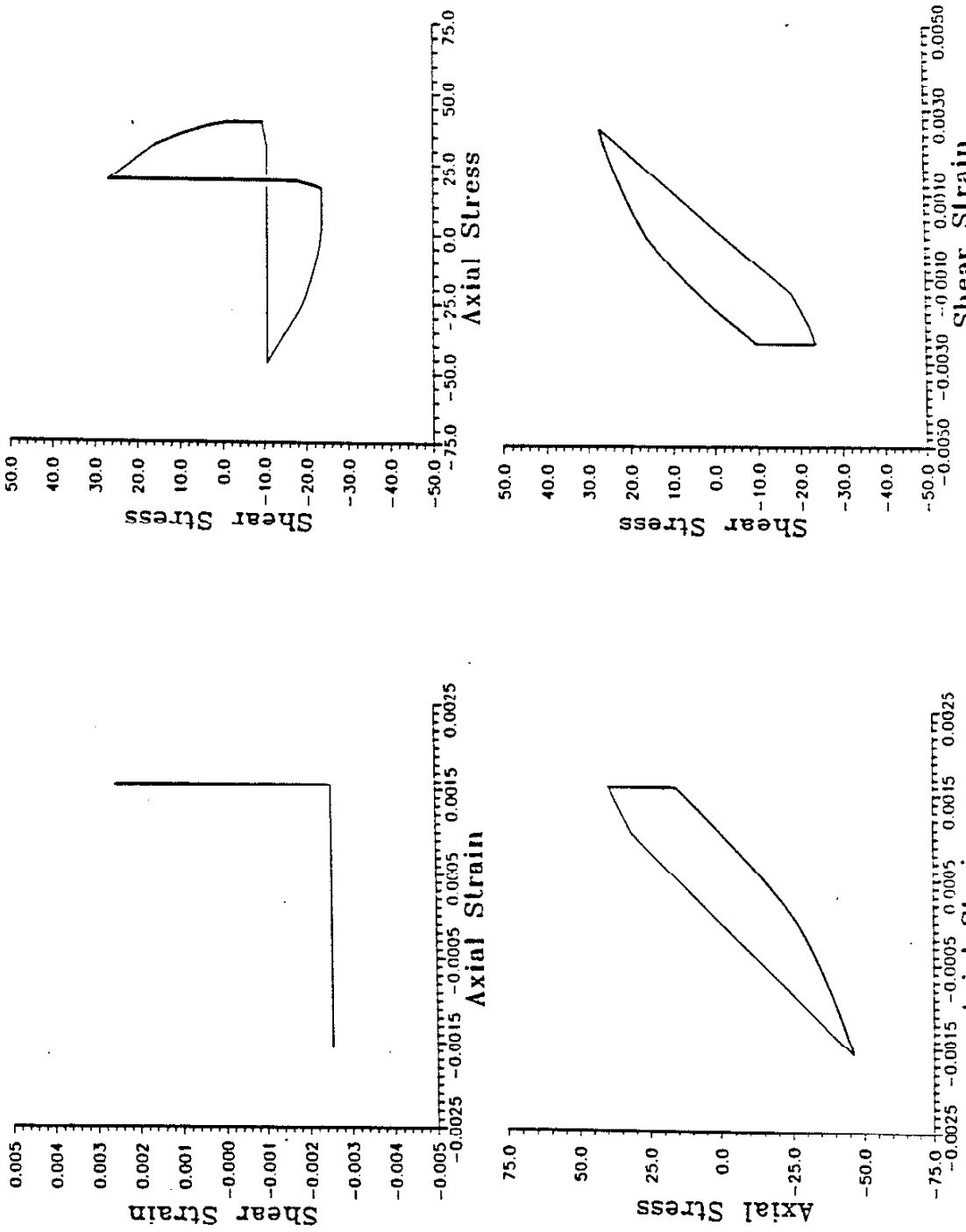

Figure 5.6b Predicted (ε_{eff} = 0.0015 in/in) Stress-Strain Response for SAE 1045 Steel Right Angle Path

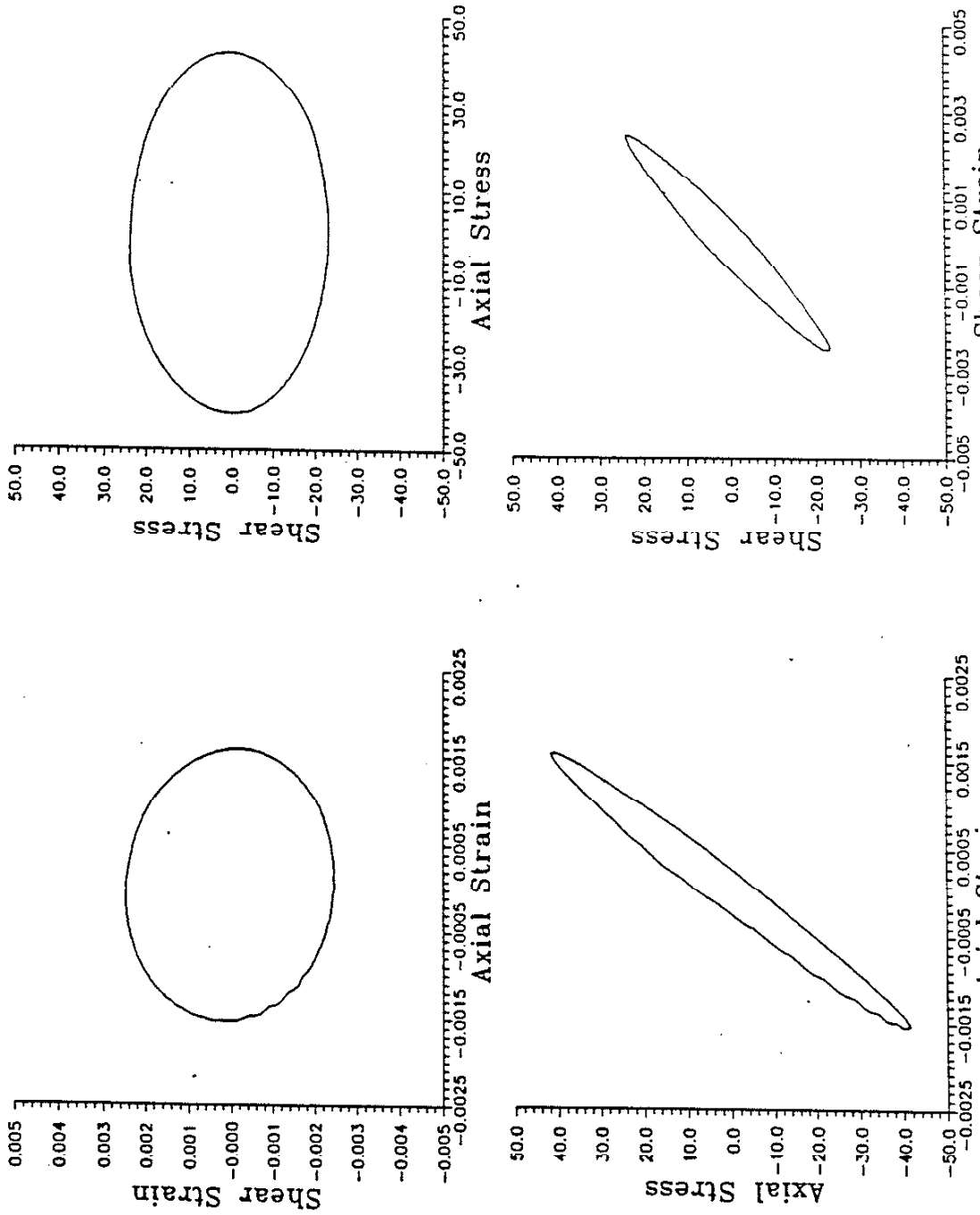

Figure 5.7a Measured Stress-Strain Response for SAE 1045 90° Out-of- Phase Path

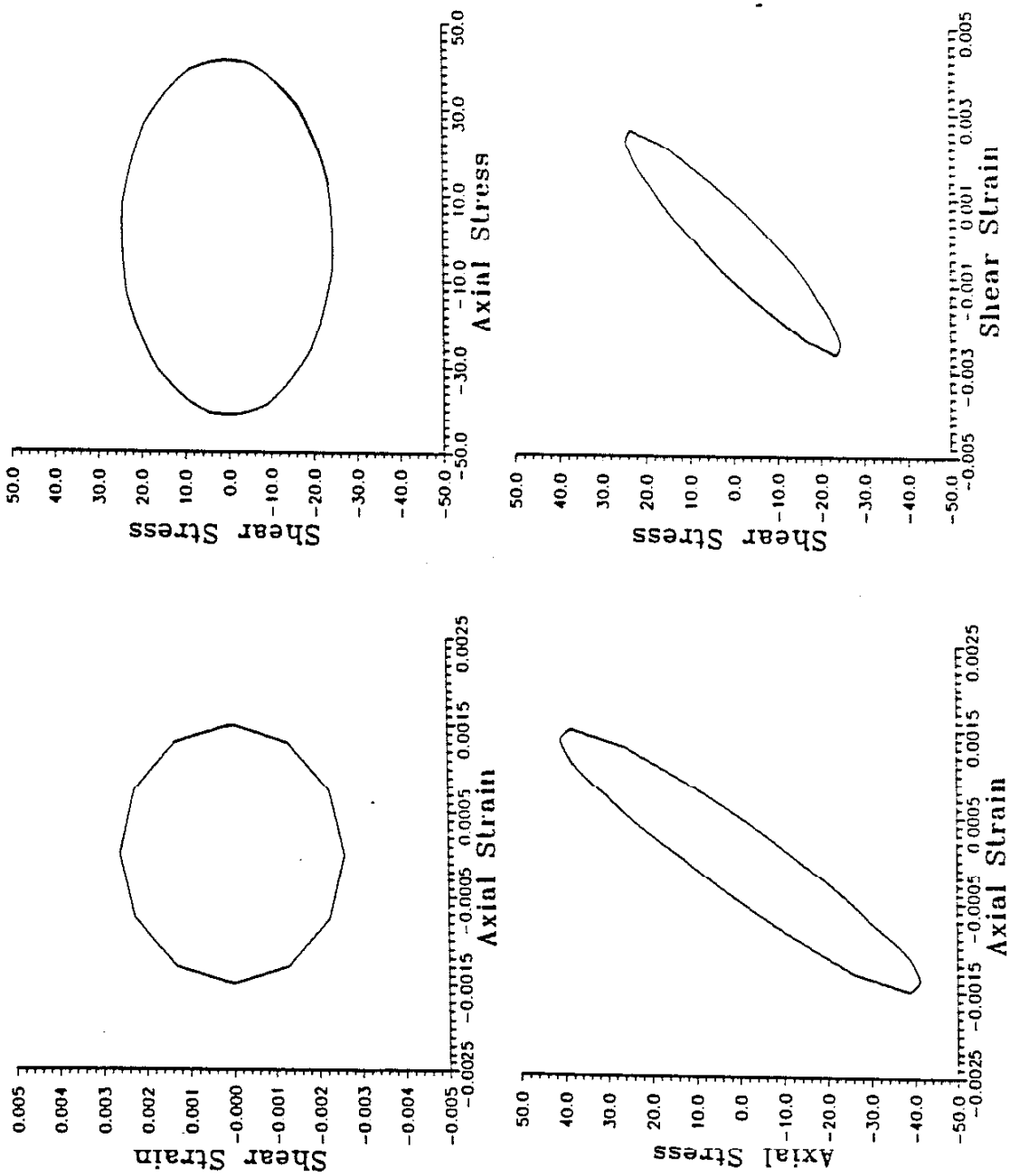

Figure 5.7b Predicted Stress-Strain Response for SAE 1045 90° Out-of-Phase Path

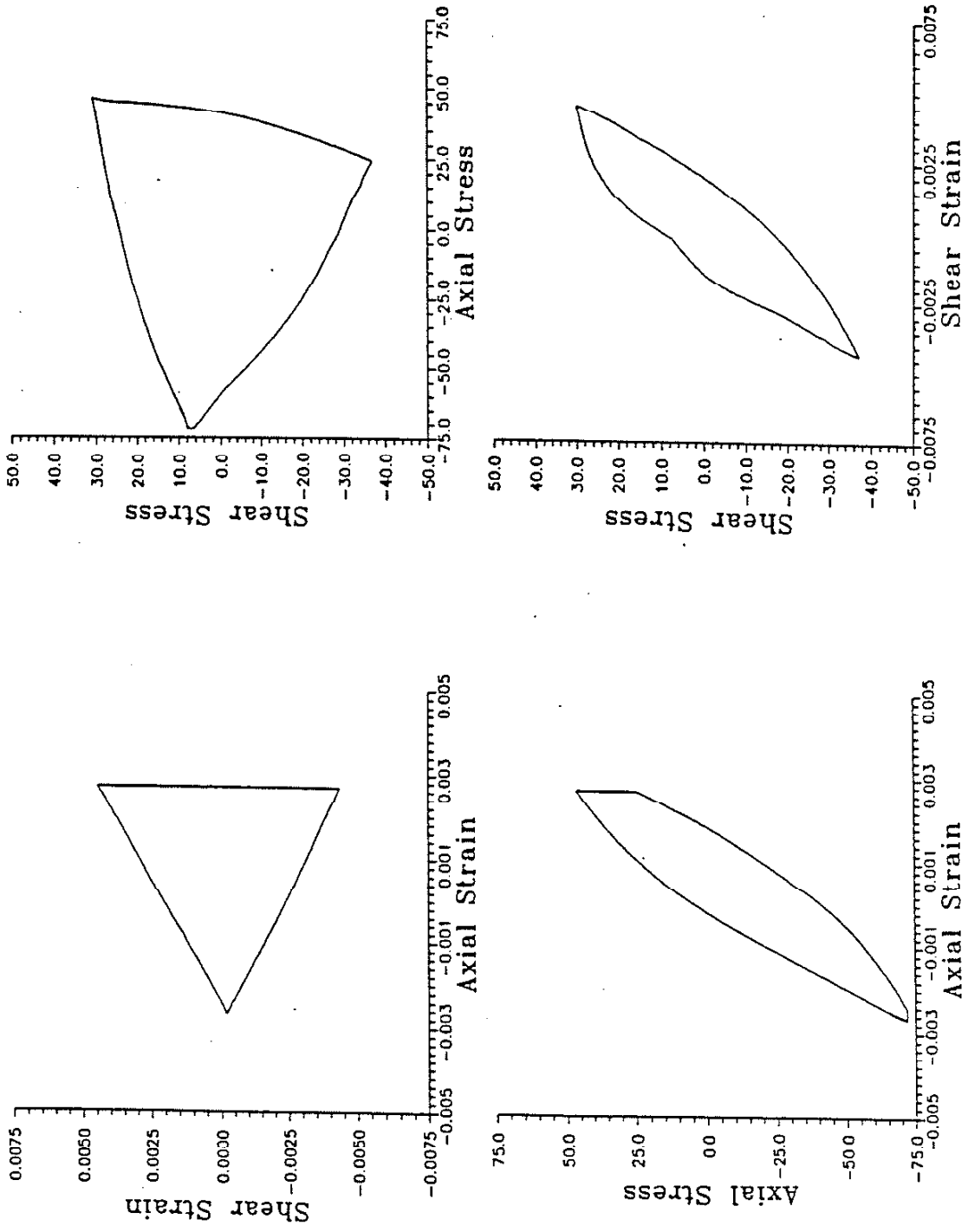

Figure 5.8a Measured (ε_{eff} = 0.0025 in/in) Stress-Strain Response for SAE 1045 Steel Triangle Path

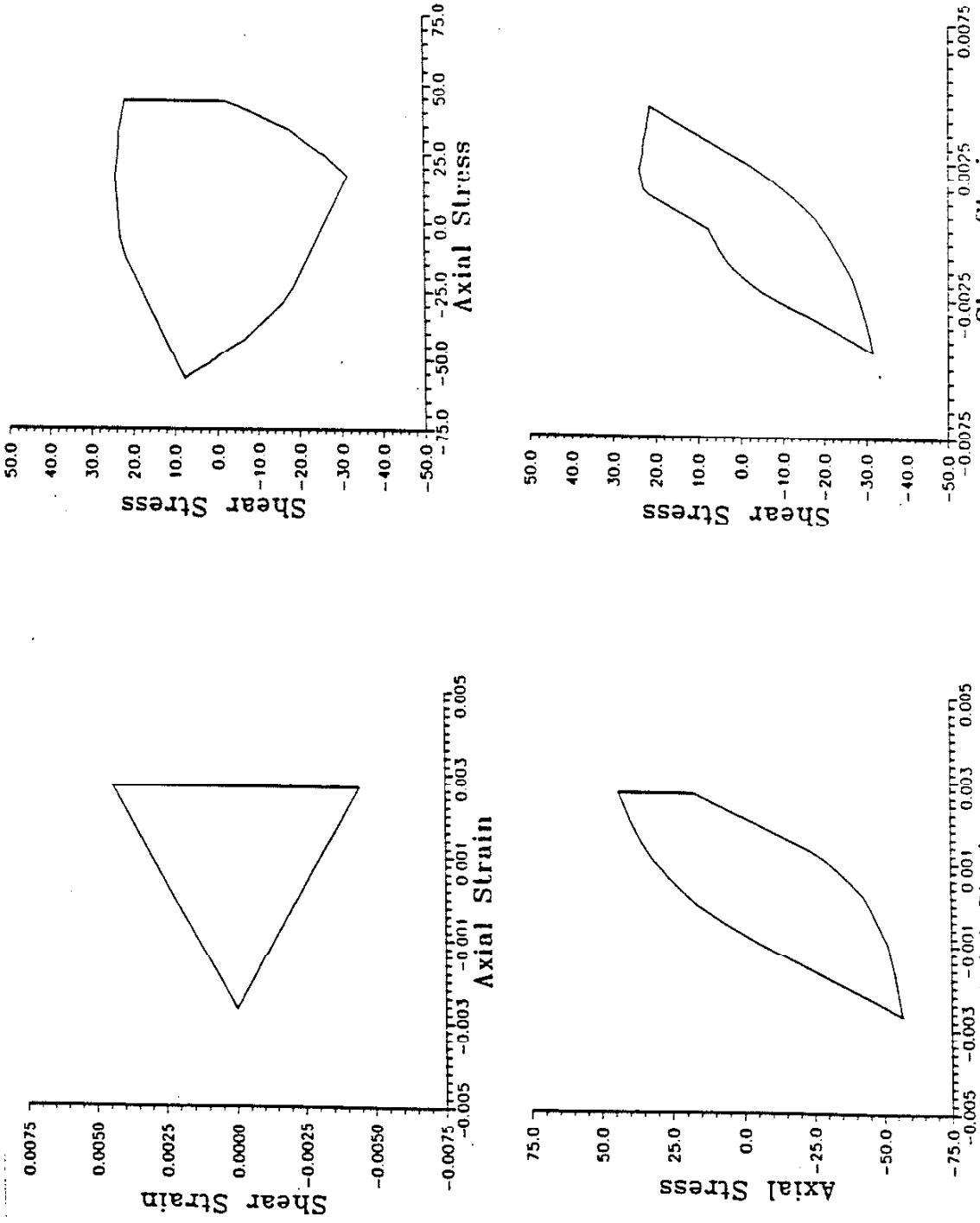

Figure 5.8b Predicted (ε_{eff} = 0.0025 in/in) Stress-Strain Response for SAE 1045 Steel Triangle Path

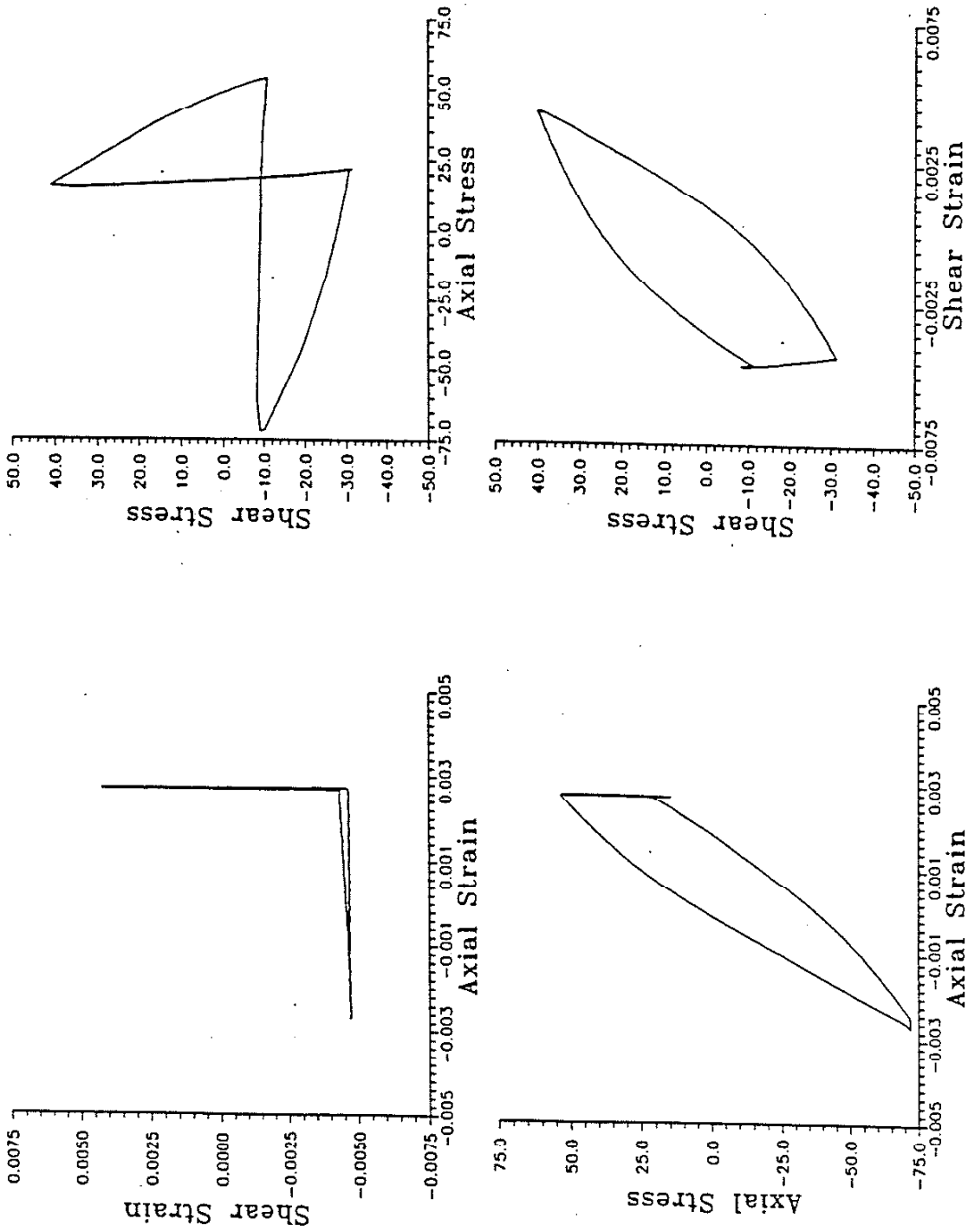

Figure 5.9a Measured (ϵ_{eff} = 0.0025 in/in) Stress-Strain Response for SAE 1045 Steel Right Angle Path

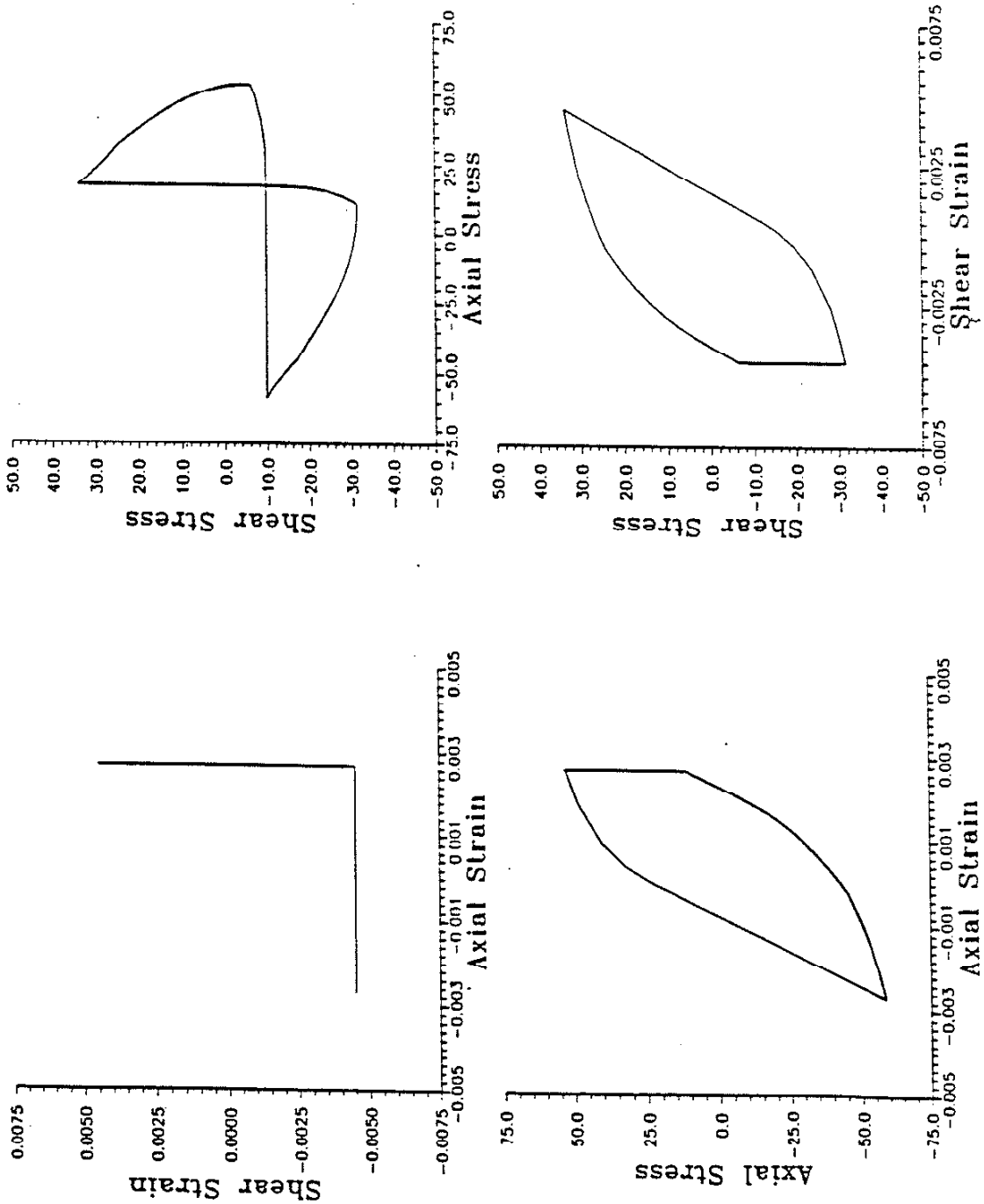

Figure 5.9b Predicted (ε_{eff} = 0.0025 in/in) Stress-Strain Response for SAE 1045 Steel Right Angle Path

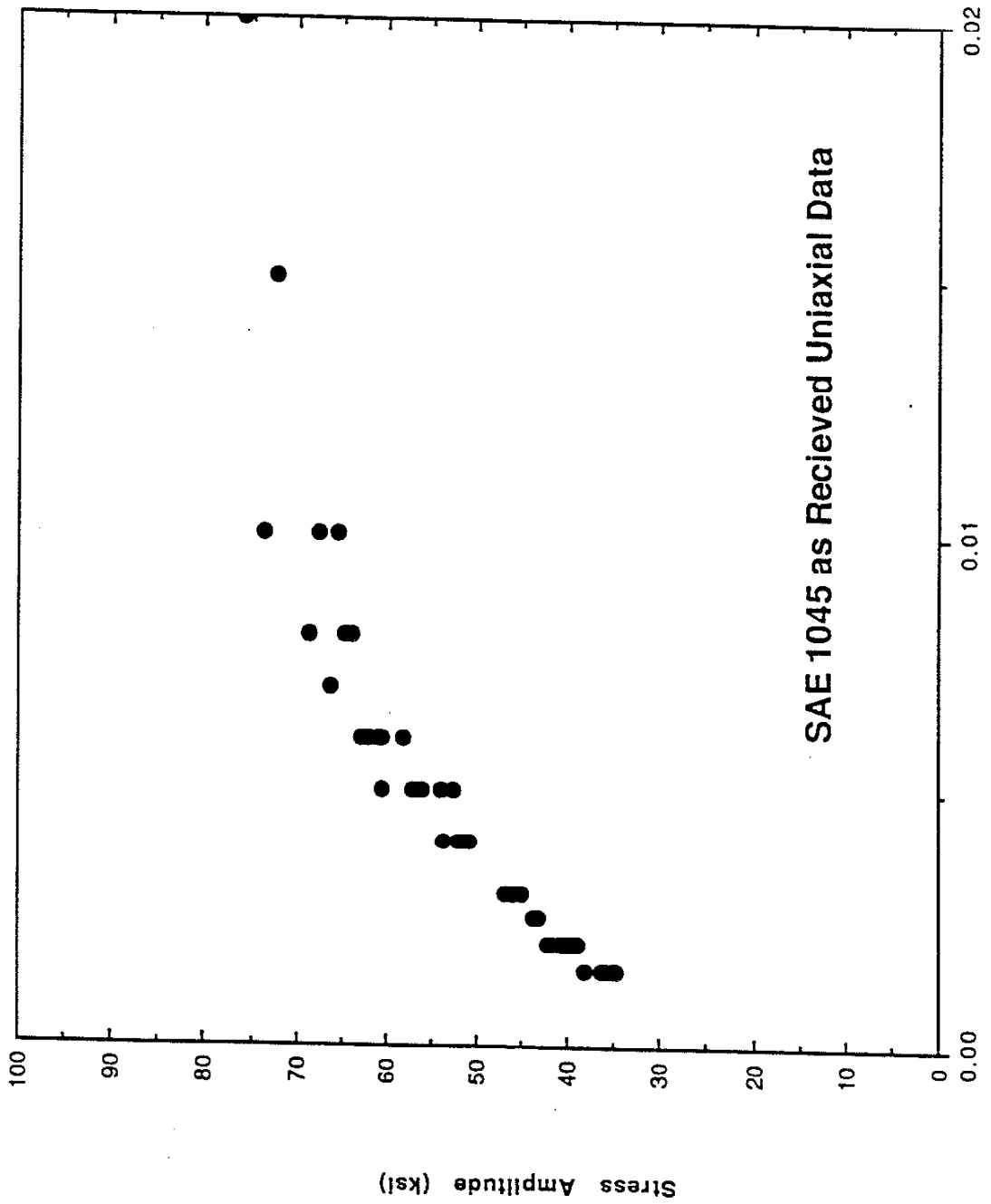

Figure 5.10 Cyclically Stable Uniaxial Stress-Strain Response of SAE 1045 Steel

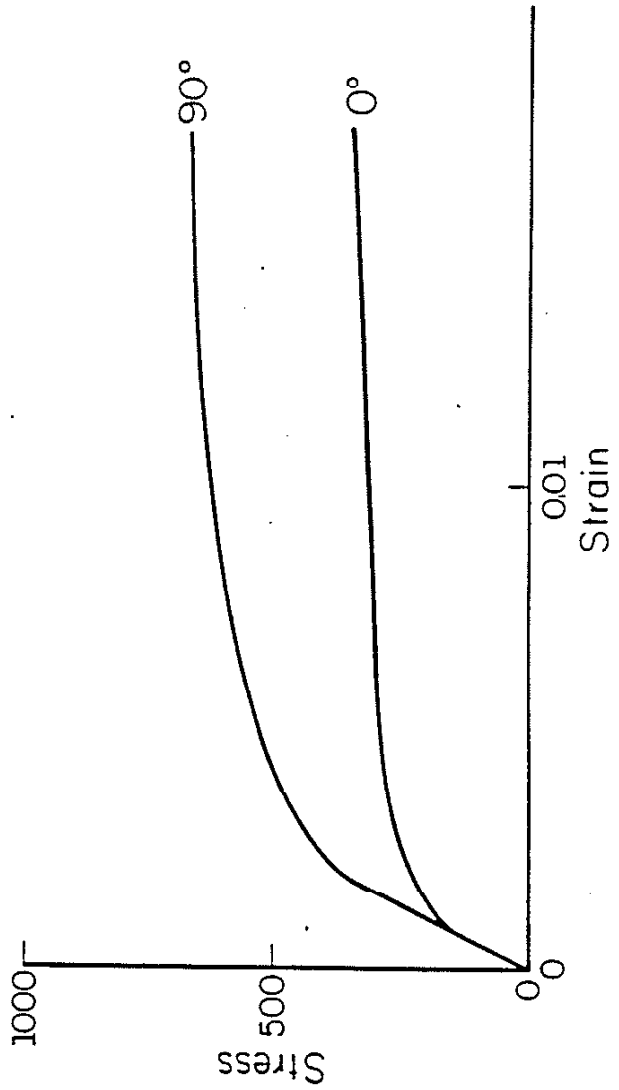

Figure 5.11 Cyclically Stable Uniaxial Stress-Strain Response of SS304 for Uniaxial and 90° Out-of-Phase Loading

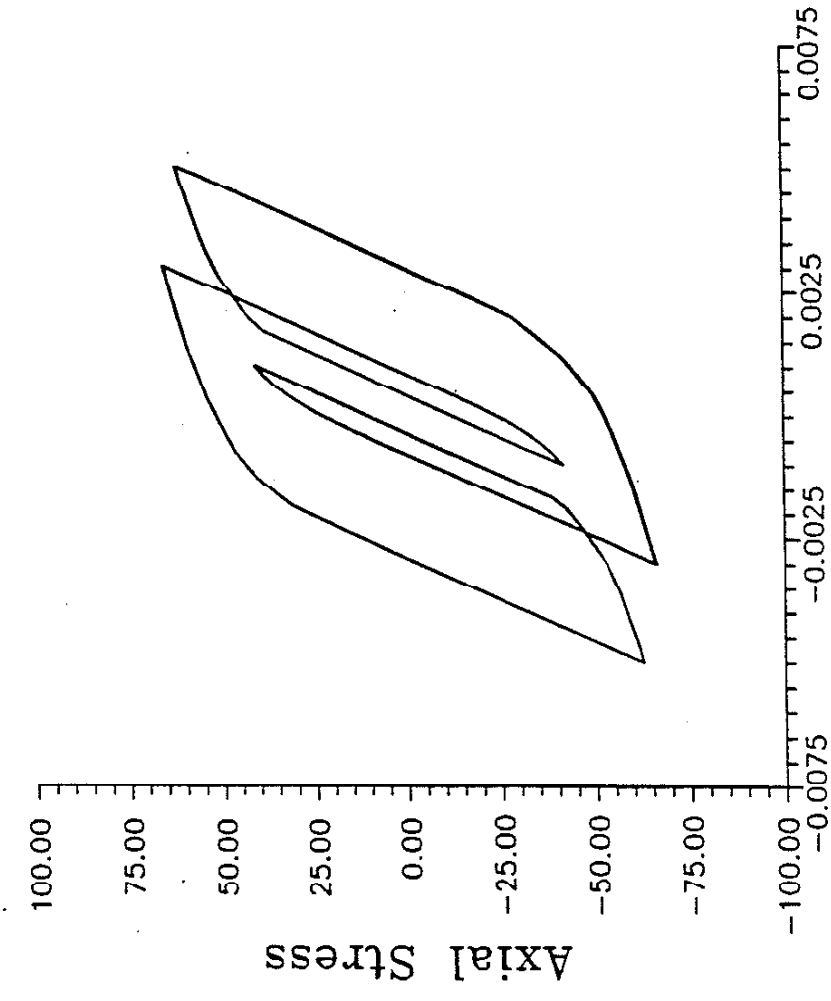

Figure 5.12 Predicted Uniaxial Variable Amplitude Stress-Strain Response Using Two Surface Model

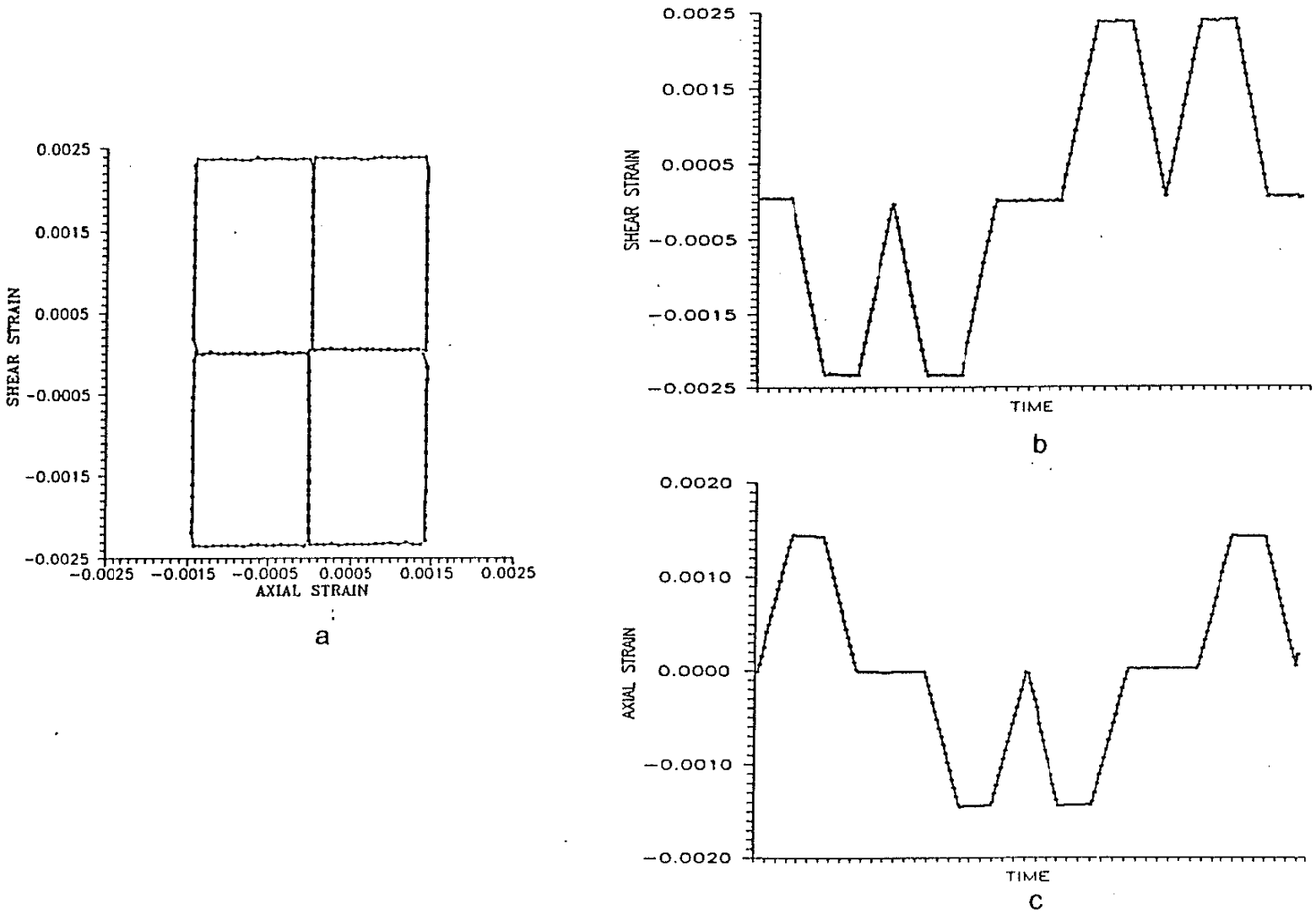

Figure 5.13 a) Tension-Torsion Strain Controlled "Four Box Loading Path"
b) Shear Strain History
c) Axial Strain History

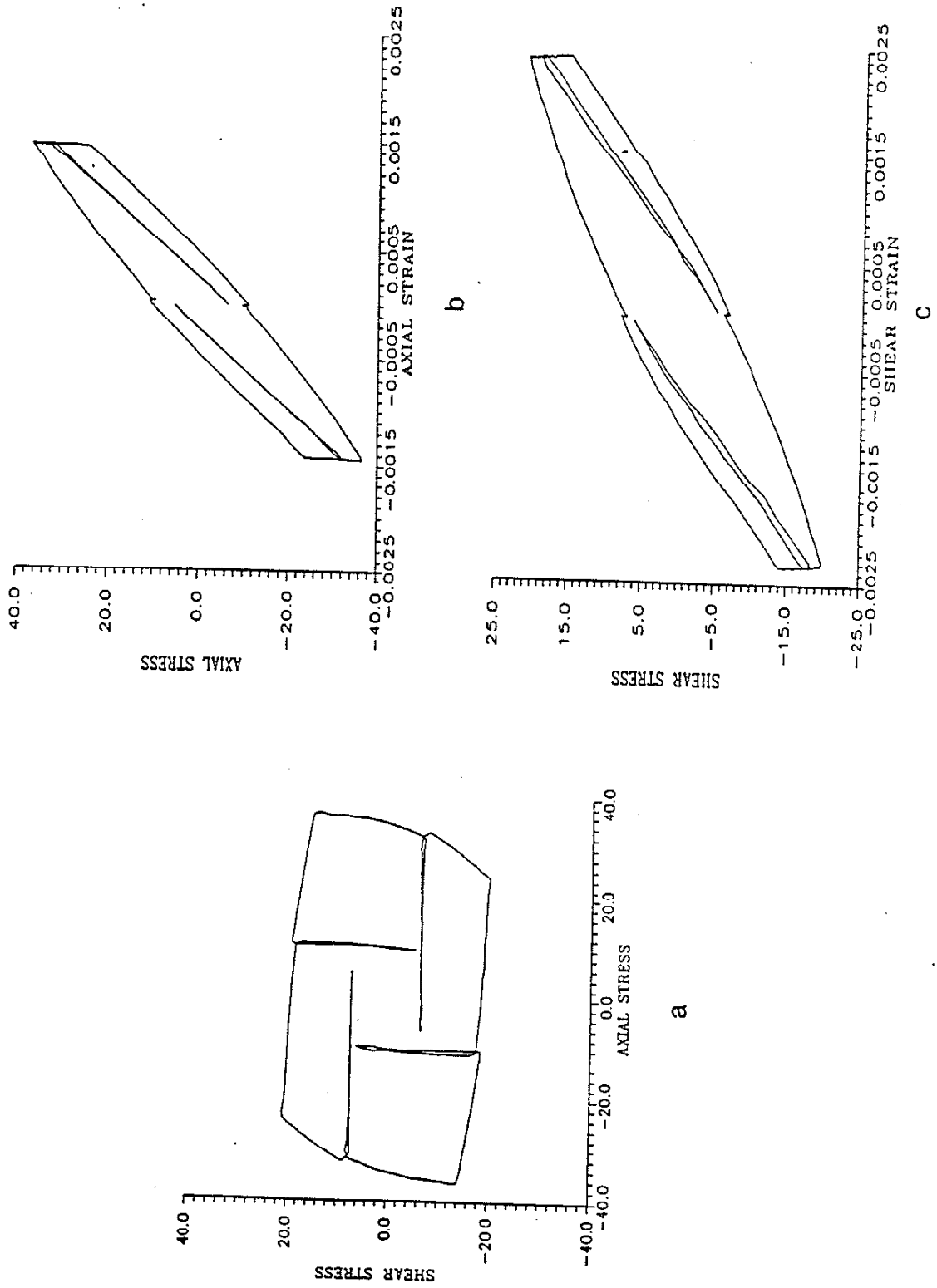

Figure 5.14 a) Axial-Shear Stress Response
b) Axial Stress-Strain Response
c) Shear Stress-Strain Response

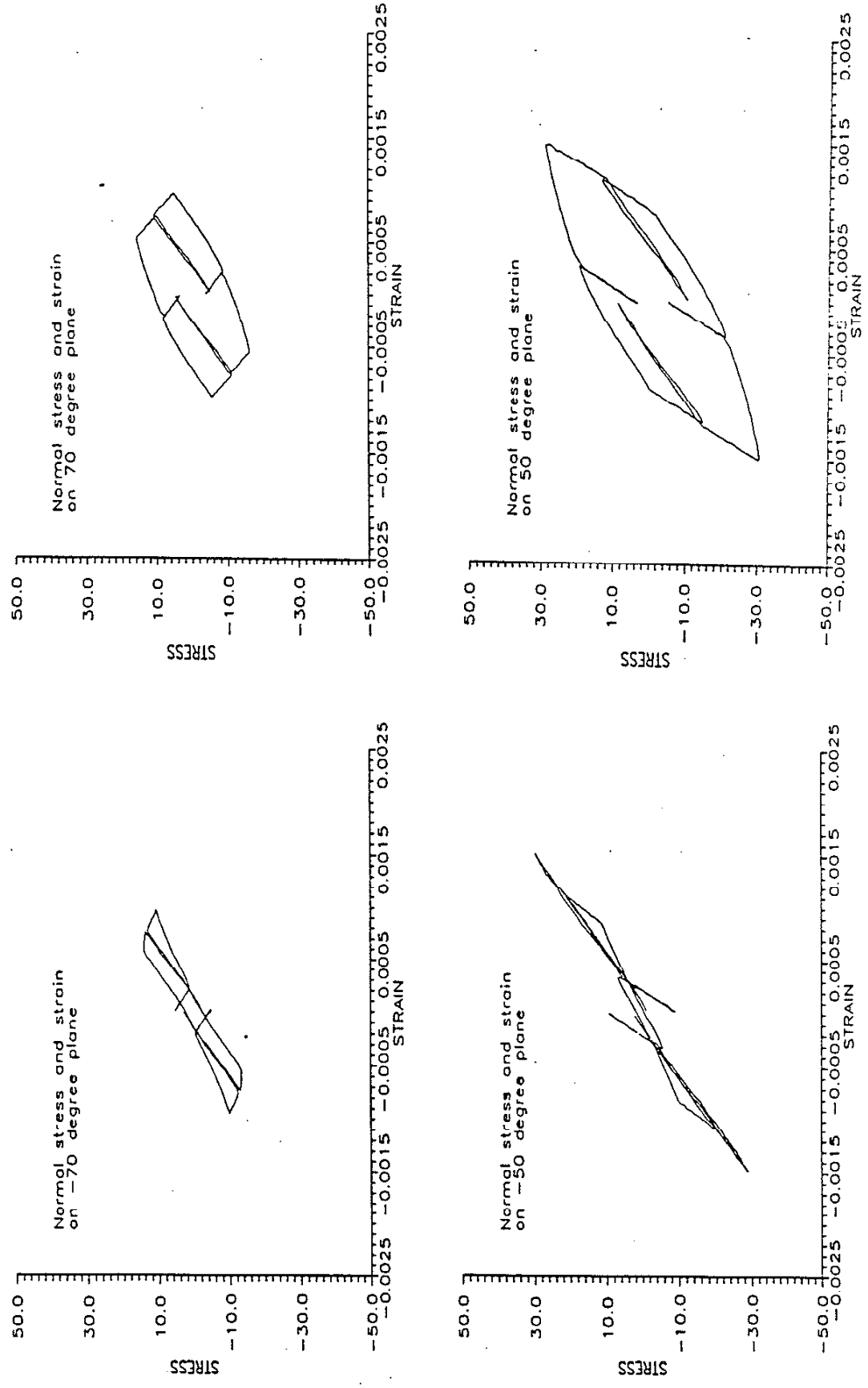

Figure 5.15 a) Normal Stress-Strain Response on Planes Rotated -70°, 70°, -50°, 50° from the Horizontal

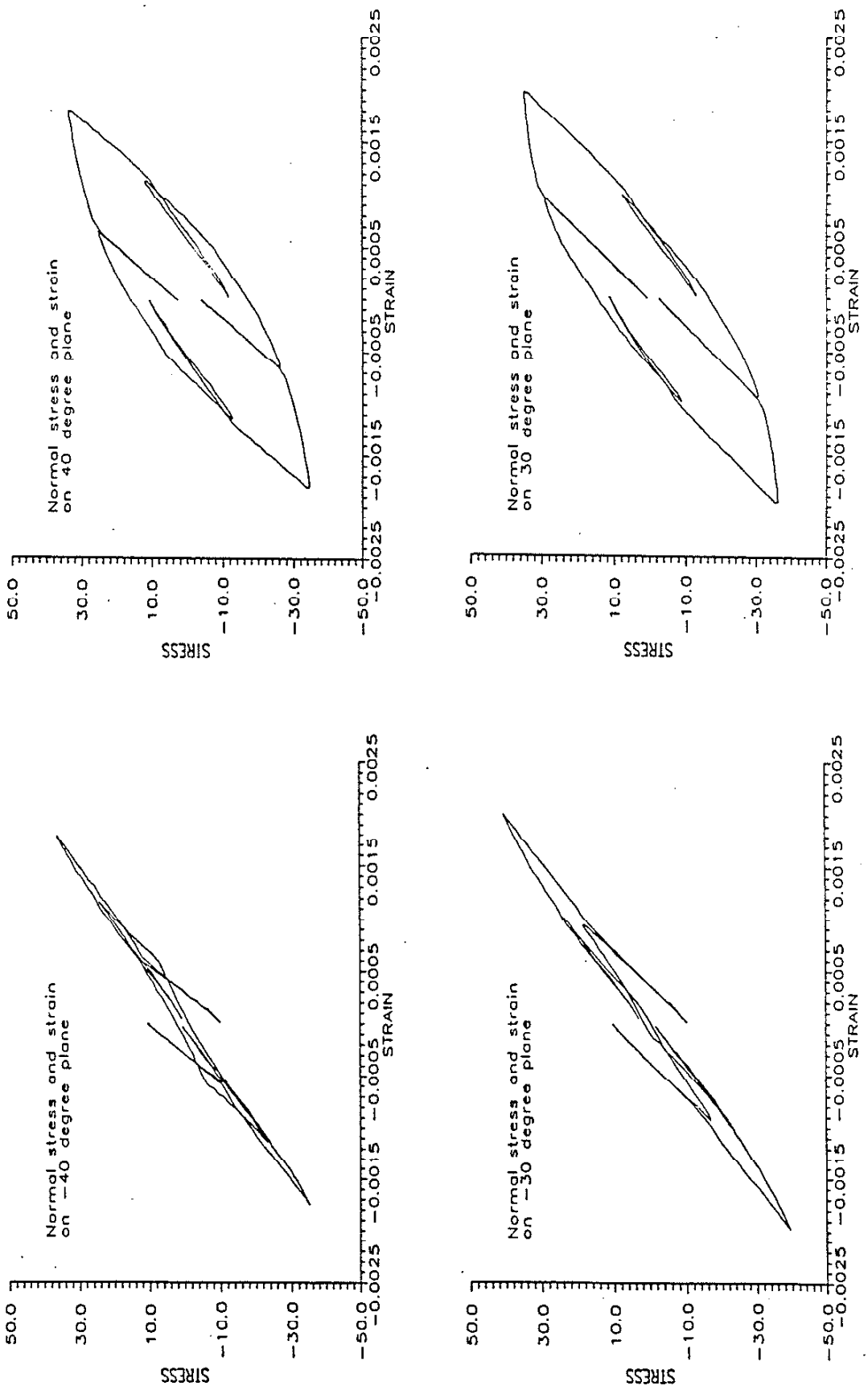

Figure 5.15 b) Normal Stress-Strain Response on Planes Rotated -40°, 40°, -30°, 30° from the Horizontal

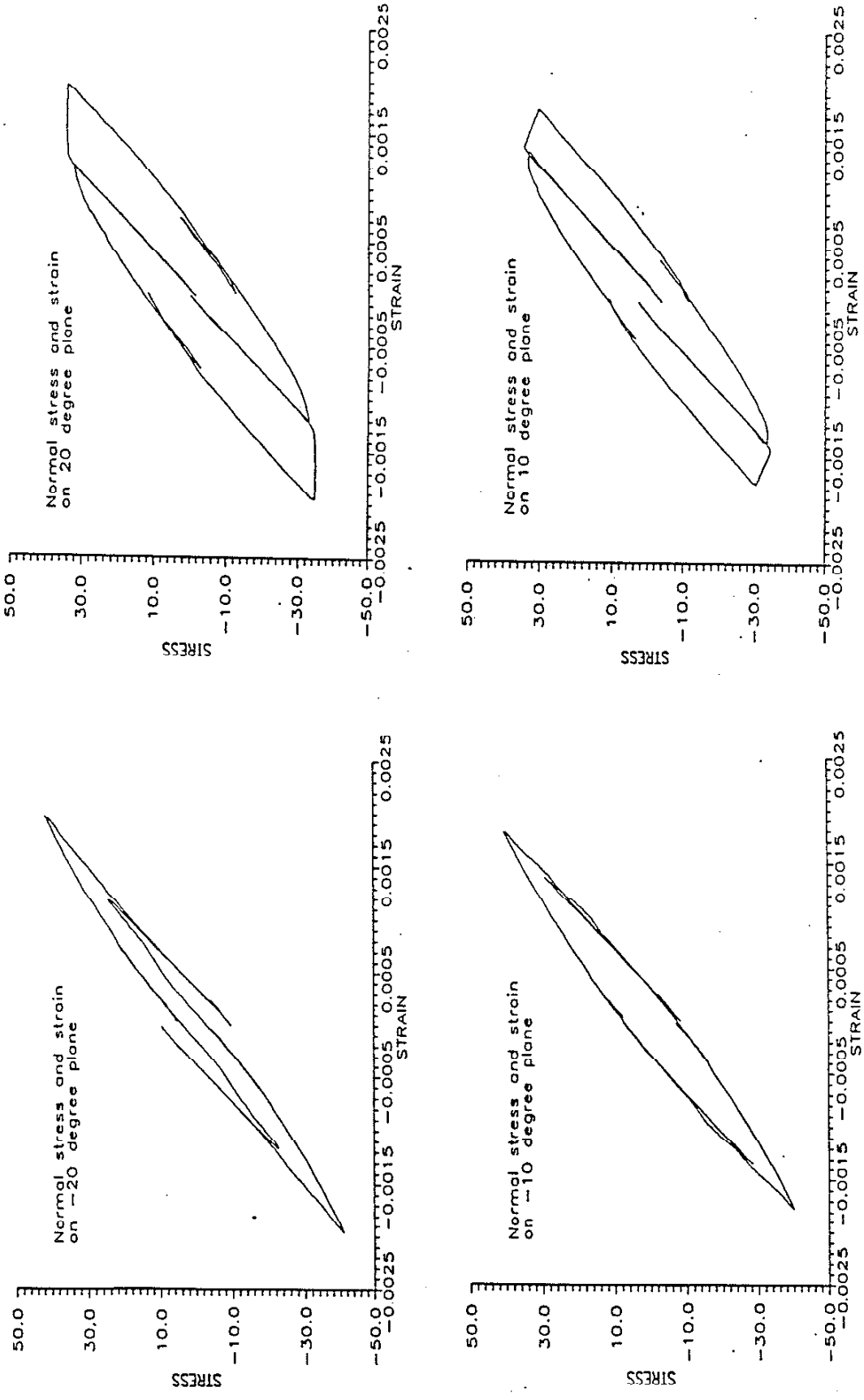

Figure 5.15 c) Normal Stress-Strain Response on Planes Rotated -20°, 20°, -10°, 10° from the Horizontal

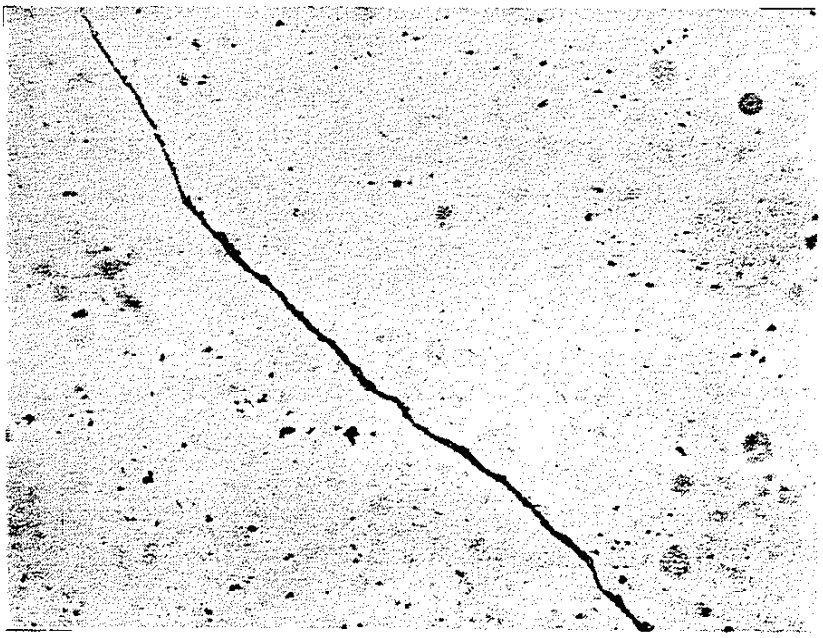

Figure 5.16 Cracking Observed in Thin Wall Tube Subjected to Four Box Loading Path

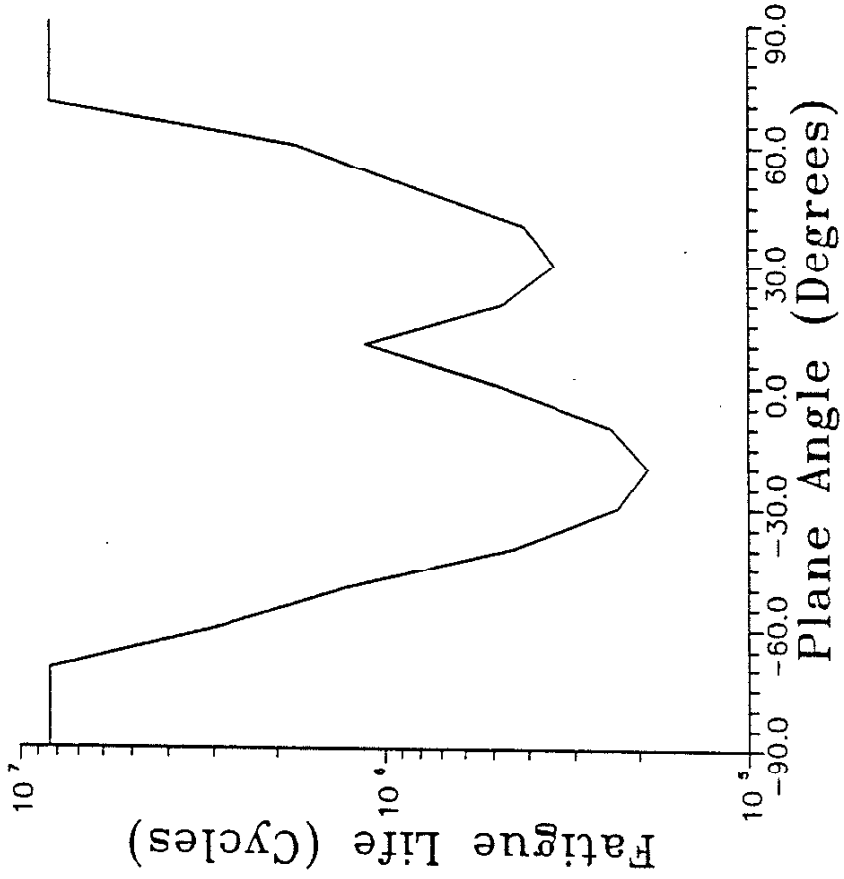

Figure 5.17 Life Prediction Results from Computer Model

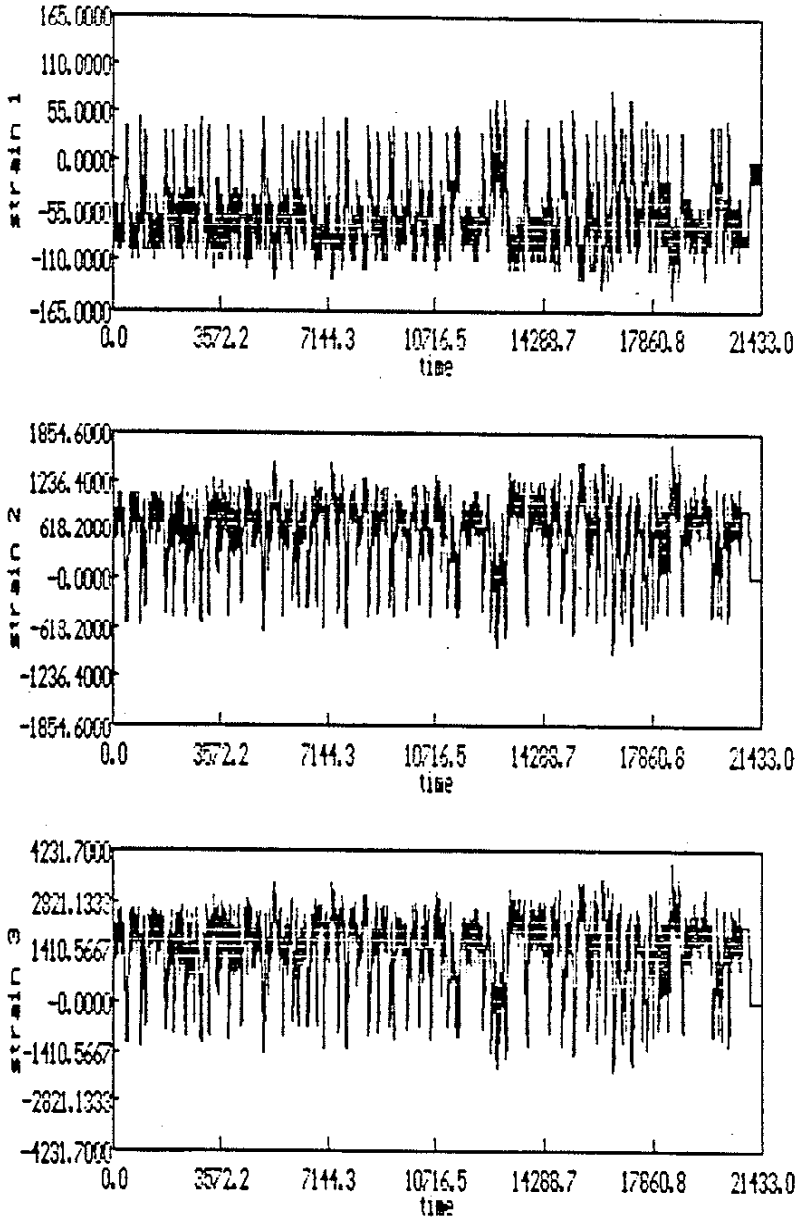

Figure 5.18 a) Strain Histories Obtained from the Strain Gauge Rosette Oriented at 0, 45, 90 Degrees in Bending Test

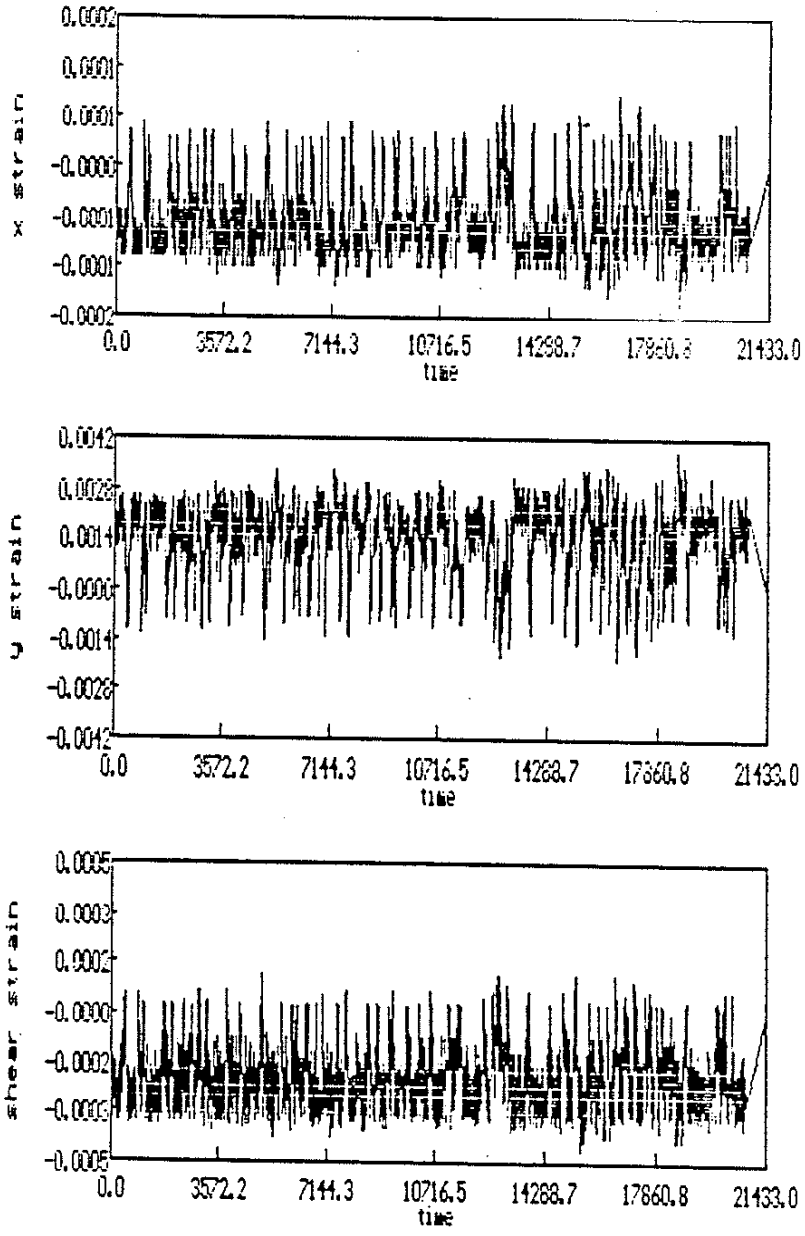

Figure 5.18 b) ε_x, ε_y and γ_{xy} Strain Histories from the Strain Gauge Rosette Oriented at 0, 45, 90 Degrees in Bending Test

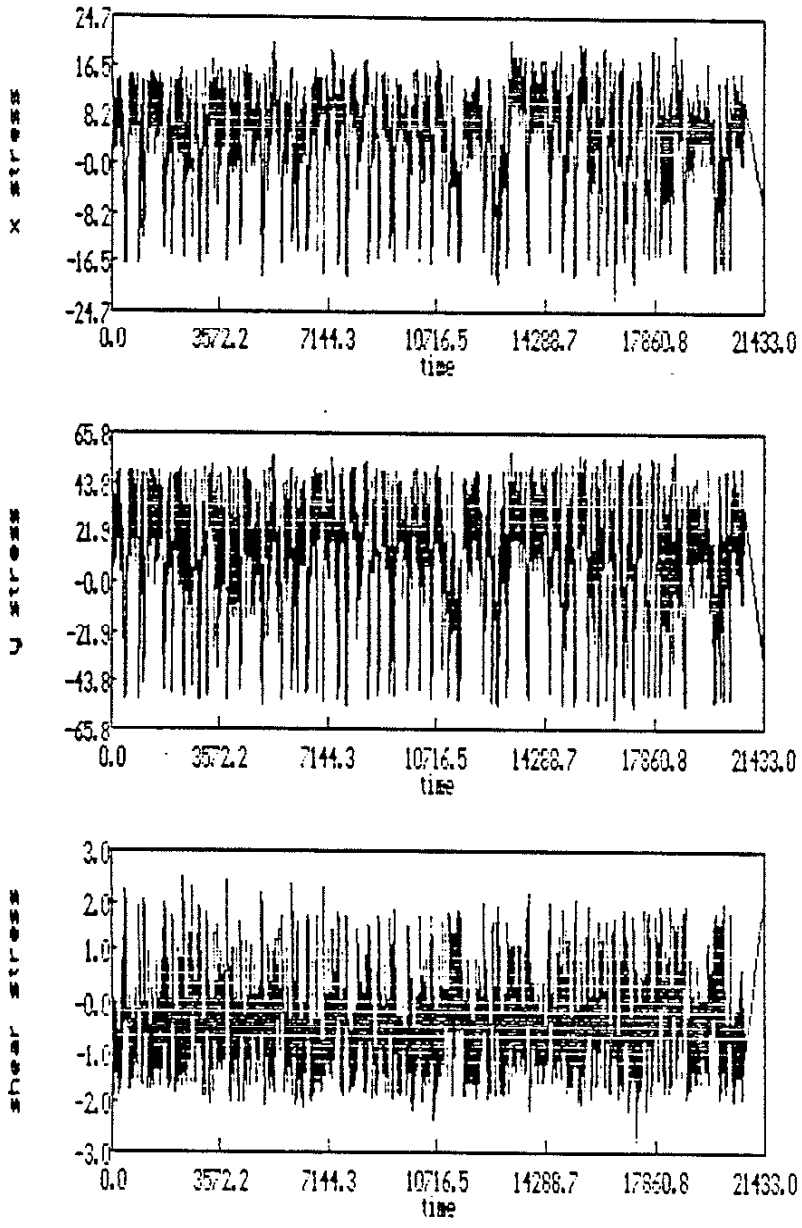

Figure 5.18 c) σ_x, σ_y and τ_{xy} Stress Histories Predicted from the Strain Gauge Rosette Oriented at 0, 45, 90 Degrees in Bending Test

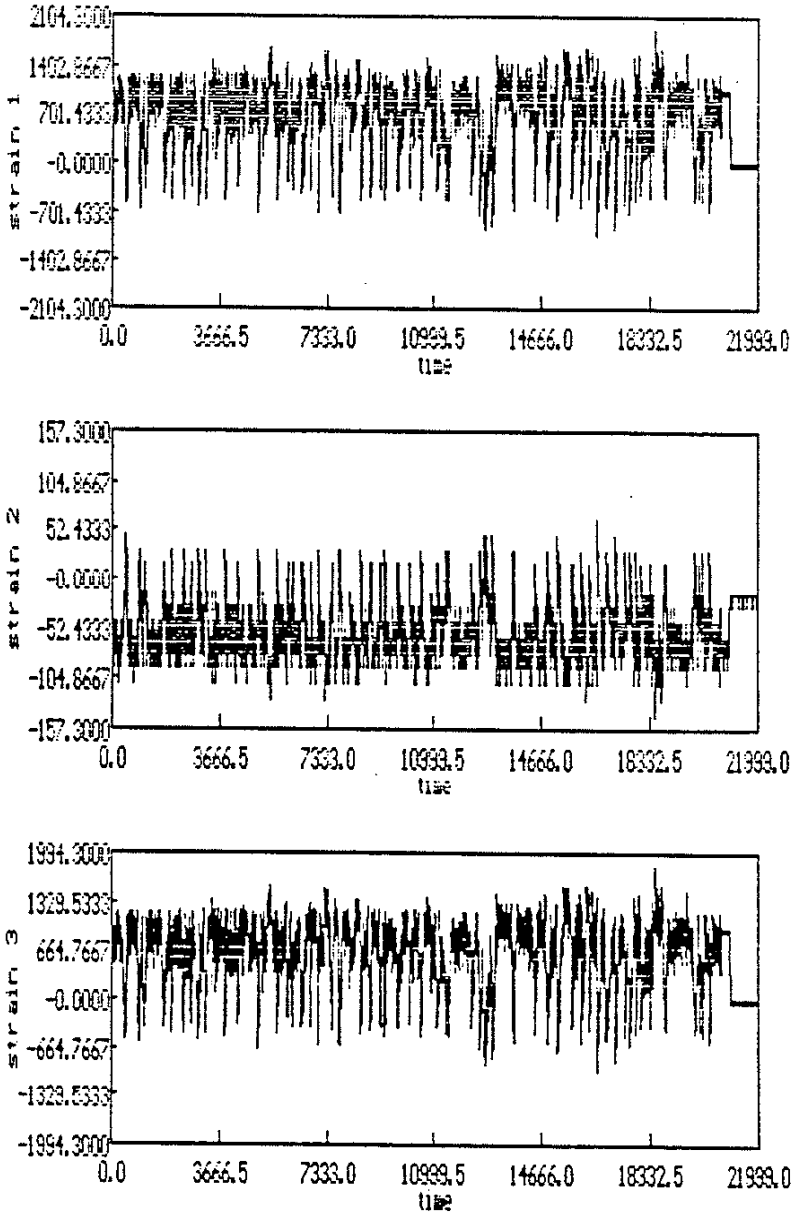

Figure 5.19 a) Strain Histories Obtained from the Strain Gauge Rosette Oriented at -45, 0, 45 Degrees in Bending Test

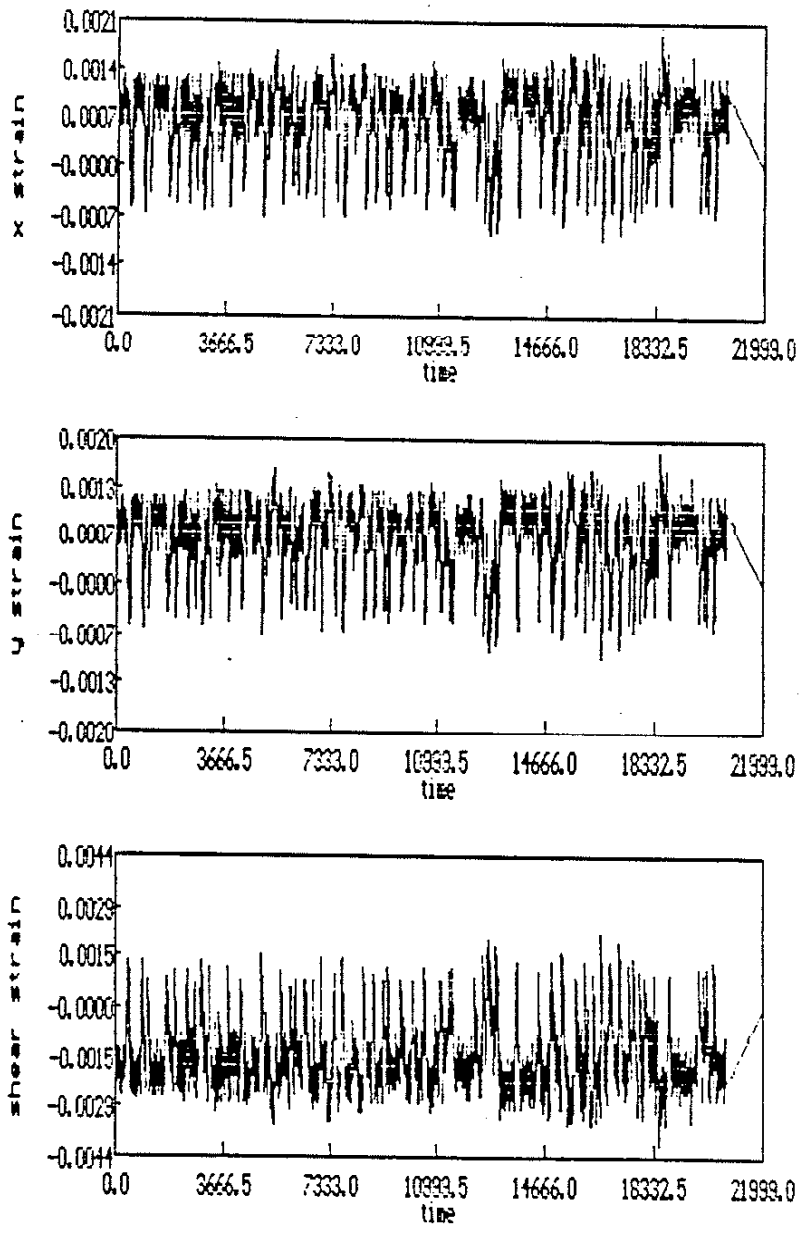

Figure 5.19 b) ε_x, ε_y and γ_{xy} Strain Histories from the Strain Gauge Rosette Oriented at -45, 0, 45 Degrees in Bending Test

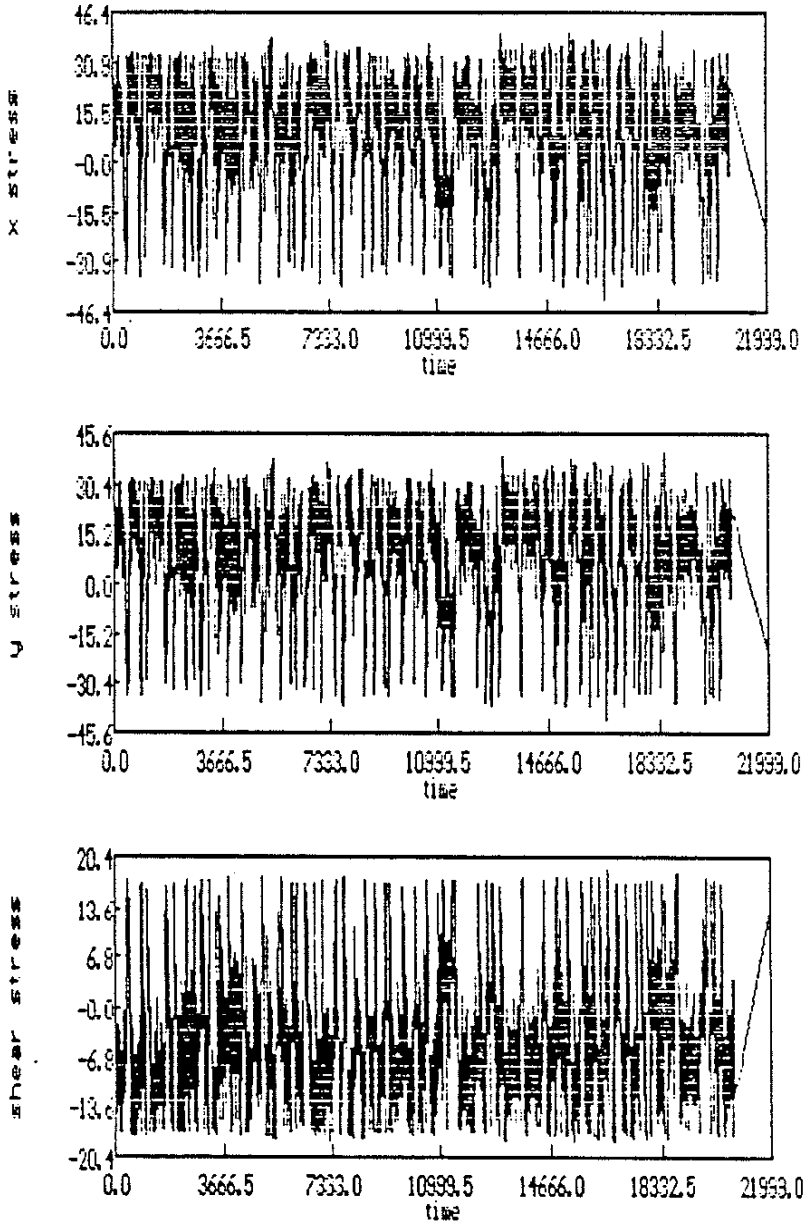

Figure 5.19 c) σ_x, σ_y and τ_{xy} Stress Histories Predicted from the Strain Strain Gauge Rosette Oriented at -45, 0, 45 Degrees in Bending Test

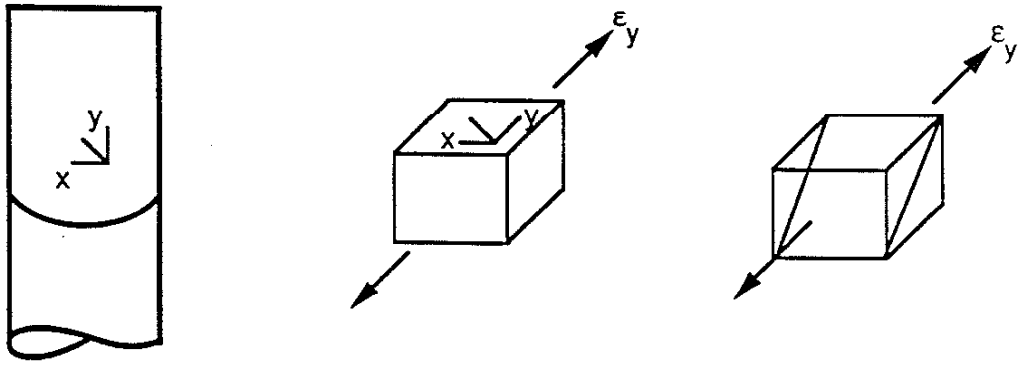

Figure 5.20 Predicted Failure Plane for 0, 45 and 90° Gauge in Bending Test

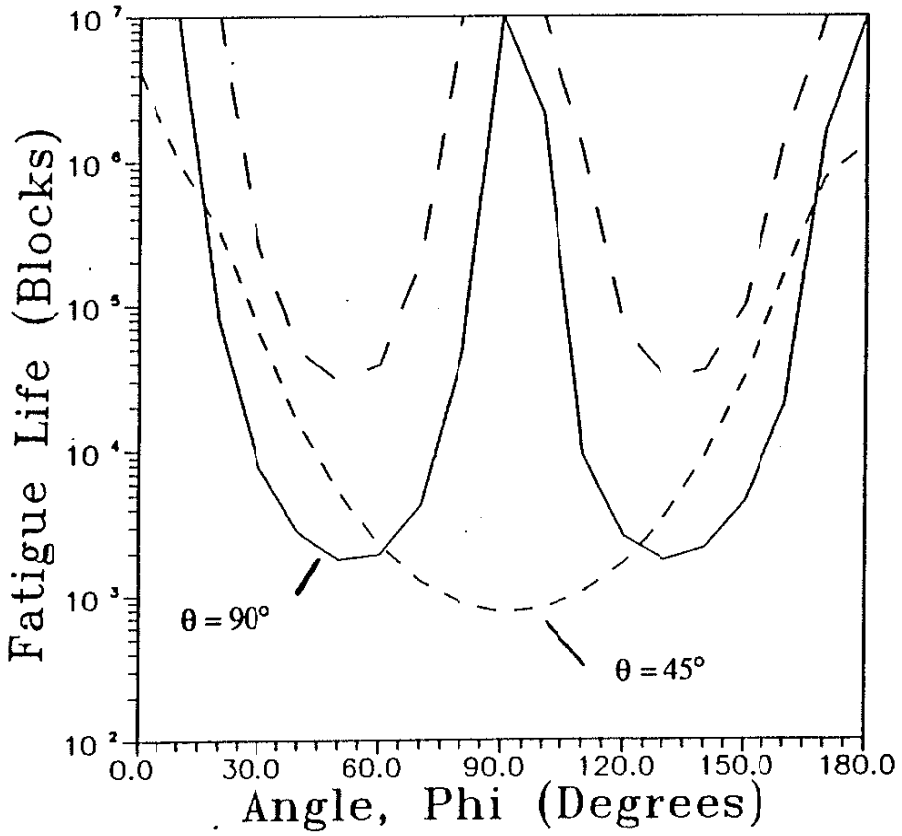

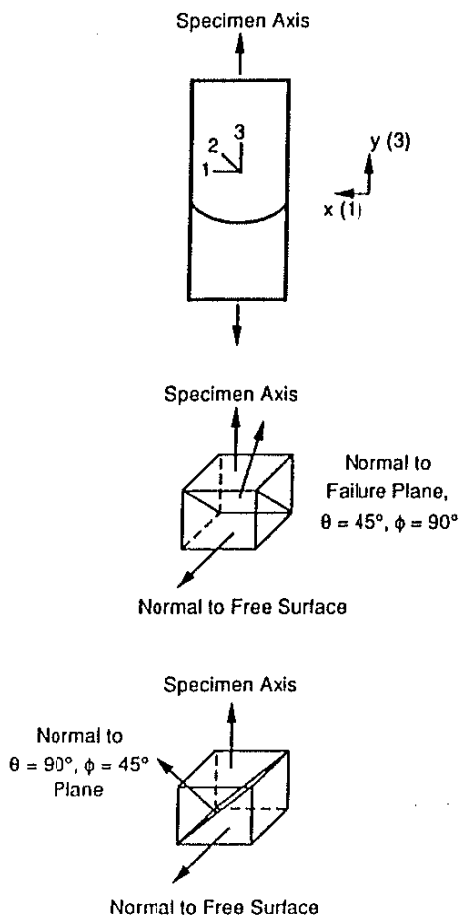

Figure 5.21 a) Shear Model Fatigue Life Plot for 0, 45, 90° Gauge in Bending Test

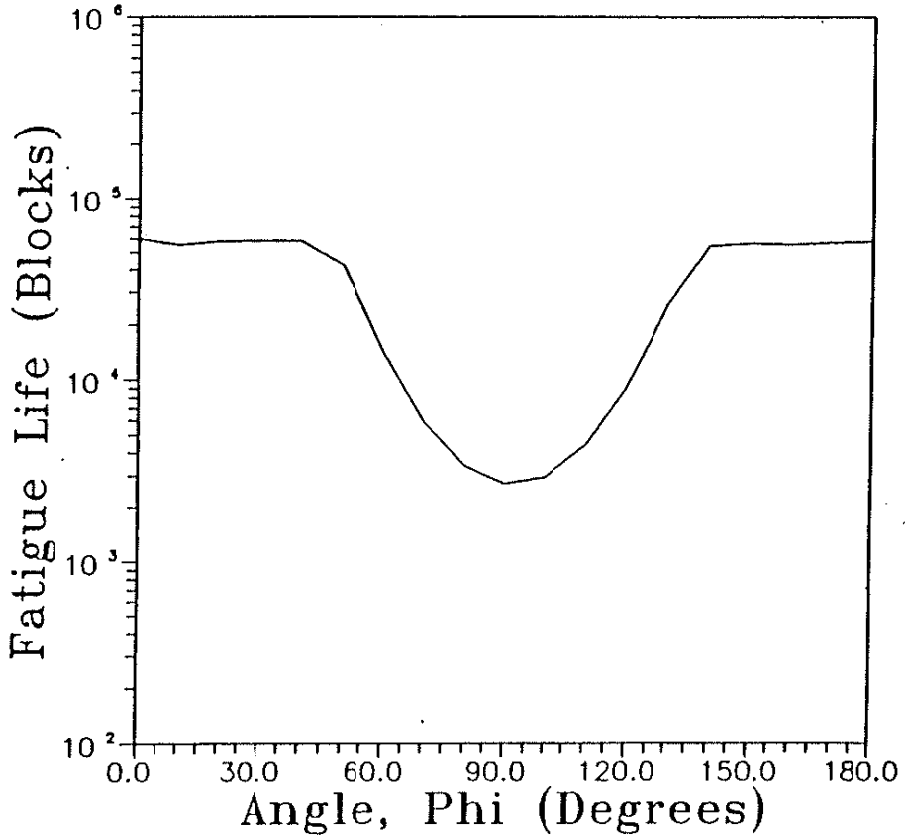

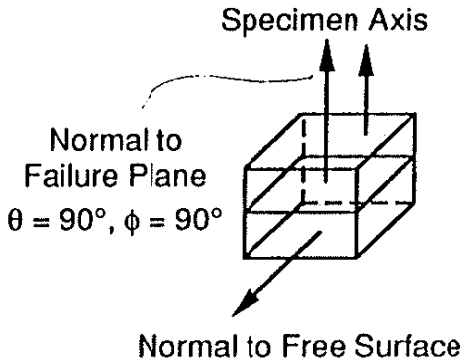

Figure 5.21 b) Tensile Model Fatigue Life Plot for 0°, 45°, 90° Gauge in Bending Test

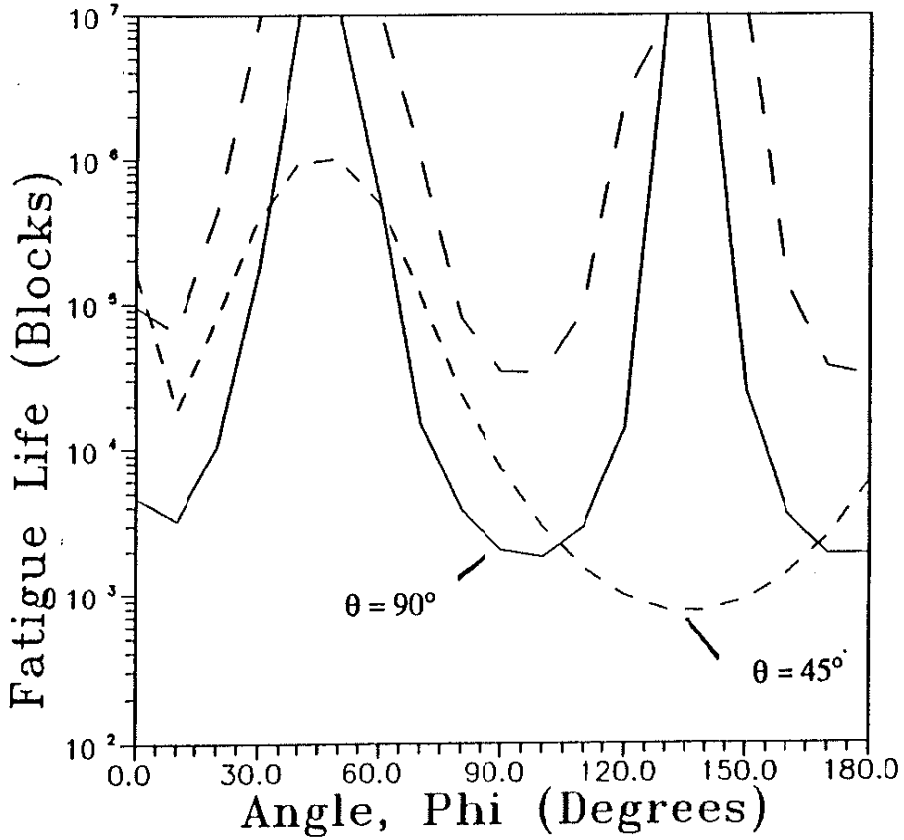

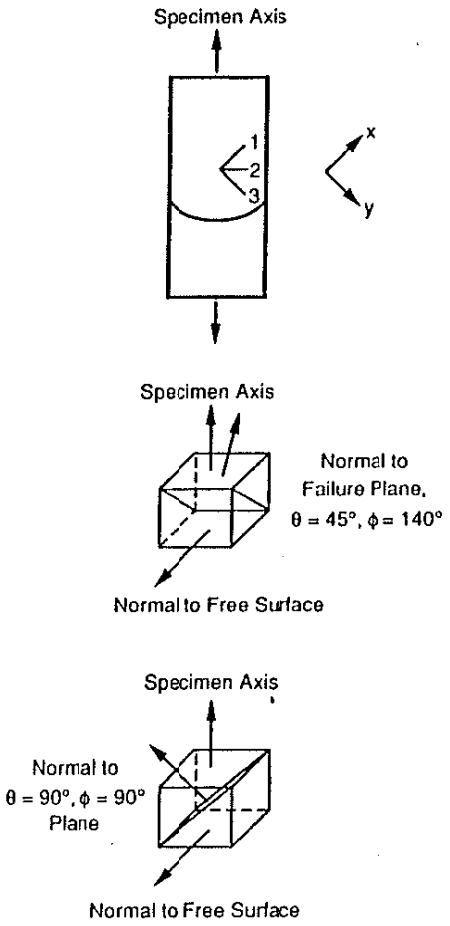

Figure 5.22 a) Shear Model Fatigue Life Plot for -45°, 0°, 45° Gauge in Bending Test

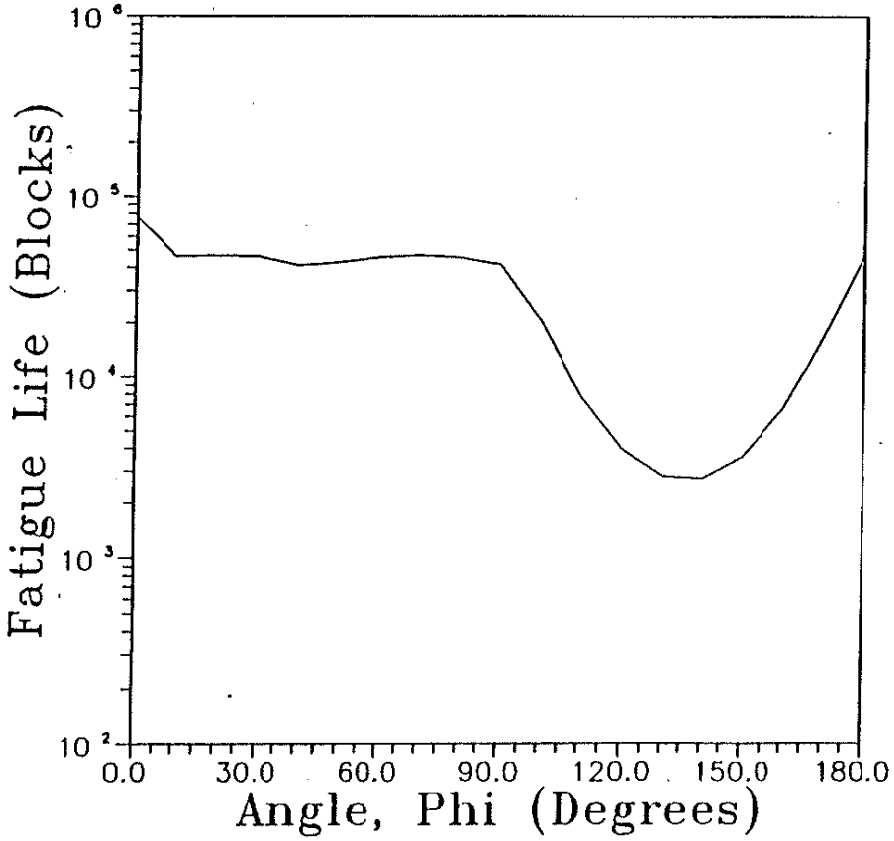

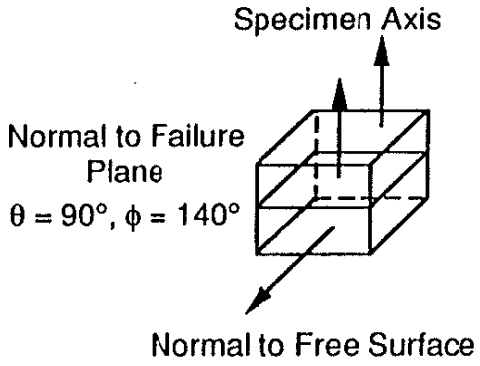

Figure 5.22 b) Tensile Model Fatigue Life Plot for -45°, 0°, 45° Gauge in Bending Test

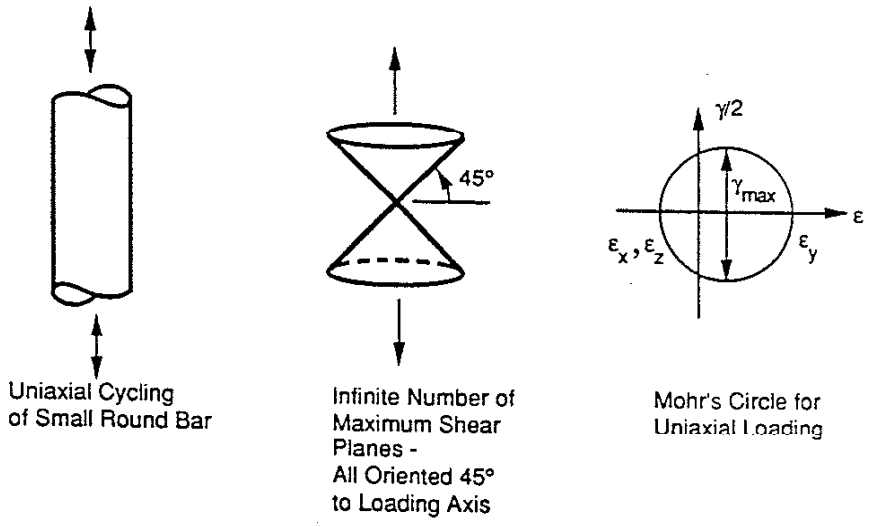

Figure 5.23 Maximum Shear Planes are Oriented 45° to Loading Direction or Axis of Small Round Bar

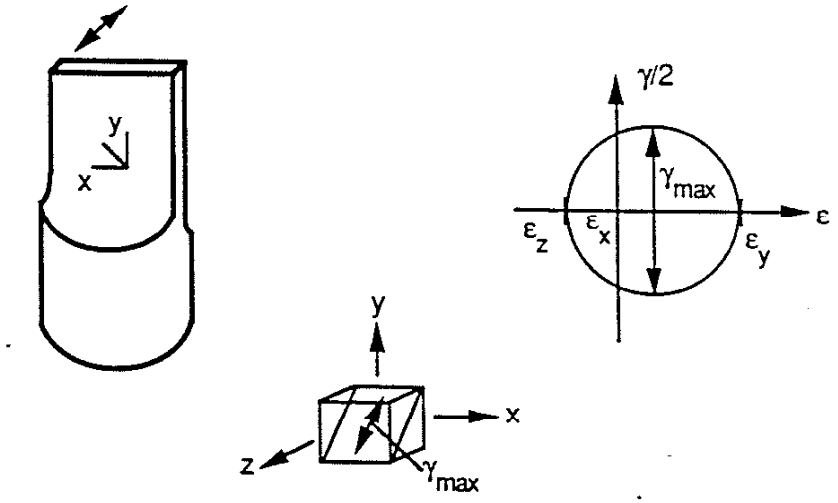

Figure 5.24 Mohr's Circle of Strain for Bending Tests

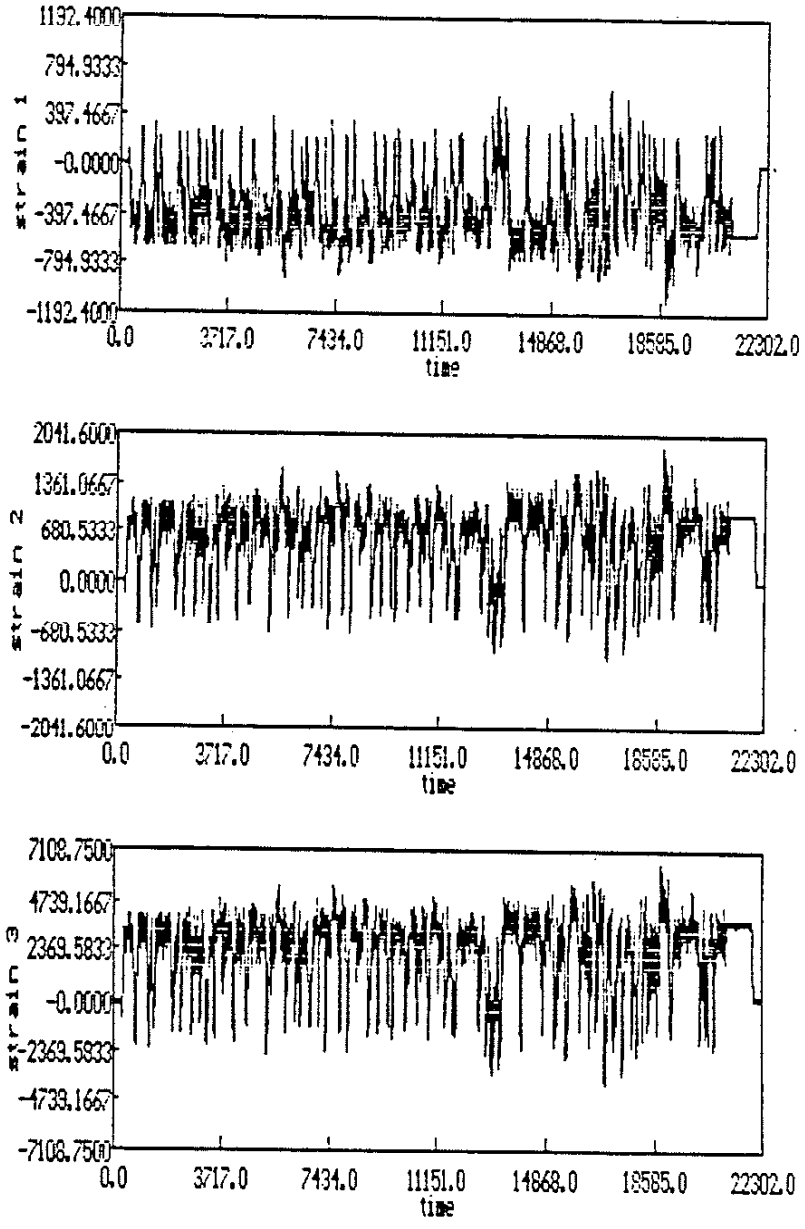

Figure 5.25 a) Strain Histories Obtained from the Strain Gauge Rosette in Proportional Loading

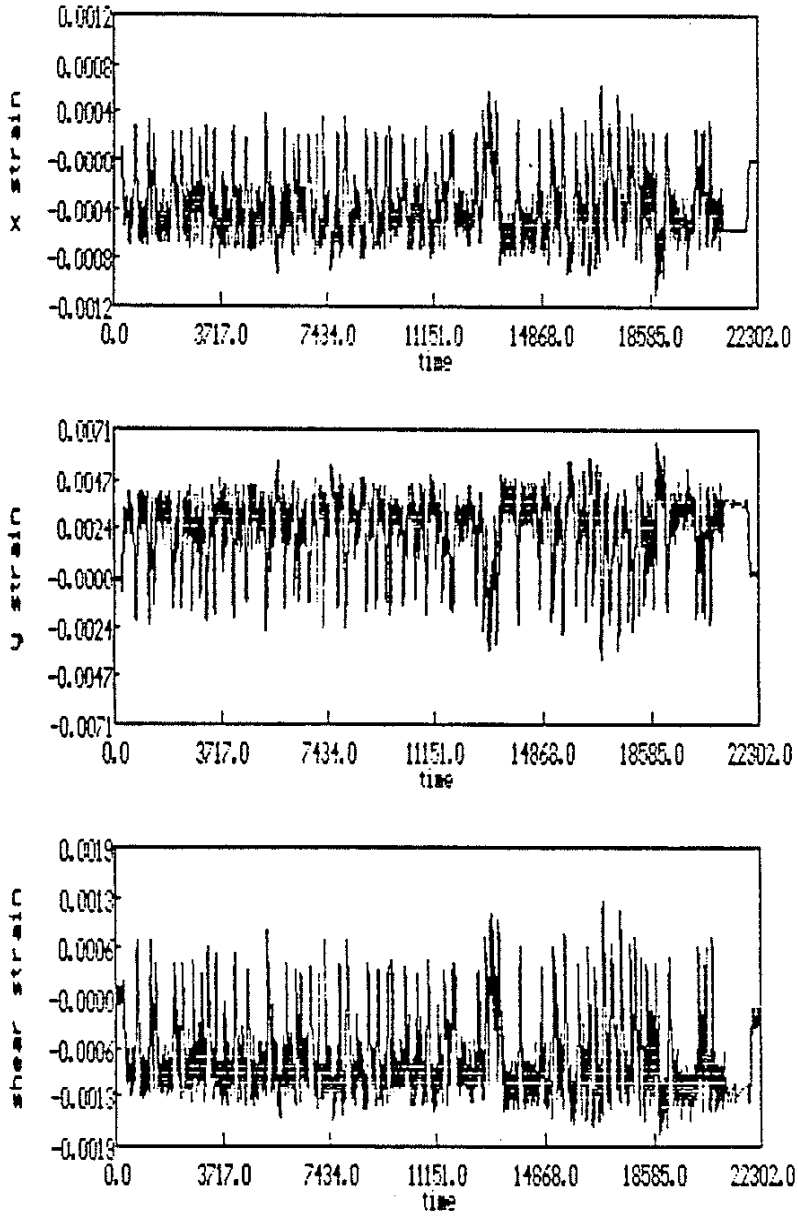

Figure 5.25 b) ε_x, ε_y and γ_{xy} Strain Histories for Proportional Loading

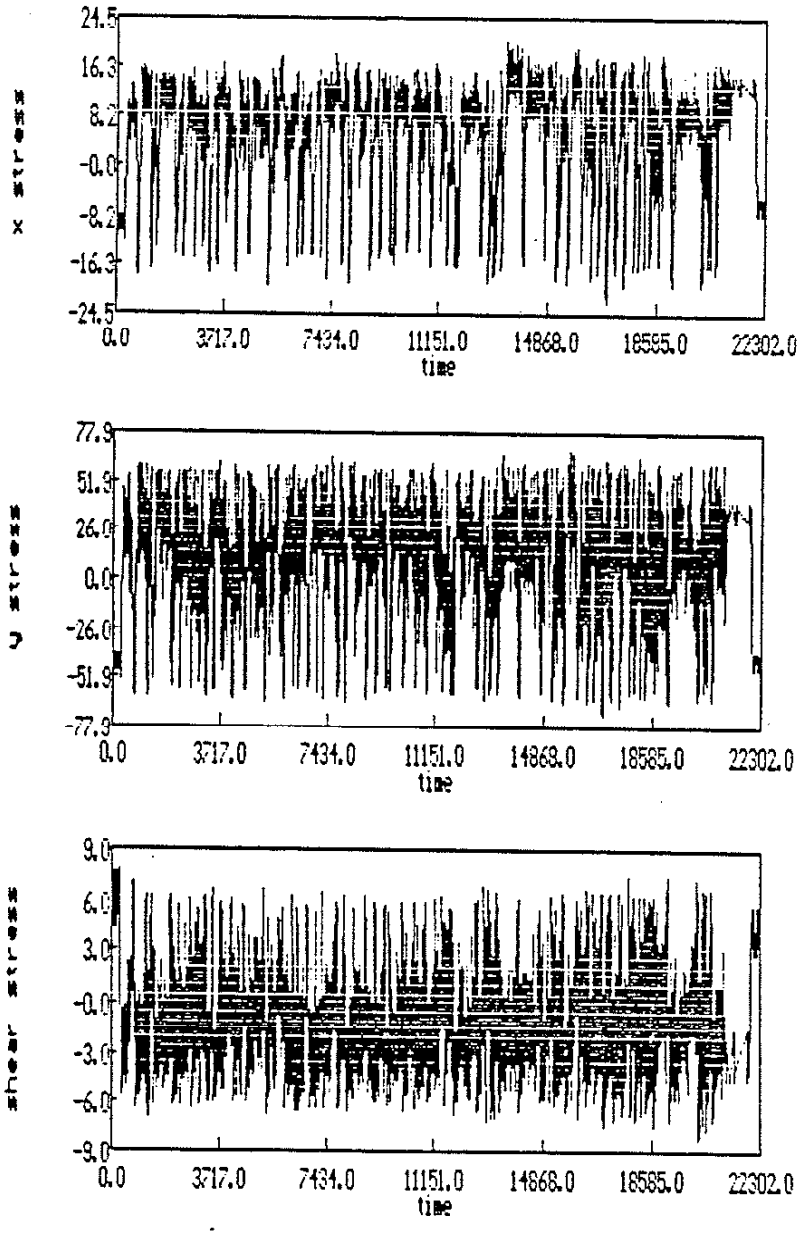

Figure 5.25 c) σ_x, σ_y and τ_{xy} Stress Histories for Proportional Loading

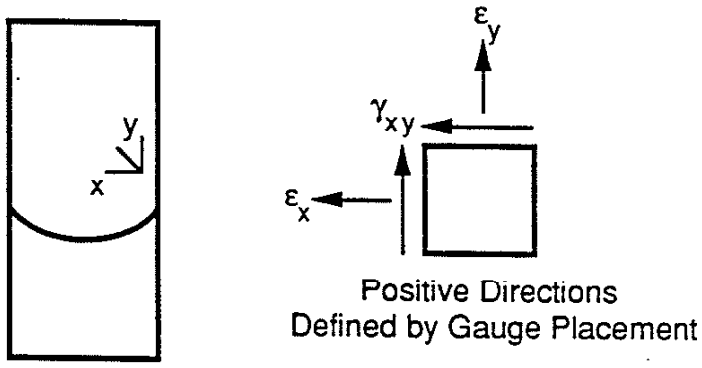

Figure 5.26 Positive Direction of Stresses and Strains Defined by Gauge Placement

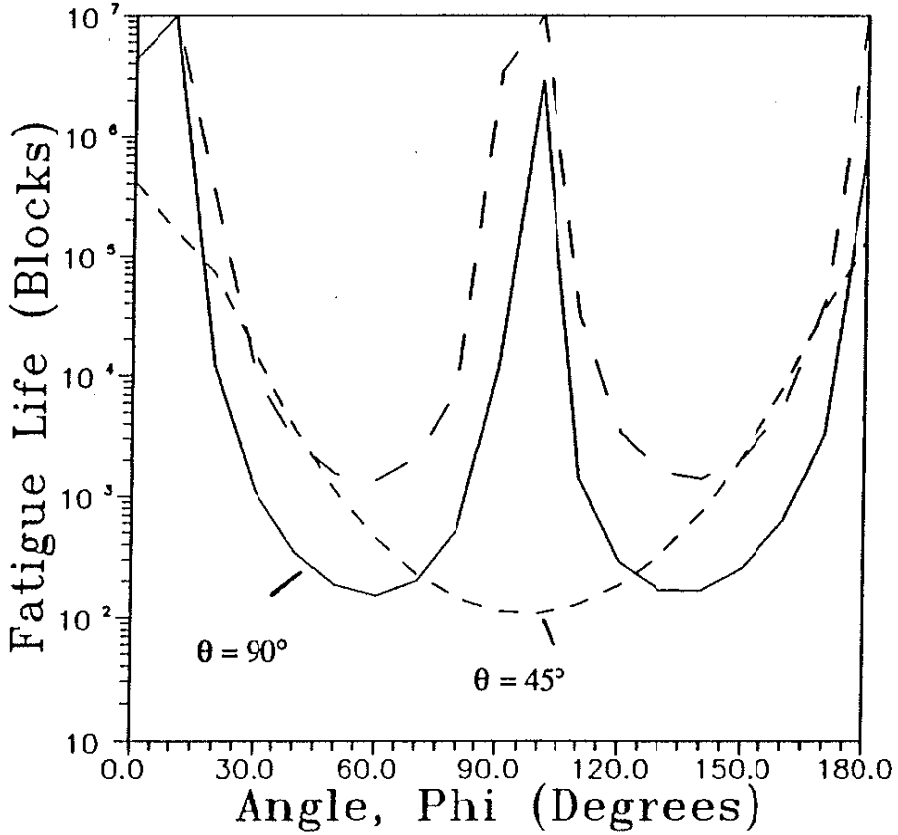

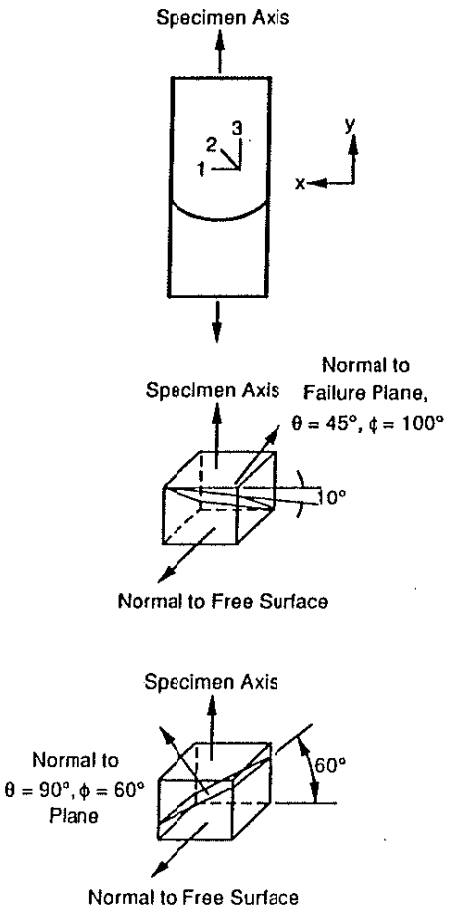

Figure 5.27 a) Shear Model Fatigue Life Plot for Proportional Loading

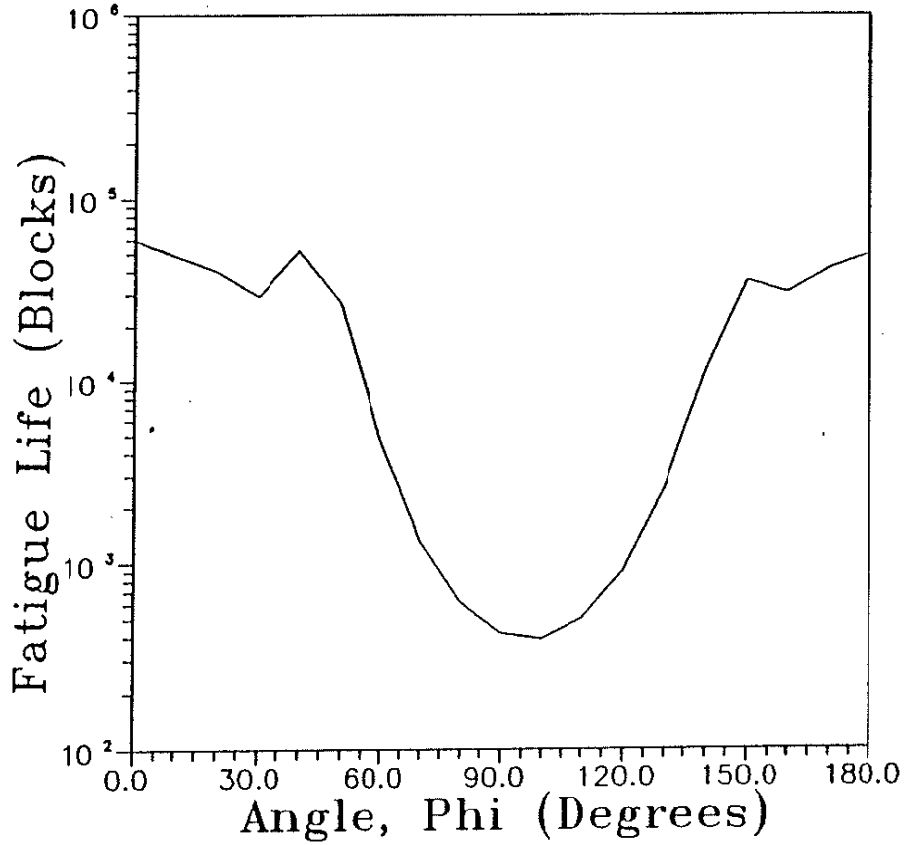

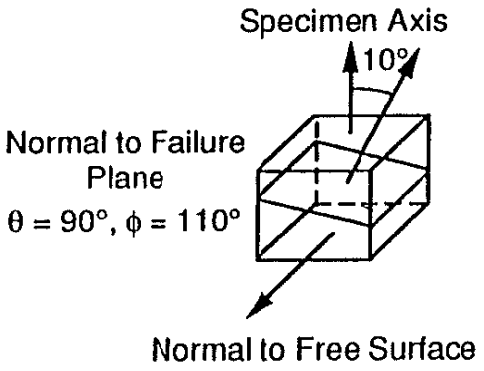

Figure 5.27 b) Tensile Model Fatigue Life Plot for Proportional Loading

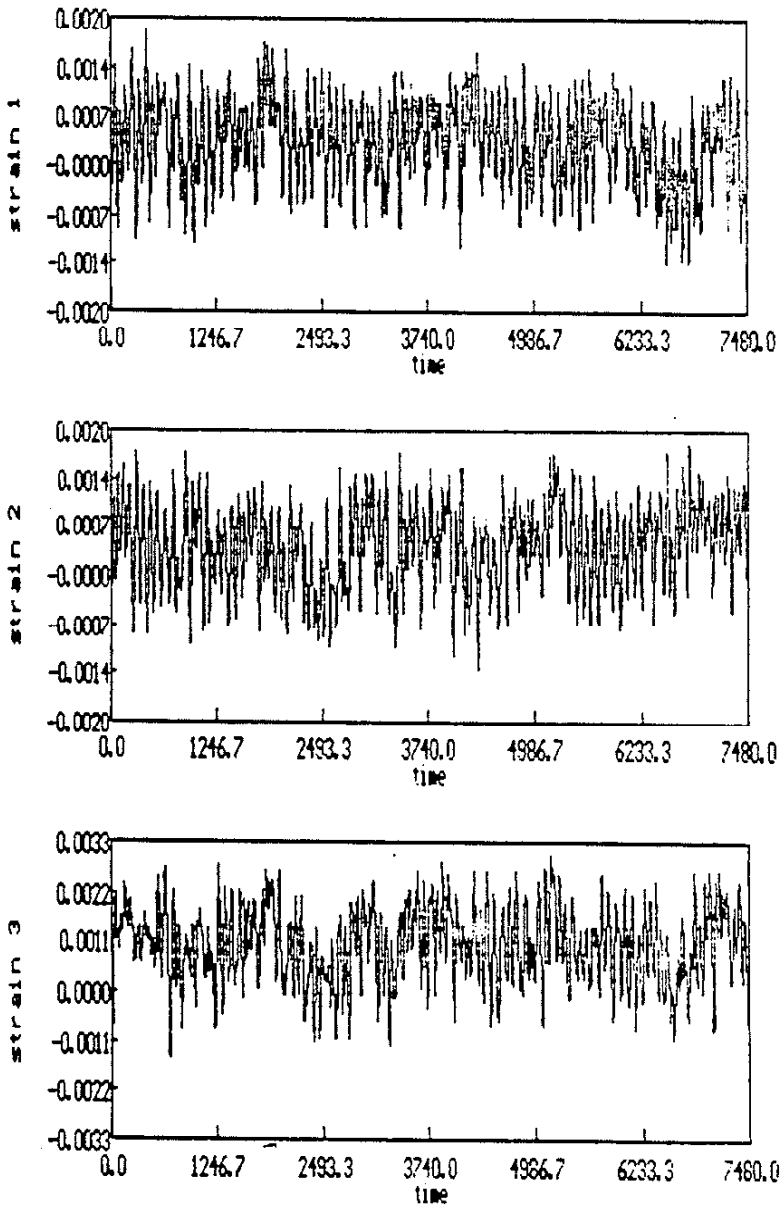

Figure 5.28 a) Strain Histories Obtained from the Strain Gauge Rosette in 46% Load Level, Nonproportional Test

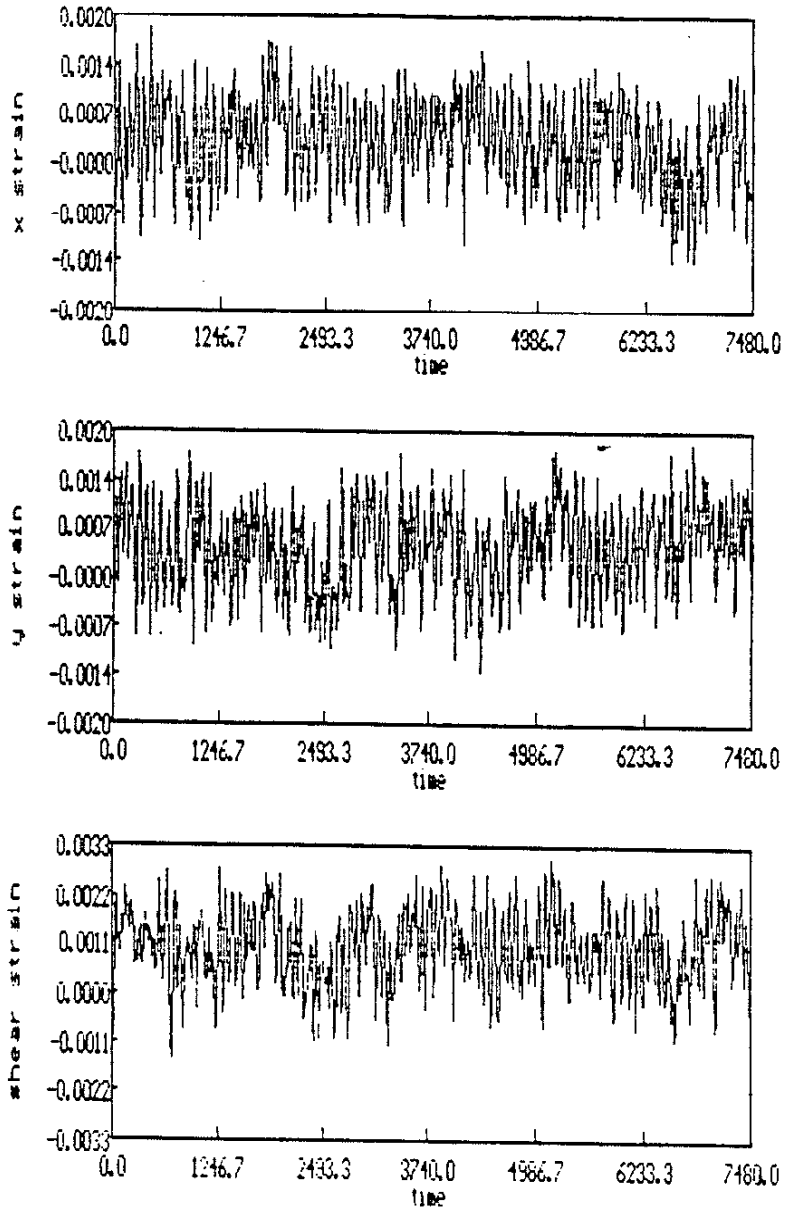

Figure 5.28 b) ε_x, ε_y and γ_{xy} Strain Histories for 46% Load Level, Nonproportional Test

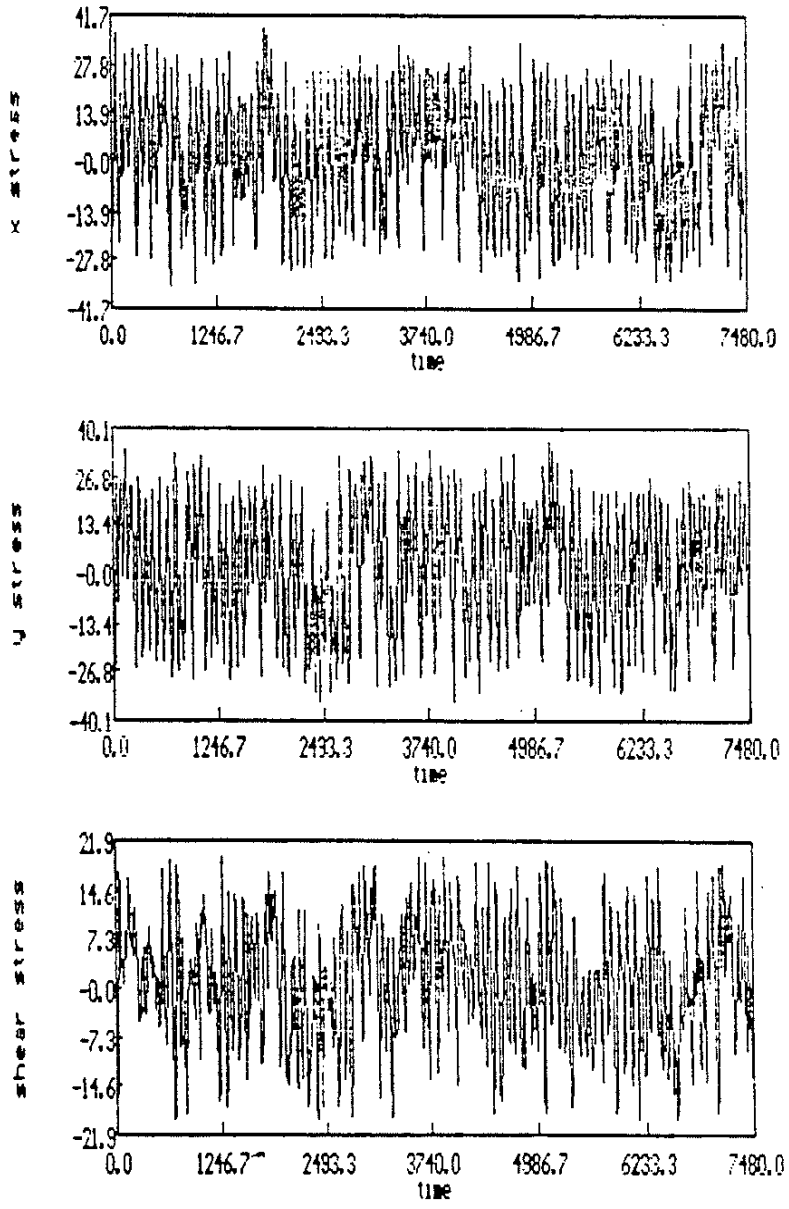

Figure 5.28 c) σ_x, σ_y and τ_{xy} Stress Histories in 46% Load Level, Nonproportional Test

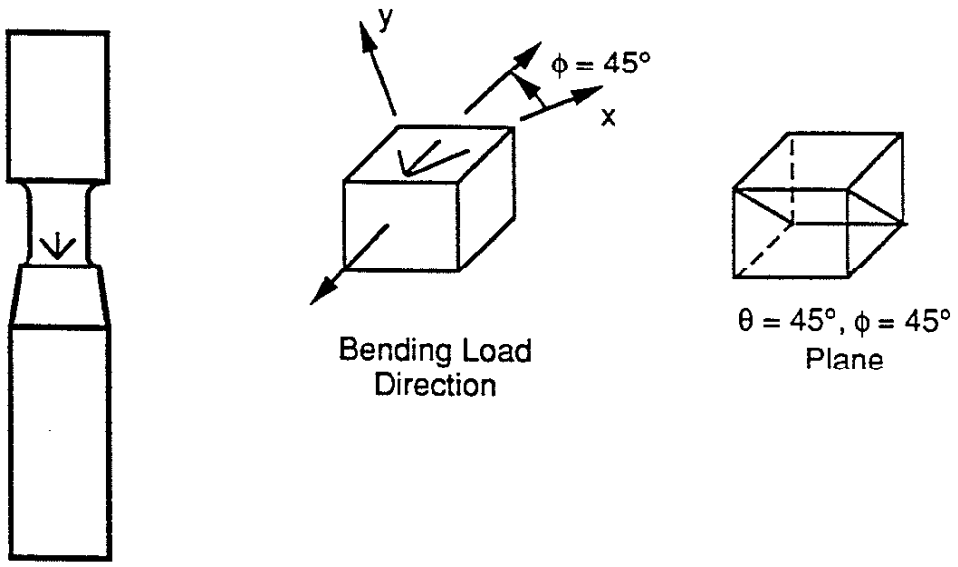

Figure 5.29 Orientation of Failure Plane Predicted in Nonproportional, 46% Load Level Test

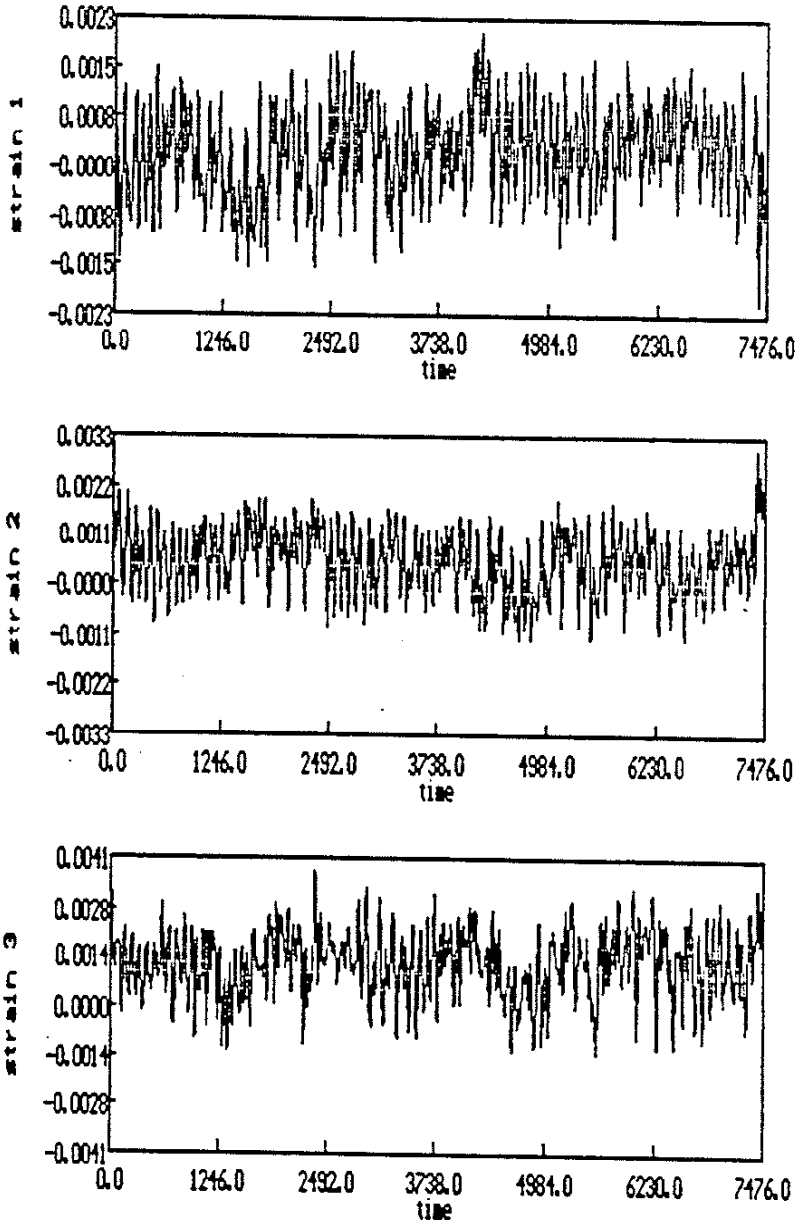

Figure 5.30 a) Strain Histories Obtained from the Strain Gauge Rosette in 51% Load Level, Nonproportional Test

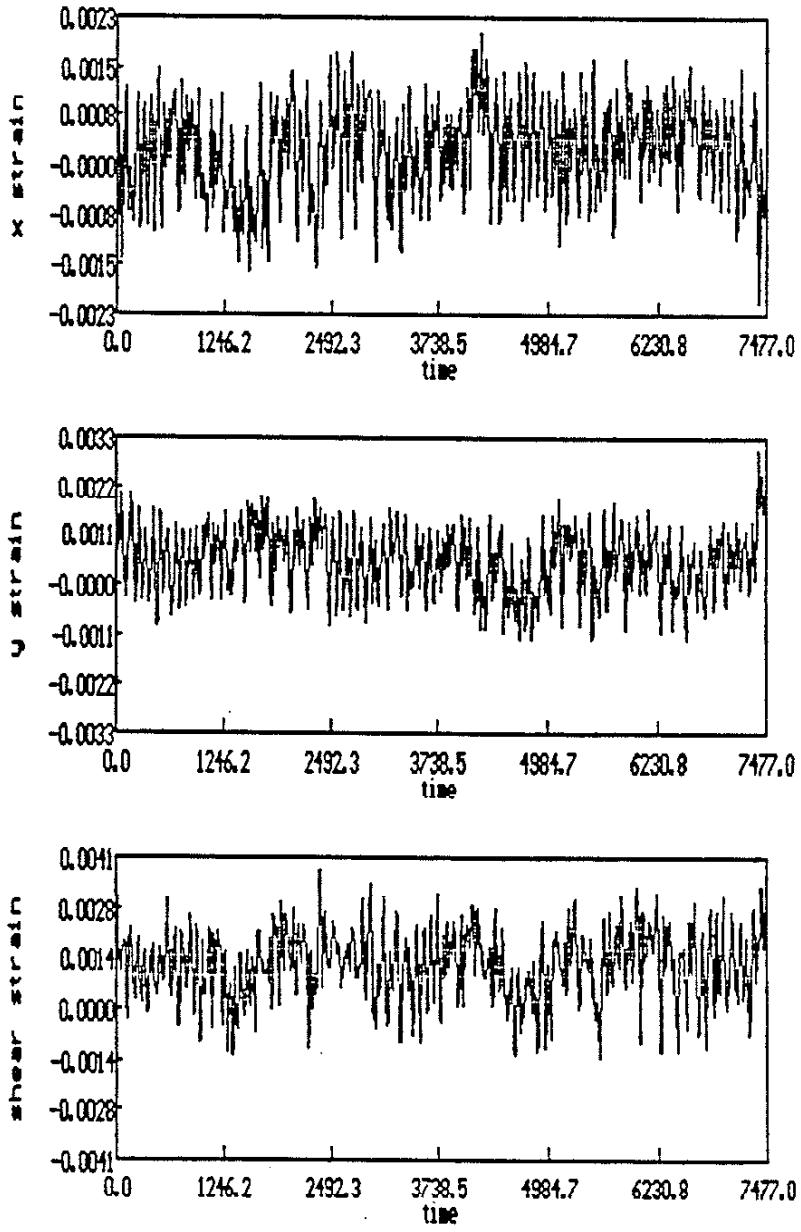

Figure 5.30 b) ε_x, ε_y and γ_{xy} Strain Histories for 51% Load Level, Nonproportional Test

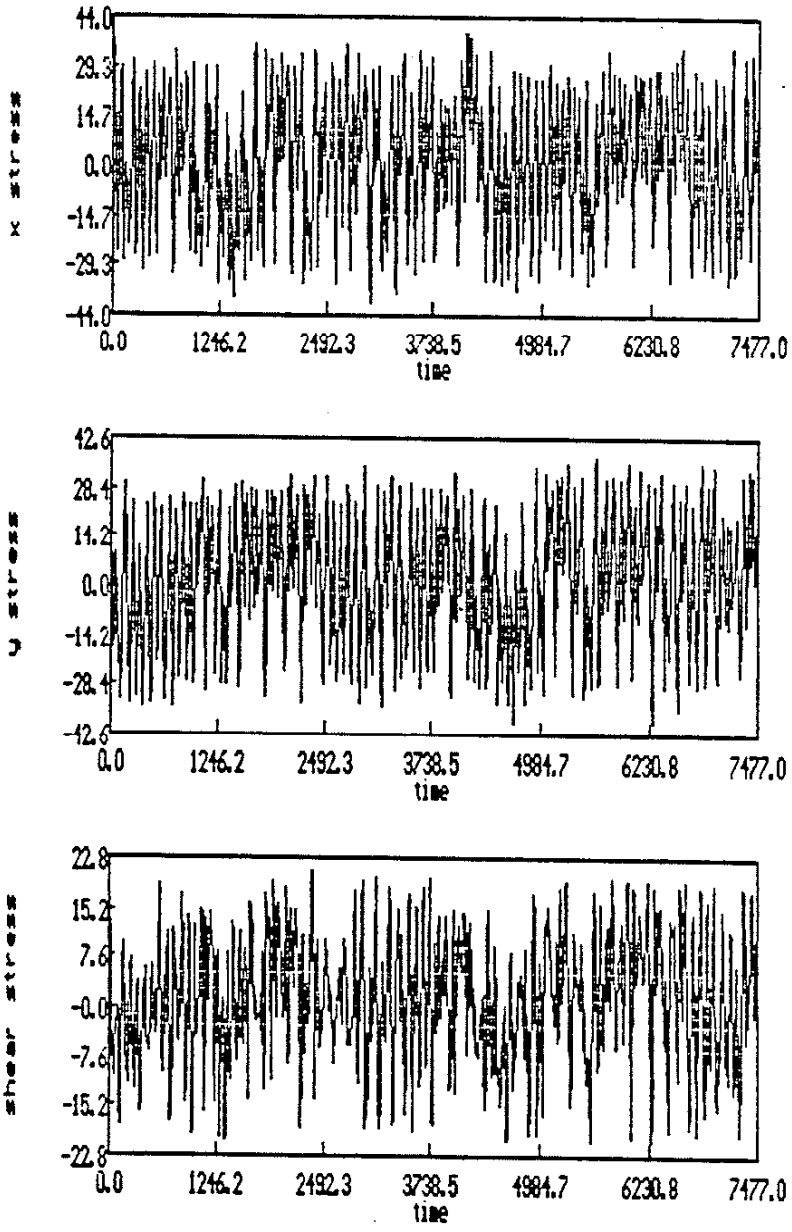

Figure 5.30 c) σ_x, σ_y and τ_{xy} Stress Histories Predicted for 51% Load Level, Nonproportional Test

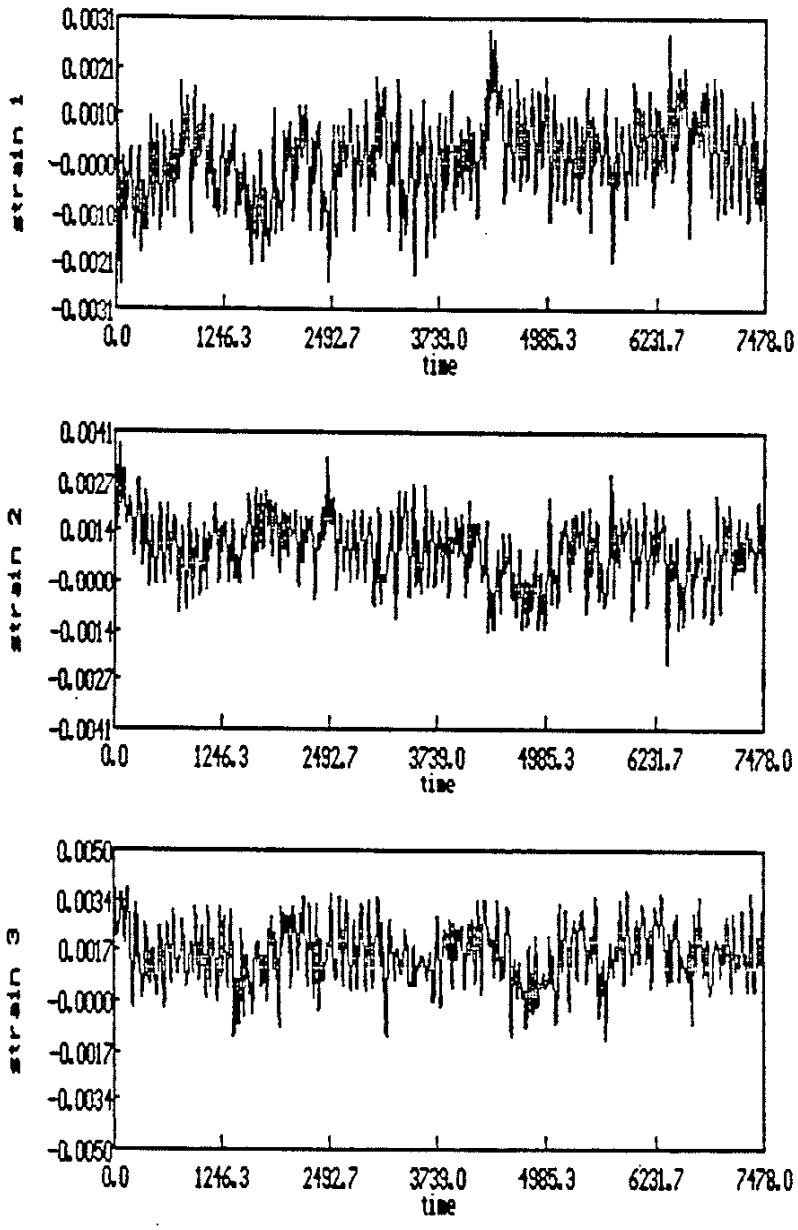

Figure 5.31 a) Strain Histories Obtained from the Strain Gauge Rosette in 55% Load Level, Nonproportional Test

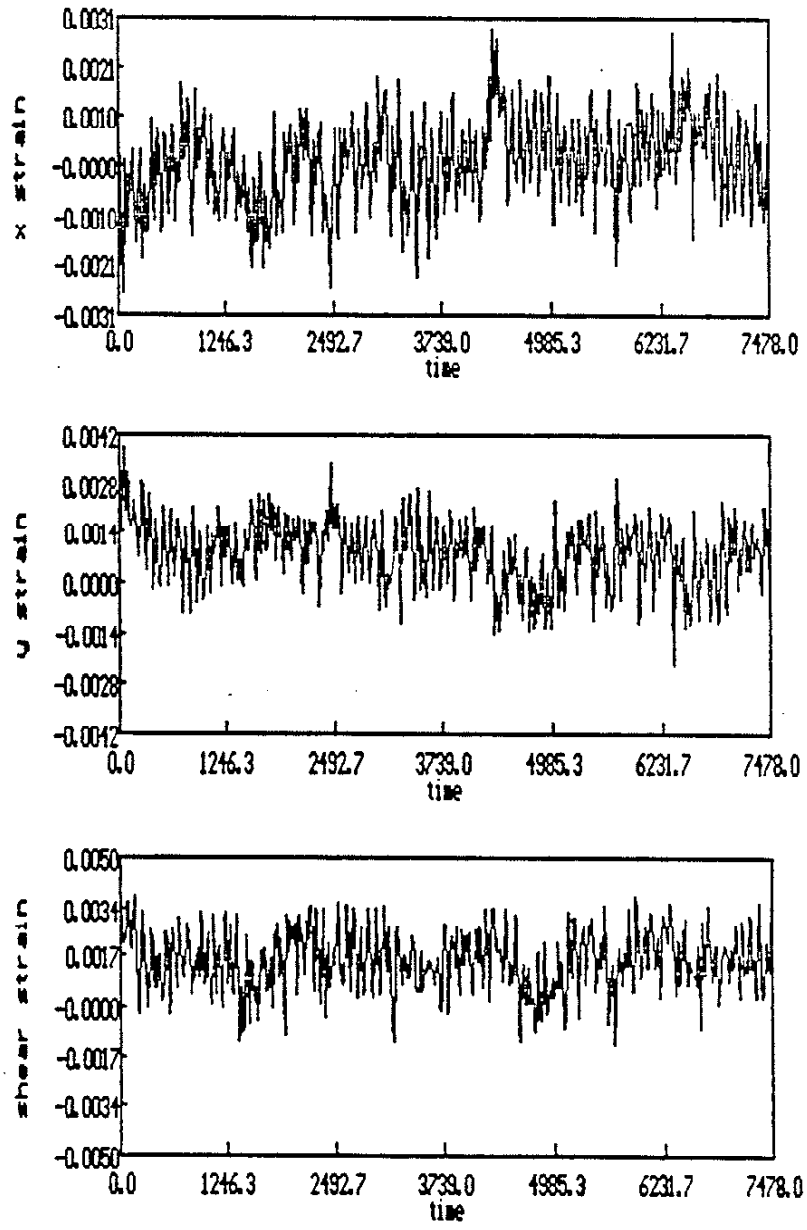

Figure 5.31 b) ε_x, ε_y and γ_{xy} Strain Histories for 55% Load Level, Nonproportional Test

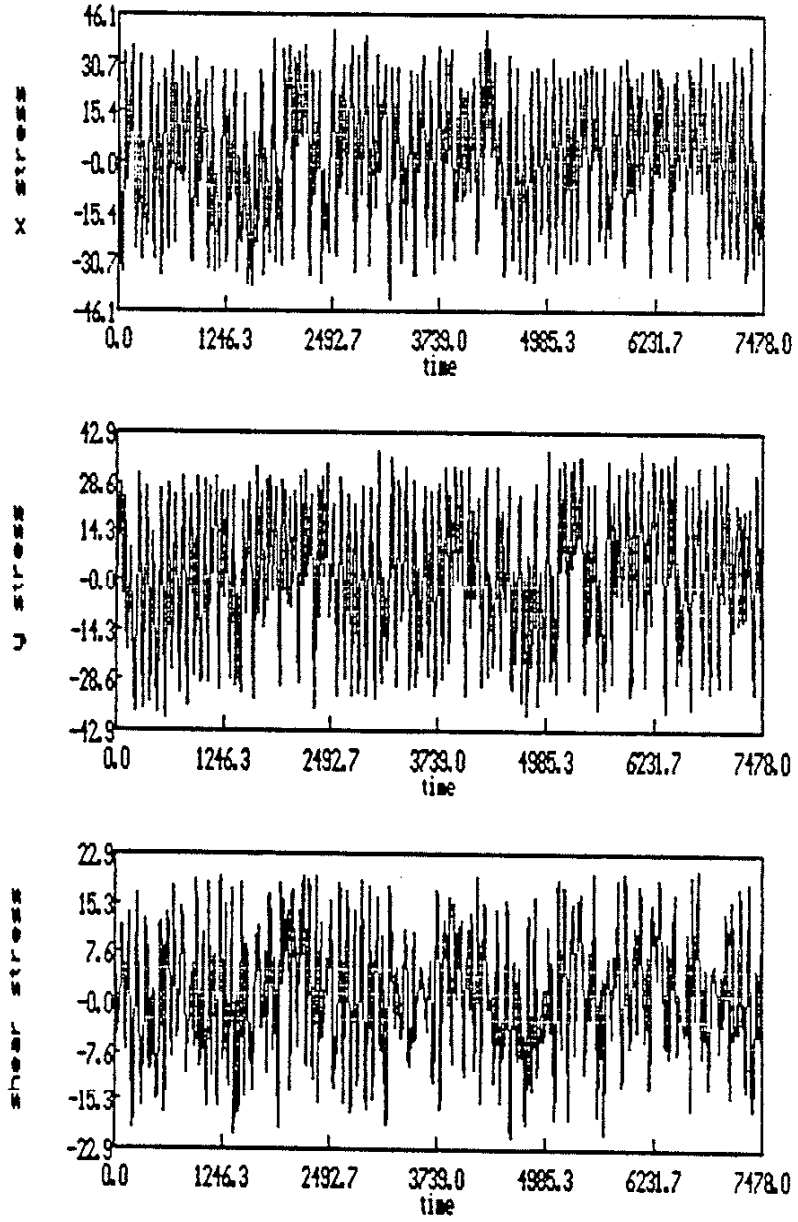

Figure 5.31 c) σ_x, σ_y and τ_{xy} Stress Histories Predicted for 55% Load Level, Nonproportional Test

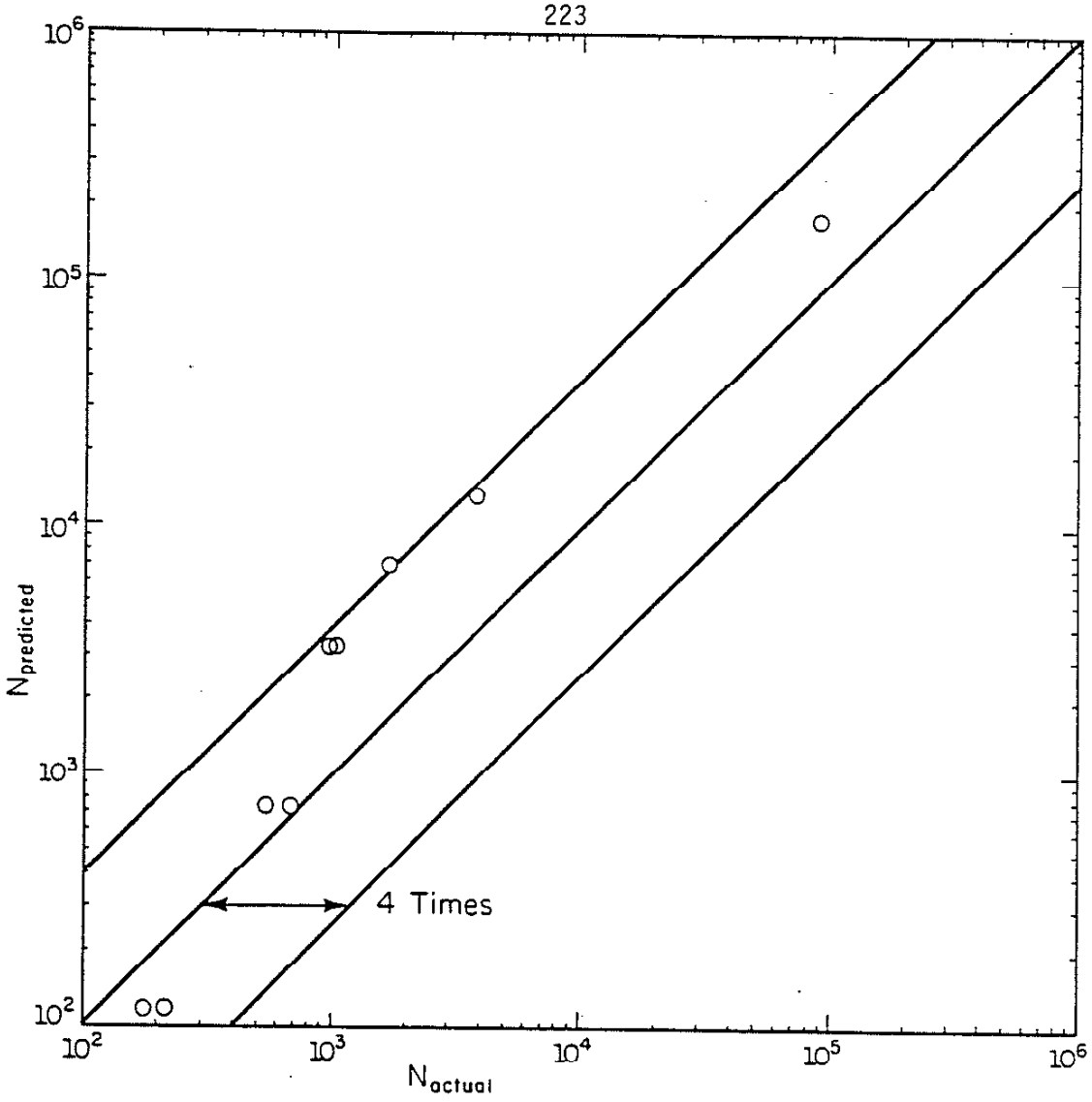

Figure 5.32 Comparison of Predicted and Experimental Variable Amplitude Multiaxial Fatigue Lives

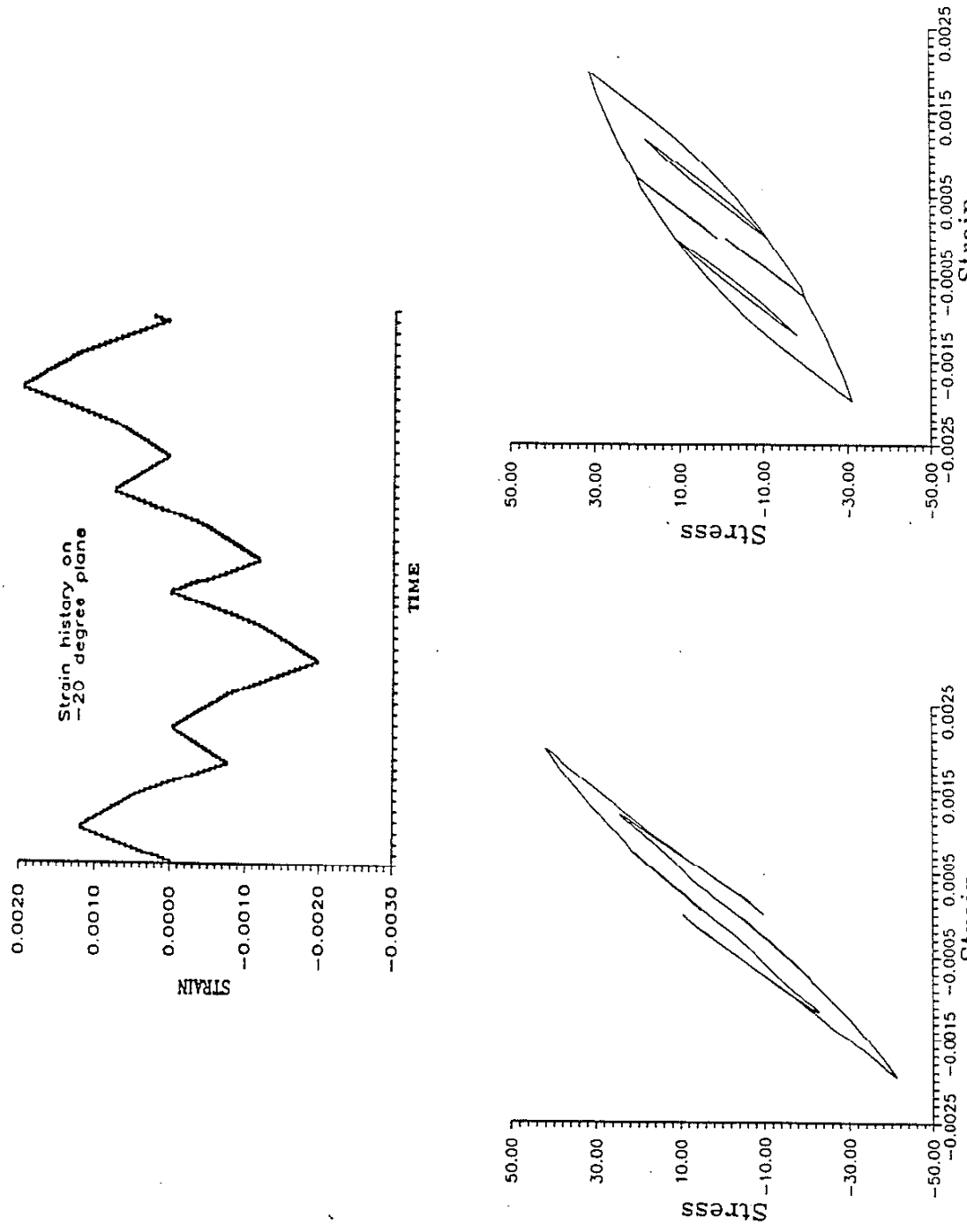

Figure 6.1 (a) Strain History on -20° Plane (b) Measured Multiaxial Stress Strain Response (c) Predicted Uniaxial Stress Strain Response

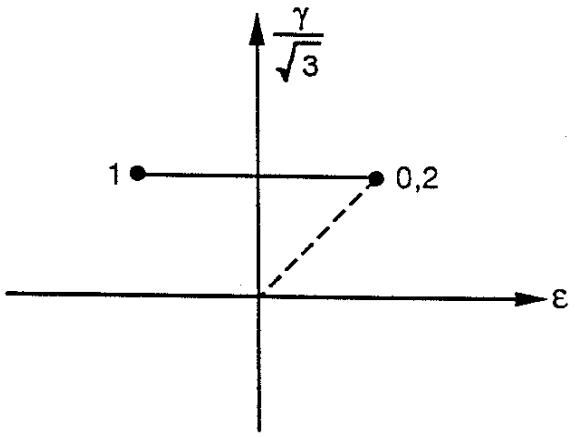

Loading Case 1

Point 0 $\varepsilon_x = -0.00075$ $\varepsilon_y = 0.0025$ $\gamma_{xy} = 0.0025$

Point 1 $\varepsilon_x = 0.00075$ $\varepsilon_y = -0.0025$ $\gamma_{xy} = 0.0025$

Point 2 $\varepsilon_x = -0.00075$ $\varepsilon_y = 0.0025$ $\gamma_{xy} = 0.0025$

Loading Case 2

Point 0 $\varepsilon_x = -0.0015$ $\varepsilon_y = 0.005$ $\gamma_{xy} = 0.003$

Point 1 $\varepsilon_x = 0.0015$ $\varepsilon_y = -0.005$ $\gamma_{xy} = 0.003$

Point 2 $\varepsilon_x = -0.0015$ $\varepsilon_y = 0.005$ $\gamma_{xy} = 0.003$

Figure 6.2 Example Loading Path Made Up of Completely Reversed Uniaxial Strain and a Torsional Mean Strain.

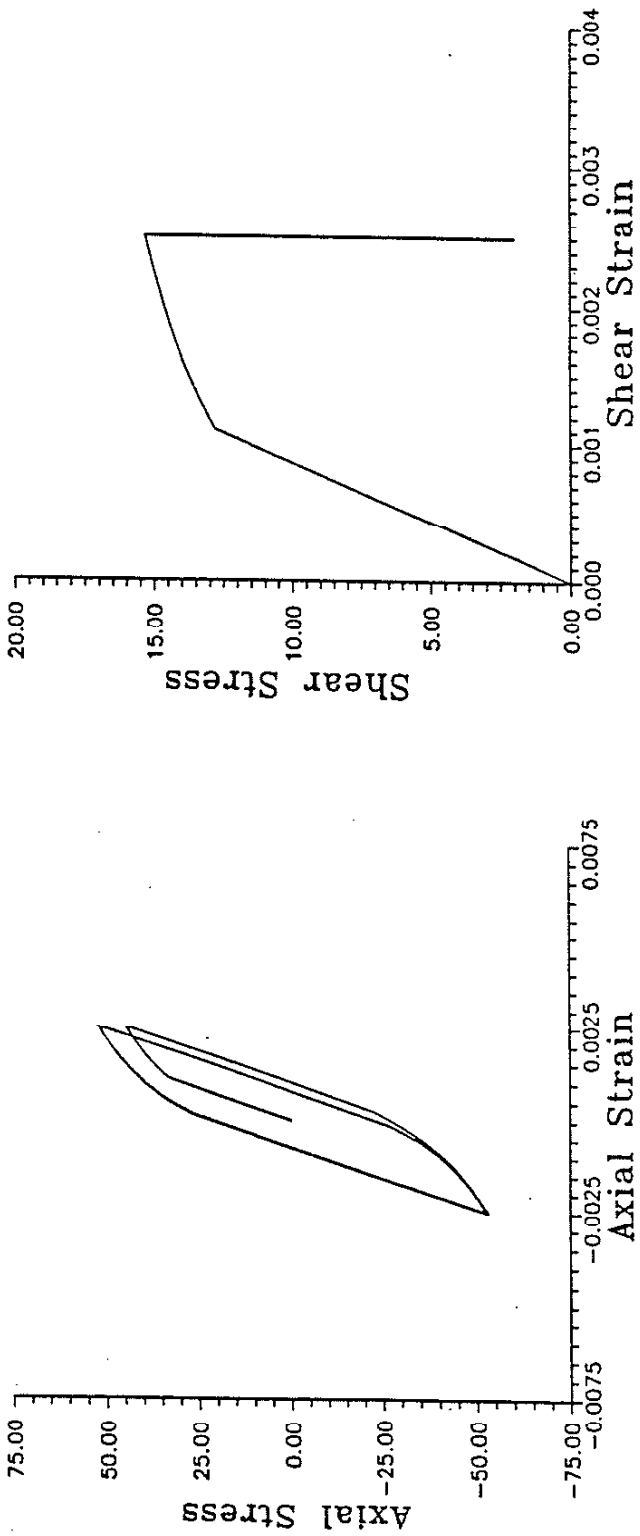

Figure 6.3 Predicted Axial and Shear Stress-Strain Response for Example Loading Path with $\epsilon_a = 0.0025$, $\gamma_m = 0.0025$

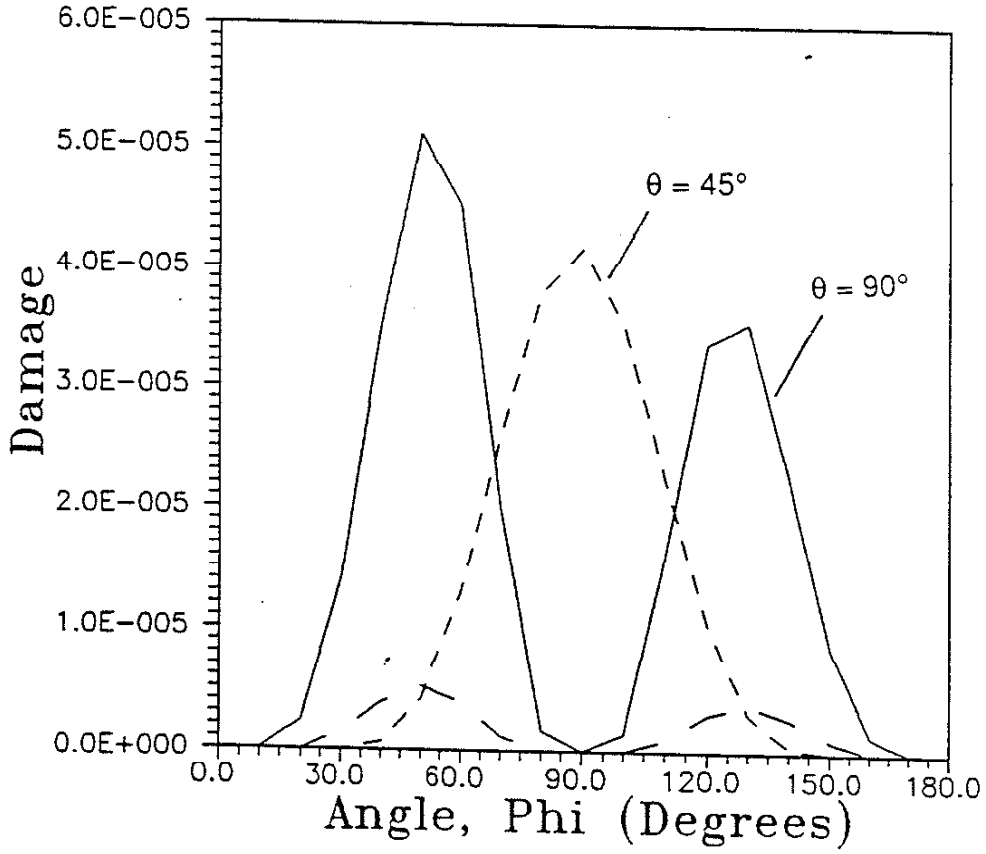

Figure 6.4 Plot of Shear Damage Per Plane for Example Loading Case with $\varepsilon_a = 0.0025$, $\gamma_m = 0.0025$

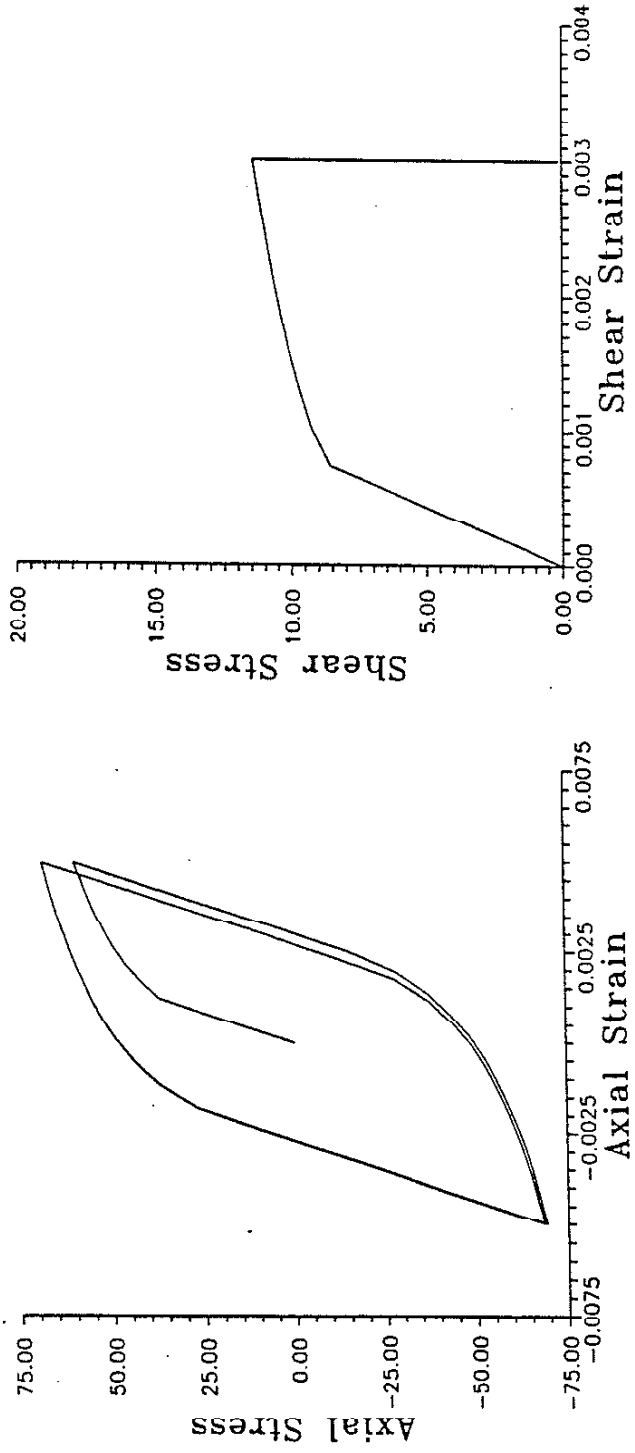

Figure 6.5 Predicted Axial and Shear Stress-Strain Response for Example Loading Path with $\varepsilon_a = 0.005$, $\gamma_m = 0.003$

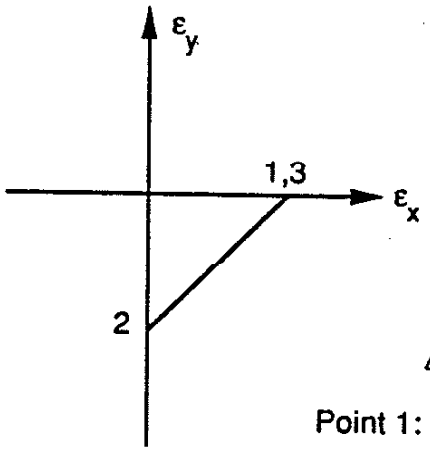

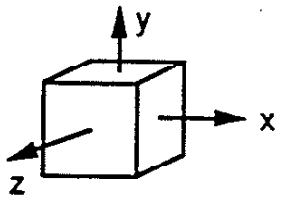

Applied Loading

$\Delta\varepsilon_x = \varepsilon,\ \Delta\varepsilon_y = \varepsilon,\ \Delta\gamma_{xy} = 0$

Point 1: $\varepsilon_x = \varepsilon \quad \varepsilon_y = 0 \quad \gamma_{xy} = 0$

Point 2: $\varepsilon_x = 0 \quad \varepsilon_y = -\varepsilon \quad \gamma_{xy} = 0$

Point 3: $\varepsilon_x = \varepsilon \quad \varepsilon_y = 0 \quad \gamma_{xy} = 0$

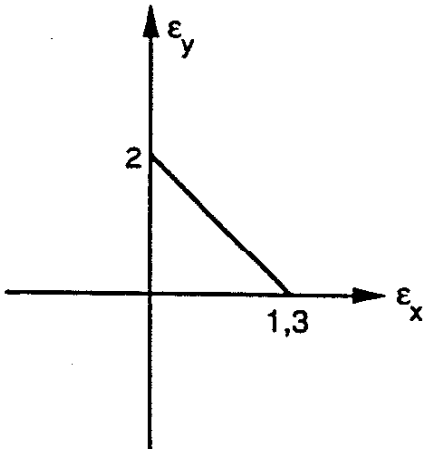

Applied Loading

$\Delta\varepsilon_x = \varepsilon,\ \Delta\varepsilon_y = \varepsilon,\ \Delta\gamma_{xy} = 0$

Point 1: $\varepsilon_x = \varepsilon \quad \varepsilon_y = 0 \quad \gamma_{xy} = 0$

Point 2: $\varepsilon_x = 0 \quad \varepsilon_y = \varepsilon \quad \gamma_{xy} = 0$

Point 3: $\varepsilon_x = \varepsilon \quad \varepsilon_y = 0 \quad \gamma_{xy} = 0$

Figure 6.6 Two Loading Paths (a) Mean Compressive Strain (b) Mean Tensile Strain

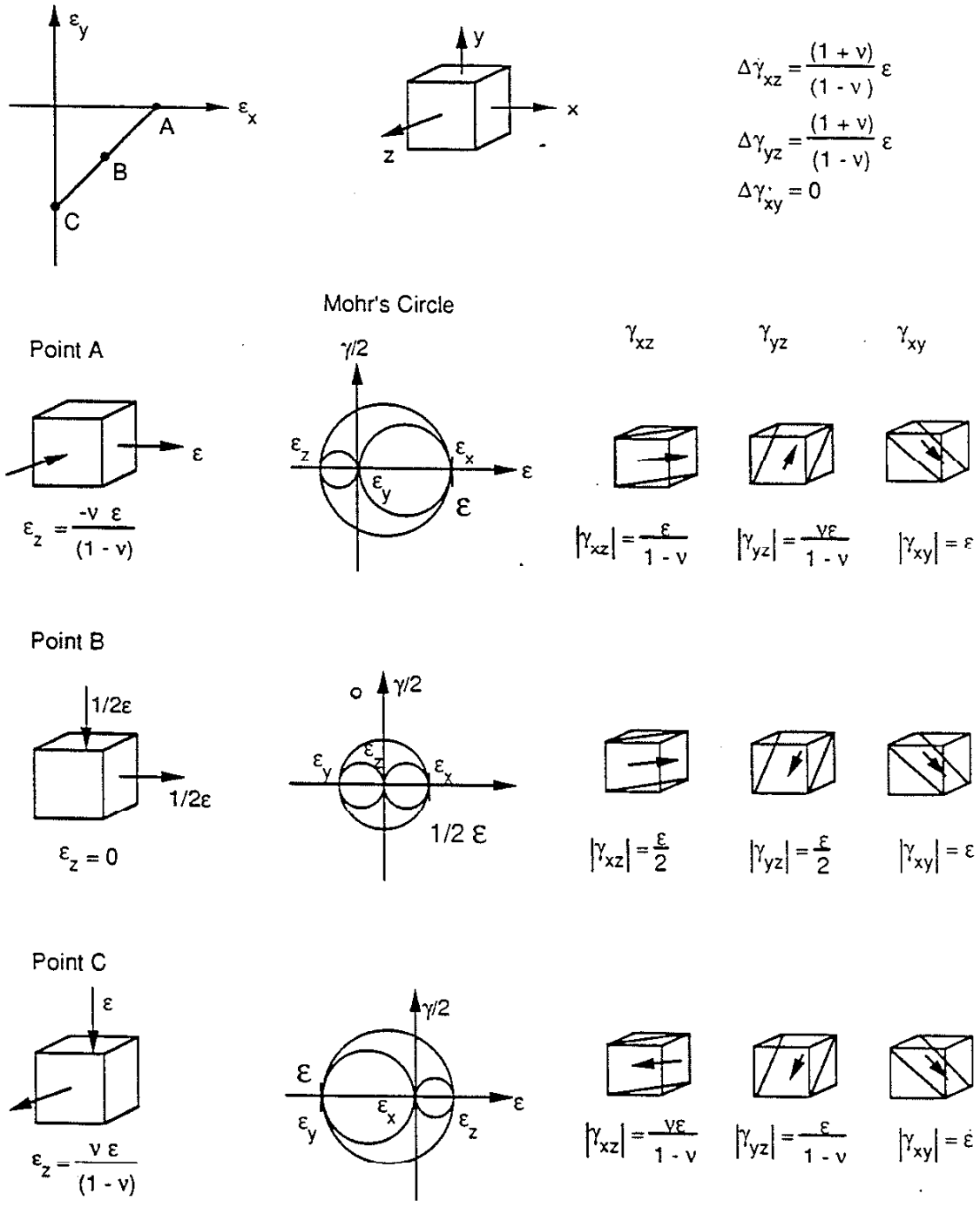

Figure 6.7 Applied Loading, Mohr's Circle of Strain, and the Value of Shearing Strain on Three Planes for Three Points in the Loading Cycle (Loading Path One)

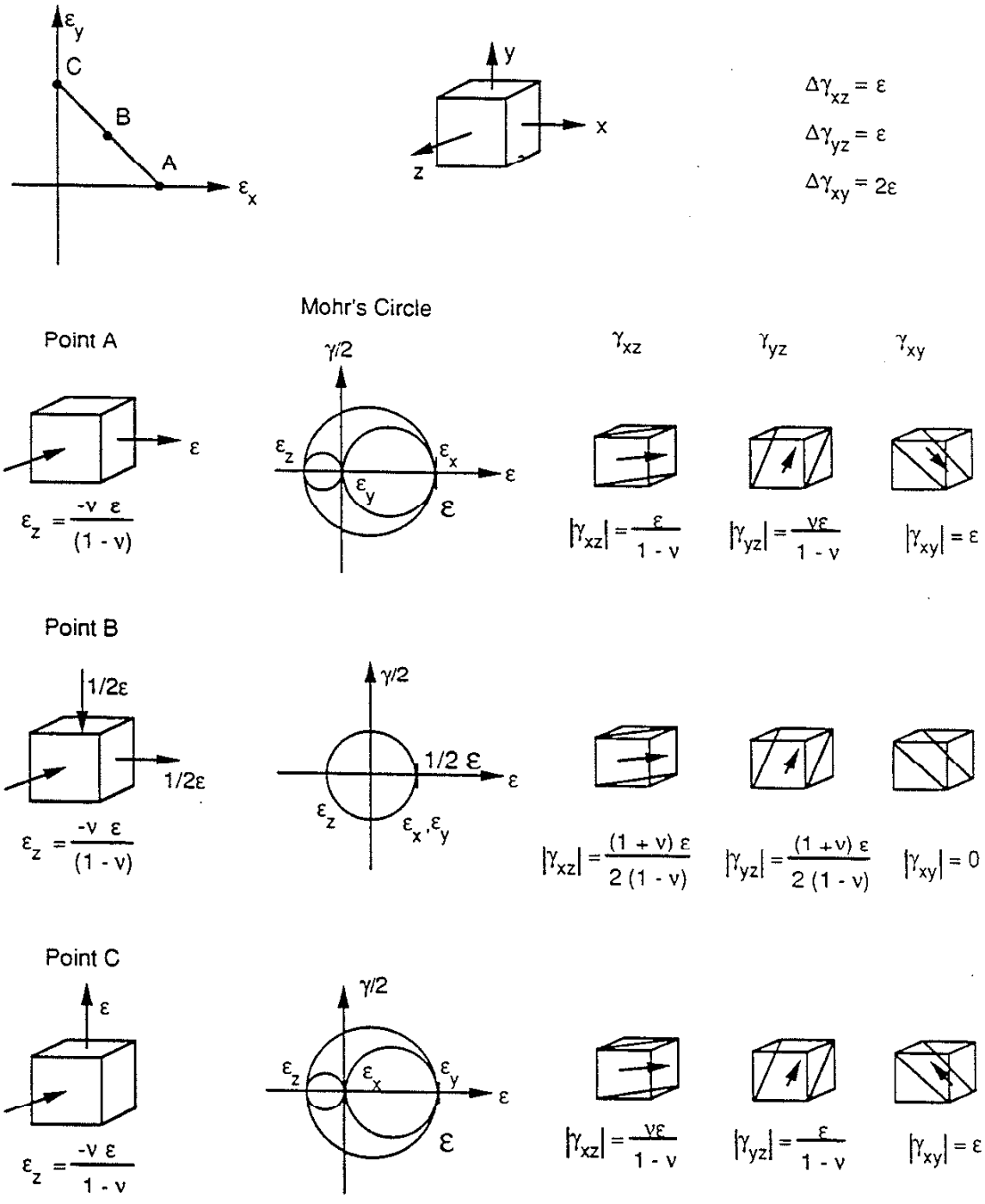

Figure 6.8 Applied Loading, Mohr's Circle of Strain, and the Value of Shearing Strain on Three Planes for Three Points in the Loading Cycle (Loading Path Two)

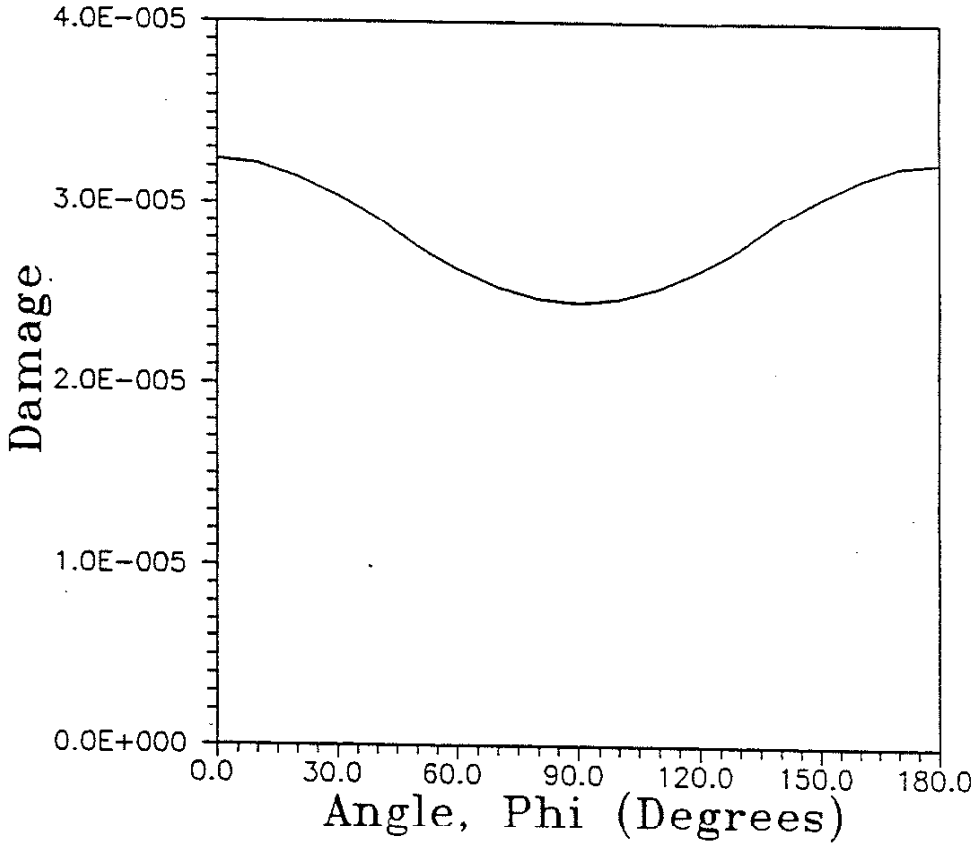

Figure 6.9 Plot of Shear Damage per Plane for Loading Case One

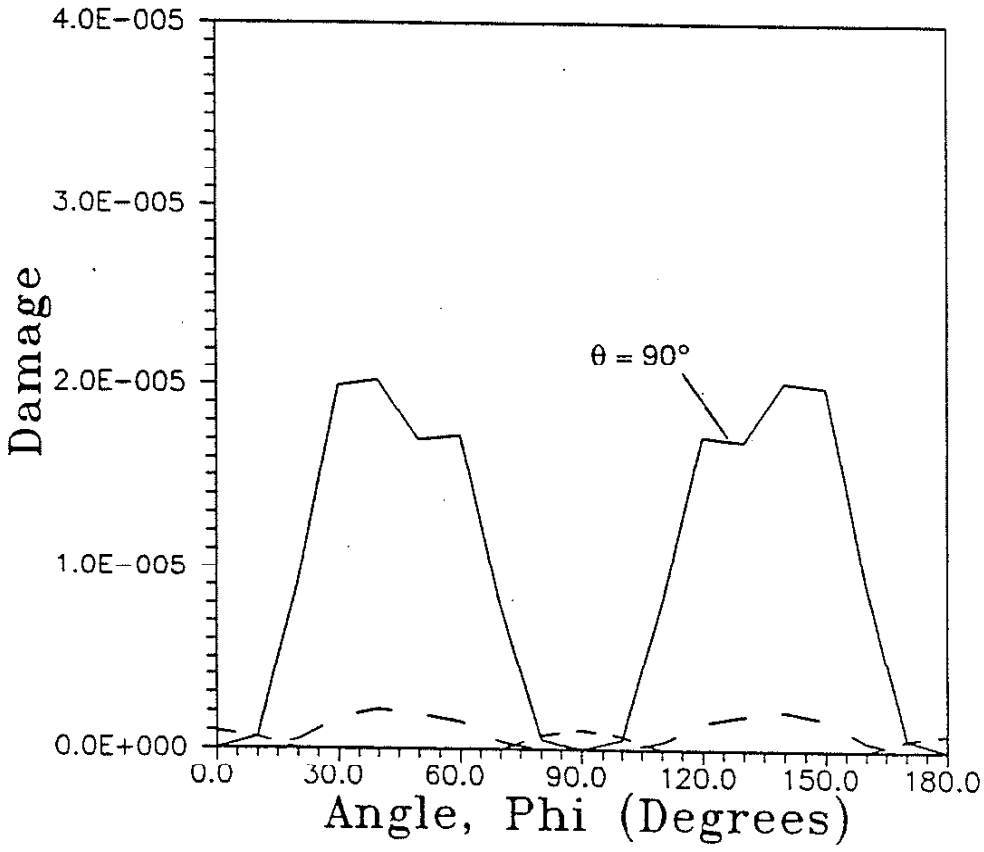

Figure 6.10 Plot of Shear Damage per Plane for Loading Case Two

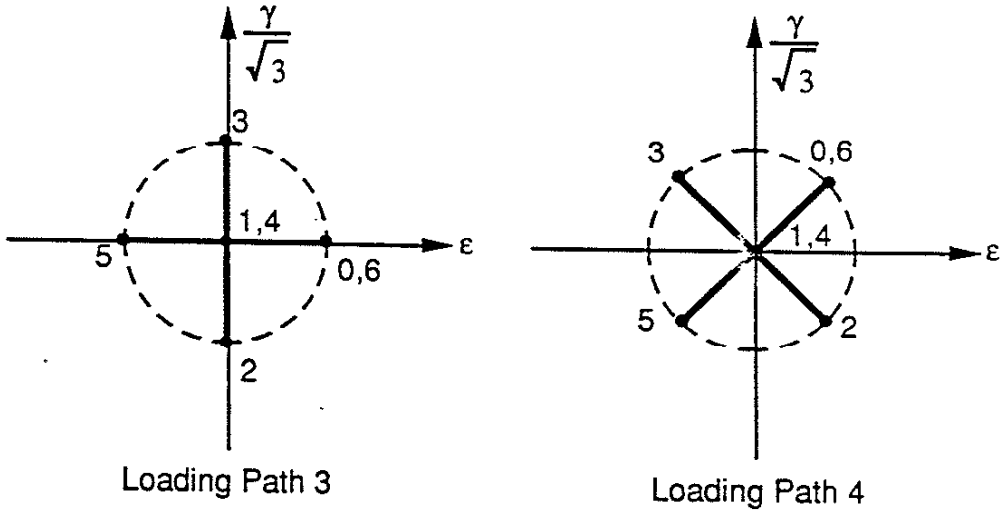

Figure 6.11 Two Loading Paths, Path Three and Path Four, used for Analysis

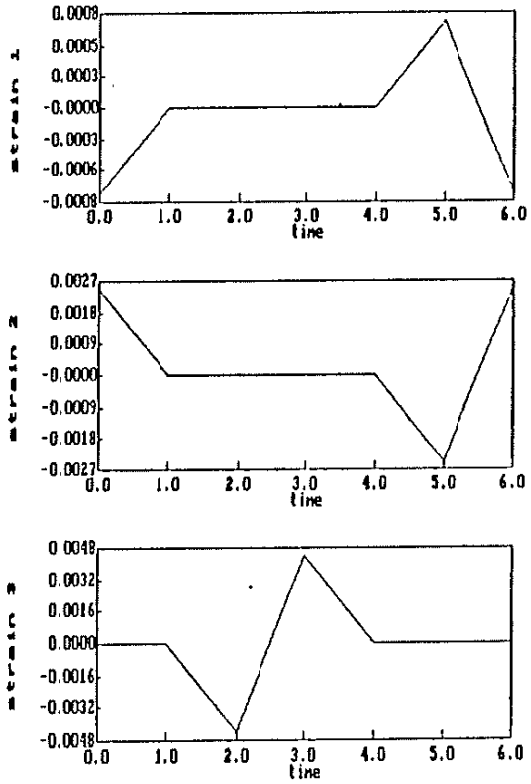

Figure 6.12 Strain Histories for Loading Path Three

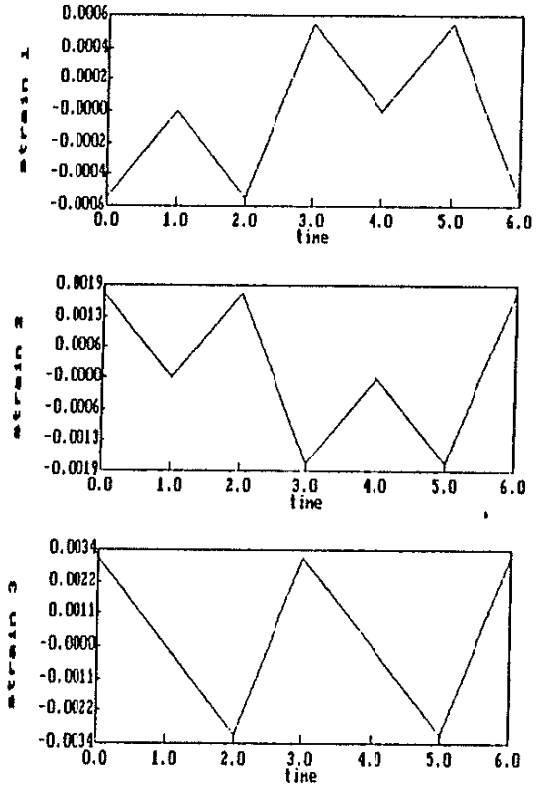

Figure 6.13 Strain Histories for Loading Path Four

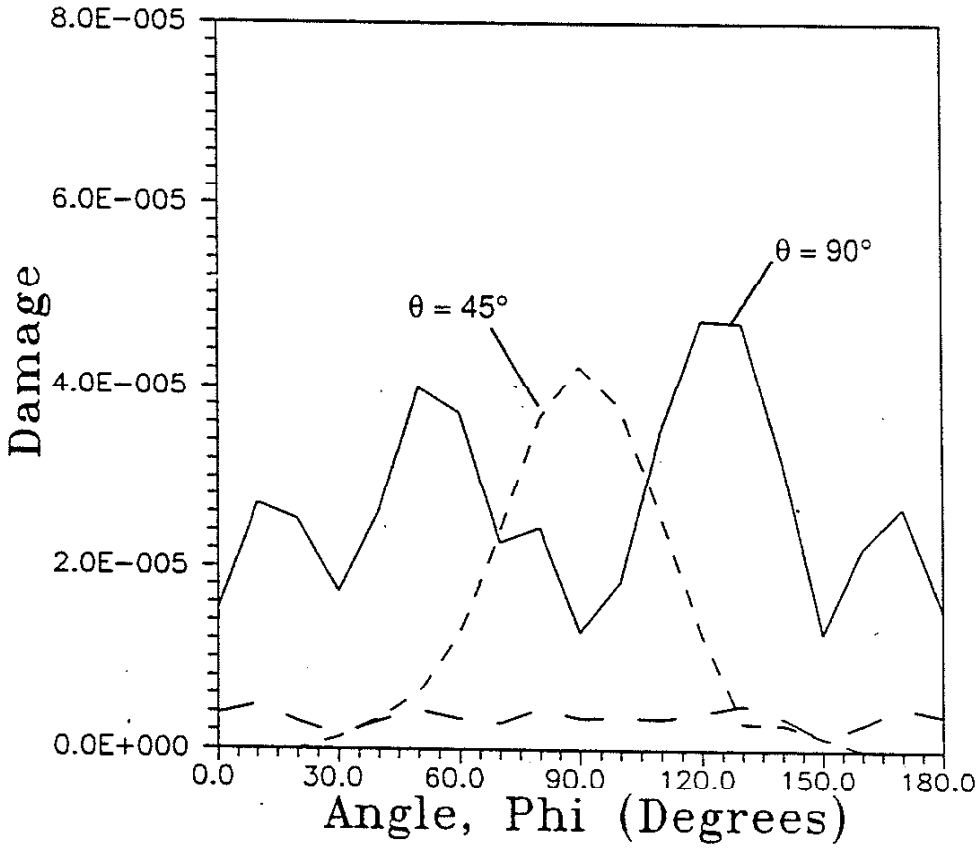

Figure 6.14 Plot of Shear Damage per Plane for Loading Case Three

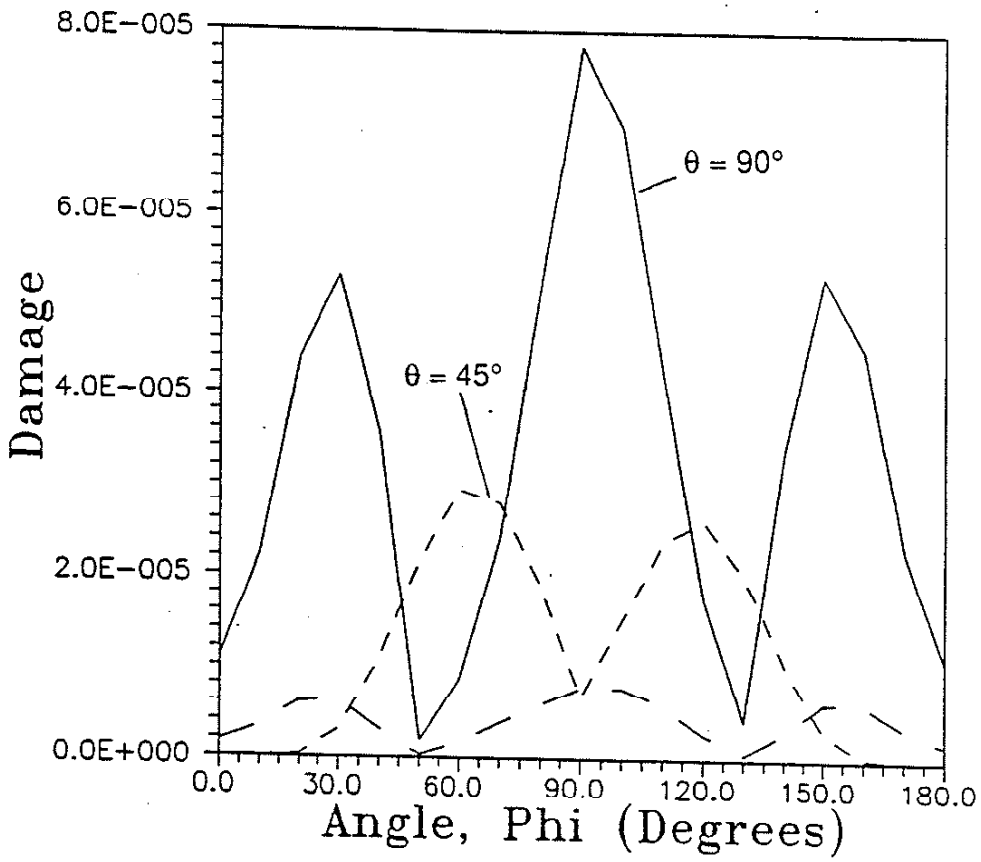

Figure 6.15 Plot of Shear Damage per Plane for Loading Case Four

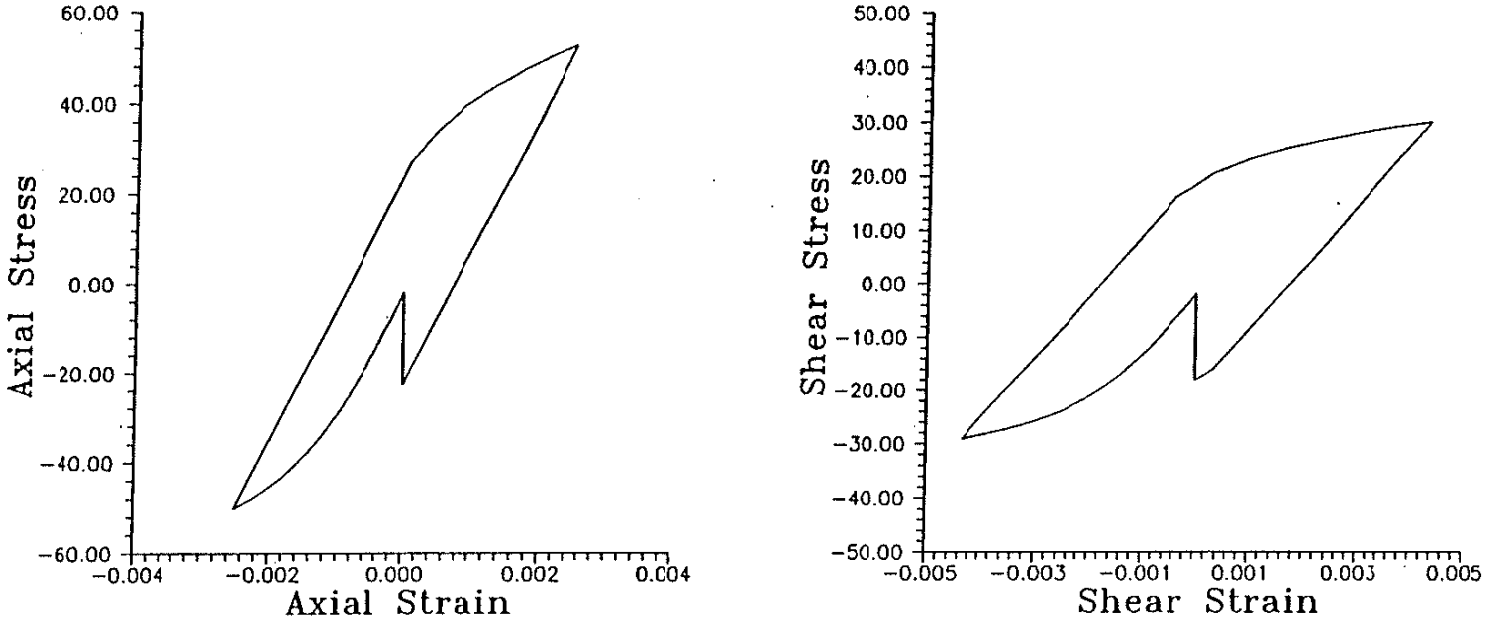

Figure 6.16 Axial and Shear Stress-Strain Response for Loading Path Three

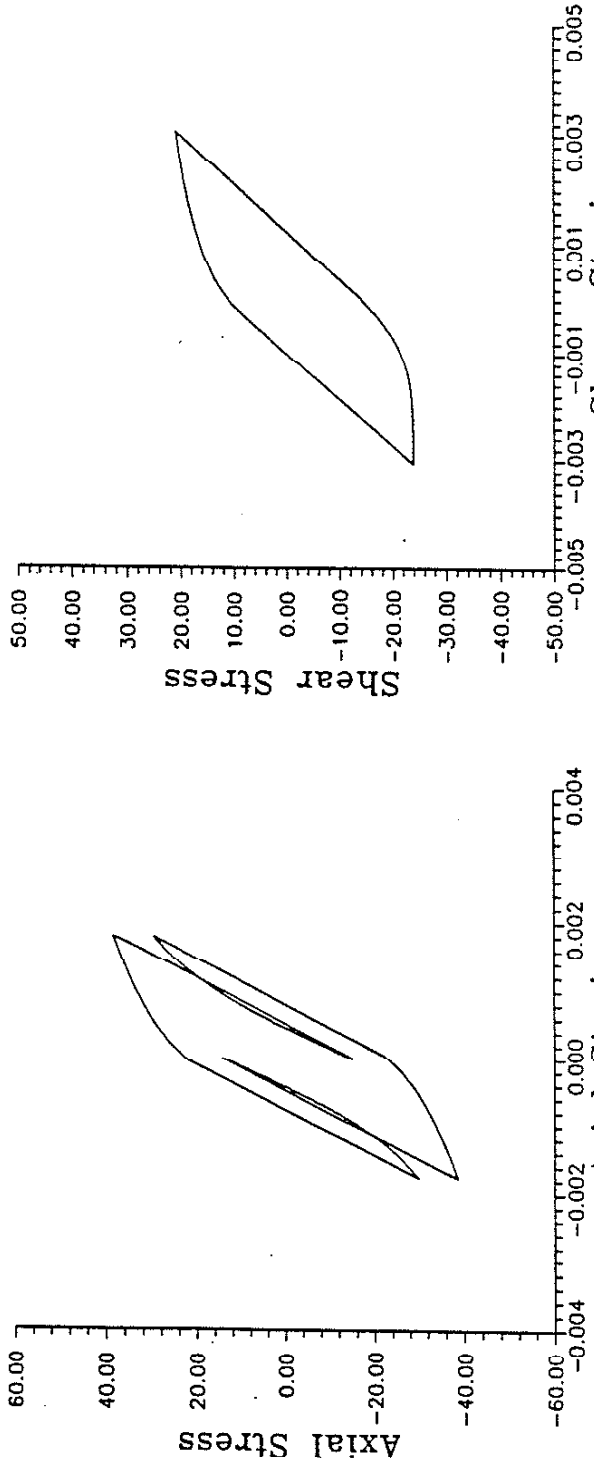

Figure 6.17 Axial and Shear Stress-Strain Response for Loading Path Four

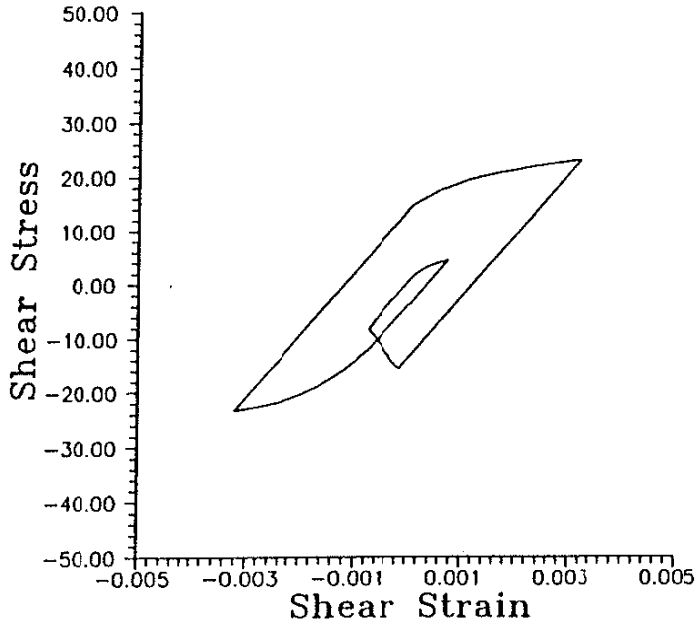

Figure 6.18 Shear Stress-Strain Response on $\phi = 130^{c}$ Plane

APPENDIX A: EDITING EXAMPLES

To understand the procedure for editing multiaxial histories, it is convenient to look at two examples. The first example is a uniaxial loading history. Procedures used for uniaxial editing are reviewed. Next, a multiaxial example is presented. The modifications to the uniaxial procedure are pointed out and discussed.

Figure A.1 shows an example of a uniaxial strain history. Assuming that the editing level is larger than the small subcycles (i.e., cycle BC) then the edited history should be that shown in Fig. A.2. This is obtained by following the few basic rules stated below. These are discussed in a step-by-step manner in the evaluation of the history given in Fig. A.1.

Uniaxial Editing Rules

Four data points are used for the evaluations of peaks and for the editing procedure. These points are:

i) "Last valid peak" (Last peak stored. Initially, the first point in the data file is labeled the "last valid peak".)

ii) Second_point

iii) Third_point

iv) Fourth_point

Rule 1: Using the three points, Second_point, Third_point and Fourth_point, determine if the Third_point is a reversal. If (Fourth_point - Third_point) is of opposite sign or equal to (Third_point - Second_point) then Third_point is a reversal). If Third_point is not a reversal, the value of Fourth_point becomes the Third_point and a new value of Fourth_point is read from the data file.

Rule 2: If Third-point is a reversal, using the three points, Last Valid peak, Second_point and Third_point determine if the Second_point is a possible peak. If (Second_point - Last valid peak) is of opposite sign or equal to (Third_point -Second_point) then the Second_point is a possible peak.

Rule 3: If the Third_point is a reversal and if the Second_point is a possible peak then:

A) If |Third_point - Second_point| > Edit Level then Second_point is now "Last valid peak" and is consequently stored. The value of the Third_point then becomes the Second_point and the next data point is read in from the data file as value for the new Third_point.

B) If |Third_point - Second_point| < Edit Level then Second_point remains a possible peak and the current Third_point value is dropped and a new Third_point is obtained by reading in the next point in the data file.

Rule 4: If the Third_point is a reversal and Second_point is not a possible peak then, drop the Second_point. The current Third_point then becomes the Second_point and the next point in the data file becomes the Third_point.

These rules are followed to obtain the history in Fig. A.2. This is discussed step-by-step below.

1. Last valid peak = Initial point = A
   Second_point = B
   Third_point = C, (Hereafter these are just listed in order of the last valid peak, second_point, third_point. In this case, ABC.)
   Fourth_point = D
   From Rule 1: (D-C) and (C-B) are of opposite sign, therefore C is a reversal.
   From Rule 2: (C-B) and (B-A) are of opposite sign, therefore B is a possible peak. From Rule 3B, |C-B| < Edit Level, therefore drop C and read in the next data point, D, to be the new Third_point.

2. From Rule 1 point D is a reversal. For points ABD, (B-A) and (D-B) are of the same sign, therefore from Rule 4, drop B. D now becomes the Second_point and E the Third_point.
3. For ADE, (D-A) and (E-D) are of opposite sign. Therefore, D is a possible peak. Since |E-D| < Edit Level, drop E. The new Third_point is F.
4. For ADF, (D-A) and (F-D) are of the same sign. Drop D. Therefore Second_point = F and Third_point = G.
5. For AFT, (F-A) and (G-F) are opposite in sign. F is a possible peak. (G-F) < Edit Level, therefore drop G. The Third_point now is H.
6. For AFH, (F-A) and (H-F) are opposite in sign. |H-F| < Edit Level, drop H, Third_point = I.
7. For AFI, (F-A) and (I-F) are of opposite sign. |I-F| > Edit Lever. From Rule 3A, store F. F is now Last Valid Peak, Second_point = I, and Third_point = J.

This process continues until all data is read. Figure A.2 shows the edited results for this example. The last data point in the file is stored as a peak.

When editing a multiaxial loading history, certain modifications must be made to the uniaxial editing procedure due to the multiaxial stress-strain response of a material. The editing procedure must be modified to enable all channels to be edited while maintaining the relationships between the channels with respect to time. This is discussed below. The rules for the multiaxial editing procedure are then given and explained using an example.

Multiaxial Editing Rules

For each channel, channel, x four data points are used:

i) Last valid Peak_x

ii) Second_point_x

iii) Third_point_x

iv) Fourth_point_x

Rule 1: Using the three points, Second_point_x, Third_point_x, and Fourth_point_x, determine if the Third_point_x is a reversal. If (Fourth point_x - Third_point_x) is of opposite sign or equal to (Third_point_x - Second_point_x)

then Third_point_x is a reversal. If Third_point_x is not a reversal, the value of Fourth_point_x becomes the Third_point_x and a new value of Fourth_point_x is read from the data file.

Rule 2: If the Third_point is a reversal, then using the three points, Last Valid peak_x, Second_point_x and Third_point_x determine if the Second_point_x is a possible peak. If (Second_point_x - Last valid peak_x) is of opposite sign or equal to (Third_point_x - Second_point_x) then the Second_point_x is a possible peak.

Rule 3: If the Third_point is a reversal and if the Second_point_x is a possible peak then:

A) If |Third_point_x - Second_point_x| > Edit Level then Second_point_x is now "Last valid peak_x" and flag to store the data is set. The value of the Third_point_x then becomes the Second_point_x and the next data point is read in from the data file as value for the new Third_point_x.

B) If |Third_point_x - Second_point_x| < Edit Level then Second_point_x remains a possible peak and the current Third_point_x value is dropped and a new Third_point_x is obtained by reading in the next point in the data file.

Rule 4: If the Third_point is a reversal and if Second_point_x is not a possible peak then:

Drop the Second_point_x. The current Third_point_x then becomes the Second_point_x and the next point in the dat file becomes the Third_point_x.

After the data on all channels corresponding to the current time is evaluated, if the store-flag is set then data from all channels corresponding to

the time of "last valid peak" are stored. In addition, if there are any current "possible peaks" that have not been stored yet, these are also stored. (Data corresponding to any specific time is stored only once and all channels of data are stored for this time.)

Multiaxial Example

An example of three multiaxial loading histories, simulating data taken from a strain gauge rosette, is shown in Fig. A.3. The multiaxial editing rules are followed to obtain the edited history shown in Fig. A.4. This procedure is discussed step-by-step below.

1.

1.1 Last valid peak_1 = A_1
Second_point_1 = B_1
Third_point_1 = C_1
(Hereafter, these are just listed in order of the Last valid peak_x, Second_point_x, Third_point_x. In this case, A_1, B_1, C_1.)
Fourth_point = D_1
From Rule 1: (D_1-C_1) and (C_1-B_1) are of opposite sign. Therefore C_1 is a reversal. From Rule 2: (C_1-B_1) and (B_1-A_1) are opposite sign and B_1 is a possible peak. From Rule 2B: $|C_1-B_1|$ < Edit Level, therefore drop C_1 and read in next data point, D_1, for Third_point_1.

1.2 $A_2B_2C_2$, Fourth_point = D_2
From Rule 1: (D_2-C_2) and (C_2-B_2) are of opposite sign, therefore C_2 is a reversal. From Rule 2: (C_2-B_2) and (B_2-A_2) are of opposite sign so B_2 is a possible peak. From Rule 3A: $|C_2-B_2|$ > Edit Level. Set flag to store data. Last valid peak_2 = B_2, Second_point_2 = C_2, Third_point_2 = D_2.

1.3 $A_3B_3C_3$, Fourth_point = D_3
From Rule 1: (C_3-B_3) and (B_3-A_3) are of same sign and thus C_3 is not a reversal. Drop C_3 and now Third-Point_3 = D_3.

Since the store-flag is set, store the data (the three strain values) corresponding to the time of the new last valid peak as well as the data corresponding to any current possible peaks that have not already been stored. From channel 2, B_2 was identified as a valid peak. Therefore B_1, B_2, B_3 strains are stored. From channel 1, B_1 was identified as a possible peak. However, the B strains were stored due to channel 2 and they must be stored only once.

2.

2.1 $A_1B_1D_1$
From Rule 1 and using data point E_1, D_1 is identified as a reversal.
From Rule 2, however, B_1 is not a possible peak (and is already stored).
From Rule 4, Second_point_1 = D_1, Third_point = E_1.

2.2 $B_2C_2D_2$
From Rule 1 and E_2, D_2 is not a reversal.
Thus, the Third_point_2 = E_2.

2.3 $A_3B_3D_3$
From Rule 1 and E_3, D_3 is not a reversal.
Thus, Third_point_3 = E_3.

3.

(Using similar procedures as above, the following explanation is abbreviated.)

3.1 $A_1D_1E_1$
E_1 is a reversal. D_1 is a possible peak.
$|E_1-D_1|$ < Edit Level. Drop E_1, Third_point_1 = F_1.

3.2 $B_2C_2E_2$
E_2 is a reversal. C_2 is a possible peak.
$|E_2-C_2|$ > Edit Level. Set store flag.
Last valid peak = C_2. Second_point_2 = E_2,
Third_point_2 = F_2.

3.3 $A_3B_3E_3$
E_3 is not a reversal. Drop E_3, Third_point_3 = F_3.

Since the store-flag is set, store the three strain values corresponding to the time fo C_2. (Store C_1, C_2, C_3.) Also store possible peaks. From channel 1, store strains corresponding to the time of D_1; store D_1, D_2, D_3.

4.

4.1 $A_1D_1F_1$
F_1 is a reversal. D_1 is not a peak, drop D_1. Second_point_1 = F_1, Third_point_1 = G_1.

4.2 $C_2E_2F_2$
F_2 is not a reversal, Third_point_2 = G_2.

4.3 $A_3B_3F_3$
F_3 is not a reversal, drop F_3, Third_point_3 = G_3.

5.

5.1 $A_1F_1G_1$
G_1 is a reversal. F_1 is a possible peak,
$|G_1-F_1|$ < Edit Level, drop G_1. Third_point_1 = H_1.

5.2 $C_2E_2G_2$
G_2 is a reversal. E_2 is a possible peak.
$|G_2-E_2|$ > Edit Level. Set store-flag.
Last valid peak_2 = E_2, Second_point_2 = G_2,
Third_point_2 = H_2.

5.3 $A_3B_3G_3$
G_3 is not a reversal, drop G_3, Third_point_3 = H_3.

Since store-flag is set, store strains corresponding to E_2. (Store E_1, E_2, E_3.) Store possible peak strains. F_1 is a possible peak. Therefore store F_1, F_2, F_3.

This process continues until the edited history shown in Fig. A.4 is obtained. In this example, only one extra set of data points was stored. These were the D strains.

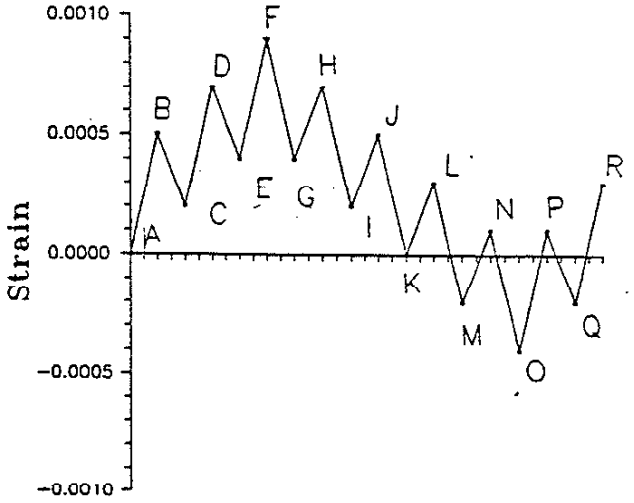

Figure A.1 Uniaxial Strain History

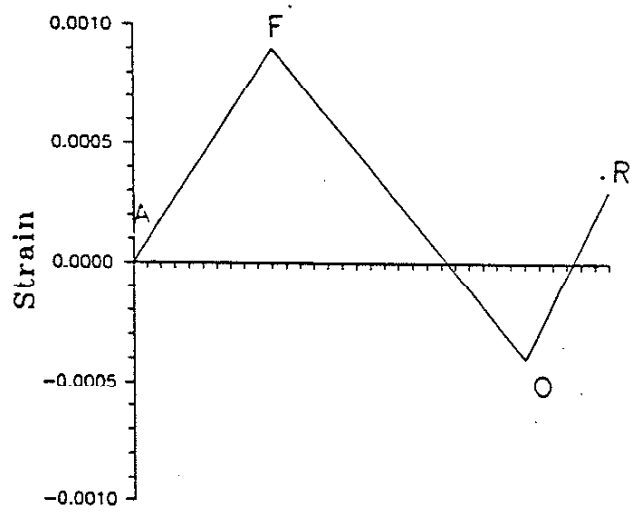

Figure A.2 Edited Uniaxial Strain History

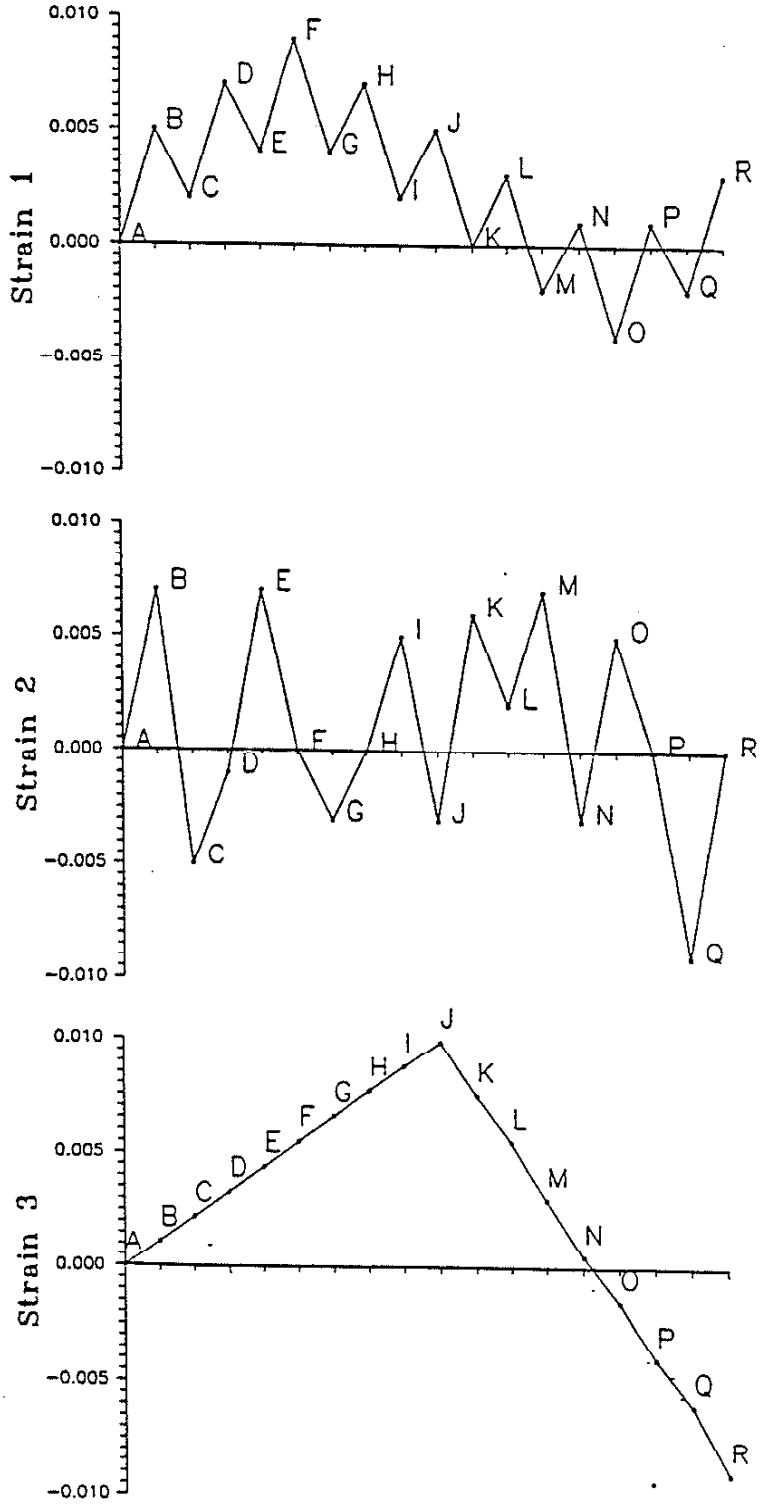

Figure A.3 Multiaxial Strain Histories

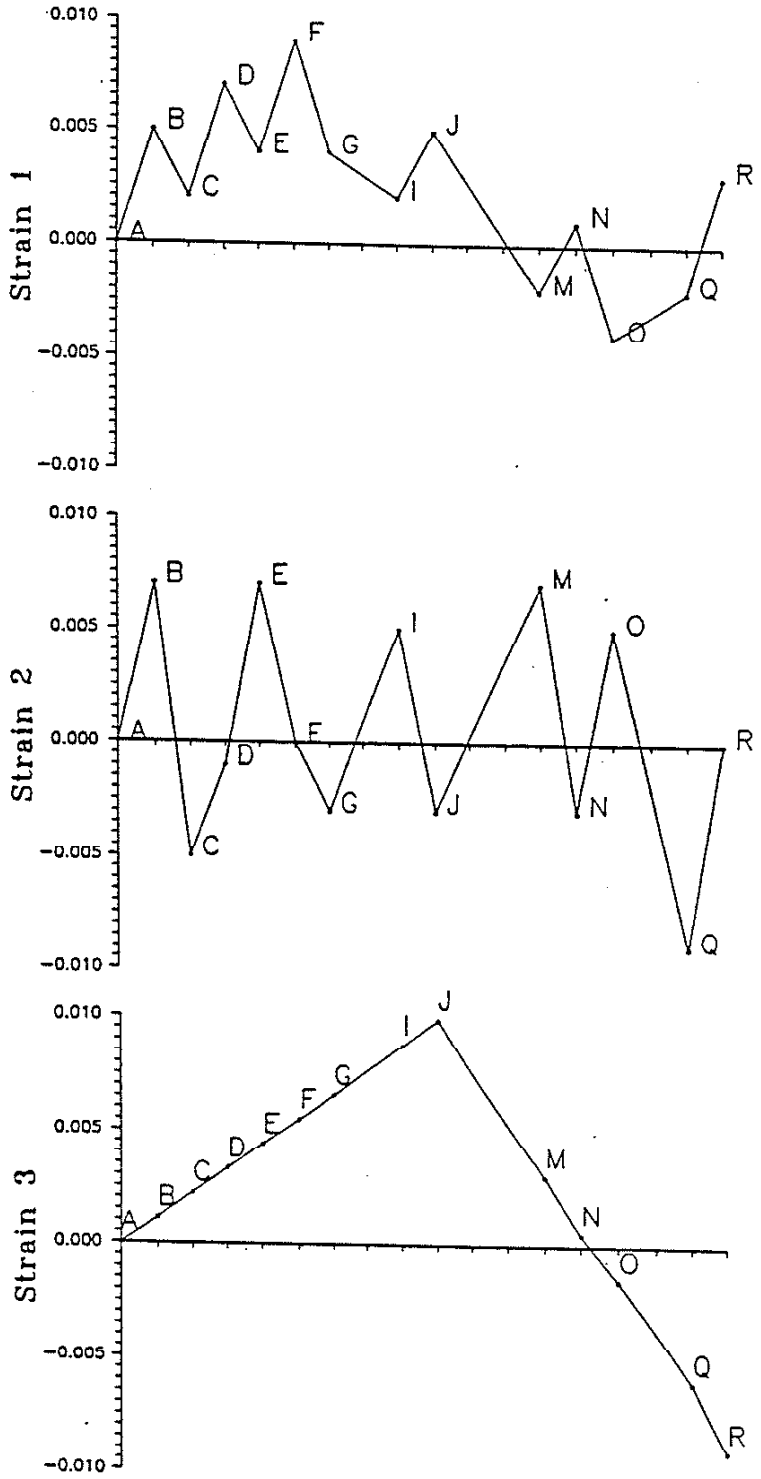

Figure A.4 Edited Multiaxial Strain Histories

APPENDIX B: IDENTITIES AND PROOFS USED IN DEVELOPMENT OF NON-PROPORTIONAL CYCLIC PLASTICITY MODEL EQUATIONS

The equation of the yield surface is taken to be

$$f = 3/2\ (S_{ij} - S^c_{ij})\ (S_{ij} - S^c_{ij})$$

Identity 1. $\dfrac{\partial f}{\partial \sigma_{kl}} = \dfrac{\partial f}{\partial S_{kl}}$

Proof:

$$\frac{\partial f}{\partial \sigma_{kl}} = (2)\frac{3}{2}\left[\frac{\partial}{\partial \sigma_{kl}}(S_{ij} - S^c_{ij})\right]\left[(S_{ij} - S^c_{ij})\right]$$

$$= 3\left[\frac{\partial}{\partial \sigma_{kl}}\left\{(\sigma_{ij} - 1/3\delta_{ij}\sigma_{mm}) - (\alpha_{ij} - 1/3\delta_{ij}\alpha_{mm})\right\}\right]\left[(S_{ij} - S^c_{ij})\right]$$

$$= 3\left[(\delta_{ik}\delta_{lj} - 1/3\delta_{ij}\delta_{mk}\delta_{ml})\right]\left[(S_{ij} - S^c_{ij})\right]$$

$$= 3\left[(S_{kj}\delta_{lj} - 1/3S_{ii}\delta_{mk}\delta_{ml}) - (S^c_{kj}\delta_{lj} - 1/3S_{ii}\delta_{mk}\delta_{ml})\right]$$

Since $S_{ii} = 0$, this reduces to

$$\frac{\partial f}{\partial \sigma_{kl}} = 3\left[S_{kl} - S^c_{kl}\right] \qquad \text{(B.1)}$$

$$\frac{\partial f}{\partial S_{kl}} = 2\frac{(3)}{2}\left[\frac{\partial}{\partial S_{kl}}(S_{ij} - S_{ij}^{c})\right]\left[(S_{ij} - S_{ij}^{c})\right]$$

$$= 3\left[\delta_{ik}\delta_{lj}\right]\left[(S_{ij} - S_{ij}^{c})\right]$$

$$\frac{\partial f}{\partial S_{kl}} = 3\left[S_{kl} - S_{kl}^{c}\right] \qquad \text{(B.2)}$$

From (B.1) and (B.2)

$$\boxed{\left(\frac{\partial f}{\partial \sigma_{kl}} = \frac{\partial f}{\partial S_{kl}}\right)}$$

Identity 2. $\frac{\partial f}{\partial \sigma_{ij}} d\sigma_{ij} = \frac{\partial f}{\partial S} dS_{ij}$

Proof:

From Identity 1,

$$\frac{\partial f}{\partial \sigma_{ij}} = \frac{\partial f}{\partial S_{ij}}$$

therefore

$$\frac{\partial f}{\partial \sigma_{ij}} d\sigma_{ij} = \frac{\partial f}{\partial S_{ij}} dS_{ij}$$

can be restated as

$$\frac{\partial f}{\partial S_{ij}} d\sigma_{ij} = \frac{\partial f}{\partial S_{ij}} dS_{ij}$$

From von Mises yield criteria the left-hand side of the equation is

$$\frac{\partial f}{\partial \sigma_{ij}} d\sigma_{ij} = 3\,(S_{ij} - S_{ij})\, d\sigma_{ij} \qquad \text{(B.3)}$$

Expanding the right-hand side of the equation results in

$$\frac{\partial f}{\partial S_{ij}} dS_{ij} = \frac{\partial f}{\partial S_{ij}} (d\sigma_{ij} - 1/3\ \delta_{ij} d\sigma_{kk})$$

Using von Mises yield criteria, this is

$$\frac{\partial f}{\partial S_{ij}} dS_{ij} = 3(S_{ij} - S_{ij}^{c})(d\sigma_{ij} - 1/3\ \delta_{ij} d\sigma_{kk})$$

Since

$$S_{ij}\delta_{ij} = 0$$

this is

$$\frac{\partial f}{\partial S_{ij}} dS_{ij} = 3\ (S_{ij} - S_{ij}^{c})\ d\sigma_{ij} \qquad \text{(B.4)}$$

from (B.3) and (B.4)

$$\boxed{\frac{\partial f}{\partial \sigma_{ij}} d\sigma_{ij} = \frac{\partial f}{\partial S_{ij}} dS_{ij}}$$

Identity 3. $S_{ij}dS_{ij} = S_{ij}d\sigma_{ij}$

Proof:

$$S_{ij}dS_{ij} = S_{ij}(d\sigma_{ij} - 1/3\delta_{ij}d\sigma_{mm})$$

$$= S_{ij}d\sigma_{ij} - 1/3S_{jj}d\sigma_{mm}$$

Since $S_{jj} = 0$

$$\boxed{(S_{ij}dS_{ij} = S_{ij}d\sigma_{ij})}$$

APPENDIX C: EXAMPLES OF PLANE ORIENTATIONS

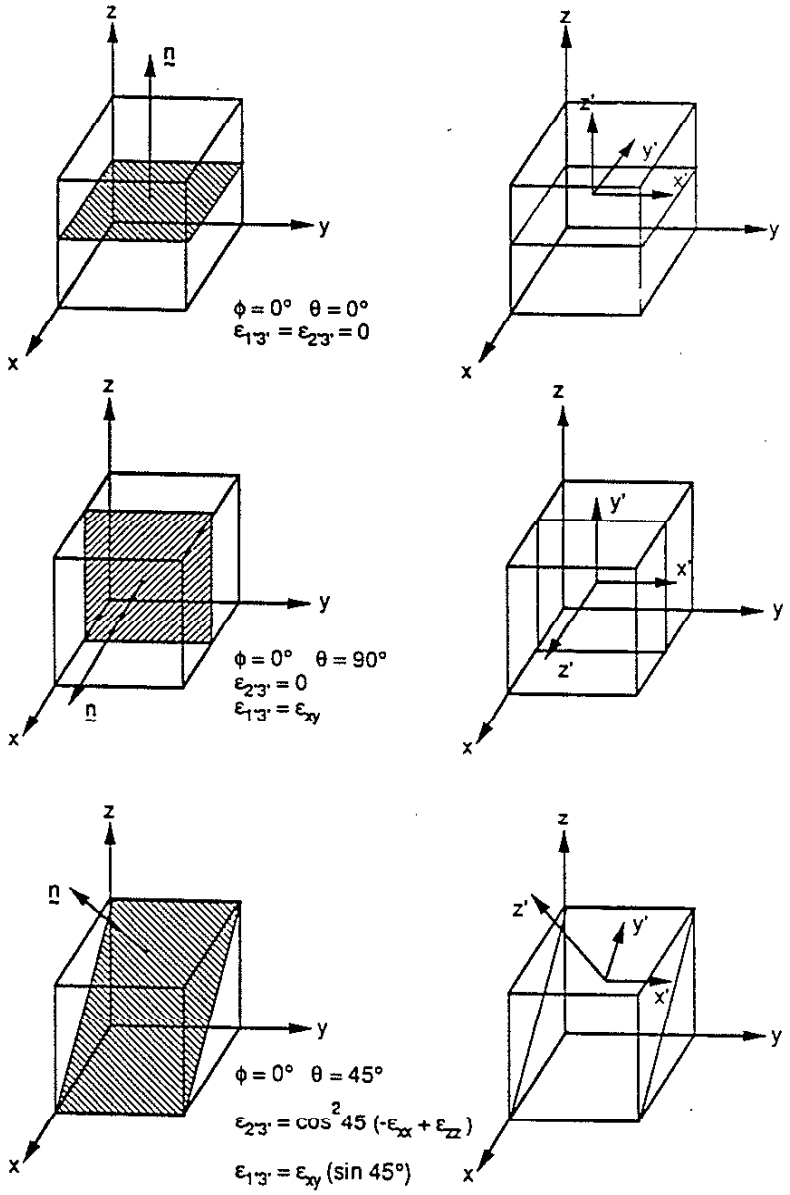

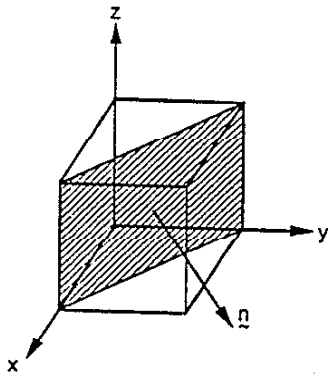

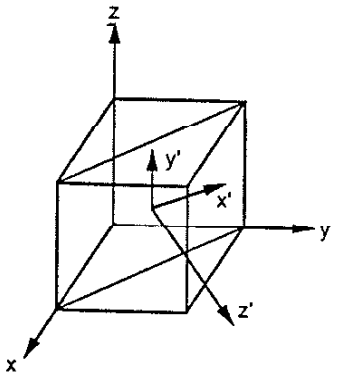

$\phi = 45°\ \ \theta = 90°$

$\varepsilon_{1'3'} = -\varepsilon_{xx} \cos^2 45° + \varepsilon_{yy} \sin^2 45°$

$+ \varepsilon_{xy} (-\sin^2 45 + \cos^2 45°)$

$\varepsilon_{1'3'} = \varepsilon_{xx} \cos^2 45° + \varepsilon_{yy} \sin^2 45°$

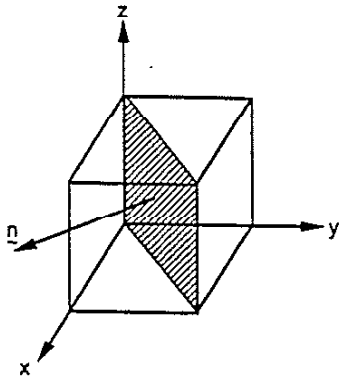

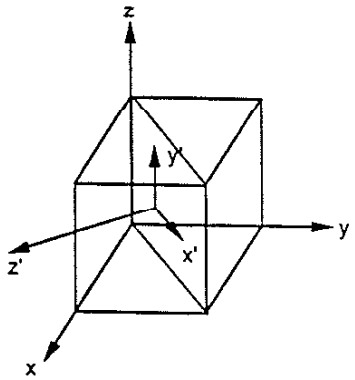

$\phi = -45°\ \ \theta = 90°$

$\varepsilon_{23} = 0$

$\varepsilon_{13} (-\sin(-45°) \cos(-45°) \varepsilon_{xx}) + (\sin(-45°) \cos(-45°) \varepsilon_{yy}$

$+ \varepsilon_{xy} (-\sin^2(-45°) + \cos^2(-45°))$

APPENDIX D: INPUT VALUES USED FOR NONPROPORTIONAL HISTORIES

Channel 1				Channel 2						
NO	VALUE	RATE	LOAD	NO	VALUE	RATE	LOAD		PEAK	PEAK
1	-9.30	.7	-470	1	66.28	1.0	3310	1	0.0	0.0
2	67.40	.9	3370	2	-37.21	.5	-1870	2	.7	1.0
3	-30.23	.9	-1520	3	15.12	.4	750	3	1.6	1.4
4	67.44	.9	3370	4	-27.91	.7	-1400	4	2.5	1.8
5	-32.56	.9	-1630	5	43.02	.8	2150	5	3.4	2.5
6	61.63	.7	3080	6	-43.02	.5	-2160	6	4.3	3.3
7	-18.60	.8	-930	7	11.63	.6	580	7	5.0	3.8
8	67.44	.8	3370	8	-48.84	.6	-2450	8	5.8	4.3
9	-22.09	.8	-1110	9	20.93	.4	1040	9	6.7	5.0
10	65.12	.8	3250	10	-27.91	.7	-1400	10	7.5	5.4
11	-24.42	.8	-1230	11	51.16	.9	2550	11	8.3	6.2
12	62.79	.4	3130	12	-43.02	.5	-2160	12	9.1	7.0
13	18.60	.5	930	13	13.95	.4	690	13	9.5	7.6
14	70.93	.9	3540	14	-34.88	1.1	-1750	14	10.0	8.0
15	-25.58	.8	-1280	15	81.40	1.0	4070	15	10.9	9.1
16	65.12	.4	3250	16	-24.42	.4	-1230	16	11.7	10.1
17	16.28	.4	810	17	20.93	.5	1040	17	12.1	10.5
18	62.79	.7	3130	18	-32.56	1.0	-1630	18	12.6	11.0
19	-16.28	.8	-820	19	74.42	.4	3720	19	13.3	11.9
20	68.61	.9	3430	20	27.91	.4	1390	20	14.1	12.4
21	-29.07	.4	-1460	21	73.26	.9	3660	21	15.0	12.8
22	15.12	.4	750	22	-24.42	.9	-1230	22	15.4	13.7
23	-30.23	.8	-1520	23	69.77	.4	3480	23	15.8	14.6
24	55.81	.5	2790	24	25.58	.5	1270	24	16.6	15.0
25	5.81	.6	290	25	76.74	.4	3830	25	17.1	15.4
26	69.77	.9	3480	26	27.91	.5	1390	26	17.6	15.9
27	-26.74	1.0	-1340	27	82.56	1.1	4120	27	18.5	16.4
28	76.74	.6	3830	28	-32.56	.9	-1630	28	19.5	17.5
29	11.63	.5	580	29	67.44	.6	3370	29	20.1	18.4
30	67.44	.6	3370	30	4.65	.6	230	30	20.6	19.0
31	4.64	.6	230	31	74.42	1.1	3720	31	21.2	19.6
32	70.93	.5	3540	32	-39.54	.5	-1980	32	21.8	20.6
33	15.12	.5	750	33	16.28	.5	810	33	22.3	21.2
34	72.09	.4	3600	34	-37.20	1.1	-1860	34	22.8	21.7
35	23.26	.4	1160	35	87.22	1.0	4360	35	23.3	22.8
36	67.44	.9	3370	36	-22.09	.7	-1110	36	23.7	23.8
37	-27.91	.9	-1400	37	55.81	.4	2790	37	24.6	24.5
38	69.77	.4	3480	38	11.63	.6	580	38	25.5	24.9
39	22.09	.4	1100	39	74.42	.6	3720	39	25.9	25.5
40	68.61	.5	3430	40	13.95	.6	690	40	26.3	26.1
41	18.60	.4	930	41	81.40	1.0	4070	41	26.8	26.7
42	66.28	.4	3310	42	-31.40	.9	-1570	42	27.2	27.7

Maximum "Value" = 100.00 (100 percent)
Maximum "Load" = 5000 pounds
Maximum "No" = 212 (212 points in load history)

43	17.44	.5	870	43	69.77	.6	3480	43	27.7	28.7
44	70.93	.8	3540	44	2.33	.8	110	44	28.2	29.3
45	-18.60	.8	-930	45	88.37	1.0	4410	45	29.0	30.1
46	69.77	.5	3480	46	-23.26	.8	-1170	46	29.8	31.1
47	18.60	.5	930	47	60.47	.5	3020	47	30.3	31.9
48	74.42	.5	3720	48	3.49	.7	170	48	30.8	32.4
49	23.26	.4	1160	49	83.72	.5	4180	49	31.3	33.1
50	66.28	1.0	3310	50	27.91	.5	1390	50	31.7	33.7
51	-37.21	.9	-1870	51	79.07	1.2	3950	51	32.6	34.1
52	63.95	.5	3190	52	-52.33	1.1	-2620	52	33.5	35.3
53	5.81	.6	290	53	65.12	.5	3250	53	34.1	36.4
54	68.61	.4	3430	54	13.95	.5	690	54	34.7	36.9
55	22.09	.6	1100	55	73.26	1.0	3660	55	35.1	37.4
56	87.21	.6	4360	56	-30.23	.5	-1520	56	35.7	38.4
57	20.93	.4	1040	57	23.26	.4	1160	57	36.3	38.9
58	68.61	.9	3430	58	-20.93	.8	-1050	58	36.7	39.3
59	-25.58	.9	-1280	59	65.12	1.0	3250	59	37.6	40.1
60	74.42	.8	3720	60	-47.67	1.0	-2390	60	38.5	41.1
61	-13.90	.7	-700	61	55.81	.4	2790	61	39.3	42.1
62	67.44	.8	3370	62	8.14	.6	400	62	40.1	42.5
63	-19.77	.8	-990	63	68.61	.9	3430	63	40.9	43.1
64	62.79	.8	3130	64	-29.07	.7	-1460	64	41.7	44.0
65	-19.77	.9	-990	65	52.33	.8	2610	65	42.4	44.7
66	74.42	.9	3720	66	-34.88	1.1	-1750	66	43.3	45.5
67	-19.77	.8	-990	67	79.07	1.0	3950	67	44.1	46.6
68	69.77	1.0	3480	68	-25.58	.9	-1280	68	45.0	47.5
69	-34.88	1.1	-1750	69	69.77	.5	3480	69	45.9	48.4
70	86.05	1.0	4300	70	18.60	.6	930	70	47.0	48.9
71	-24.42	.5	-1230	71	81.40	.9	4070	71	48.1	49.5
72	24.42	.4	1220	72	-20.93	.6	-1050	72	48.5	50.4
73	-19.77	.9	-990	73	48.84	.4	2440	73	48.9	51.1
74	77.91	1.0	3890	74	4.66	.5	230	74	49.8	51.5
75	-34.88	1.0	-1750	75	59.30	.5	2960	75	50.9	52.0
76	72.09	.6	3600	76	5.81	.5	290	76	51.8	52.5
77	11.63	.6	580	77	55.81	.5	2790	77	52.4	52.9
78	77.91	1.0	3890	78	6.98	.5	340	78	53.0	53.4
79	-26.74	.9	-1340	79	55.81	.4	2790	79	54.0	53.8
80	72.09	.9	3600	80	8.41	.5	420	80	54.9	54.3
81	-23.26	.5	-1170	81	60.47	.8	3020	81	55.8	54.7
82	27.91	.4	1390	82	-22.09	.9	-1110	82	56.2	55.5
83	-15.12	.8	-760	83	76.74	.6	3830	83	56.6	56.4
84	70.93	.8	3540	84	8.14	.8	400	84	57.4	57.0

85	-19.77	.7	-990	85	100.00	.5	5000	85	58.3	57.9
86	59.30	.8	2960	86	51.16	.4	2550	86	59.0	58.3
87	-27.91	.9	-1400	87	95.35	.5	4760	87	59.8	58.7
88	65.12	.8	3250	88	43.02	.4	2150	88	60.6	59.2
89	-20.93	.9	-1050	89	88.37	.6	4410	89	61.4	59.6
90	72.09	.8	3600	90	18.60	.4	930	90	62.3	60.3
91	-18.60	.7	-930	91	66.28	.8	3310	91	63.1	60.7
92	58.14	.4	2900	92	-23.26	1.0	-1170	92	63.8	61.5
93	13.95	.5	690	93	82.56	1.0	4120	93	64.2	62.5
94	70.93	.5	3540	94	-26.74	.9	-1340	94	64.8	63.5
95	18.60	.5	930	95	69.77	.9	3480	95	65.3	64.4
96	68.61	.9	3430	96	-24.42	.7	-1230	96	65.7	65.3
97	-27.91	1.0	-1400	97	47.67	.7	2380	97	66.6	65.9
98	79.07	.7	3950	98	-27.91	.9	-1400	98	67.6	66.6
99	5.81	.5	290	99	68.61	.9	3430	99	68.3	67.5
100	61.63	.4	3080	100	-32.56	.9	-1630	100	68.8	68.5
101	17.44	.5	870	101	69.77	.7	3480	101	69.2	69.4
102	67.44	.8	3370	102	-9.30	.7	-470	102	69.6	70.1
103	-19.77	.8	-990	103	67.40	.9	3370	103	70.4	70.8
104	72.09	.9	3600	104	-30.23	.9	-1520	104	71.3	71.7
105	-25.58	.4	-1280	105	67.44	.9	3370	105	72.2	72.6
106	20.93	.4	1040	106	-32.56	.9	-1630	106	72.6	73.6
107	-26.74	.9	-1340	107	61.63	.7	3080	107	73.1	74.4
108	68.61	.8	3430	108	-18.60	.8	-930	108	73.9	75.2
109	-20.93	.7	-1050	109	67.44	.8	3370	109	74.8	76.0
110	50.00	.4	2500	110	-22.09	.8	-1110	110	75.4	76.8
111	6.98	.5	340	111	65.12	.8	3250	111	75.8	77.6
112	66.28	1.0	3310	112	-24.42	.8	-1230	112	76.4	78.4
113	-37.21	.5	-1870	113	62.79	.4	3130	113	77.3	79.2
114	15.12	.4	750	114	18.60	.5	930	114	77.8	79.6
115	-27.91	.7	-1400	115	70.93	.9	3540	115	78.2	80.1
116	43.02	.8	2150	116	-25.58	.8	-1280	116	78.8	81.0
117	-43.02	.5	-2160	117	65.12	.4	3250	117	79.6	81.8
118	11.63	.6	580	118	16.28	.4	810	118	80.1	82.3
119	-48.84	.6	-2450	119	62.79	.7	3130	119	80.7	82.7
120	20.93	.4	1040	120	-16.28	.8	-820	120	81.3	83.4
121	-27.91	.7	-1400	121	68.61	.9	3430	121	81.8	84.2
122	51.16	.9	2550	122	-29.07	.4	-1460	122	82.5	85.1
123	-43.02	.5	-2160	123	15.12	.4	750	123	83.4	85.5
124	13.95	.4	690	124	-30.23	.8	-1520	124	83.9	85.9
125	-34.88	1.1	-1750	125	55.81	.5	2790	125	84.4	86.7
126	81.40	1.0	4070	126	5.81	.6	290	126	85.4	87.2

127	-24.42	.4	-1230	127	69.77	.9	3480	127	86.4	87.8
128	20.93	.5	1040	128	-26.74	1.0	-1340	128	86.8	88.7
129	-32.56	1.0	-1630	129	76.74	.6	3830	129	87.3	89.6
130	74.42	.4	3720	130	11.63	.5	580	130	88.3	90.2
131	27.91	.4	1390	131	67.44	.6	3370	131	88.7	90.7
132	73.26	.9	3660	132	4.64	.6	230	132	89.2	91.3
133	-24.42	.9	-1230	133	70.93	.5	3540	133	90.1	91.9
134	69.77	.4	3480	134	15.12	.5	750	134	90.9	92.4
135	25.58	.5	1270	135	72.09	.4	3600	135	91.3	93.0
136	76.74	.4	3830	136	23.26	.4	1160	136	91.8	93.4
137	27.91	.5	1390	137	67.44	.9	3370	137	92.3	93.8
138	82.56	1.1	4120	138	-27.91	.9	-1400	138	92.8	94.7
139	-32.56	.9	-1630	139	69.77	.4	3480	139	93.8	95.6
140	67.44	.6	3370	140	22.09	.4	1100	140	94.7	96.0
141	4.65	.6	230	141	68.61	.5	3430	141	95.3	96.5
142	74.42	1.1	3720	142	18.60	.4	930	142	96.0	96.9
143	-39.54	.5	-1980	143	66.28	.4	3310	143	97.0	97.4
144	16.28	.5	810	144	17.44	.5	870	144	97.5	97.8
145	-37.20	1.1	-1860	145	70.93	.8	3540	145	98.0	98.3
146	87.22	1.0	4360	146	-18.60	.8	-930	146	99.2	99.1
147	-22.09	.7	-1110	147	69.77	.5	3480	147	100.2	99.9
148	55.81	.4	2790	148	18.60	.5	930	148	100.9	100.4
149	11.63	.6	580	149	74.42	.5	3720	149	101.3	100.9
150	74.42	.6	3720	150	23.26	.4	1160	150	101.9	101.4
151	13.95	.6	690	151	66.28	1.0	3310	151	102.4	101.8
152	81.40	1.0	4070	152	-37.21	.9	-1870	152	103.1	102.7
153	-31.40	.9	-1570	153	63.95	.5	3190	153	104.1	103.7
154	69.77	.6	3480	154	5.81	.6	290	154	105.0	104.2
155	2.33	.8	110	155	68.61	.4	3430	155	105.6	104.8
156	88.37	1.0	4410	156	22.09	.6	1100	156	106.4	105.2
157	-23.26	.8	-1170	157	87.21	.6	4360	157	107.5	105.8
158	60.47	.5	3020	158	20.93	.4	1040	158	108.2	106.4
159	3.49	.7	170	159	68.61	.9	3430	159	108.8	106.9
160	83.72	.5	4180	160	-25.58	.9	-1280	160	109.5	107.7
161	27.91	.5	1390	161	74.42	.8	3720	161	110.0	108.7
162	79.07	1.2	3950	162	-13.90	.7	-700	162	110.5	109.5
163	-52.33	1.1	-2620	163	67.44	.8	3370	163	111.7	110.2
164	65.12	.5	3250	164	-19.77	.8	-990	164	112.8	111.0
165	13.95	.5	690	165	62.79	.8	3130	165	113.2	111.8
166	73.26	1.0	3660	166	-19.77	.9	-990	166	113.8	112.5
167	-30.23	.5	-1520	167	74.42	.9	3720	167	114.7	113.4
168	23.26	.4	1160	168	-19.77	.8	-990	168	115.2	114.3

169	-20.93	.8	-1050	169	69.77	1.0	3480	169	115.6	115.1
170	65.12	1.0	3250	170	-34.88	1.1	-1750	170	116.4	116.1
171	-47.67	1.0	-2390	171	86.05	1.0	4300	171	117.5	117.2
172	55.81	.4	2790	172	-24.42	.5	-1230	172	118.4	118.2
173	8.14	.6	400	173	24.42	.4	1220	173	118.9	118.6
174	68.61	.9	3430	174	-19.77	.9	-990	174	119.4	119.1
175	-29.07	.7	-1460	175	77.91	1.0	3890	175	120.3	120.0
176	52.33	.8	2610	176	-34.88	1.0	-1750	176	121.1	121.0
177	-34.88	1.1	-1750	177	72.09	.6	3600	177	121.9	122.0
178	79.07	1.0	3950	178	11.63	.6	580	178	122.9	122.5
179	-25.58	.9	-1280	179	77.91	1.0	3890	179	123.9	123.1
180	69.77	.5	3480	180	-26.74	.9	-1340	180	124.8	124.1
181	18.60	.6	930	181	72.09	.9	3600	181	125.2	125.0
182	81.40	.9	4070	182	-23.26	.5	-1170	182	125.8	125.9
183	-20.93	.6	-1050	183	27.91	.4	1390	183	126.8	126.4
184	48.84	.4	2440	184	-15.12	.8	-760	184	127.4	126.8
185	4.66	.5	230	185	70.93	.8	3540	185	127.8	127.6
186	59.30	.5	2960	186	-19.77	.7	-990	186	128.3	128.4
187	5.81	.5	290	187	59.30	.8	2960	187	128.8	129.1
188	55.81	.5	2790	188	-27.91	.9	-1400	188	129.3	129.9
189	6.98	.5	340	189	65.12	.8	3250	189	129.7	130.8
190	55.81	.4	2790	190	-20.93	.9	-1050	190	130.2	131.6
191	8.41	.5	420	191	72.09	.8	3600	191	130.6	132.4
192	60.47	.8	3020	192	-18.60	.7	-930	192	131.1	133.3
193	-22.09	.9	-1110	193	58.14	.4	2900	193	131.9	134.0
194	76.74	.6	3830	194	13.95	.5	690	194	132.8	134.4
195	8.14	.8	400	195	70.93	.5	3540	195	133.4	134.9
196	100.00	.5	5000	196	18.60	.5	930	196	134.2	135.4
197	51.16	.4	2550	197	68.61	.9	3430	197	134.7	135.8
198	95.35	.5	4760	198	-27.91	1.0	-1400	198	135.1	136.7
199	43.02	.4	2150	199	79.07	.7	3950	199	135.6	137.7
200	88.37	.6	4410	200	5.81	.5	290	200	136.0	138.4
201	18.60	.4	930	201	61.63	.4	3080	201	136.6	138.9
202	66.28	.8	3310	202	17.44	.5	870	202	137.1	139.3
203	-23.26	1.0	-1170	203	67.44	.8	3370	203	137.9	139.8
204	82.56	1.0	4120	204	-19.77	.8	-990	204	138.9	140.6
205	-26.74	.9	-1340	205	72.09	.9	3600	205	139.9	141.4
206	69.77	.9	3480	206	-25.58	.4	-1280	206	140.8	142.3
207	-24.42	.7	-1230	207	20.93	.4	1040	207	141.6	142.7
208	47.67	.7	2380	208	-26.74	.9	-1340	208	142.3	143.2
209	-27.91	.9	-1400	209	68.61	.8	3430	209	143.0	144.1
210	68.61	.9	3430	210	-20.93	.7	-1050	210	143.9	144.9

211	-32.56	.9	-1630	211	50.00	.4	2500	211	144.8	145.5
212	69.77	.7	3480	212	6.98	.5	340	212	145.8	145.9

TOTAL TIME= 146.5 SEC 2.4 MIN.

REFERENCES

2.1 Wetzel, R. M. (ed.), Fatigue Under Complex Loading: Analyses and Experiments, Society of Automotive Engineers, Warrendale, PA, 1977.

2.2 Manual on Low Cycle Fatigue Testing, ASTM STP 465, 1969.

2.3 ASTM Standard E606-80, Annual Book of ASTM Standards, 1980.

2.4 SAE Fatigue Design Handbook, Vol. 4, J. A. Graham, ed., Society of Automotive Engineers, Inc., 1968.

2.5 Tipton, S. M., "Fatigue Behavior under Multiaxial Loading in the Presence of a Notch: Methodologies for the Prediction of Life to Crack Initiation and Life Spent in Crack Propagation," Ph.D. Thesis, Mechanical Engineering Dept., Stanford University, Stanford, CA, 1984.

2.6 Sonsino, C. M., and Grubisic, V., "Fatigue Behavior of Cyclically Softening and Hardening Steels under Multiaxial Elastic-Plastic Deformation," Multiaxial Fatigue, ASTM STP 853, K. J. Miller and M. W. Brown, Eds., ASTM, Philadelphia, 1985, pp. 586-605.

2.7 Kanazawa, K., Miller, K. J., and Brown, M. W., "Low Cycle Fatigue under Out-of-Phase Loading Conditions," J. of Engineering Materials and Technology, Trans. ASME (H), Vol. 99, 1977, pp. 222-228.

2.8 Doong, Shiing-Hwa, "A Plasticity Theory of Metals Based on the Dislocation Substructure," Materials Engineering Report No. 148, University of Illinois at Urbana-Champaign, UILU-ENG-89-3602, 1988.

2.9 Nishino, S., Hamada, N., Sakane, M., Ohnami, M., Matsumura, N., Tokizane, M., "Microstructural Study of Cyclic Strain Hardening Behavior in Biaxial Stress States at Elevated Temperature," Fatigue and Fracture of Engineering Materials and Structures, Vol. 9, No. 1, 1986, pp. 65-77.

2.10 Cailletaud, G., Doquet, V., and Pineau, A., "Prediction of Macroscopic Multiaxial Behavior from Microstructural Observations," to be published in the Proceedings of the Third Int. Conf. on Biaxial/Multiaxial Fatigue, Vol. 1, held April 3-6, 1989 in Stuffgart, West Germany.

2.11 Fatigue Mechanisms: Advances in Quantitative Measurement of Physical Damage, Lankford, J., Davidson, D. L., Morris, W. L., Wei, R. P. (eds.), ASTM STP 811, ASTM 1983, (Summary), pp. 487-492.

2.12 Parsons, M. W., and Pascoe, K. J., "Observations of Surface Deformation, Crack Initiation and Growth in Low-Cycle Fatigue under Biaxial Stress," Materials Science and Engineering, Vol. 22, 1976, pp. 31-50.

2.13 Bannantine, J. A., and Socie, D. F., "Observations of Cracking Behavior in Tension and Torsion Low Cycle Fatigue," Low Cycle Fatigue, ASTM STP 942, H. D. Solomon, G. R. Halford, L. R. Kaisand, and B. N. Leis (Eds.), ASTM, Philadelphia, 1988, pp. 899-921.

2.14 Socie, D. F., Waill, L. A., and Dittmer, D. F., "Biaxial Fatigue of Inconel 718 Including Mean Stress Effects," Multiaxial Fatigue, ASTM STP 853, K. J. Miller and M. W. Brown, (Eds.), ASTM, Philadelphia, 1985, pp. 463-481.

2.15 Hua, C. T., and Socie, D. F., "Fatigue Damage in 1045 Steel under Variable Amplitude Biaxial Loading," Fatigue of Engineering Materials and Structures, Vol. 8, No. 2, 1985, pp. 101-114.

2.16 Marco, A. M., and Starkey, W. L., "A Concept of Fatigue Damage," Trans. American Society of Mechanical Engineers, Vol. 76, 1954, pp. 627-632.

2.17 Nisitani, H., Japan Society of Mechanical Engineers Bulletin, Vol. 11, No. 48, 1968, pp. 947-957.

2.18 Nisitani, H., and Kawano, Japan Society of Mechanical Engineers Bulletin, Vol. 15, No. 82, 1972, pp. 433-438.

2.19 Robillard, M., and Cailletaud, G., "Directionally Defined Damage in Multiaxial Low Cycle Fatigue: Experimental Evidence and Tentative Modeling," to be published in the Proceedings of the Third Int. Conf. on Biaxial/Multiaxial Fatigue, Vol. 1, held April 3-6, 1989 in Stuffgart, West Germany.

2.20 Socie, D. F., and Shield, T. W., "Mean Stress Effects in Biaxial Fatigue of Inconel 718," Journal of Engineering Materials and Technology, Trans. ASME, Vol. 106, 1984, pp. 227-232.

2.21 Socie, D. F., and Bannantine, J. A., "Bulk Deformation Fatigue Damage Models," Materials Science and Engineering, A103, 1988, pp. 3-13.

2.22 Brown and Miller, "A Theory for Fatigue under Multiaxial Stress-Strain Conditions," Proc. Inst. Mech. Engrs., Vol. 187, pp. 745-755.

2.23 Garud, Y. S., "Multiaxial Fatigue: A Survey of the State of the Art," J. of Testing and Evaluation, Vol. 9, No. 3, May 1981, pp. 165-178.

2.24 Krempl, E., "The Influence of State of Stress on Low-Cycle Fatigue of Structural Materials: A Literature Survey and Interpretive Report," ASTM STP 649, Philadelphia, 1974.

2.25 Jordan, E. H., "Fatigue-Multiaxial Aspects," Pressure Vessels and Piping: Design Technology-1982-A Decade of Progress, ed. by Zamrik and Dietrich, ASME, New York, 1982, pp. 507-518.

2.26 Ellyin, F., and B. Valaire, "Development of Fatigue Failure Theories for Multiaxial High Strain Conditions," SM Archives, Vol. 10, Martinus Nijhoff Publishers, 1985, pp. 45-85.

2.27 Sines, G., "Failure of Materials under Combined Repeated Stresses Superimposed with Static Stresses," Tech. Note 3495, National Advisory Council for Aeronautics, Washington DC, 1955.

2.28 Sines, G., "Behavior of Metals under Complex Static and Alternating Stresses," Metal Fatigue, ed. by Sines and Waisman, McGraw-Hill, 1959.

2.29 Fuchs, H. O., "Fatigue Research with Discriminating Specimens," Fatigue of Eng. Mat. and Struct., Vol. 2, No. 2, 1979, pp. 207-215.

2.30 ASME Boiler and Pressure Vessel Code, Section III, Code Case N-47-12, Rules for Construction of Nuclear Power Plant Components, 1980.

2.31 Garud, "A New Approach to the Evaluation of Fatigue under Multiaxial Loadings," Trans. of the ASME, J. of Eng. Matl's. and Tech., Vol. 103, April 1981, pp. 118-125.

2.32 Ellyin, F., and Golos, K., "Multiaxial Fatigue Damage Criterion," J. of Eng. Matl's. of Tech., Trans of the ASME, Vol. 110, Jan. 1988, pp. 63-68.

2.33 Radakrishnan, V. M., "An Analysis of Low Cycle Fatigue Based on Hysteresis Energy," Fatigue of Eng. Matl's. and Struct., Vol. 3, 1980, pp. 75-84.

2.34 Jordan, E. H., Brown, M. W., and Miller, K. J., "Fatigue under Severe Nonproportional Loading," Multiaxial Fatigue, ASTM STP 853, K. J. Miller and M. W. Brown, Eds., ASTM, Philadelphia, 1985, pp. 569-585.

2.35 Andrews, R. M., and Brown, M. W., "Out-of-Phase Cyclic Deformation and Fatigue Fracture Studies on 316 Stainless Steel," Biaxial and Multiaxial Fatigue, EGF3, Mechanical Eng. Publications, London, pp. 641-658.

2.36 Findley, W. N., "A Theory for the Effect of Mean Stress on Fatigue of Metals under Combined Torsional and Axial Load or Bending," J. of Engineering for Industry, Vol. 81, Nov. 1959, pp. 301-306.

2.37 McDiarmid, D. L., "A General Criterion of Fatigue Failure Under Multiaxial Stress," 2nd Int. Conf. on Pressure Vessel Technology, II-61, 1973, pp. 851-862.

2.38 Kandil, F. A., Brown, M. W., and Miller, K. J., "Biaxial Low-Cycle Fatigue Fracture of 316 Stainless Steel at Elevated Temperatures," Book 280, The Metals Society, London, 1982, pp. 203-210.

2.39 Lohr, R. D., and Ellison, E. G., "A Simple Theory for Low Cycle Multiaxial Fatigue," Fatigue of Engineering Materials and Structures, Vol. 3, No. 1, 1980, pp. 1-17.

2.40 Fatemi, A., and Socie, D. F., "A Critical Plane Approach to Multiaxial Fatigue Damage Including Out-of-Phase Loading," Fatigue and Fracture of Engineering Materials and Structures, Vol. 11, No. 3, 1988, pp. 149-165.

2.41 Fatemi, A., and Kurath, P., "Multiaxial Fatigue Life Predictions under the Influence of Mean-Stresses," J. of Engineering Materials and Technology, Trans. ASME, Vol. 110, 1988, pp. 380-388.

2.42 Socie, D. F., "Multiaxial Fatigue damage Models," J. of Engineering Materials and Technology, Trans. ASME, Vol. 109, 1987, pp. 293-298.

2.43 Smith, R. N., Watson, P., and Topper, T. H., "A Stress Strain Function for the Fatigue of Metals," J. of Materials JMLSA, Vol. 5, No. 4, 1970, pp. 767-778.

2.44 Tipton, S. M., and Nelson, D. V., "Fatigue Life Predictions for a Notched Shaft in Combined Bending and Torsion," Multiaxial Fatigue, ASTM STP 853, K. J. Miller and M. W. Brown, (Eds.), ASTM, Philadelphia, 1985, pp. 514-550.

2.45 Kurath, P., Downing, S. D., and Galliart, D. R., "Summary of Non-Hardened Notched Shaft Round Robin Test Program," to be published by the Society of Automotive Engineers Fatigue Design and Evaluation Committee.

2.46 Leis, B. N., and Laflen, J. H., "Problems in Damage Analysis Under Nonproportional Cycling," J. of Engineering Materials and Technology, Trans. ASME, Vol. 102, 1980, pp. 127-134.

2.47 McDiarmid, D. L., "Designing for High-Cycle Biaxial Fatigue Using Surface Strain Records," Multiaxial Fatigue, ASTM STP 853, K. J. Miller and M. W. Brown, Eds., ASTM, Philadelphia, 1985, pp. 431-439.

2.48 Macha, E., "Generalized Strain Fatigue Criterion for Materials under Multiaxial Random Loadings," presented at the Third Int. Conf. on Biaxial/Multiaxial Fatigue, April 3-6, 1989, Stuttgart, West Germany, pp. 21.1-21.17.

2.49 Williams, R. A., Placek, R. J., Klufas, O., Adams, S. L., and Gonyea, D. C., "Biaxial/Torsional Fatigue of Turbine-Generator Rotor Steels," Multiaxial Fatigue, ASTM STP 853, K. J. Miller and M. W. Brown, Eds., ASTM, Philadelphia, 1985, pp. 440-462.

2.50 Hoffman, M., and T. Seeger, "Local Strain Approach in Multiaxial Fatigue: Feasibilities and Current Limitations," Low Cycle Fatigue and Elasto-Plastic Behavior of Materials, ed., by K-T. Rie, Elsevier Applied Science, Ltd., 1987, pp. 493-498.

2.51 Socie, D. F., "Multiaxial Fatigue Damage Assessment," Low Cycle Fatigue and Elasto-Plastic Behavior of Materials, ed. by K-T. Rie, Elsevier Applied Science, Ltd., 1987, pp. 465-472.

3.1 Doong, Shiing-Hwa, "A Plasticity Theory of Metals Based on the Dislocation Substructure," Materials Engineering Report No. 148, University of Illinois at Urbana-Champaign, UILU-ENG89-3602, 1988.

3.2 Garud, "A New Approach to the Evaluation of Fatigue under Multiaxial Loadings," Trans. of the ASME, J. of Eng. Matl's. and Tech., Vol. 103, April 1981, pp. 118-125.

3.3 Drucker, D. C., and Palgen, L., "On Stress-Strain Relations Suitable for Cyclic and Other Loading," J. of Applied Mechanics, Vol. 48, Sept. 1981, pp. 479-485.

3.4 Mròz, Z., "On the Description of Anisotropic Workhardening," J. Mech. Phys. Solids, Vol. 15, 1967, pp. 163-175.

3.5 Dafalias, Y. F., and Popov, E. P., "A Model of Nonlinearly Hardening Materials for Complex Loading," Acta Mechanica, Vol. 21, 1975, pp. 173-192.

3.6 Krieg, R. D., "A Practical Two Surface Plasticity Theory," J. of Applied Mechanics, Sept. 1975, pp. 641-646.

3.7 McDowell, D. L., "A Two Surface Model for Transient Nonproportional Cyclic Plasticity," J. of Applied Mechanics, Vol. 52, June 1985, pp. 298-308.

3.8 Drucker, D. C., "Some Implications of Work Hardening and Ideal Plasticity," Quarterly of Applied Mathematics, Vol. 7, 1950, pp. 411-418.

3.9 von Mises, R., "Mechanik det Festen Körper im Plastisch Deformablen Zustano," Göttinger Nachrichten, Math. Phys. Kl, 1913, p. 582.

3.10 Tresca, H., Mémoire sur L'Ecoulement des Corps Solides," Mém. près. Acad. Sci., Paris 18, 1868, p. 733.

3.11 Hill, R., The Mathematical Theory of Plasticity, Oxford University Press, 1950.

3.12 Hodge, P. G. Jr., "The Theory of Piecewise Linear Isotropic Plasticity," IUTAM Colloquium, Madrid, 1955.

3.13 Prager, W., "The Theory of Plasticity: A Survey of Recent Achievements," Proc., Inst. Mech. Engrs., Vol. 169, 1955, pp. 41-57.

3.14 Hodge, P. G. Jr., discussion of "A New Method of Analyzing Stresses and Strains in Work-hardening Plastic Solids," W. Prager, J. of Applied Mechanics, Vol. 24, No. 3, Sept. 1957, pp. 482-483.

3.15 Ziegler, H., "A Modification of Prager's Hardening Rule," Quarterly of Applied Mathematics, Vol. 17, No. 1, 1959, pp. 55-65.

3.16 Lamba, H. S., "Nonproportional Cyclic Plasticity," Ph.D. Thesis, T and A M Report No. 413, University of Illinois at Urbana-Champaign.

3.17 Hunsaker, B., Vaughn, D. K., and Stricklin, J. A., "A Comparison of the Capability of Four Hardening Rules to Predict a Material's Plastic Behavior," J. of Pressure Vessel Technology, Trans. ASME, Feb. 1976, pp. 66-74.

3.18 Sotolongo, W., "On the Numerical Implementation of Cyclic Elasto-Plastic Material Models," M.S. Thesis, Georgia Institute of Technology, Feb. 1985.

3.19 Prandtl, L., "Spannungsverteilung in Plastischen Koerpern," Proceedings of the First Int. Congress on Applied Mechanics, Delft, Technische Boekhandel en Druckerij, J. Waltmann, Jr., 1925, pp. 43-54.

3.20 E. Reuss, "Beruecksichtigung Der Elastischen Formaenderungen in der Plastizitaetstheorie, Z. Angew. Math. Mech., Vol. 10, 1930, pp. 266-274.

3.21 Drucker, D. C., "A More Fundamental Approach to Plastic Stress-Strain Relations," 1st U.S. Congress of Applied Mechanics, A.S.M.E., N.Y., 1952, pp. 487-491.

3.22 Matsuishi, M., and Endo, T., "Fatigue of Metals Subjected to Varying Stress," paper presented to Japan Society of Mechanical Engineers, Fukuoka, Japan, March 1968.

3.23 Annual Book of ASTM Standards, Section 3 - Metals Test Methods and Analytical Procedures, Vol. 0.3-01-Metals-Mechanical Testing; Elevated and Low-Temperature Tests, PA, 1986, pp. 836-848.

3.24 Downing, S. D., and Socie, D. F., "Simplified Rainflow Counting Algorithms," International Journal of Fatigue, Vol. 4, No. 1, Jan. 1982, pp. 31-40.

3.25 Miner, M. A., "Cumulative Damage in Fatigue," Journal of Applied Mechanics, Vol. 12, Trans. of ASME, Vol. 67, 1945, pp. A159-A164.

4.1 Socie, D. F., Waill, L. A., and Dittmer, D. F., "Biaxial Fatigue of Inconel 718 Including Mean Stress Effects," Multiaxial Fatigue, ASTM STP 853, K. Miller and M. W. Brown, Eds., ASTM, Philadelphia, 1985, pp. 463-481.

4.2 Bannantine, J. A., "Observations of Tension and Torsion Fatigue Cracking Behavior and the Effect on Multiaxial Damage Correlations," University of Illinois, Materials Engineering Report No. 128, UILU-ENG-86-3605, July 1986.

4.3 Hua, C. T., "Fatigue Damage and Small Crack Growth during Biaxial Loading," Materials Engineering Report No. 109, University of Illinois, UILU-ENG-84-3609, July 1984.

4.4 Subramanian, S., "Strain Path Dependence of Multiaxial Fatigue," M.S. Thesis, University of Toledo, Toledo, Ohio, Aug. 1989.

4.5 Fatigue Under Complex Loading: Analyses and Experiments, Wetzel (editor), Society of Automotive Engineers Advances in Engineering, Vol. 6, SAE, Warrendale, PA, 1977.

4.6 Kurath, P., Downing, S. D., and Galliart, D. R., "Summary of Non-Hardened Notched Shaft Round Robin Test Program," to be published by the Society of Automotive Engineers Fatigue Design and Evaluation Committee.

4.7 Downing, S. D., and Galliart, D. R., "A Fatigue Test System for a Notched Shaft in Combined Bending and Torsion," Multiaxial Fatigue, ASTM STP 853, K. J. Miller and M. W. Brown, Eds., ASTM, Philadelphia, 1985, pp. 24-32.

4.8 Fash, J. W., "An Evaluation of Damage Development during Multiaxial Fatigue of Smooth and Notched Specimens," Ph.D. Thesis, Materials Engineering Report No. 123, University of Illinois, UILU-ENG-85-3607, August, 1985.

5.1 McDowell, D. L., "An Experimental Study of the Structure of Constitutive Equations for Nonproportional Cyclic Plasticity," J. of Engineering Materials and Technology, ASME Trans., Vol. 107, Oct. 1985, pp. 307-315.

5.2 Kanazawa, K., Brown, M. W., and Miller, K. J., "Cyclic Deformation of 1% Cr-Mo-V Steel Under Out-of-Phase Loads," Fatigue of Engineering Materials and Structures, Vol. 2, 1979, pp. 217-228.

5.3 Brown, M. W., and Miller, K. J., "Biaxial Cyclic Deformation Behavior of Steels," Fatigue of Engineering Materials and Structures, Vol. 1, 1979, pp. 93-106.

5.4 Hua, C. T., "Fatigue Damage and Small Crack Growth during Biaxial Loading," Materials Engineering Report No. 109, University of Illinois at Urbana-Champaign, UILU-ENG84-3609, July 1984.

5.5 Fatemi, A., and Socie, D. F., "A Critical Plane Approach to Multiaxial Fatigue Damage Including Out-of-Phase Loading," Fatigue and Fracture of Engineering Materials and Structures, Vol. 11, No. 3, 1988, pp. 149-165.

MATERIALS ENGINEERING—MECHANICAL BEHAVIOR

College of Engineering, University of Illinois at Urbana-Champaign

Report No.

138 "The Effects of Strain Induced Softening on the Load Carrying Capability of Components," James L. Handrock, November 1987 (UILU-ENG 87-3604).

139 "Fatigue Crack Closure and Crack Growth Outside the Small Scale Yielding Regime," R. Craig McClung, December 1987 (UILU-ENG 87-3605).

140 "A Micro-mechanistic Life Prediction Model Suitable for Isothermal and Thermo-mechanical Fatigue," Richard W. Neu, January 1988 (UILU-ENG 88-3601).

141 "Adhesion, Microstructure and Interface Studies of Evaporated and Ion Plated Copper and Chromium Coatings," Jeffrey C. Logas and J. M. Rigsbee, February 1988 (UILU-ENG 88-3602).

142 "A Long-Life Regime Probability-Based Fatigue Design Method for Weldments," Sahng Kyoo Park and F. V. Lawrence, Jr., June 1988 (UILU-ENG 88-3603).

143 "Post-Weld Laser-Treatment of 18 Ni (250) Maraging Steel," Grzegorz Banas, James Michael Rigsbee and Frederick V. Lawrence, Jr., July 1988 (UILU-ENG 88-3604).

144 "Structure and Properties of Ion Plated Aluminum Coatings," Howard S. Savage and J. M. Rigsbee, October 1988 (UILU-ENG 88-3605).

145 "The Effects of Weld Geometry on Weld Quality and Fatigue Properties of Galvanized HSLA Laser Seam Weldments," Ming Ke and Frederick V. Lawrence, Jr., October 1988 (UILU-ENG 88-3606).

146 "Structure and Properties of Titanium Nitride Strengthened Microlaminate Composites," John H. Givens and J. M. Rigsbee, November 1988 (UILU-ENG 88-3607).

147 "Biaxial-Tension Fatigue of Inconel 718," Daniel L. Morrow, February 1989 (UILU-ENG 89-3601).

148 "A Plasticity Theory of Metals Based on the Dislocation Substructures," Shiing-Hwa Doong, February 1989 (UILU-ENG 89-3602).

149 "Structure, Chemistry, and Electrochemical Behavior of Mixed Metal (Ruthenium, Titanium) Oxides," Joseph E. Suarez and J. M. Rigsbee, May 1989 (UILU-ENG 89-3603).

150 "The Effect of Casting Porosity on the Fatigue Life of Lost-Foam Cast Iron and Aluminum-Silicon 319," Anthony J. Biell IV and Frederick V. Lawrence, Jr., August 1989 (UILU-ENG 89-3604).

151 "A Variable Amplitude Multiaxial Fatigue Life Prediction Method," Julie Ann Bannantine, October 1989 (UILU-ENG 89-3605).